CRANFIELD UNIVERSITY

School of Water, Energy and Environment
(SWEE)

ABDULRAHMAN ALENEZI

Academic Year 2016 -2017

PhD

Supervisor: Dr. Joao Amaral Teixeira
Dr. Abdulmajid Addali

CRANFIELD UNIVERSITY

School of Water, Energy and Environment
(SWEE)

PhD Thesis

Academic Year 2015 – 2016

ABDULRAHMAN ALENEZI

Heat Removal in High Pressure Turbine Seal Segments

Supervisor: Dr. Joao Amaral Teixeira
Dr. Abdulmajid Addali
February, 2017

This thesis is submitted in partial fulfilment of the requirements for the degree of Doctor of Philosophy

To the soul of my father and mother

ACKNOWLEDGEMENTS

All praise to Allah (God), the most Merciful, the most Gracious, for all the uncountable bounties He has granted me and for helping me to successfully finish my research.

My sincere debt of gratitude goes to my supervisors, Dr. J. A. Teixeira and Dr. A. Addali they patiently provided the vision, encouragement and advice necessary for me to precede through the doctoral program and complete my PhD.

Special thanks to Dr. Hamad Alhajeri, Dr. Abdulrahman Almutairi and Dr. Abdulaziz Gamil on their motivation and encouragement to achieve such work along with their continued input, support and enlightenment throughout the study. Your outstanding help will never be forgotten.

I wish to thank my mother who passed away when I was 18, my father who also passed away during my research period. Their love provided my inspiration and was my driving force. I owe them everything and wish if I could have the chance show them just how much I love and appreciate them.

I wish to also thank my wife, her love and support provided me with strength to finish this journey. My sisters and brothers, their love and encouragement gave the strength.

They all already have my heart so I will just give them a heartfelt “thanks.”

ABSTRACT

An important parameter for turbomachinery designers is “clearance control”, because the clearances between interfaces must be set to optimum values to maximize power output, operational life and efficiency. Leakage of hot gas resulting from excessive clearance, can lead to flow instabilities, components overheating, lower cycle efficiency and a dramatic increase in specific fuel consumption (SFC).

Seal segments are used to reduce blade tip leakage, maintain coolant air flow and the stability of rotor-dynamic systems, helping to maximize blade performance. Seal segments in the High-Pressure Turbine (HPT) stages are one of the hottest components as they face the hot gases coming from the combustion chamber with temperatures which can reach 1700 ^{0}C and which makes them subject to oxidation, erosion, and creep. Thus, seal segments need to be protected. They are currently cooled using jet impingement techniques, passing cooling air (supplied by the high-pressure stage of the compressor) through channels to directly impinge on the hot surfaces.

The focus of this research was to improve the jet impingement cooling of the seal segments in HPTs by investigating methods that provide more effective heat removal. The role played by configurations of ribs (surface roughness using bespoke turbulators), custom-made seal-segments, and surface features such as contouring, both in isolation and combination, were investigated using numerical methods. A set of 174 simulations were carried including the use of uniform and non-uniform roughness elements with different shapes and heights.

Firstly, three different uniform roughness elements were tested, a square cross-sectional continuous rib, a hemi-spherical pin-fin and a cubical pin-fin for three jet impingement angles of α=90°, 60° and 45°. Each roughness element was also tested for six different heights (e) between 0.25 mm and 1.5 mm in

increments of 0.25 mm. Results are presented in the form of average Nusselt number $\overline{N_u}$ within and beyond the stagnation region.

- For α=90º, maximum enhancement of $\overline{\boldsymbol{N_u}}$ was obtained using a cubical pin-fin with e=0.5 mm which gave a 7.2% increase, compared to the no-rib case. A continuous rib of height e=0.25 mm gave a small increase in $\overline{\boldsymbol{N_u}}$. Cubical and spherical pin-fins gave maximum heat transfer rates at e=0.5 mm and 0.75 mm respectively. At e=1.5 mm, a dramatic decrease in $\overline{\boldsymbol{N_u}}$ was observed.
- For both α=45º and 60º, significant improvement in $\overline{\boldsymbol{N_u}}$ was found for all ribs. The best performance was for the hemi-spherical pin-fin, adding about 5.0% and 4.4% to the $\overline{\boldsymbol{N_u}}$, for 45º and 60º respectively compared to the no-rib case. This was closely followed by the cubical pin-fin and continuous rib.

Secondly, the effect of using a roughness element with a square cross section in the shape of a circle, on the average Nu was investigated for four different radial locations (R), three jet angles (α) and six rib heights (e).

- For α=90º, a rib height that equalled the velocity boundary layer thickness was the most effective for enhancing heat transfer **(e = ??)**. However, too high a rib, say 1.25 or 1.50 mm gave a lower heat transfer rate than the no-rib case.
- For inclined jets, the most effective rib height to enhance heat transfer was 0.25 mm regardless of the rib location.
- For α=45º, placing the rib at R/D=1.5 gives a heat transfer enhancement of between 2.3% and 6.8% for all rib heights. For α= 45º and 60º maximum enhancement was 7% and 4%, respectively, at R/D=3 with rib height e=0.25 mm.

Finally, the roughness element used was continuous, of square cross-section, in the shape of tear drops and reversed tear drops. This meant the rib did not act as a total barrier to flow in either the uphill or downhill directions.

TABLE OF CONTENTS

LIST OF FIGURES

LIST OF TABLES

Nomenclature

Symbol	Description	Units
C_p	Specific heat	$[J/kg.K]$
D	*Hydraulic* diameter	$[m]$
h	Convective heat transfer coefficient	$[W/m^2K]$
L	Domain length	[m]
N_u	Nusselt number	[-]
Nu_{stag}	Stagnation Nusselt number	[-]
$\overline{N_u}$	Average Nusselt number	[-]
$\overline{N_{u_o}}$	Baseline case average Nusselt number	[-]
P	Mean pressure	[Pa]
Pr	Prandtl number	[-]
q_w	Wall heat flux	$[W/m^2]$
r	radial distance	[m]
r_c	Recovery factor, $= \frac{p_2}{p_1}$	[-]
r_1	Length of low-pressure region before the rib	[m]
r_2	Length of low-pressure region after the rib	[m]
Re	Jet Reynolds number	$[m^3/s]$
T	Mean temperature	[K]

T_{ref}	Reference temperature	[° C]
T_{aw}	Adiabatic wall temperature	[°C]
T_w	Wall temperature	[° C]
T_j	Jet temperature	[° C]
T_∞	Free stream temperature	[° C]
$T^{`}$	Fluctuating temperature	[K]
T_i	Turbulence intensity	[-]
U_f	Jet velocity	[m/s]
$\overset{+}{U}$	Velocity	[m/s]
U_τ	Shear velocity	[m/s]
U_i	Mean velocity	[m/s]
$U^{`}$	Fluctuating velocity	[m/s]
u_∞	Free stream velocity	[m/s]

Greek Symbols

Sym-bol	**De-scrip-tion**	**Units**
α	angle of impingement	$[\,^{o}\,]$
k	thermal diffusivity	$[m^2/s]$
μ	viscosity	$[kg/ms]$
ν	kinematic viscosity	$[m^2/\,s]$
ρ	density	$[kg/m^3]$
y	Axial distance measured from nozzle exit	[m]
$\overset{+}{y}$	Near-wall distance	[m]
τ	Shear stress	[Pa]
δ	boundary layer thickness	[m]

1 Introduction

1.1 Thermodynamics of gas turbine

In a gas turbine (GT) engine, the turbine is located downstream of both the compressor and the combustor, see Figures 1-2 and 1-3, which means that the flow into the turbine has a pressure of up to 40 bar, and a temperature of up to 1700 0C. The gas kinetic energy is converted into jet thrust, and as the high pressure, high temperature gas flows past the turbine's rotor blades, the turbine converts these to kinetic energy of rotation which is transmitted to a shaft, producing a torque. The GT is therefore a heat engine which follows the Joule-Brayton cycle where four main processes occur, induction, compression, combustion and exhaust. Combustion takes place at a constant pressure while both compression and extraction are isentropic processes as shown in Figure 1-1

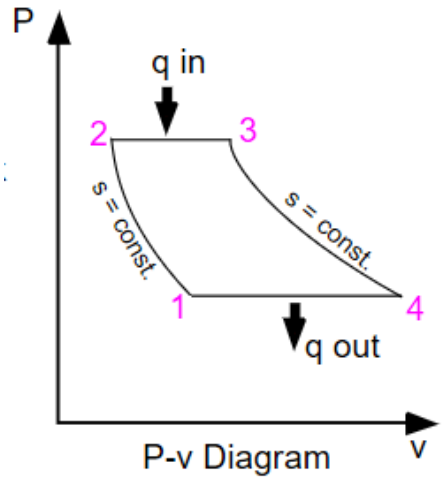

Figure 1-1 : P-V Gas turbine closed cycle

GTs operate either on an open cycle (aerospace turbines, Figure 1-2) or closed cycle (land-based turbines, Figure 1-3) depending on the use of the exhaust gas. The land-based turbines are used in industries to produce shaft power while aerospace turbines are used in aircraft to produce, essentially, thrust

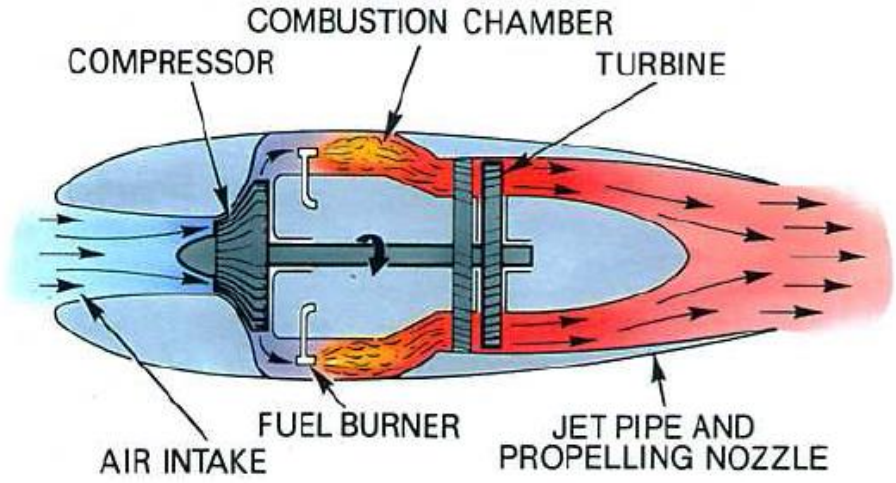

Figure 1-2: Turbo-Jet engine [1]

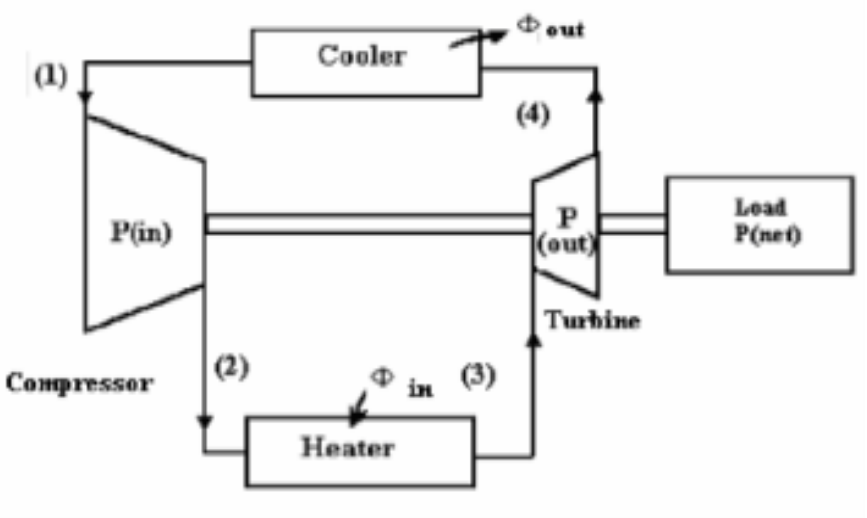

Figure 1-3 : Block diagram of closed gas turbine cycle (Land-Based) [1]

The efficiency of the GT closed cycle is the ratio between the net power output of both the turbine and the compressor to the combustion heat input:

$$\boldsymbol{Efficiency\ (\eta) = \frac{net\ work\ output}{heat\ supplied} = \frac{W_{34}-W_{12}}{Q_{23}} = \frac{C_p(T_3-T_4)-C_p(T_2-T_1)}{C_p(T_3-T_2)} = 1-\frac{T_4}{T_3}} \qquad (1.1)$$

Using the isentropic p-T relation:

$$\boldsymbol{\frac{T_2}{T_1} = r^{\frac{\gamma-1}{\gamma}} = \frac{T_3}{T_4}} \qquad (1.2)$$

Where r is the pressure ratio, $r = \frac{p_2}{p_1}$, T_1, T_2, are compressor inlet and outlet temperatures, T_3, T_4 are turbine inlet and outlet temperatures, Υ=1.4 for air, this leads to:

$$\boldsymbol{\eta = 1 - \left(\frac{1}{r}\right)^{\frac{\Upsilon-1}{\Upsilon}}} \qquad (\mathbf{1.3})$$

Where Υ=1.4 for air,

Equations 1.2 and 1.3 show that the GT thermal efficiency increases by increasing the GT inlet temperature and overall pressure ratio. Raising the turbine inlet temperature has always been an area of great research interest ever since the GT was first introduced. However, this temperature is limited by the turbine blade material melting point unless blade cooling is used, which was introduced into civilian engines in the early 1940's. Today, turbine blade cooling allows advanced turbines to operate at temperatures as high as 1700 ^{0}C which is beyond the melting point of most advanced blade materials [2]. A compressor discharges bleed air (1%-3% of total flow) with a temperature of about 600-700 ^{0}C to cool the hot turbine components [3] . However, this cooling technique should be efficient and consume the minimum mass flow rate in order not to reduce cycle efficiency [4]

1.2 Heat Transfer Characteristics

Flow can exist in three regimes, laminar, turbulent or in the transitional phase. Laminar, or streamline, flow occurs at relatively low flow velocities and can be characterized as layers of fluid flowing in parallel with no disruption between them. Turbulent flow, however, occurs at high velocity with the existence of random fluctuations and disruptions. The flow regime can be specified by the value of Reynolds number (R_e), the most significant dimensionless number in fluid dynamics, and which is defined as the ratio of inertial and viscous forces. Based on the use of bulk velocity (U) and nozzle diameter (D), Reynolds number can be defined as:

$$\boldsymbol{R_e = \frac{\rho UD}{\mu} = \frac{UD}{\nu}} \qquad (\mathbf{1.4})$$

Where ρ is the density of the fluid, μ is its dynamic viscosity and ν is its kinematic viscosity.

The Prandtl number (Pr) is a dimensionless number which can be used to define the boundary layer thickness. It is a fluid property which depends on the fluid state and represents the ratio of fluid kinematic viscosity, ν, to thermal conductivity, k. Its value can be found in property tables:

$$\boldsymbol{P_r = \frac{\nu}{k} = \frac{\mu . C_P}{k}} \qquad (\mathbf{1.5})$$

Where *k* is the thermal conductivity and Cp is the specific heat at constant pressure.

The Nusselt number (N_u) is the ratio of convective to conductive heat transfer and is a significant non-dimensional parameter used evaluate heat transfer. Nu is a function of R_e and P_r

$$\boldsymbol{N_u = f(R_e , P_r)} \qquad (\mathbf{1.6})$$

N_u is the ratio of convective to conductive heat transfer If it's value is close to unity that means both convection and conduction have a similar magnitude and the flow is almost stationary or laminar. However, if Nu has a large value, it means more heat is convected than conducted and the flow will be turbulent. Nu can be defined as:

$$\boldsymbol{N_u = \frac{Convective\ heat\ transfer}{Conductive\ heat\ transfer} = \frac{h . D}{k}} \qquad (\mathbf{1.7})$$

Where h, the heat transfer coefficient is given by:

$$\boldsymbol{h = \frac{q_w}{T_w - T_{ref}}} \qquad (\mathbf{1.8})$$

Where q_w is heat flux and T_w is wall temperature.

Usually T_{ref} is either the jet temperature (T_j) or the adiabatic wall temperature (T_{aw}), the latter can be obtained from the non-dimensional recovery factor,

$$\boldsymbol{recovery\ factor = \frac{T_{aw} - T_j}{U_j^2/2C_p}} \qquad (\mathbf{1.9})$$

The Nusselt number varies depending on which temperature ($T_j\ or\ T_{aw}$) is chosen as the reference temperature. For low Reynolds numbers, the difference in the value of the Nusselt number will not be noticeable. However, for large Reynolds numbers, the reference temperature must be correctly chosen. How to choose the reference temperature was explained by [5] and [6]

The average Nusselt number ($\overline{N_u}$) over a circular plate can be obtained by:

$$\boldsymbol{\overline{N_u} = \bar{h}\,\frac{D}{k} = \frac{2}{R}\int_0^R N_u(r)\,\mathrm{dr}} \qquad (\mathbf{1.10})$$

Where r is the radial distance from the stagnation point

1.2.1 Thermal boundary layers

Convective heat transfer occurs when there is an exchange in thermal energy between a heated surface and a fluid. Temperature difference between the wall and the fluid would create such thermal energy exchange. When the fluid layer becomes in contact with the stationary heated wall, its velocity is equal to zero due to the no-slip condition and its temperature would be the same as the wall temperature. If the fluid is stationary and in contact with a heated wall, then conduction heat transfer would occur between the fluid and the wall. Figure 1-4 shows a typical velocity and thermal boundary layer of a flow over a plate.

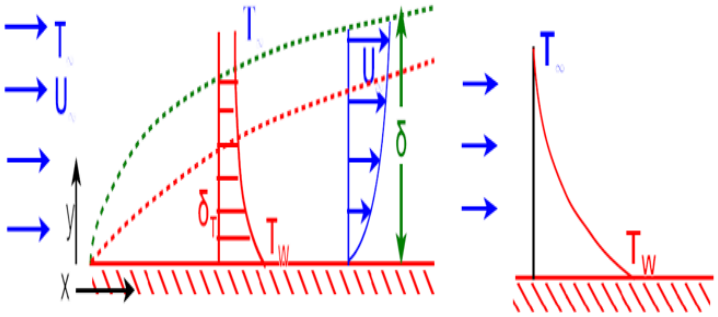

Figure 1-4 Thermal boundary layer for external flow [7]

Consider a fluid with freestream velocity where U_∞ is the freestream velocity, and T_∞ is the freestream temperature, T_w is the wall temperature as shown in Figure 1-4. Across the boundary layer that develops along the wall, the fluid temperature changes from its freestream value, T_∞ , to the wall value, T_w.

A thermal boundary layer therefore develops of thickness δ_T, defined as the distance at which

$$(T - T_w) = 0.99(T_\infty\text{-}T_w) \qquad (1.11)$$

The temperature boundary layer thickness can usually be calculated using the equation

$$\frac{(T_w - T)}{(T_w - T_\infty)} = \left(\frac{y}{\delta_T}\right)^{1/7} \qquad (1.12)$$

Where y is the vertical distance from the wall as show in Figure 1-5 below,

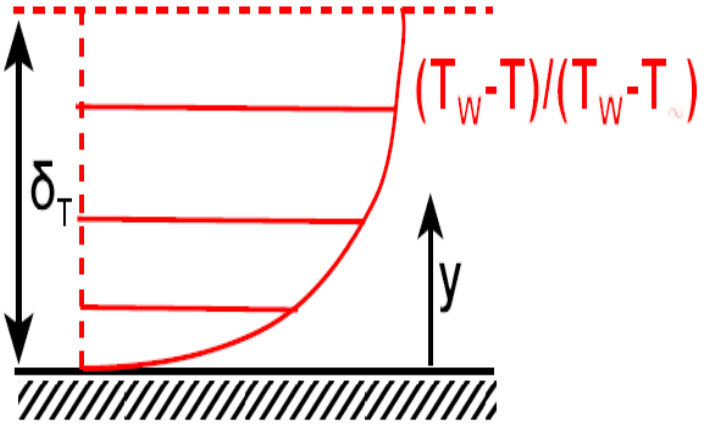

Figure 1-5 Thermal boundary layer thickness (δ_T) [7]

1.3 Gas turbine blade cooling

Cooling of components can be achieved using air or liquid. Due to its high specific heat capacity, liquid cooling might seem to be the more efficient choice but it should not be used in jet engines because of leakage and corrosion problems. Air cooling has the major advantage that it can be discharged into the main flow without any complications. Typically 1-3% of the intake air is bled from the compressor main flow and used as cooling air, reducing blade temperature by 200-300 ^{0}C [3]. The types of cooling mechanisms used in GT blades can be classified generally as either internal or external cooling, though all use air as a cooling fluid to remove heat from turbine blades. Each technique; pin fin, film, convective, impingement cooling, cooling effusion, etc., is different in its own way.

Turbines operate under extreme conditions; each blade operates under large centrifugal loads due to a rotation speed of around 10,000 rpm (a common speed) and high temperatures. To overcome the associated problems of oxidation, erosion and creep, different complex cooling techniques have been used over the years, see Figure 1-6, typically using either new materials or more efficient cooling techniques.

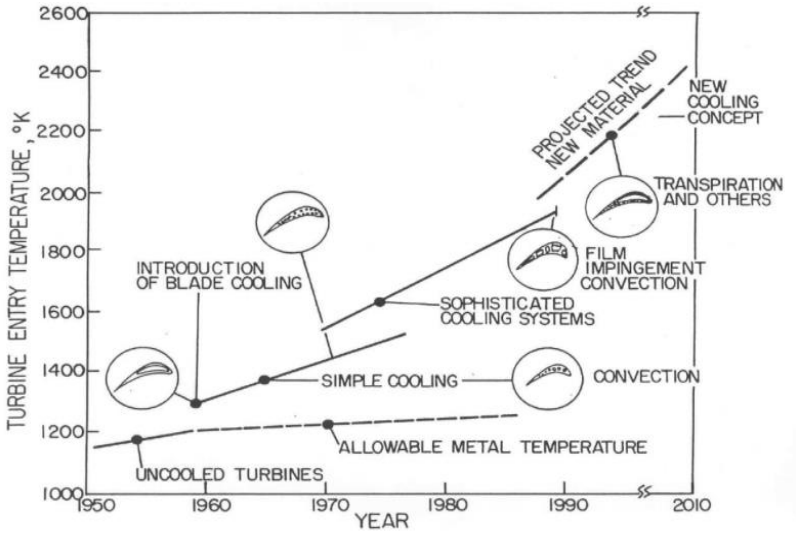

Figure 1-6: Chronology of turbine entry temperature [1]

Figure 1-7 below shows a typical nozzle guide vane (NGV) and turbine blade cooling configuration

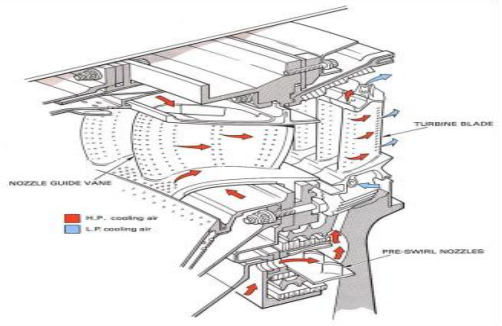

Figure 1-7: Typical NGV and blade cooling configuration [1]

1.3.1 External cooling

I. Film cooling

Film cooling (also called thin film cooling) is an effective cooling method that works by generating a thin layer of air on the turbine blade surface using small holes in the blade. This air layer acts as a thermal barrier protecting the blade surface from high temperature gases. The holes can have several shapes with different blade locations but they are most often on the blade leading edge [8].

This cooling technique uses internal convection heat transfer to cool hot turbine components such as shrouds, turbine blade surfaces, endwalls and blade tips through a variety of film hole designs. Figure 1-8 shows a typical film cooling configuration on a turbine blade where coolant enters the bottom side of the blade directed by a passage and exits the blade through discrete holes. A concise description of film cooling is:

"Film cooling is the introduction of a secondary fluid (coolant or injected fluid) at one or more discrete locations along a surface exposed to a high temperature environment to protect the surface not only in the immediate region of injection but also in the downstream region" [6]

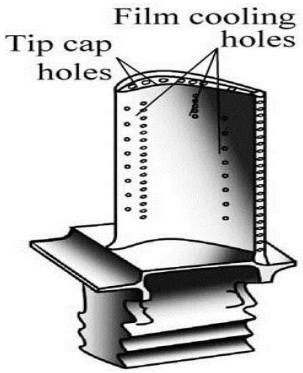

Figure 1-8: Film cooling configuration [1]

II. Cooling Effusion

Porous material with a large number of small orifices can be added to the blade surface. Ideally, these porous holes should be large enough not to be blocked by impurities but small enough to prevent excessive interaction between air jet and mainstream. Effusion cooling forces cooling air to form a smooth film or a boundary layer to help improve the effectiveness of conventional film cooling. The size and the number of cooling holes are the main difference between effusion and film cooling, effusion has bigger holes with diameters close to 0.2 mm. These bigger holes affect the amount of coolant air exiting from each hole, its pressure, and velocity [9]

III. Pin fin cooling

In order to enhance heat transfer in the blade trailing edge, film cooling is used but in addition, an array of pin fins may be added to the blade surface to enhance heat transfer when the high-velocity coolant flows across the fins. Fin type, spacing between fins and fin shape play a significant role in enhancing heat transfer. Armellini [10] employed a rectangular cooling channel using a 2-D PIV technique with four type of fins; square, circular, triangular and rhomboidal (Figure 1-9) . Flows with three different Reynolds numbers, 800, 1800 and 2800 were used and the author observed the upwash flow was weakened by using triangular and rhomboidal fins. For the rhomboidal fins 100% vortex shedding occurred at Re of 1800 and 2800, but for triangular fins vortex shedding reached 100% only at Re of 2800. However, vortex shedding did not reach 100% for either square or circular fins at any of the three Reynolds numbers.

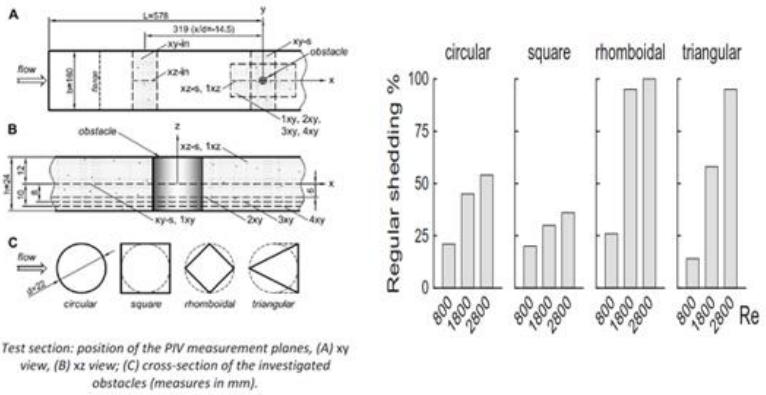

Figure 1-9: Pin fin shapes and vortex shedding [10]

1.3.2 Internal cooling

Turbine blade internal cooling efficiency depends on the design of the passages inside the blades which carry the coolant air and transfer it to the outside of the blades. Impingement and pin-fin cooling are techniques for internal cooling. Jet impingement is an efficient cooling technique applied to the inner surface of the blade through small holes in the passages so that the cooling fluid impinges

directly on the hot regions. Thus, it is used where the highest thermal loads apply (i.e. the leading edge region) as shown in Figure 1-10.

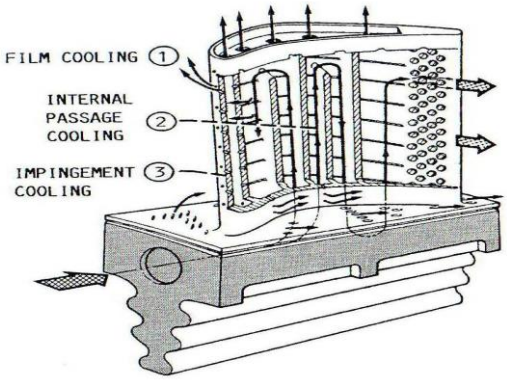

Figure 1-10: Typical gas turbine blade cooling 3D configuration [1]

Jet Impingement cooling is the most used technique for internal cooling. It is a complex technique introduced in the early 1960's and has proven to be very effective for increasing the heat transfer rate compared to other cooling techniques. It is applied mostly on the inner surface of the blade through small holes in the inner passages to directly impinge on the hot regions as shown in Figure 1-11 . The jet impingement heat transfer rate from or to a surface depends on several parameters including: Reynolds number, jet-to-target distance (H/D), nozzle geometry, turbulence model, target surface roughness and jet temperature as indicated by [11] (this will be discussed in the next chapter in more detail).

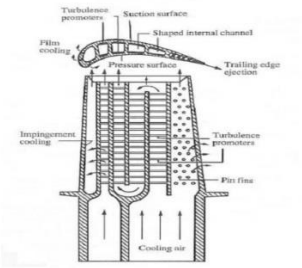

Figure 1-11: Impingement cooling in HPT blade [12]

1.4 High pressure turbine (HPT) seal segments

The seal segments are located in the first turbine stage which is one of the hottest sections of the engine between casing and top of the turbine blade. It is used to reduce the blade over tip leakage helping to maximise blade performance.

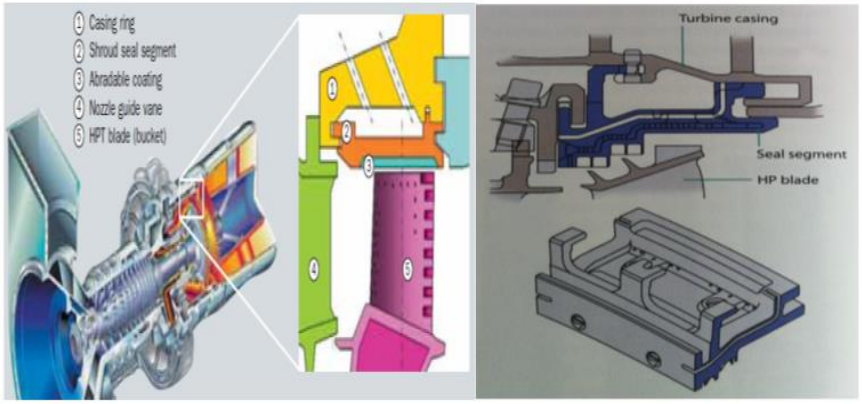

Figure 1-12: Location of seal segments in HPT [13]

Figure 1-12 represents a cooled turbine shroud segment for a GT engine, having an axially extending shroud ring segment with an inner surface, an outer surface, an upstream flange and a downstream flange. The flanges mount the shroud ring within an engine casing. A perforated cooling air impingement plate is attached to the outer surface of the shroud ring between the upstream flange and the downstream flange, with an impingement plenum defined between the impingement plate and the outer surface. The cooling passages in the ring segment are extended axially to between the impingement plenum and an outlet. A channel adjacent to the outlet directs cooling air from the outlet towards a downstream stator vane to cool the stator vane.

1.5 Motivation

This research project has been motivated primarily by the importance of the topic for the development of the GT engine. Gas path sealing at the blade tip, and inter-stage sealing have been major concerns in the design and development of aircraft engines since the introduction of the GT engine in the late 1960's. Effective blade tip sealing has been a difficult challenge due to the small clearance between the blade tip and the casing (shroud) which can vary due to changes in centrifugal forces and temperatures between being stationary and rotating under load. In aero engines, tip sealing is even more challenging due to the frequent and extreme changes in operational conditions; between taxi-ing, take-off, cruising and landing.

Secondly the project has been motivated by the commercial implications of improved cooling of seal segments. Improved blade tip sealing in HPTs and high-pressure compressors (HPCs) are important because maintaining the optimum clearance will increase engine efficiency, reduce specific fuel consumption, extend component life (time-on-wing), and compressor stall margin. Typical annual cost of maintaining and overhauling large commercial GT engines can easily exceed $1M [2].

The third consideration was that information about HPT seal segment internal cooling available in open sources is limited. This research makes a contribution to the study of seal segment cooling strategies and expands the knowledge available in the public domain on the design of efficient HPT seal segments cooling technique. A limitation of the literature in the public domain was that the jets issuing from the nozzles were perpendicular to the heated surface, this study extends the information available to impingement angles of 40^0 and 60^0 and shows this to have a significant effect on the heat transfer rate.

The final consideration was the extension of current knowledge. Seal segments are currently cooled using jet impingement with an inclined circular single

jet (see Figure 1-12) which has proven to be an effective cooling technique in many industrial applications . However, studies in the literature have reported that the local Nusselt number of artificially roughened plates can be increased substantially compared with that of a smooth wall. This possible dramatic increase in heat transfer helped inspire this study which will investigate geometrical modifications of both seal segment surface roughness and impingement jet angles to determine heat transfer characteristics and how they could be increased for such applications.

1.6 Aims and Objectives

The aim of this investigation is to maximise the heat transfer of seal segments by determining the most effective plane and cross-sectional shapes, and heights of surface ribs added to a flat plate to act as turbulator configurations, for different jet impingement angles.

The objectives that lead to the meeting of these aims are to:

1- Perform a set of numerical investigations to validate the numerical models available for this research and identify modelling performance of various turbulence modelling techniques (k-ε and k-ω) for flat plates (surfaces). The seal segment surface considered in this research will be a flat surface, ignoring all extra fittings.

2- Investigate numerically the effect of simulated surface roughness on heat transfer by using various types of roughness elements. Each roughness element was to be tested for six different heights (e) from 0.25 mm to 1.5 mm in incremental steps of 0.25 mm for three different jet angles (α) of 90º, 60º and 45º.

3- Investigate numerically the effect of using a uniform roughness element geometry in the shape of a circle with square cross section on the average heat transfer. The effectiveness of the roughness element will be tested for four different rib radial locations (R), six heights (e) and three jet angles (α).

4- Investigate numerically the effect of using a non-uniform roughness element geometry under the influence of inclined jet. The elements took the shape of square cross-section continuous ribs which had the plan contour of tear drops and reversed tear drops.

1.7 Contribution to knowledge

In general, information about HPT seal segment internal cooling available in open sources is limited. This research makes a contribution to the study of seal segment cooling strategies and expands the knowledge available in the public domain on the design of efficient HPT seal segments cooling technique.

In addition, the majority of the studies of HPT seal segment design reported used turbulators of a single height, with uniform shape, fixed at a given location on the heated surface. This research has contributed to the investigation of cooling parameters for the improved removal of heat by including modifications of the HPT seal segment surface by adding different types of rib surface roughening elements, with both uniform and non-uniform shapes.

Uniquely, this research aimed to improve the overall heat transfer on a flat plate by investigating non-uniform turbulator shapes, with varying heights and locations based on a deep pre-study of flow contours over the heated surface. In addition, the ribs added to the baseplate had a more random character which differs from the reports in the literature which tended to focus on regular patterns of discrete dimples, pins or ribs.

1.8 Thesis structure and dissertation summary

This section presents a brief introduction to the structure and contents of the nine chapters forming this thesis.

Chapter 1 provides an introduction to the research area by presenting a brief background of relevant GT thermodynamics including heat transfer characteristics, gas turbine blade cooling and high pressure turbine seal segments. Motivation for the research, its aims and objectives and contribution to knowledge, are given.

Chapter 2 presents a literature review of jet impingement cooling techniques. The chapter has been divided into three sections. The first presents research into fluid flow characteristics; including all aspects of jet flow, stagnation point heat transfer, and heat transfer distribution. The second section describes studies that focused on heat transfer enhancement techniques such as nozzle geometry, Intermittency, surface finish, turbulence promoters and angle of impingement. The last section contains concluding remarks identifying gaps in the available literature that have influenced this study.

Chapter 3 compares the results of the validation tests against experimental work. The chapter is divided into two sections; first validation of the 2-D axisymmetric model using an orthogonal jet, and second validation of the 3-D model for inclined jets. Both validations were made against the experimental results of O'Donovan and Murray [14] and [15]. The chapter includes details of both experimental and numerical methodology.

Chapter 4 describes results of simulating the heat transfer and fluid flow of an air jet impinging on a flat, smooth plate. The parameters considered for characterizing the fluid flow are vorticity, turbulence intensity and flow velocity. Heat transfer distribution across the impinged surface was considered as measuring the behaviour of the system, the simulated values were recorded and analyzed and the

correlation between heat transfer and fluid flow was obtained for time averaged data.

Chapter 5 addresses the effect of simulated surface roughness on heat transfer. This was achieved by investigating the heat transfer in two cases: a smooth, horizontal surface (the baseline case) and the same surface with three different roughness elements, square cross-sectional continuous rib, a hemi-spherical pin-fin and cubical pin-fin added to it. Each roughness element was tested for six different heights (e) from 0.25 mm to 1.5 mm in incremental steps of 0.25 mm for three different jet angles (α) of 90º, 60º and 45º.

Chapter 6 assesses the introduction of a uniform roughness element with square cross section, with a plan shape of a circle, on the average Nu. The effectiveness of the roughness element was tested for four different radial locations and six heights. The chapter is divided into two main sections: normal jet impingement (α=90º) and Inclined jet impingement (α=45º and α=60º).

Chapter 7 addresses the use of roughness elements of non-uniform plan shape designed to enhance heat transfer in the uphill direction especially for the lower inclined angle (α=45º) where less uphill flow takes place. These ribs were square cross-section, continuous, with the plan shape of a tear drop and reversed tear drop. Each roughness element was tested for two radial locations, six different heights and two angles of jet inclination.

Chapter 8 concludes the thesis. A summary of dissertation and key findings with contributions to knowledge highlighted.

Chapter 9 presents ideas for future work.

2 Literature Review

The complexity of impinging jet flow makes the heat transfer from the surface subjected to such flow multifaceted and difficult to resolve. However, a range of jet configurations and parameters have been investigated in terms of both heat transfer and fluid flow. The main objective of this research is to study the heat transfer mechanisms for an impinging air jet so most of the research reviewed in this chapter are investigations of the characteristics of both heat transfer and fluid flow for jet impingement.

This chapter has been divided into four sections. The first presents a general overview from the literature on different types of turbulence models. The second part includes research that investigated fluid flow characteristics. This includes all aspects of jet flow, stagnation point heat transfer, and heat transfer distribution. The third section describes studies that focused on heat transfer enhancement techniques such as nozzle geometry, Intermittency, surface finish, turbulence promoters and angle of impingement. The last section contains concluding remarks identifying gaps in the available literature that have influenced this study.

2.1 Turbulence model

In designing impinging jet device, the prediction of heat transfer coefficient profile (i.e. Nu), pressure drops and fluid flow per unit target area is required by the hardware designer. The use of either a calculation method and/or hardware models should be accurate enough to save time and money by minimizing the amount of hardware tests required as the use of those reliable models provides flexibility, fast and inexpensive alternative than experimental studies. Three main well know equations are involved in modelling any incompressible turbulent flow; mass, momentum and conservation of energy equations. For jet impingement applications, it is a quite big challenge to predict the accurate turbulent jet behaviour for turbulent flow occurs in the whole domain downstream of the nozzle.

Computational Fluid Dynamics (CFD) uses finite element, finite difference and finite volume methods to compute heat transfer coefficient and velocity profile; however, it is difficult to accurately predict these values due the complicit interaction between turbulent flow and wall unless a use of stable turbulence models employing efficient computation grids to accurately resolve both nozzle upstream and downstream flow with boundary conditions of zero-gradients and constant static pressure. Turbulence models will be viewed briefly but critically below.

2.1.1 DNS and LES

Solving Navier-Stokes, continuity and energy mass diffusion equations by using an extreme small grid to fully resolve of all the turbulent flow properties is the purpose of the direct numerical simulation (DNS) method. The use of small grid is time consuming but it is necessary because in jet impingement, the scales of microscopic turbulent length are too small comparing to macroscopic lengths involved (e.g. H and D) which also limit the use of this method to Lower Reynolds numbers than those in the gas turbine internal cooling applications [14] To overcome this, the use of the large eddy simulation (LES) is an efficient alternative CFD model which gives a better understanding of the effect of formation ,propagation and eddies flow over both heart transfer characteristics and velocity field, however, even with the advantage of this method adopting high Reynolds numbers, this method consumes a great amount of time and computing power for high accuracy results. Cziesla [15] employed LES model using a slot jet to predict Local Nusselt number within 10% of experimental measurements reporting that although particular codes is limited to Mach number <=1, the use of LES model for turbulent flow may not have either upper or lower limit on Re but for laminar flow, the use of DNS offers a better accuracy due to the small influence of turbulence over the time-averaged techniques which be discussed below. Briefly, when computational cost and time is not a real concern, LES method is the right choice.

2.1.2 The RANS approach

Reynolds averaged Navier-Stokes (RANS) model uses time-averaged equations seeking for time consuming and uncostly computational solution. Two main categories Reynolds-averaged Navier-Stokes (RANS) model uses in jet flow applications, eddy-viscosity model which considers the turbulent viscosity as a scalar quantity assuming isotropy normal stresses and the costly full second moment closure (SMC) model [16]. SMC model works based on the idea of tracking all Reynolds stresses or different nonuniform turbulent viscosity components using semi-empirical equations to approximate both Reynolds stresses and heat fluxes based on expected physical trends than direct deviation.

2.1.3 Near-wall treatment

how the flow behaves inside the whole computational domain and especially near the target surface (wall) which plays a major role in predicting both flow behaviour and heat transfer coefficient for both steady and transient models as reported by [17] facing a difficulty in understanding how the decelerating fluid interacts with the wall forming a turbulent region. Within viscous sublayer region, the heat transfer rate has a larger magnitude than outside it as shown by numerical solutions. The spatial region on the other hand in which the most heat and mass gradient occur is the region where turbulence models have difficulty predicting it, therefore, a high-resolution grid need to be established near the wall in order to account for the flow behaviour in the entire turbulent boundary layer which ofcourse requires a suitable model able to predict turbulent behaviour near this wall which consumes a lot of computational time.

2.1.4 The k-ε Model

The low computational cost eddy-viscosity model (k-ε) calculates Reynolds stresses as a function of velocity gradients using Boussinesq hypothesis based on how the flow behave at high Reynolds numbers which produces acceptable results for free-shear flows but unfortunately poor simulation results in jet flow applications, so it usually can be used as a benchmark to compare with other models [17] . The k-ε model got its name based on the use of dissipation equation

to track independently both turbulent energy k and dissipation rate ε based on the expected trends and it requires the user at each boundary layer to specify ε which has an unknown finite value at the walls. In impinging jet applications, the k- ε model is unfortunately gives poor results in stagnation and wall jet regions, predicting the location of separation point and predicting the formation of Nu secondary peaks. The standard version of this model applies only on flows with high Reynolds number and users usually use it to predict the velocity profile by the use of wall functions. Craft [17] used one of the earliest and widely used model, the Launder and Sharma low Reynolds number model using CFD to predict the velocity-temperature correlation proportional to the temperature gradient under the influence of turbulence models and different Reynolds numbers for jet impingement application employing the k and ε conservation equations and compare results with experimental data. For the test case of Re=23,000, a value up to four times larger of centreline wall-normal-root-mean square velocity (rms) was reported than the value reported by Cooper [18] in his experimental work, another over prediction up to 40% of the value of Nu located in the core impingement region with no prediction of Nu secondary peak at r/D=2 with a maximum error of Nu value of 15% occurring within 1<r/D<3. As for wall normal (rms) velocity, at (r/D)=0.5 corresponding to the jet edge, an over prediction by this model was also occurred with 15-20% wall-parallel velocity errors as this error increases up to 50% close to the wall and which was also confirmed by Heyerichs and Pollard [19] in their numerical investigation reporting an error of (-21.5% to -27.8%) in Nu values in stagnation region and (32-38.4%) error at Nu secondary peak. The poor results by using the standard k- ε model in jet impingement applications encouraged Craft [20] later on to investigate this model more and then improve it for better Nu predictions in especially in the (r/D<2).

2.1.5 The k-ω Model

the energy dissipation rate per unit of turbulent kinetic energy (ω) used by this model is determined experimentally by the use of conversation equation rather than a direct calculation from the velocity field in order to solve for turbulent kinetic energy (k) Wilcox [21] . This model gives good results of flow properties near wall-jet in both sub-layer and logarithmic region without the need of damping functions which makes this model generates better predictions of the turbulent length scale than the k-ε model but for Nu profile, it gives an error of approximately 30% comparing to experimental Nu profile. Unlike the k-ε model, this model has a better turbulent length scale that allows the user to specify the turbulence conditions at the wall. Park [22] used the k- ω model equations and showed improved results but a noticeable error of about 50% lower in the secondary Nu peaks along horizontal distance at Re=25,100 comparing to the experimental results which leads to an error of about 100% of local Nu values as a result of this misplacing where Heyerichs [19] reported an over predicted error of 18% of local Nu values and a secondary peak closer to the jet centre than the experimental results. In impingement jet applications, in terms of matching both experimental and numerical curve shapes, the low-Re model offers good results but as for using this model with wall functions, poor results should be expected. Chen [23] performed a successful numerical investigation of single slot jet impinging a flat plate with high Prandtl numbers from 1 to 2400 using the k- ω model for mass transfer. He claimed, by the use of very high grid densities, an agreement of 10% of experimental data in the impingement region

2.2 Fluid flow characteristics

A study of fluid flow characteristics is discussed here to gain a better understanding of its impact on heat transfer, particularly heat transfer related to jet impingement. Identifying fluid flow characteristics is essential to the study of jet flow behavior and how such jets interact with the plate on which the jet flow impinges.

Gardon and Akfirat [24] discussed the importance of turbulence in determining the heat transfer performance of impinging jets. They continued the earlier research work performed on axisymmetric and two-dimensional jets.

Figure 2-1 presents the turbulence and velocity distributions in a free jet. As soon as air jet leaves the nozzle, it entrains ambient air from the surroundings. The width of the mixing region grows continuously forming a potential core, as mentioned previously. Their slot jet measurement results showed that a similar potential core extended about five slot widths from the nozzle exit. Beyond that point, the centerline axial velocity decayed with axial distance. Compared to pipe flow, a free jet generates higher flow turbulence levels of up to 30% which enhance mixing. It is worthwhile to remember that despite the axial velocity decreasing, turbulence levels continue to rise. Turbulence even attempts to penetrate into the potential core region, but peak turbulence levels at the centreline do not occur until downstream of the potential core.

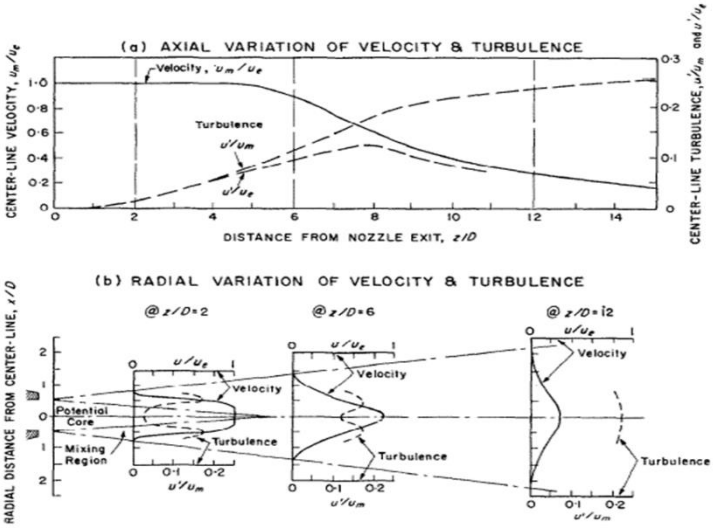

Figure 2-1: Schematic diagram presenting velocity and turbulence distributions in an axisymmetric jet [24]

Wang, et al. [25] investigated, numerically, fluid flow behavior of single jet jet impingement on a flat plate for different jet flow speeds, nozzle diameters, jet inclined angles and jet-to-target spacings. The fluid flow dynamics and structure of such processes is very complicated and Computational Fluid Dynamics (CFD) methods were used to compute the fluid flow pressure and velocity fields based on conservation of mass, momentum and energy. Turbulence model RNG k-ε was used in the simulation, and the SIMPLE (Semi-Implicit Method for Pressure-Linked Equations) algorithm was chosen for solving numerical models of the domain with inlet velocity as the boundary condition for nozzle inlet and outlet pressure as outlet boundary condition.

Figure 2-2 shows the schematic diagram for the CFD simulation. Based on their simulation, Wang, et al., [25] concluded that the peak pressure occurred at the flow stagnation point not the impingement point (Figure 2-2) and the pressure, measured radially, decayed rapidly. In contrast, the fluid flow velocity was found to be weak at the stagnation point. The fluid flow velocity decayed in a radial direction, gradually reducing to zero. Their tests showed that the fluid flow velocity was affected by all the nozzle parameters including diameter, spacing, and angle of impingement. For constant jet velocity at the nozzle, the shallower

the jet angle, the greater the peak velocity in the longitudinal direction, while the stagnation point became closer to the jet centreline. However, the peak pressure was found to depend only on the jet flow velocity.

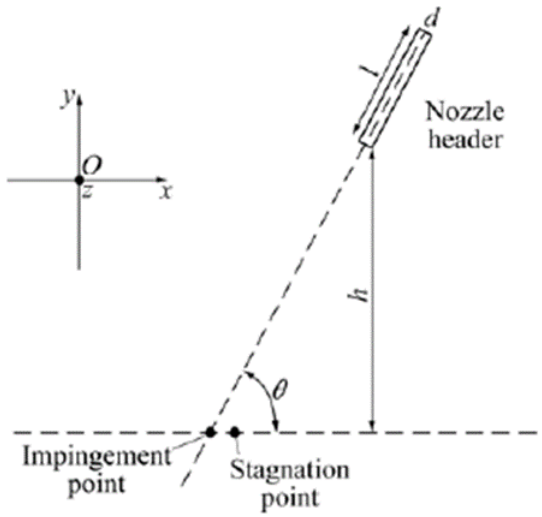

Figure 2-2: Schematic of CFD simulation model set-up [25]

Katti, et al., [26] conducted an experimental study using wall static pressure distribution measurements when a single row of circular jets impinged on a cylindrical concave surface. Their study also included pressure sensitivities to different surface curvature ratios, jet-to-jet distance, and jet-to-plate distance. They concluded that the peak pressure maximum occurs at 0^0 curvature (flat plate) and decreases along the curvature at 30^0 and 60^0. As expected for a given curvature, the stagnation pressure decreases with increasing jet to plate distance. At a given curvature, the pressure at the stagnation point did not occur at the center of the jet hole. It is believed that the jet flow may have experienced a slight additional “push” before it impinges on the plate in the direction of the jet flow. This shift in flow direction became more severe with the higher jet to plate spacing. At large curvature ratios, the influence of pitch on the peak pressure is much less. In addition, vena-contracta effects due to the different jet holes were found to reduce the value of the peak pressure as the curvature ratio increased from 4.25 to 8.50. At larger pitches of 4d and 5.6d, it was found that secondary

pressure peaks appear along the stagnation line regardless of the degree of curvature. Such peak was deemed to be due to wall jet collision on the concave surface along the longitudinal line as result of up-wash.

Flow issuing from a circular jet and impinging on a flat plate much more complex than flow over the plate. The heat transfer characteristics of the heated target surface with jet Reynolds number, the ratio of jet spacing to the jet width and jet exit mean velocity profile have been studied based on averaged heat transfer coefficients, stagnation point Nusselt numbers, and local heat transfer coefficients. Katti and Prabhu [27] conducted an experiment to study the correlation between local heat transfer coefficients of a flat, smooth surface and static wall pressure for axisymmetric jet impingement. They identified three different regions based on different flow characteristics: the stagnation region, transition region, and wall jet region. Their results were similar to previous findings where an increase in near-wall turbulence intensity was found with increased jet-to-plate spacing.

Lin, et al., [28] experimentally investigated heat transfer and fluid flow behavior of a confined slot jet impingement. They concluded the entrainment of ambient air due to the jet alone is insignificant at low jet Reynolds number (Re = 1226). Below this Reynolds number, flow was considered laminar with turbulence intensities less than 5% on the jet centreline at the nozzle exit. At higher Reynolds number, the flow becomes transitional/turbulent with higher turbulence intensity levels. Similar to other reported results, Lin identified that jet Reynolds number significantly impacted on flow stagnation and local and average Nusselt numbers where the ratio of jet separation distance to nozzle width has insignificant effect on heat transfer.

The heat transfer and fluid flow characteristics of a single circular impinging jet taking into account the buoyancy forces in a small cross-sectional space was studied numerically by Ichimiya, et., al., [29] both the velocity vectors and the temperature distribution were calculated and analysed. The mean Nusselt number was represented by the jet Reynolds number and the nozzle-to-plate spacing.

Local heat flux visualization was accomplished using thermosensitive liquid crystals. The numerical calculations were based on the continuity, momentum and energy equations. The study concluded that, after jet impingement, the heat transfer and flow could be categorized as having three regions: a two-dimensional forced convection region, a three-dimensional mixed convection region, and a three-dimensional natural convection region. In the mixed convection region, it was found that rising and falling peripheral flows caused streak lines to appear on the impingement surface. For a given spacing between the nozzle and the plate, increasing the Reynolds number caused a small recirculation flow near the impingement surface to move downstream. The streak lines were found downstream of the flow recirculation region. At a given Reynolds number, increasing nozzle spacing moved flow recirculation on the impingement surface downstream. However, such recirculation flow does not appear clearly for larger nozzle spacings. It was believed that the forced convection region moved to the natural convection region

2.2.1 Jet flow characteristics

To gain a better understanding of the local heat transfer rate due to the impact of jet flow from a nozzle onto a plate, it is essential to explore and identify jet flow characteristics and development before and after the jet impinges on the plate.

Jambunathan, et al., [11] summarized jet flow characteristics based on orthogonal impingement from an air jet located above a plane surface. Four different zones were identified, see Figure 2-3 below. These zones corresponded to:

1.) Initial mixing region zone: the developing flow region where the air is entrained into the jet core flow from the surrounding ambient air. A mixing free shear layer is developed whose width increases due to diffusion until it extends to the center line at a point downstream from the jet exit. Up to this point, where the shear layer ends, is referred to as the potential core in which the local jet velocity is about 95% of the nozzle exit velocity. Reduction of jet velocity occurs within this region.

2.) Established jet zone: beyond the potential core, the jet axial velocity reduces with increasing distance from the jet exit. Schlichting et. al., [30] reported that the reduction of jet velocity and jet half width is directly proportional to the downstream distance beyond the potential core.

3.) Deflection zone: a narrow region just before the jet impinges on the plate. Static pressure increases in this region as a result of the rapid reduction of the axial velocity of the jet. As the jet flow slows, its direction changes and is deflected outwards. Tani et. al., [31] estimated this zone starts at a height of about two nozzle diameters away from the plate surface, while Giralt, et al., [32] suggested a shorter distance of 1.2 nozzle diameter.

4.) Wall-jet zone: inside wall jet region, the local velocity is a maximum near the wall at the jet centreline before slowly reducing as the air flows along the wall away from the jet impingement location. Due to the near wall velocity, local heat

transfer from the wall is higher inside the wall jet zone than for the remainder of the plate. Such heat transfer enhancement is largely due to turbulent viscous sheared flow generated from the interaction of the wall jet and the surrounding air. This shear flow increased the heat transfer rate from the plate through the flow boundary layer near the wall.

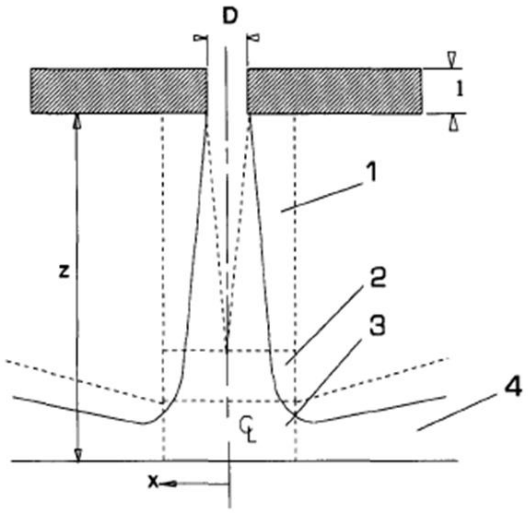

Figure 2-3: Jet flow zones division reported by Jambunathan et. al., [11]

Jet impingement research work has been widely studied but only a few workers have reported the effect of potential core impact on the plate surface heat transfer rate. Ashforth-Frost, et. al., [33] conducted an experiment using liquid crystal thermography and Laser-Dopper anemometry to quantify the effects of nozzle geometry variations and semi-confinement on the nozzle jet potential core at flows for which Re = 22,500. Variations in the potential core were then further investigated to identify the effect on the heat transfer rate magnitude and distribution on the plate surface.

A fully developed jet flow has a longer potential core at almost 7% compared to a flat jet configuration. The increased potential core length enhanced the heat transfer rate on the plate due to the generation of higher turbulence levels. This research showed that an additional 20% longer potential core extension could be achieved with the semi-confinement installation. However, semi-confinement also reduced entrainment which directly lowered the axial turbulence at

the jet impingement point on the plate. As result, the heat transfer rate was reduced by up to 10%. Overall, the heat transfer process performance can be largely characterized by the jet flow process and geometry of the nozzle. Some key jet flow parameters include turbulence intensity of the flow, axial velocity distribution at the nozzle exit, and jet Reynolds number. Research has shown that the heat transfer reaches its peak at the tip of the potential core, which is typically located between 4.7 to 7.7 nozzle diameters downstream of the exit ($4.7 < H/D < 7.7$) .

Li et. al., [34] conducted an experimental study of jet flow structure for the special condition of an airfoil located inside the potential core region of a planar jet. Inside the potential core, the experiment was set-up so that the highly unsteady jet shear layer did not impinge directly on the airfoil's leading edge, see Figure 2-4.

The results showed that at low airfoil angle of attack (i.e. $\alpha < 20^0$) no oscillation was observed. However, when the angle of attack reached 30^0, the jet-airfoil impingement flow structure exhibited self-sustained oscillations. The oscillating unsteady airfoil wake induced oscillations in the jet shear layer at a rate similar to the airfoil vortex shedding frequency . Both volume flow rate and momentum thickness were found to increase due to this flow oscillation. Using arguments based on absolute/convective linear stability theory, it was suggested that this induced flow oscillation was closely correlated to the mean velocity of the potential core region.

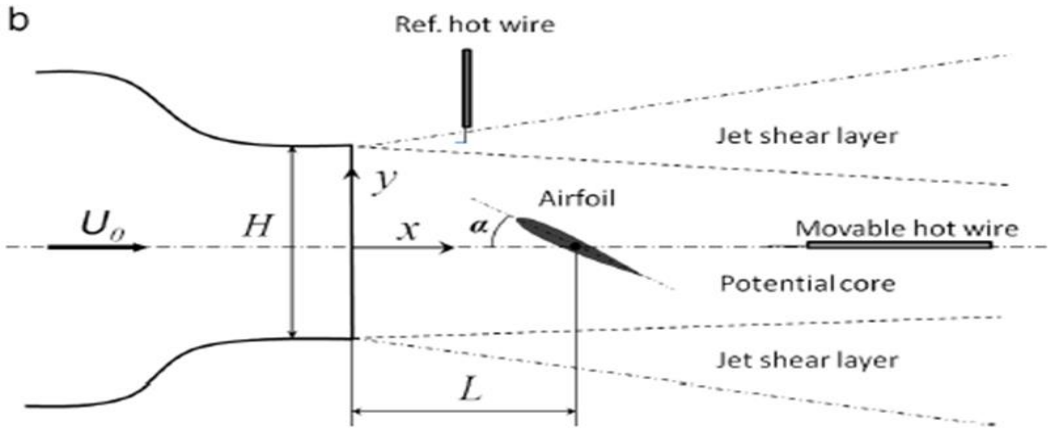

Figure 2-4: Schematic of experimental set-up of planar jet impinging on airfoil Li et. al.,[34]

Several industrial applications using liquid jet impingement for heat transfer enhancement have found considerable success to maintain low mass flow rates. Elison, et. al., [35] experimentally tested small diameter nozzles under low jet Reynolds number flow conditions (i.e. Re < 7000) for both free-surface and submerged cases. Their studies focused on identifying the effects on the local heat transfer characteristics due to different flow structures developed at the nozzle exit, including laminar, transition and fully turbulent flow. Their results demonstrated that the Nusselt number varies with $Re^{0.5}$ and $Re^{0.8}$ for turbulent and laminar jet flow conditions respectively. Inside the laminar regime, the $Re^{0.8}$ correlations for a free-surface configuration was identified as resulting from a broadening of surface-tension-induced jet modification to the flow structures. For the submerged jet configuration, however, it was believed that such correlation was due to the increase of jet flow turbulence due to the effects of jet instabilities. Earlier research showed that nozzle-to-plate spacing variations have very little effect on the heat transfer rate for the free surface configuration. However, for a submerged jet, the heat transfer rate correlated more closely to the regular jet turbulent flow.

Ashforth-Frost, et al., [36] measured both nozzle jet flow velocity and turbulence levels for semi-confined configurations. Their experimental set-up had a

flow Reynolds number of 20,000, and jet nozzle-to-plate spacings of H/D = 4 and 9.2. These results showed that, compared to the confined configuration the potential core of the semi-confined case is slightly longer due to limited flow entrainment and less spreading of the jet flow. Their data also suggested that the heat transfer rate on the plate is directly proportional to the jet impingement velocity and turbulence levels. Their jet velocity profile obtained from experimental measurement is shown in Figure 2-5. Jet flow transition to turbulence was found to have occurred on the plate wall when the plate was positioned within the jet potential core region. This flow transitioning characteristic is due to low turbulence levels at the jet stagnation point. However, when the plate is located inside the jet established region the heat transfer pattern on the impingement plate decreased along the plate, and the flow turbulence levels at the stagnation point were found to be consistent with the well-established turbulent flow.

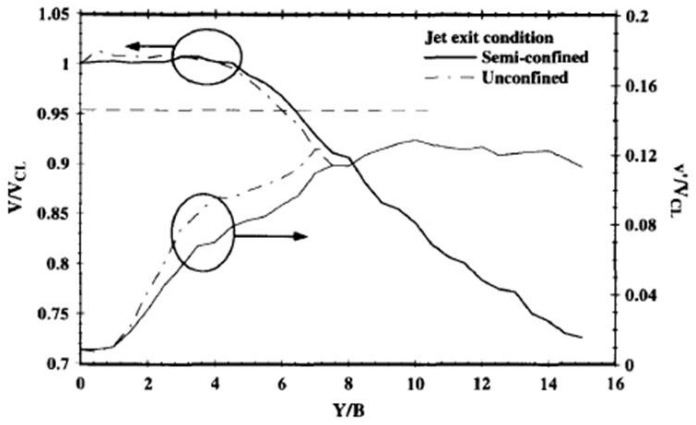

Figure 2-5: Nozzle jet velocity delay along centreline for both semi-confined and unconfined configurations, Ashforth-Frost et. al.,[36]

Vortex pairing controlled jet flow was applied experimentally to heat transfer for an axisymmetric impinging jet configuration, by Hwang, et al., [37] The control mechanisms used included both acoustic excitation and secondary shear flow control. The acoustics excitation was obtained by acoustic wave generation at the jet periphery. The secondary shear flow control was achieved using co-flows or counter-flows around the core jet stream. These mechanisms modified and controlled the flow vortex structures in the jet and, therefore, the Nusselt number

based heat transfer rate. The flow pattern results for a free jet with and without the secondary flow control are shown in Figure 2-6.

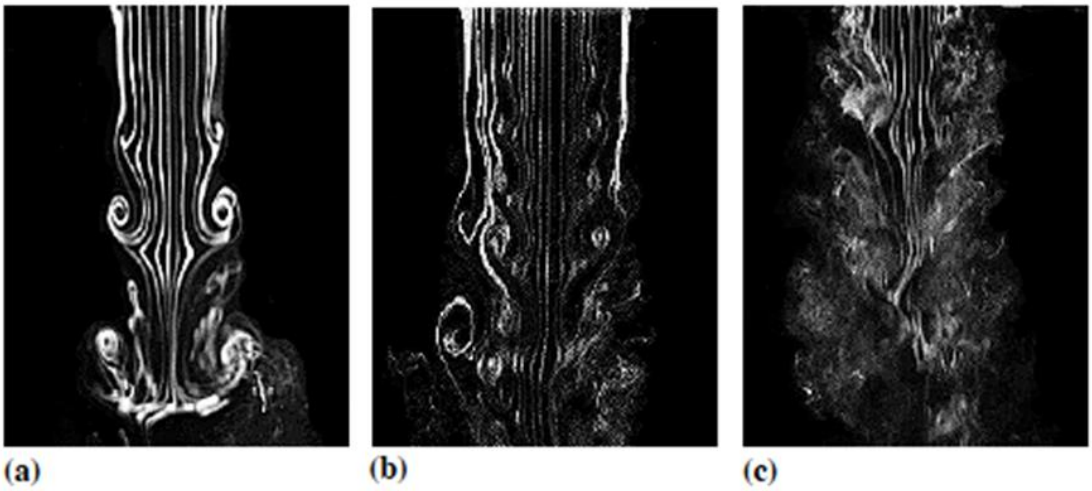

Figure 2-6: Different vortex pairing of free jet flow with secondary jet flow control mechanism, Hwang, et al., [37] **(a) R=1.0 without secondary flow control (b) R=0.45 with co-blowing flow control (c) R=1.45 with flow control with acoustic excitation**

For the free, circular jet shown in Figure 2-6 (a) with Re=34,000 a shear layer is convected downstream forming a ring vortex. Such ring vortices can undergo strong pairing development and, as explained previously, when inside the mixing layer, the vortices grow with distance from the nozzle exit and, finally, after passing the end of the potential core dissipate. With co-blowing flow at R=0.45 , an additional shear layer formed between the main core jet stream and the surrounding air which was not present with the regular free jet flow. This additional shear layer is created by the additional secondary flow ejected from a concentric tube around the main jet. The presence of the secondary shear layer delays the main jet flow development and suppresses vortex pairing due to a higher rate of entrainment from the ambient air. Mixing layer thickness increases and thereby the potential core length. Considering the acoustic excitation shown in Figure 2-6 (c) with R=1.45, two shear layers form much earlier in the main jet flow development due to higher shear between the main and the secondary flows. This results

in a shorter potential core in the streamwise direction and slightly higher flow turbulence intensity. The impact of these flow structures on the heat transfer is also reported. As the jet flow development is promoted by the acoustic excitation, the heat transfer rates are also shown to increase due to higher turbulence intensity.

The shear stress distribution around the stagnation point is considered highly important in determining the local heat transfer coefficients. Such shear stress distribution needs to be determined to obtain low turbulence. Guo and Wood, [38] conducted detailed measurements of jet flow fluctuating pressure and velocity components (streamline, spanwise and cross-stream) along the stagnation streamline of the impingement of a planar jet . Because the target plate was located inside the potential core region, the flow was identified as having irrotational and turbulent behavior. This irrotational fluid motion was induced largely by mixing layer formation and growth rates. Both streamwise normal stress and pressure fluctuations data showed increasing with decreasing mean flow velocity before being dampened by the presence of the plate.

In the frequency domain, both spectra of the streamwise velocity fluctuations and pressure showed higher magnitude in the low-frequency range but the attenuation on the plate occurs in a much higher frequency range. Their measured plate shear stress data also showed the jet turbulence to have very little effect, especially inside near the stagnation point containing laminar flow and turbulence flow downstream regions. They concluded that even a high turbulence intensity level at the nozzle exit is a secondary influence on the shear stress levels on the plate surface around the stagnation region.

Narayanan, et al., [39] demonstrated experimentally flow structure and heat transfer of a submerged, turbulent, slot jet impingement plate for both the transitional (nozzle to surface spacing of H/D = 3.5) and potential core (nozzle-to-surface spacing of 0.5) regions. Their results were consistent with previous findings in which peak heat transfer rate occurs in the jet impingement region and then gradually and consistently decreased inside the wall-bounded flow region for transitional jet impingement. High heat transfer is deemed due to the high

turbulence near the plate surface from spanwise vortex generation. In the wall-bounded region where heat transfer decreased monotonically, the data showed no correlation with the highly fluctuating velocity in the streamwise direction.

However, the gradients of RMS surface pressure fluctuations were found to correlate well with the near-wall streamwise fluctuating velocity, being almost inversely proportional. For the potential core jet impingement region, the primary peak heat transfer was found in the impingement region. Downstream there was a region which contained both a local minimum and a secondary peak in the heat transfer. Peak heat transfer correlated well with the peak near-wall flow turbulence in the streamwise direction. However, it was concluded that local heat transfer coefficients could not be dependent solely on the near-wall streamwise turbulence, its dependence on outer shear layer variations have to be taken into account.

The formation of vortex structure in free jets has been widely studied for a long time. Oyakawa, et al., [40] have discussed the characteristics of flow behavior and thermal flow fields for free and impinging jets generated from a circular jet at Re=9,700. Since the vortex ring formed due to the shear layer increases the heat transfer coefficient, their research included the processes of formation and decay of vortex rings. The visualization results for vortex ring distribution showed almost the same patterns for both free and impinging jets. For different jet configurations, the vortex ring scale was found to have its peaks at different values of X/D, where X was axial location and D was the jet diameter. The vortex rings were initially produced by shear layer development via the Kelvin-Helmholz instability mechanism as shown in Figure 2-7. During the vortex ring development process, the vortices grew and combined with each other before breaking down and becoming transformed to turbulent flow. Based on frequency analysis and measuring the scale of the vortex rings, the potential core was found not a continuous phenomenon disregard of the impingement plate installation.

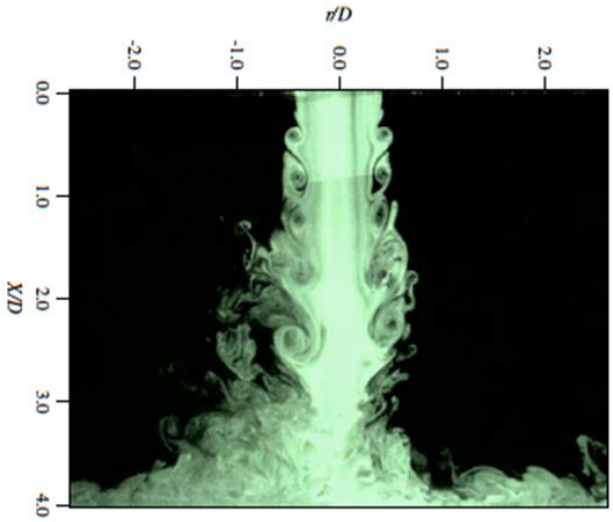

Figure 2-7: Flow visualization of impingement jet at H/D=4.0 [40]

Garimella, et., al., [41] studied experimentally the variations in the heat transfer from small heat sources (electronic components) subject to a confined and axisymmetric impinging jet with changes in nozzle geometry. Different nozzle aspect ratios were tested (in the range Garimella 0.25 to 12) with different nozzle diameters (between 0.79 and 6.35 mm). The Reynolds number of the flow was from 4,000 to 23,000. Nozzle to heat source spacings was between 1 and 14 jet diameters. The results have shown that at very small values of nozzle aspect ratio (< 1), the heat transfer coefficients of the small heat sources were highest. When nozzle aspect ratio was increased to between 1 and 4, the heat transfer coefficients reduced sharply. However, when the nozzle aspect ratio was increased to between 8 and 12, the heat transfer coefficients increased again. It was proposed that these variations of heat transfer coefficients were due to flow separation and reattachment phenomenon occurring in the nozzle and its effects on the flow velocity profile at the nozzle exit. As nozzle to heat source target spacing is increased, the nozzle aspect ratio had less influence regardless of Reynolds number. The experimental data also suggested that increasing nozzle diameter increased turbulence intensity and thus the heat transfer coefficients. Based on measured data, a correlation was obtained between stagnation point Nusselt number and jet Reynolds number.

Impingement jet techniques have also been applied to oil-cooling of engines where an oil jet was used to cool such hot surfaces as cylinder heads or pistons. Ma, et al., [42] conducted similar experimental research, evaluating heat transfer coefficients for a vertical heated surface subject to oblique impingement from a liquid oil jet. The jet operating range focused on higher Prandtl number conditions and low Reynolds numbers ($235 < Re < 1745$) . The jet was circular, free and used transformer oil. Jet velocity was between 5.3 to 19.4 m/s and jet inclination angle varied from 45^0 to 90^0, see Figure 2-8.

The experiment results suggested that as the jet inclination angle increased, the corresponding maximum local Nusselt number decreased, with a correlation between maximum Nusselt number and jet Reynolds number at the different inclination angles. The relative displacement of the location of the maximum heat transfer point from the stagnation point was found to correlate well with the jet inclination angle. Compared to a submerged jet, free-surface oil jet configuration was found to have less impact on such displacement. The local Nusselt number distribution along the x-axis on the plate (see Figure 2-8) was increasingly asymmetric about the maximum heat transfer point with the greater jet inclination angle. However, the y-axis distribution of local Nusselt number was found to be independent of both the Reynolds number and jet angle.

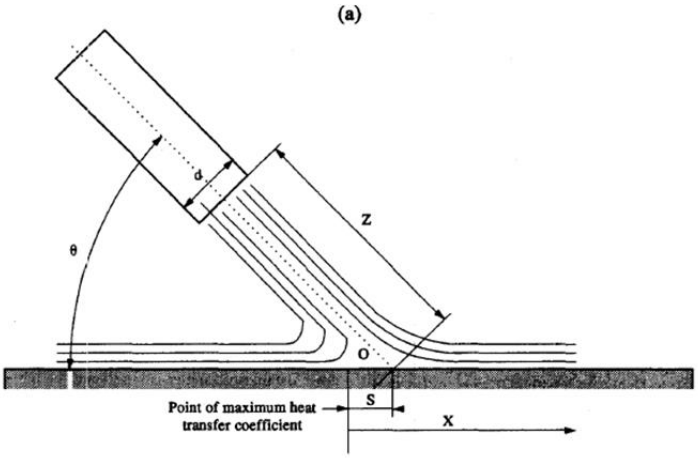

Figure 2-8: Oblique jet impingement set-up, Ma et al., [42]

The major effect of the inclination angle of the jet was further explored by Ma et al., [43]. In this detailed research, the characteristics of the local convective heat transfer from a heated plate subject to oblique jet impingement were investigated. The results for the local convective heat transfer were found to have similar trends to the local heat transfer coefficients reported by Ma et al., previously [42] The displacement of the point of maximum local heat transfer from the stagnation point was found to correlate with jet inclination angle for a submerged oil jet. Compared to a free-surface oil jet, the submerged oil jet displacement was found to be slightly higher. The experimental results also suggested that the maximum heat transfer coefficients reduced with the higher jet inclination angle.

In many industrial applications, the surface roughness is commonly found due to material and manufacturing processes, Gabour and Lienhard [44] investigated jet impingement cooling effects due to surface roughness. It is widely believed that the presence of surface protrusions increases the heat transfer rate of a wall surface because the protrusions pierce the thermal sub-layer. In their report, they mentioned that, typically, surface roughness scaling is related to the fluid friction velocity on the surface and expected it to approach zero at the stagnation point . However, strain rate or radial velocity gradient is widely used to characterize the stagnation point. This investigation used fully a developed turbulent water jet impinging on a heated rough surface. The jet diameters were from 4.4 - 9.0 mm and were used with jet Reynolds number from 20,000 - 84,000. The Prandtl number was in the range 8.2-9.1. The surface roughness was characterized by the root mean square height of the protrusions and for nine surfaces tested, ranged from 4.7-28.2 μm. The experimental results showed drastic improvement of local Nusselt number (by almost 50%) for a roughened surface compared to a smooth plate. An important relation between local heat transfer rate, RMS roughness and jet diameter was also identified. For a given jet diameter and roughness height, there is a minimum required jet Reynolds number to increase heat transfer rate above that for a smooth plate.

Bouchez and Goldstein [45] investigated the cooling effect due to cross-flow blowing over jet impingement. The experimental results showed that cooling

performance decreases with the jet blowing rate as expected. Such cross flow cooling method has been shown to achieve 60% with blowing rate of 12with nozzle-to-plate spacing of 6 jet diameters. Such spacing was previously considered to give maximum heat transfer. At high jet impingement rates, the cross-flow creates a recirculation zone above stagnation point on the impingement surface.

The plate cooling effect was found to be well correlated to jet cross-flow rate. This showed the dependence of heat transfer rate on the density ratio of jet and cross-flow fluid at low cross-flow rates but it is independent at high cross-flow rates. Such observations are consistent with the notion that the temperature profile on the heated wall should be a function of nozzle-to-wall distance, blowing rate, and density ratio of jet and cross-flow fluid. At low blowing rate, the cross-flow did not have sufficient momentum to break through into the layer forming the main fluid stream and therefore had very limited interaction with the heated wall. When mainstream fluid temperature is lowered, such impingement is rather less effective. At high cross-flow rates, the density ratio had little effect on plate cooling.

An array of impinging jets has been found useful in turbine blade cooling and high local transport coefficients can be achieved with high mass and/or heat transfer in the jet impingement region.

Goldstein, at. el., [46] investigated a jet array impingement on a flat heated surface. Heat transfer information was obtained from a variable constant-heat-flux boundary using a liquid crystal display. Compared to single jet, the array configurations achieved higher heat transfer coefficients at a smaller spacing (L/D=2) than with the larger spacing (L/D=6). Maximum and minimum heat transfer coefficients were measured, especially at smaller jet spacings. Three co-linear jet configurations showed a local minimum at the central jet. When a larger number of jets was used, mixing-induced turbulence due to flow interaction generated disturbances at the centers of all the jets. As result of this, local minima at the stagnation points disappeared when using multiple jets. The authors suggested their measurement technique could be improved by using finer measurement of

heating losses from the system and that such heat losses should be avoided to allow the higher accuracy of convective heat flux measurements.

Colucci et., al., [47] created a special nozzle shaped geometry based on a hyperbolic configuration to test its impact on the local heat transfer coefficient using a confined impinging air jet. The experimental arrangement used a low nozzle to plate spacing of between 0.25 to 6.0 with jet Reynolds number in the range 10,000 to 50,000. The results showed that the local Nusselt numbers are strongly correlated to both the jet Reynolds number and the offset. However, at larger separation spacing (H/D=6.0), the local Nusselt number became insensitive to nozzle geometry. The local Nusselt number distribution was consistent with previous reports, where the maximum value occurs at the stagnation point and reduces radially from the jet center. The absolute values of local Nusselt numbers at all locations was found to increase proportionally with higher jet Reynolds number. At small spacing (H/D<1.0), the experiment showed the appearance of two maximum Nusselt numbers on the plate surface. The location of the first maxim a consistently occurred at the same spot while the location of the second maximum varied with offset, nozzle shape, and jet Reynolds number. Both maxima were more obvious at higher jet Reynolds numbers and/or smaller nozzle-to-plate spacings. The amplitude of the first maximum appears to be larger than the second at low jet Reynolds number and larger values of H/D. When jet Reynolds number increased and H/D decreased, the second maximum becomes the larger. Based on experiment observations, it was concluded that the location of the second maximum was affected by the nozzle geometry, and depended on the jet outlet radius. The bigger the jet outlet radius, the greater the radial distance of the second maximum from the jet centreline. The hyperbolic shape is shown to have higher local Nusselt numbers than the nozzle orifice shape.

Many different nozzle shapes have been studied in order to enhance heat transfer and improve jet impingement performance. These include slots, squared-edge orifices, and converging and diverging circular nozzles. Square-edge orifices have been identified as producing higher turbulence levels, which promotes better heat transfer, than other contoured nozzle shapes. However, it is difficult

to attain a low-pressure drop using a square-edged orifice. Therefore; an optimal shape is desired to combine both pressure drop and heat transfer performance. Brignoni and Garimella [48] investigated the effect of varying nozzle geometry, from squared-edged to chamfered edges, on the local heat transfer distribution and pressure drop for a confined axis-symmetric air jet impinging on a small heat source. Unlike their previous work on contoured and hyperbolic shapes, the construction of a chamfered nozzle shape requires only simple machining and makes such a design attractive for practical consideration.

Table 2-1 below summarises and compares all the experimental set ups encountered in this section of the literature review.

Table 2-1: Summary of experimental and numerical set ups identified in the literature review

First author	Data	Fluid	Nozzle geometry	Nozzle diameter (width) (mm)	Re (jet velocity) (m/s)	H/D (H/W)	Jet angle (α°)	Data	Other Data	Measurement technique
WANG, B.	2013	Air	circular	2.5,5,10,15	(5,10,15,20)		30-90	velocity	pressure	CFD[1]
Katti, V.	2013	Air	circular		20,000	1-6	90	pressure coefficient	N/A	pressure tabs
Katti, V.	2007	Air	circular	7.35	12,000-18,000	0.5-8	90	Nu	h	infrared camera
Lin, Z.H.	1996	Air	slot	(5)	190-1537	1-8	90	Nu	turbulence	heated plate
Ichimiya, K.	2003	Air	circular	20	400-2000	0.25-1	90	$\overline{Nu}$		LCT[2]
Tani, I.	1966	Air	circular	52, 83	(30)	2-15	90	pressure	velocity	pilot tube
Giralt, F.	1977	Air	circular	28, 31.75	30,000-80,000	1.2-25	90	pressure	velocity	pressure tabs
Ashforth-Frost, S	1996	Air	circular	10	22500	4.6-7.7	90	velocity	turbulence	LDA[3] , LCT
Li,Yong	2016	Air	rectangular	250X50	11700	-	0-45	velocity	temperature	velocity/temp. hot-wire
Elison, B.	1993	Air	circular	0.25-0.58,	300-7000	-	90	Nu	temperature	thermocouple
Ashforth-Frost	1997	Air	slot	(30)	20,000	4-9.2	90	velocity	turbulence	hot-wire
Hwang, S.D.	2001	Air	circular	24.6	34,000	4,8,12	90	velocity	turbulence	hot-wire
Guo, Y.	2001	Air	slot	(300)	(30)	2,4,5	90	velocity	pressure	pressure tabs
Narayanan, V.	2004	Air	slot	(12.7)	23,400	3.5 ,5	90	velocity		LDA
Garimella, S.	1995	Air	circular	0.79-6.35	4000-23,000	1-14	90	temperature	h	thermocouple
Ma, C.	1996	Air	circular	0.987	235-1745	fixed	45-90	temperature		thermocouple
Gabour, L.	1994	Water	circular	4.4-9	20,000-84,000	0.9-19.8	90	temperature		thermocouple
Colucci, D.	1996	Air	hyperbolic	12.7	10,000-50,000	0.26-6	90	Nu	temperature	LCT
Brignoni, L.	2000	Air	orifice	3.18	5000-20,000	1, 4	90	pressure		Pressure tab

[1] Computational Fluid Dynamics [2] Liquid Crystal Thermography [3] Laser–Droppler anemometry

2.2.2 Stagnation Point Heat Transfer

Over the past few decades, much research has been published on heat transfer characteristics due to impinging jets in both single and multiple arrays. However, the stagnation region heat transfer is not well understood despite its significance in practical applications. Early work suggested that the heat transfer rate of an impinging jet is directly proportional to the temperature difference between the jet and the adiabatic wall. However, the temperature difference was found to be vary from point to point on the impingement surface.

An experimental study of jet-exit geometry showed that the jet impingement only affected the heat transfer coefficient inside the stagnation region for H/D < 6. Goldstein, et al., [49] investigated the temperature recovery factor as well as the local heat transfer distribution for an axisymmetric impinging air jet. Their experimental data suggested that the temperature recovery factor is sensitive to the nozzle to plate spacing but insensitive to the jet Reynolds number. The maximum stagnation Nusselt number was identified at a nozzle to impingement plate spacing H/D of about 8 jet diameters. At small spacing, the stagnation region recovery factor has a minimum near r/D=2 deemed to be due to the energy dissipation inside the vortex ring fluid domain in the highly curved shear layer. These orderly organized vortex ring structures remain after impingement. At the center of the vortex, an energy separation exists at its minimal level. This is represented by a local minimum in recovery factor at r/D=2. For H/D greater than 5, the stagnation point recovery factor is found to be greater than 1 when the jet flow mixes with ambient air and vortex ring breakdown occurs. In the region outside of the stagnation point, r is close to unity.

Early investigation of the central zone around the stagnation point was conducted using two-dimensional and axis-symmetric air jet impingement. Lee and Lee [50] experimentally investigated turbulent heat transfer characteristics in

a stagnation region for an axis-symmetric submerged air jet impinging on a heated flat surface. The impinging jet showed a highly complicated flow pattern inside the stagnation zone due to the complex interaction between the ambient fluid and the plate. Such complicated flow patterns are considered as due largely to the flow reflection and sudden change in flow direction to radially outwards from the stagnation point. It was demonstrated that using fully developed flow from a straight pipe nozzle (diameter D=25 mm) gave more accurate heat transfer data inside such stagnation points. Two maxima were found in the local heat transfer rates distribution profile. The primary maxima are attributed to the accelerated radial flow while the secondary maxima are due to the transition from laminar to the turbulent boundary layer.

When nozzle-to-plate spacing (H/D) bigger than 6 was used, the local heat transfer reduces monotonically with radial distance. As H/D is further increased, the Reynolds number dependence becomes more important. This outcome is attributed to the momentum exchange between jet flow and the surrounding ambient air which gave rise to the turbulent intensity of the incoming jet. The mean jet velocity profile exhibits self-similarity behavior. Figure 2-9 shows how the Nusselt number at the stagnation point changed with jet Reynolds number. The compressibility effect was not taken into account. Based on their measurements, it was shown that the Nusselt number was correlated to jet Reynolds number and nozzle-to-plate spacing (H/D) as $Nu_0 \propto Re^{0.565}(\frac{H}{D})^{0.0384}$. At H/D=2, the Nusselt number variation was shown as $Nu_0 \propto Re^{0.50}$. For the fully developed pipe jet, both the flow kinetic energy and turbulent intensity were shown to increase with H/D and the stagnation heat transfer coefficient is peak at H/D=6.

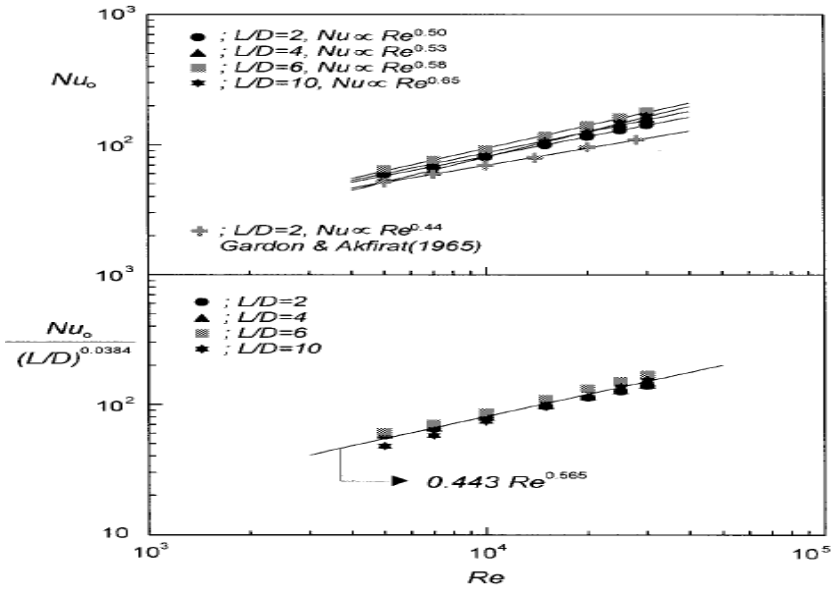

Figure 2-9: Nusselt number variations with jet Reynolds number at stagnation point, Lee., et., al, [50]

Depending on where the impingement surface is located relative to the jet nozzle, it can be either outside the potential core region or inside it, though the potential core length is sensitive to whether the jet is unconfined, semiconfined, or fully confined. The work of Ashforth-Frost and Jambunathan [33] is discussed in Section 2.1.1. Suffice it to add that they found that downstream of the potential core the increase in turbulence levels compensated for the reduction of axial jet flow velocity to maintain similar heat transfer coefficients and this persisted while turbulence levels were maintained.

The significant impact of turbulence on the stagnation point was first revealed from studies of forced convective heat transfer for a cylinder. Turbulence intensity and heat transfer have been found to be correlated. For many applications, the heat flux inside the stagnation region is important to avoid over-heating. Hoogendoorn [51] investigated the effect of flow turbulence from an impinging jet on the stagnation zone . He showed an increase in heat transfer due to the jet was similar to that for a cylinder. The jet flow traveled a small distance, z , from the nozzle exit. His experiments were conducted within the range 2 < H/D < 8. Such a region would include both potential core and jet turbulence flow. Figure

2-10 shows the stagnation point heat transfer using different flow turbulence and velocity conditions. The data showed that increase of jet turbulence due to the installation of a grid at the nozzle exit drastically increased the stagnation heat transfer rate. It was also found the stagnation heat transfer is insensitive to the turbulence scale. In additional, Hoogendoorn reported that the effect of jet Reynolds number on stagnation point could hardly be detected. For small nozzle-to-jet flow spacing distance (H/D<5) and with low jet turbulence level (<1%), the Nusselt number at the stagnation point appeared to be smaller than those around it

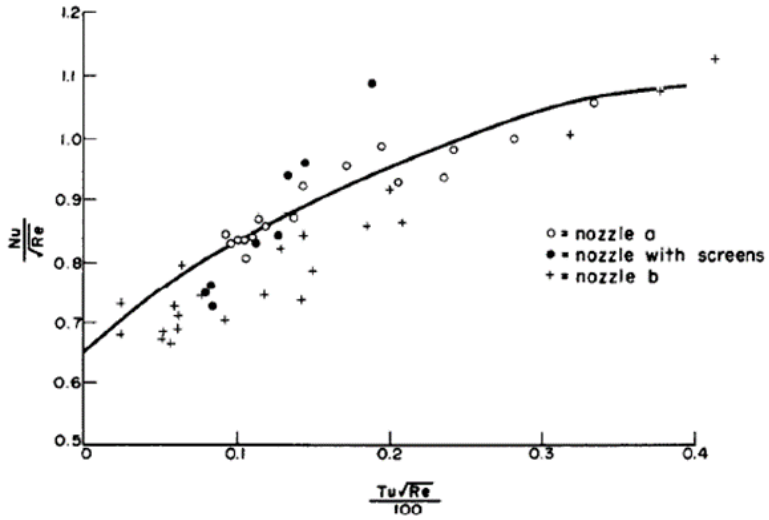

Figure 2-10: Correlation data for heat transfer in the stagnation. Hoogendoorn., et., al., [51]

Zu et al. [52] presented results of a numerical study of the heat transfer behavior of a circular air jet impinging normally onto a flat plate with a nozzle to plate spacing ratios (H/D) of 1 to 6. Their study used a Computational Fluid Dynamics (CFD) commercial package, Fluent. Seven different turbulence models were implemented to evaluate modeling prediction capabilities by comparison with the benchmark experimental data. These turbulence models were (i) the standard k-ε model, (ii) Renormalization Group (RNG) k- ε model, (iii) realizable k- ε model, (iv) standard k-ω model (v) SST k-ω model, (vi) RSM model, and (vii) time-varying Large Eddy Simulation (LES) model. Table 2-2 below compares

these models. The SST k- ω and LES models gave better accuracy in predicting both the heat transfer and fluid flow. With the high computational cost of LES, the SST k- ω turbulence model is an attractive and promising modeling option.

Figure 2-11, shows the CFD computational domain and boundary conditions set by Zu, et al., [52] and used for numerical predictions based on SST k- ω to investigate the effects of, jet Reynolds number, target spacing-to-jet diameter ratio, jet plate length-to-jet diameter ratio and jet plate width-to-jet diameter ratio on the local Nusselt number on the impinging plate surface. In order to capture accurately the heat transfer behavior at the stagnation point, a fine mesh was applied on the plate to ensure adequate resolution of the velocity and thermal boundary layers. The wall y+ values were kept below 28 and majority were less than 1. The numerical scheme was based on an implicit and segregated approach for solving the Navier-Stokes equation. The numerical results were successfully validated against the experimental curve based on the following correlation relation between stagnation point Nusselt number and both Re and H/D.

$$NU_{sg} = 0.423Re^{0.642}\left(\frac{H}{D}\right)^{-0.3} e^{-\left[0.044\left(\frac{W}{D}\right)+0.011\left(\frac{L}{D}\right)\right]}$$

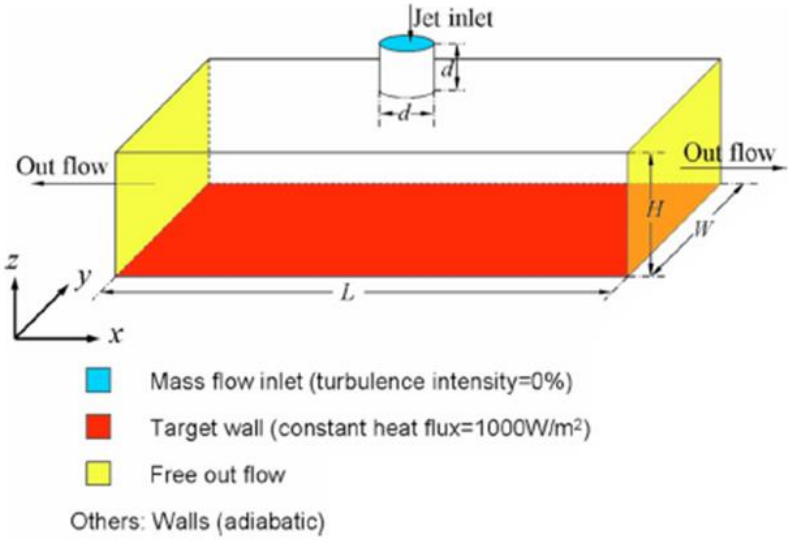

Figure 2-11: CFD modeling set-up Zu, et al., [52]

Table 2-2: Comparisons of various CFD turbulence models options for impingement heat transfer [52]

Turbulence models	Computational cost	Accuracy	Error of Nu_{sg} (versus experiments) (%)
Standard $k-\varepsilon$	Low	Poor	101
RNG $k-\varepsilon$	Low	Poor	28
Realizable $k-\varepsilon$	Low	Poor	116
Standard $k-\omega$	Moderate	Poor	67
SST $k-\omega$	Moderate	Good	7
RSM	Moderate	Poor	107
LES	High	Excellent	4

In addition to both jet Reynolds number and nozzle geometry factors, a confined jet heat transfer behavior was found to be sensitive to jet plate geometry and that of impingement plate. San and Shiao [53] studied experimentally the effects on the heat transfer behavior of a confined circular air jet impinging normally on a flat plate with different distances of the jet above the plate and different jet plate sizes. Both a continuous heated surface and a restricted flow arrangement were investigated. The results showed that the stagnation Nusselt number is related to Reynolds number as $Re^{0.638}$ and inversely proportional to $(H/D)^{0.3}$. Both (L/D) and (W/D) are also correlated to the stagnation Nusselt number based on the relation:

$$\text{Exp}[-0.044(W/d)-0.011(L/d)].$$

The stagnation Nusselt number depends more strongly on W/D than on L/D. The jet impingement plate flow arrangement and heating condition after impingement are both key factors in determining the stagnation Nusselt number dependency on H/D. At larger H/D, the length of the flow-mixing structure will also increase as result of the reduction of stagnation Nusselt number. It was found that the higher the flow temperature in the recirculation zone, the more strongly such flow mixing influences the stagnation Nusselt number. The influence of jet height on the stagnation Nusselt number was investigated before and the optimal jet height is found to be about five times the jet diameter (H/D ~ 5).

Lee and Lee [54] studied experimentally the influence of nozzle exit shapes on jet flow turbulent heat transfer augmentation for an axisymmetric submerged air jet impinging on a heated flat plate. Three different orifice nozzles were tested: standard edge, sharp edge and square-edge nozzle. The sharp-edged orifice jet produced the highest heat transfer rate inside the stagnation zone. The stagnation point Nusselt number was correlated to the nozzle-to-plate spacing (H/D) and jet Reynolds number based on $Nu_0 \propto Re^{0.573}(\frac{H}{D})^{-0.116}$ for the sharp-edged jet, $Nu_0 \propto Re^{0.571}(\frac{H}{D})^{-0.092}$ for the standard-edged jet and, for the squared-edged orifice jet, $Nu_0 \propto Re^{0.566}(\frac{H}{D})^{-0.078}$.

At nozzle-to-plate spacing, H/D=2, the Nusselt numbers inside the stagnation regions of the jets were found to be 25-55% higher than those for a fully developed pipe jet and 50-75% higher than for contoured nozzle jet configurations. These experiments showed that most of the heat transfer improvements are due to the large flow velocity gradients and higher turbulent intensity of the orifice jets. The initial flow structure near the nozzle exit was altered due to the different nozzle exit shapes and the resulting flow structure impacted on local heat transfer behavior.

Figure 2-12 below shows the local Nusselt number distribution at H/D=2. Two maxima appear for all the nozzle shapes. The first peak is about 3-6% higher than the stagnation Nusselt number, and the ratio of the magnitudes of the peaks increased with higher jet Reynolds numbers. The second peak is 2-14% lower than the stagnation Nusselt number and the ratio decreased with increasing Reynolds number. The first peak in the local Nusselt number, corresponding to maximum heat transfer rates, occurred near lateral edge location of the orifice nozzles (r/D=0.5). The first peak is due to high turbulence intensity of the flow at the nozzle edge. The large-scale toroidal vortices impinge on the plate at the local maximum location. For the sharp-edge orifice nozzle, the secondary peak is located at R/D=1.4 and is in a similar location where induced toroidal vortex interactions occur.

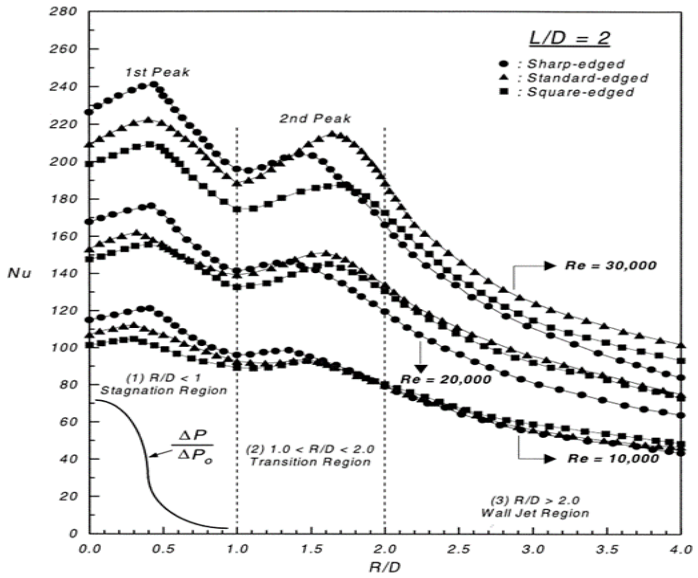

Figure 2-12: : Local Nusselt number variations with r/D at nozzle-to-plate spacing H/D=2, Lee, et., al., [54]

A separate experiment by Lee and Lee [50] investigated turbulent flow heat transfer characteristics in the stagnation region for an axisymmetric submerged air jet impinging on a heated surface plate. The temperature profile of the impinging surface was measured including the stagnation region. Their results showed the complexity of the stagnation region due to flow interaction between the ambient air and the impingement flat plate. They identified the Nusselt number relationship for nozzle-to-plate spacing and jet Reynolds number as $Nu_0 \propto Re^{0.565}(\frac{H}{D})^{0.0384}$. At small nozzle-to-plate spacing, H/D=2, the stagnation Nusselt number variation with Reynolds number is described as $Nu_0 \propto Re^{0.50}$.

Two maxima were found for the temperature distribution. The first peak was identified as due to the accelerated radial flow around the nozzle edge. The second peak corresponded to the flow transition from the laminar regime to a turbulent boundary layer. With the increase of jet Reynolds number, the locations of these maxima move outward. For large H/D (>6), the local heat transfer rate reduces monotonically with radial distance. The heat transfer is strongly dependent on Reynolds number at larger H/D due to higher turbulence intensity. As mentioned previously, a stagnation point is formed for the axis-symmetric jet while for

the two-dimensional jet a stagnation line is formed. Analytic studies for the inside of the stagnation region are relatively few and limited. For laminar flow conditions, disagreement remains on the actual dependency of the heat transfer on Reynolds number. Proposed relationship including $Re^{-0.4}$, and $Re^{-0.64}$. It has also been suggested that the Prandtl number needs to be taken into account when deriving such a relationship. Kendoush [55] derived an empirical formula for forced convective heat and mass transfer near stagnation region over a flat surface for laminar flow with different jet impingement conditions. A singularity was found in the solutions and identified as a stagnation point.

Figure 2-13 shows the stagnation Stanton number as a function of jet Reynolds number. As jet Reynolds number increased, the stagnation Stanton number decreased for all the jet profiles tested, including flat and parabolic shapes. It was found that the similarity between both the heat transfer and mass transfer conservation equations can be used to calculate the mass transfer rate from the solid surface to the impinging fluid inside the stagnation region

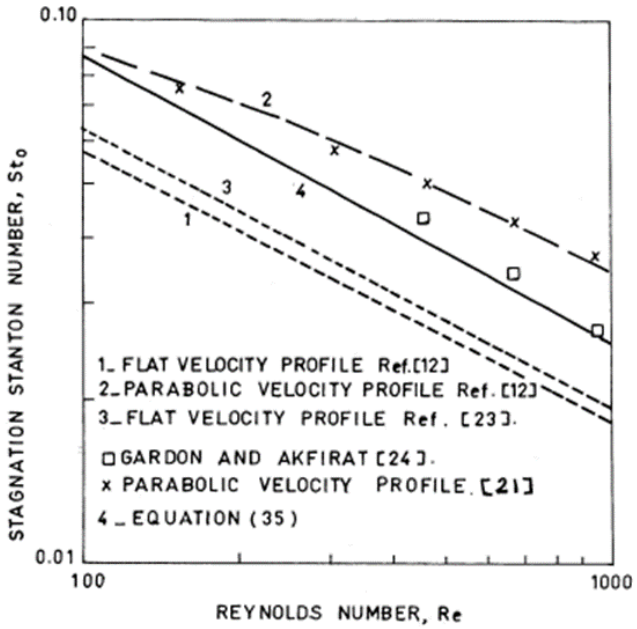

Figure 2-13: Stagnation Stanton number variation with Re[55]

There are also many explanations of the vortex structure impact on the heat transfer enhancement in the stagnation region. Sakakibara, et al., [56] experimentally measured both fluid temperature and flow velocity profiles in the stagnation region and identified pairs of counter-rotating vortices that swept cooler fluid toward the wall and carried heated fluid outwards. Such an ejection mechanism is critical to the heat flux where turbulence is dominant.

Streamwise vortex pairs travel in the fluid from the free-jet region into the stagnation region and the vortex strength increases with turbulent intensity. These vortex interactions enhance the local heat transfer rate. The high energy present is attributed to the scale of the turbulence vortex structure which is highly coherent for large-scale vortices. The vortex structure near the heated surface on which the jet impinges, match this flow structure. In between vortices, counter-rotating vortex pairs create an upwash effect while next to these vortex pairs, downwash is seen in the stagnation region. It was suggested that the amplification of the vorticity was due to convective effects while the vortex pairs were elongated by the diverging flow of the impingement jet. It was found that the wall temperature in the downwash region under the vortex pair was lower than in the upwash region. The heat flux was represented by a weighted probability density function which showed that the turbulent heat flux was due to the hot fluid from the wall caused by the upwash.

Table 2-3 below summaries and compares all the experimental and numerical set ups encountered in this section of the literature review.

Table 2-3: Summary of the jet configurations identified in the present section of literature review

First author	Date	Fluid	Nozzle geometry	Nozzle diameter (width) (mm)	Re (jet velocity) (m/s)	H/D (H/W)	Jet angle (α˚)	Data	Other Data	Measurement technique
Goldstein, R.	1986	Air	circular	12.7	61,000-124,000	2-12	90	recovery factor	temperature	thermocouple
Lee, J.	1999	Air	circular	25	5,000-30,000	2-10	90	temperature	Nu	LCT
Hoogendoorn, C.	1976	Air	circular	57	20,000-66,000	2 and 10	90	temperature	Nu	LCT
Zu, J.	2009	Air	circular	-	10,000-30,000	1-6	90	Nu		CFD
San, J.	2006	Air	circular	1.5-9	10,000-30,000	1-6	90	temperature	Nu	thermocouples
Lee, J.	2000	Air	circular	25	10,000-30,000	2-10	90	temperature	Nu	LCT
Kendoush, A.	1998	Fluid	circular/slot	-	100-1000	8-24	90	velocity	temperature	LCT
Sakakibara, J.	1996	Water	rectangular	14.5x150	2,000-20,000	8	90	velocity	temperature	DPIV[1]

[1] Digital Practice Image Velocimetry

2.2.3 Heat Transfer Distribution

Both the ratio of the jet distance from impingement surface to nozzle diameter (H/D) and the angle of inclination of the jet (*α*) have been found to have a significant effect on the heat transfer distribution over the surface in the radial direction. This section is organized into 3 sub-sections to discuss in detail the heat transfer distributions at small nozzle-to-surface spacing (H/D<2), large nozzle-to-surface spacing (H/D>2), and oblique jet conditions. This section is intended to summarize and provide a thorough overview of jet impingement.

I. Small jet to target distance (H/D≤2)

A very recent study by Kuraan, et. al., [57] who performed an experimental study of a free water jet impinging a flat surface under the influence of jet to target distance less than one. The jet to target distance was divided into two regions, the deflected region and the inertia dominant region where both regions have length of H/D≤0.4 and 0.4≤H/D≤ 1 respectively. The effects of jet to target distance on stagnation point Nusselt number and pressure were considered in this study under the influence of wide range of Re (between 4000 and 8053). New correlations of stagnation point Nu and pressure were reported on this study based on the author key findings. Figure 2-14 below demonstrates the effect of jet to target distance on normalized stagnation Nu ($Nu_o{}^*$) where a noticeable increase in $Nu_o{}^*$ within the deflected region as H/D decreases. However, this is not the case within the dominant region, where H/D had a negligible effect on $Nu_o{}^*$. This is due the fact that the inertia is the dominant factor within this region. Based on the results shown in Figure 2-14, the author reported a correlation of the normalized $Nu_o{}^*$, the normalization was made with stagnation point Nu at H/D=1. The correlation reported from the author which is within an error of $\pm 15\%$ of the experimental results is as follow:

$$Nu_o{}^* = \left[1 + \frac{1}{32}\left(\frac{H}{D}\right)^{-2}\right]^{0.3}$$

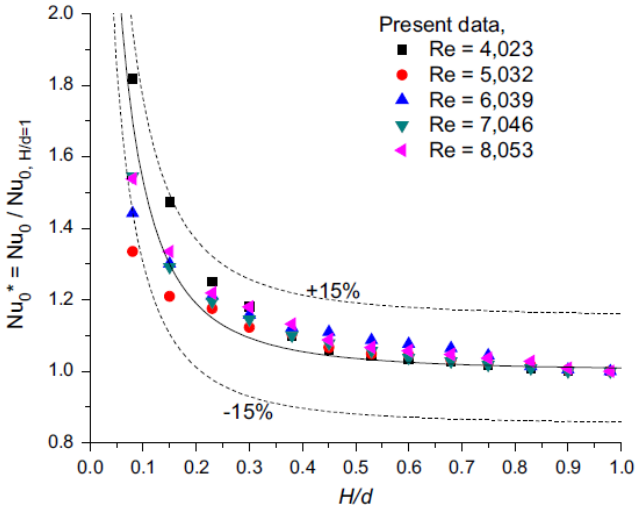

Figure 2-14: Normalized stagnation Nu for different H/D [57]**.**

Another correlation of stagnation point pressure (P_o^*) was also reported by Kuraan based on his key findings in Figure 2-15, the error of this correlation when compared to the experimental results is $\pm 20\%$:

$$P_o^* = \frac{P_o}{1/2\rho u_1^2} = 1 + \frac{K}{16}\left(\frac{H}{D}\right)^{-2}$$

Where k is the deflection coefficient which equals to 0.5 and u_1 is the jet velocity when leaving the nozzle.

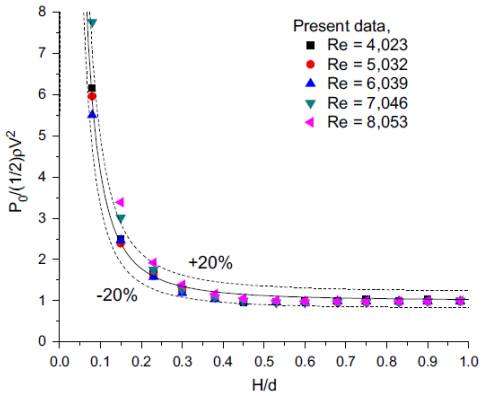

Figure 2-15: Normalized stagnation pressure for different H/D [57]**.**

Zhou, et. al., [58] studied numerically the effect of high temperature difference between the jet and the target surface on the heat transfer rate. The two-

dimensional study employed air as working fluid which was ejected from a circular jet at different Reynolds numbers of 4000,8000 and 12,000 with Mach number equals 0.3 where jet to target distance (H/D) was 2,6,10 and 14. The temperature differences (**Δ**T) investigated in this study were 200K, 400K and 600K) as such high difference effects the fluid physical properties such as density and dynamic viscosity. The V2F turbulence model was used in this study. Due to the symmetry of the flow in orthogonal jets, a 2D computational domain was used with 2DX10D in length and height, where D is the nozzle hydraulic diameter. The study adapted mesh size of 270x300 cells giving y^+ value of 0.59. The numerical results showed that, as **Δ**T increases, the air density decreases so does the heat transfer where Nu shows independency on the temperature differences.

Huang, et. al., [59] experimentally investigated heat transfer distribution as result of circular air jet impingement on a uniformly heated flat plate. Their investigation focused on determining local and averaged Nusselt numbers for low Reynolds number flows and small spacing between jet and plate. In their experiments, H/D ratios of 1 to 12 were tested with normalized radial distance from stagnation point, r/D between 0 to 10. Figure 2-16 shows Nusselt number distribution at H/D≥1. Generally, *Nu* has a clearly defined peak at the stagnation point for all values of Re, and all values of H/D. The value of *Nu* increases with Reynolds number but decrease rapidly with r/D. At the smallest jet to target spacing (H/D=1), the maximum Nusselt number was found at the stagnation point for low Reynolds numbers. However, when the Reynolds number was increased, the shape of the curve representing Nu changed and, gradually, two peaks appeared at about r/D=1.8-2.0, with a slight decrease in *Nu* at r/D= 0.

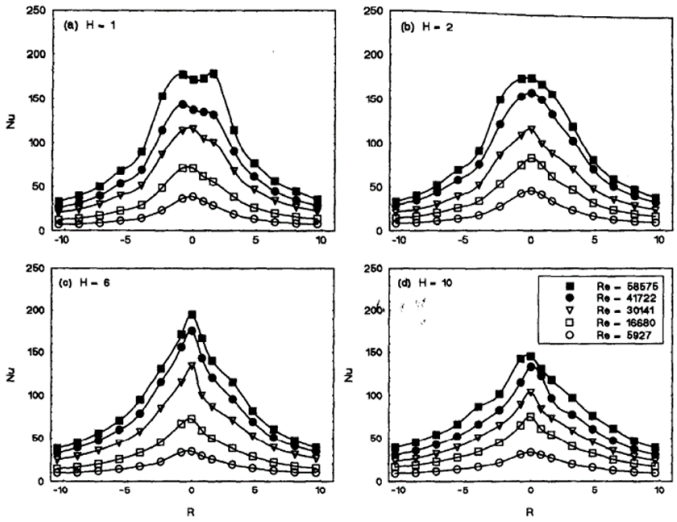

Figure 2-16: Nusselt number distribution in radial direction on the surface plate at different Reynolds number and jet to plate spacing [59]

Lytle and Webb [60] examined the effect of nozzle-to-plate spacing on the local heat transfer behavior on a flat plate for 3,600 < Re < 27,000, with H/D < 1. They studied flow structures using LDV (Laser-Doppler Velocimetry) and surface wall pressure. Their results gave a good correlation between Nu and $Re^{1/2}$. In addition, Nu varied with nozzle-to-plate spacing according to $(H/D)^{-0.288}$. A significant heat transfer enhancement was achieved by this small nozzle-to-plate spacing due to jet flow acceleration accompanied by high turbulence levels. At much smaller spacing, H/D ≤ 0.25, a local minimum was observed in the heat transfer at the stagnation point. This was surrounded by two radially symmetrical peaks, an inner primary and an outer secondary.

Using flow visualization techniques and wall pressure measurements, the physical phenomena responsible for the peaks were identified. The inner primary peak was considered due to flow acceleration near the jet exit. The outer, secondary peak was due to high turbulence levels in the flow. With increasing jet Reynolds number and larger gap between nozzle and plate, the local maxima corresponding to the outer peak Nusselt number moved radially outwardly. This work showed that it was possible to correlate the experimental curve to analysis based on laminar theory quite well.

Goldstein et., al., [46] have presented details of their experimental method to measure surface heat transfer distribution of a flat plate. They used single and multiple jet array configurations. For small jet to plate spacing (H/D=2), single jet impingement gave a local minimum Nusselt number near the centreline of the plate. Such minimum Nusselt number increased with the larger jet to plate ratio (H/D=6). At the same small jet spacing (H/D=2) using three jets in a co-linear arrangement, a local minimum was still observed at the central jet, but for the outer jets, there were no local minima. The Nu number measured for both 3-jet and 7-jet arrays showed higher heat transfer coefficients for smaller values of H/D=2 and lower heat transfer values for the larger spacing (H/D=6). This phenomenon is because of cross-flow effects arising from the use of multiple jets which enhanced flow mixing turbulence produced from flow interactions. In addition, as each jet spreads it increasingly penetrates the flow of adjacent jets and as results of such penetration, local minima disappear.

In practical engineering applications, small jet to target distances is common due to practical design structure limitations. Guo, et al., [61] studied the fluid flow and heat transfer characteristics of narrow gap jet impingement using multiple jet configurations. Their test data included jet to target spacing of H/D=0.5 and 1, with Reynolds numbers from $2x10^4$ to $5x10^4$. At H/D=0.5, under normal jet impingement conditions, the Nusselt number distribution was non-uniform, particularly in the upstream jet flow region. Their experiment tested an inclined jet version that showed better heat transfer distribution than did normal jet impingement. An optimized jet array using inclined angle of 75^0 and the same inline array showed improved heat transfer with a much higher average Nusselt number with a much more uniform distribution compared to the results obtained for normal incidence. They concluded that increasing Reynolds number gives a beneficial improvement on the local heat transfer distribution. This is particularly true for the small jet to plate spacing with a higher Nusselt number observed near the stagnation point. Figure 2-17 below shows the distribution in heat transfer rate obtained with their experimental set-up

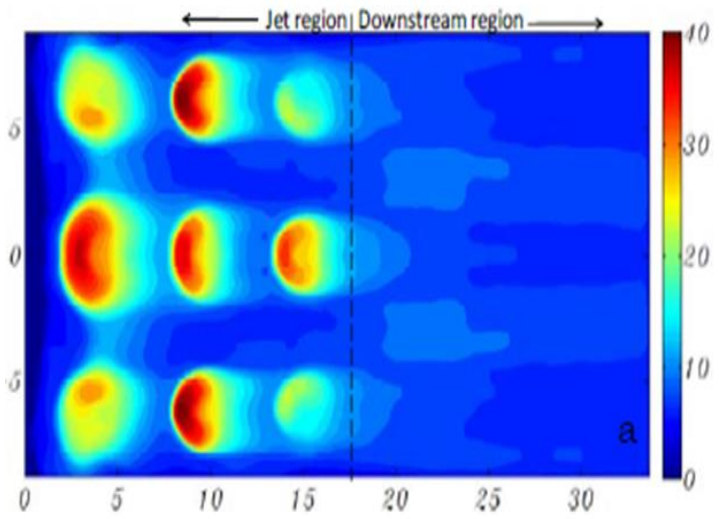

Figure 2-17: Example of plate surface Nusselt number distribution at jet Re=2x10^{4,} Guo, et al., [61]

Behnia, et al., [62] conducted a numerical study using CFD to investigate the effect of confinement on jet impingement with very small H/D (< 0.25). They chose turbulence model v^2f to capture the fluid flow and heat transfer with high accuracy. Their numerical results predicted that the confinement had critical impact only when H/D is small. Figure 2-18 shows the CFD and experimental results based on flat plate jet impingement at a Reynolds number of 23,000. Very good agreement was achieved between the experiment and v^2f turbulence model over a wide range of H/D (up to 14). Both experiment and CFD identified a peak Nusselt number at around H/D of 6-7. Such a peak Nusselt number is also consistently found in the stagnation point region. Based on their CFD analysis, fluid flow turbulence and velocity profiles are considered important effect in determining heat transfer distribution for both small and large values of H/D. This numerical study demonstrated that jet flow is not accurately captured using the k-ε model. Such a model is insufficient to predict the turbulent boundary layer profile on the plate which has significant impact on the stagnation heat transfer.

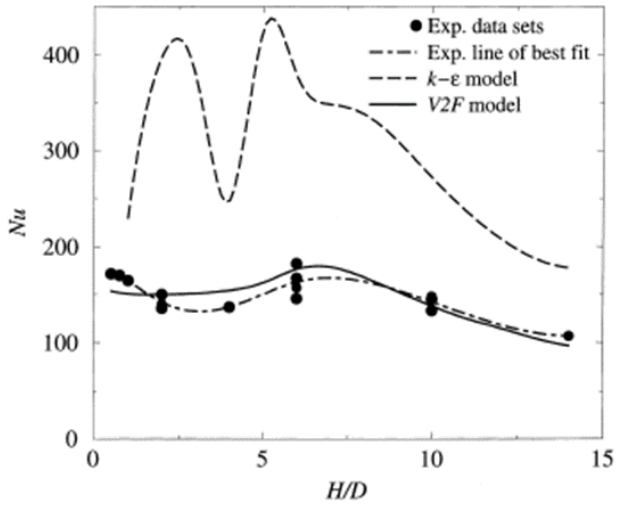

Figure 2-18: Stagnation Nusselt number with jet to plate spacing [62]

Wang, et al., [25] investigated heat transfer characteristics based on different jet parameters including jet flow speed, jet inclination angle, nozzle size and jet-to-target spacing. Figure 2-19 shows that increasing jet height will initially increase flow speed but then it will decrease gradually as jet height increases further. Pressure does not change much with different jet heights. This is due to the momentum interchange between the jet flow and the surroundings which increases with increasing distance between jet and target. The anisotropic structure of the flow is obvious in the jet axial direction when the jet angle is set at 60^0, eg., with jet diameter 5 mm, jet length 8 mm and jet height 50 mm. This flow structure was found to have a direct impact on the peak Nusselt number (and therefore high temperature) on plate impingement.

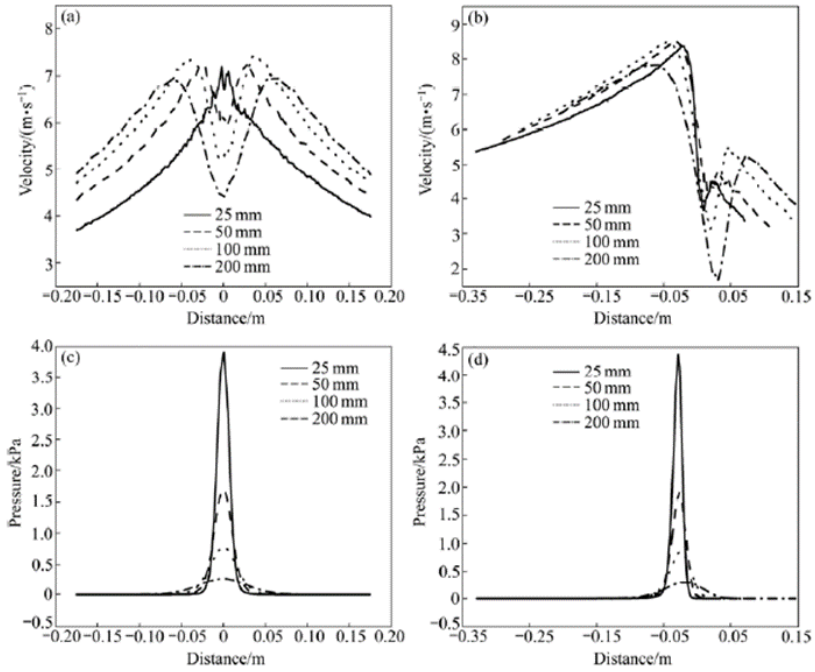

Figure 2-19: Impact of the jet to target distance on (a) Jet velocity in the transverse direction (b) Jet velocity in a longitudinal direction along centreline (c) Transverse pressure (d) longitudinal pressure along centreline [25]

Recently, Wae-Hayee, et al., [63] studied fluid flow and heat transfer characteristics of jet impingement subject to cross-flow for an in-line jet configuration and relatively short jet to plate spacing (H/D=2). They tested different ratios of the jet to cross-flow velocity of 3, 5, and 7 using a given jet Reynolds number of 13,400. Flow visualization was used and the plate surface Nusselt number was evaluated from the measurements. A numerical approach was also conducted to provide a detailed insight into flow interaction in between the jet and cross-flow during the impingement process. For H/D = 2, it was found that increasing cross-flow promoted higher heat transfer, especially at the peak Nusselt number. The maximum local Nusselt number was identified as occurring at the stagnation point when the ratio of cross-flow velocity to jet velocity was 3 when both high jet turbulent flow and high cross-flow velocity occurred simultaneously. However, the averaged Nusselt number was found to be the lowest .

Their numerical simulation study used commercial software Ansys Fluent 13.0. Geometry that matched the experiment was used in their CFD model as

shown in Figure 2-20. They chose the k-ε turbulence model to couple with the momentum and energy equations. A systematic grid dependency study was also conducted to ensure sufficient mesh resolution was applied. Based on this study, they determined that at least 2 million cell count was required to achieve y+ criteria below 5. Figure 2-20 shows the velocity vector plot in the X-Y plane illustrating how jet flow and cross-flow interact at different velocity ratios. As the cross-flow velocity increased, the jet flow was deflected sideways. In addition, the ground vortex which appeared as local flow circulation upstream of the jet at low-velocity ratio no longer existed at maximum cross-flow.

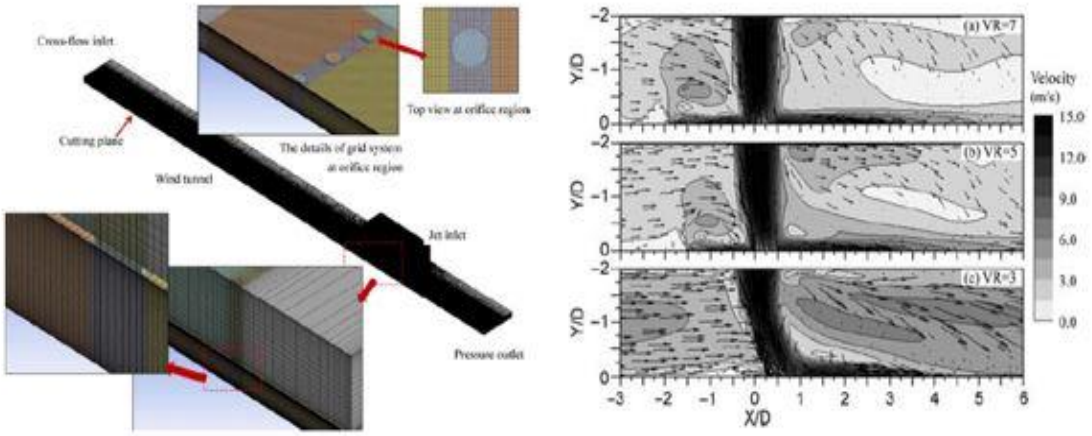

Figure 2-20: CFD model and velocity vectors distributions by M. Wae-Hayee et al.[63]

Another study made by Jensen, et. al. [64] to investigate numerically the influence of turbulence intensity at the jet inlet. A circular gas jet with jet to target distance (H/D=2) was employed in this numerical study. The paper presented the choice of turbulence model on the heated wall for high Reynolds number (Re=166000) and high temperature difference between the wall and the jet (**Δ**T=1600K) where three turbulence models were employed, low Re k-ε, RNG k-ε and V2F.

The turbulence intensity showed an obvious enhancement on heat transfer rate by a factor of 3 when increased from 1.5% to 10% where the turbulence model has also a significant influence on the heat transfer prediction especially at the

stagnation region to about a 100% differences. A correlation has been proposed relates the stagnation point heat transfer to Re, turbulence intensity.

San, et al., [65] studied jet to target spacing $1.0 \leq H/D \leq 4.0$, using circular air jet impingement on a plate in a confined channel. A staggered jet configuration was used consisting of one center jet and four surrounding jets. With increasing jet Reynolds number a higher Nusselt number was achieved in the stagnation region. Experimental correlation results showed that the stagnation Nusselt number of the center jet varied in according to $Re^{0.7}$ and $(w/d)^{0.49}$. However, the stagnation Nusselt number was found to be insensitive to H/D, S/D, and L/D. For a single confined jet, increasing the plate length had a significant impact on the stagnation Nusselt number compared to staggered jet array. This was due to flow mixing enhancement between the jet and flow recirculation in the downstream region.

Because nozzle to plate spacing varies with different designs and applications, it is useful to develop a correlation between stagnation Nusselt number and pressure as a function of nozzle to plate spacing. Choo, et al., [66] conducted an experimental study for H/D between 0.1 and 40. Both local Nusselt number and wall pressure at the stagnation points were measured and used to characterize fluid flow and heat transfer behaviour based on submerged jet impingement. Three different flow regions were investigated to evaluate the effects on each as a result of varying H/D. These regions included the jet deflection region, potential core region, and free jet region. It was found that in the jet deflection region ($L/D<0.6$), increasing H/D significantly decreased Nusselt number, heat transfer performance and wall pressure of the stagnation point. In the potential core region ($0.6<L/D<7$), the Nusselt number and wall pressure were insensitive to nozzle to plate separation. In contrast, when the plate was located within the free jet region ($7<L/D<40$), both local Nusselt number and wall pressure decrease monotonically and quite sharply with increasing H/D. Figure 2-21 shows local Nusselt number variations with H/D from 0.1 to 40.

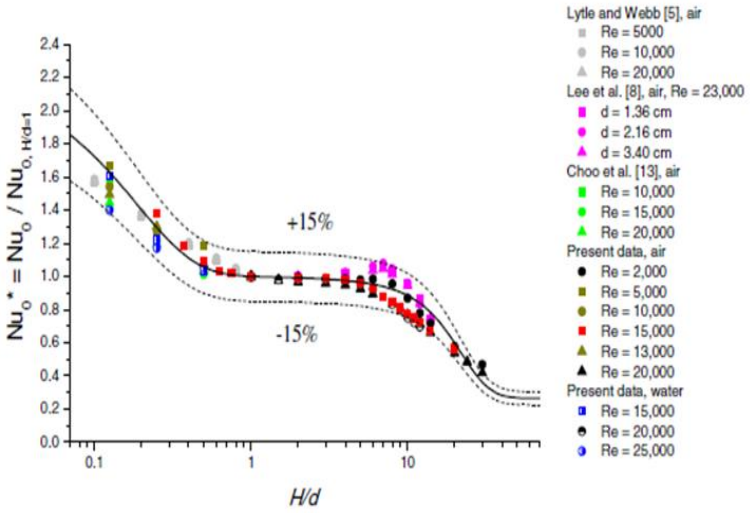

Figure 2-21: Variations of stagnation Nusselt number with nozzle to plate spacing [66]

Dutta, et al., [67] used the numerical approach to predict fluid flow and heat transfer performance sensitivity to the small nozzle to plate spacing using slot jet impingement. Their simulation predicted a secondary peak corresponding to the Nusselt number at small values of H/D. Fluent (Large Eddy Simulation [LES]) a state-of-the-art commercial CFD software package was used to determine the transient characteristics of the flow and heat transfer due to mixing flow structure. While the large-scale flow structure was resolved with a fine grid resolution, small-scale eddies were modelled using the dynamic Smagorinsky model. Two computational domains using different grid sizes were studied, including y+=4 and y+=2. Their numerical results based on inflow conditions using a vortex method was capable of capturing secondary peaks in the Nusselt number, see Figure 2-22. stagnation region is quite different from the standard log law of the wall function. The secondary peak in the Nusselt number was consistently located where strong high energy containing large eddies were to be found. Based on analysing both flow turbulence kinetic energy and mean flow axial velocity in the same peak region, these factors are considered to have significant impact on the secondary peak in the Nusselt number.

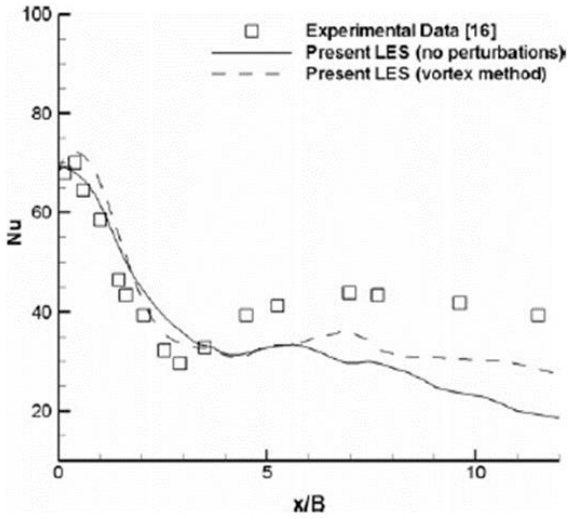

Figure 2-22: Correlation of variations of the local Nusselt number on the impingement plate using different inflow conditions from LES method[67]

Yong, et al., [68] experimentally investigated the effect of multiple rows of air jets on convective heat transfer using small jet to target spacings of H/D=2 to 4. They used multiple jets arranged either in-line or staggered based on jet-to-jet pitch ratios in both the axial flow and width directions of 2 to 5. Both arrays were tested at jet Reynolds numbers from 5000 to 25,000. As might be expected, the more dense the arrays, i.e. the closer the jets, the more heat transfer distribution showed interference from adjacent flows due to other jets. The highest heat transfer was achieved with a jet-to-jet distance ratio of 3. Based on a dense jet array configuration the smallest jet to target spacing at H/D=2 showed better heat transfer performance than the larger spacings at H/D=3 or 4. Such variations are consistent with the results for sparse arrays previously reported.

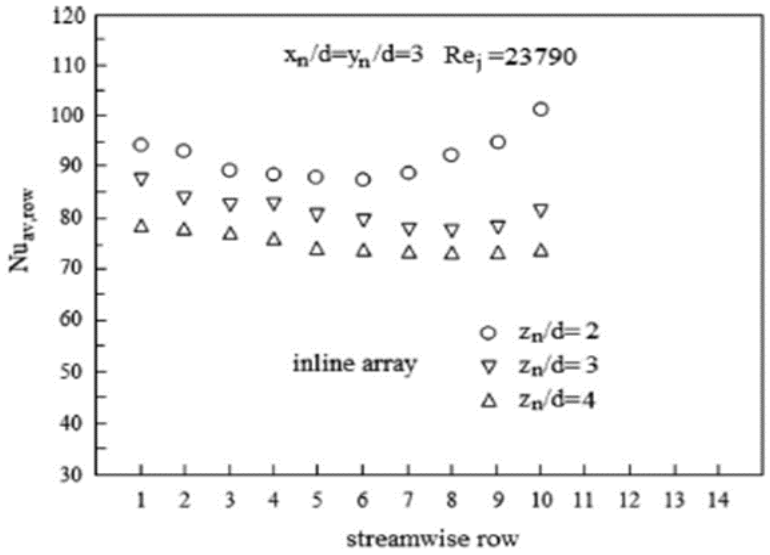

Figure 2-23: Experimental results of averaged local Nusselt number variations with jet to target spacing at H/D=2 to 4 range based on inline multiple jets array [68]

Shin, et al., [69] investigated both boiling heat transfer and single phase heat transfer. They conducted liquid jet experiments with a nozzle to plate spacings of H/D=0.5 to 4.0 using a submerged system with Reynolds numbers of 2000, 3000 and 5000. As H/D increased, liquid boiling incipience decreased. Liquid boiling was limited by its Critical Heat Flux (CHF) condition. CHF enhancement was achieved by added surface roughness, increased flow mixing and increased flow turbulence levels. As shown in Figure 2-24, H/D=1.0 gives lower CHF than H/D=0.5 or 4.0 for all Reynolds number tested. With reducing nozzle to surface spacing, strong jet flow impingement creates strong flow momentum around the stagnation point and therefore was effective in suppressing vapor bubble formation. When nozzle to surface spacing is reduced and jet velocity is increased, such a situation gave greater impact to the fully developed boiling region heat transfer performance. The results of this experiment have allowed designers of cooling systems to pay attention to the nozzle to plate spacing selection to avoid the lowest CHF by making appropriate parameter choices.

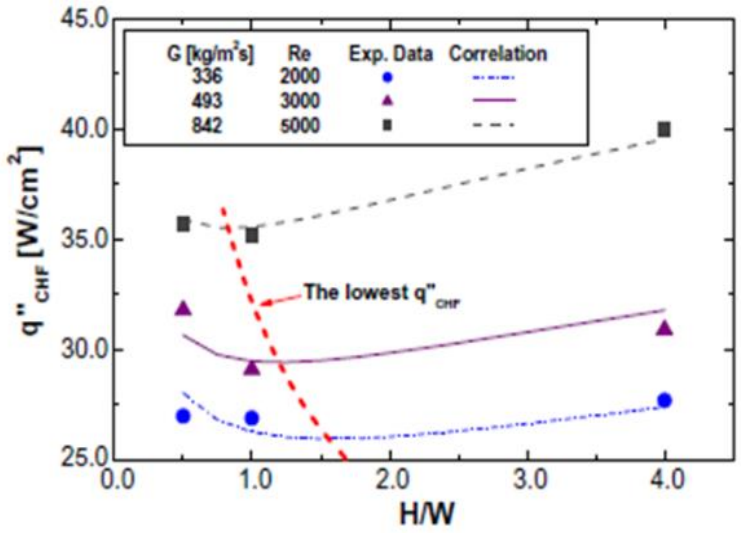

Figure 2-24: Experimental results of Critical Heat Flux (CHF) variations with different nozzle to target spacing and liquid jet flow velocity[53]

San and Shiao [53] studied jet impingement using different combinations of H/D (from 1.0 to 6.0) combined with different jet plate widths, jet plate lengths, jet diameters, and jet Reynolds numbers. The correlation of stagnation Nusselt number to H/D was established as $(H/D)^{0.3}$. Figure 2-25, shows that as H/D decreased, the stagnation Nusselt number increased consistently for all three jet Reynolds numbers (Re = 10,000, 15,000 and 30,000). Such high heat transfer performance with small spacing was mainly due to strong jet flow momentum impingement on the target. When the H/D increased, greater recirculation of the flow occurs which decreased the heat transfer on the target.

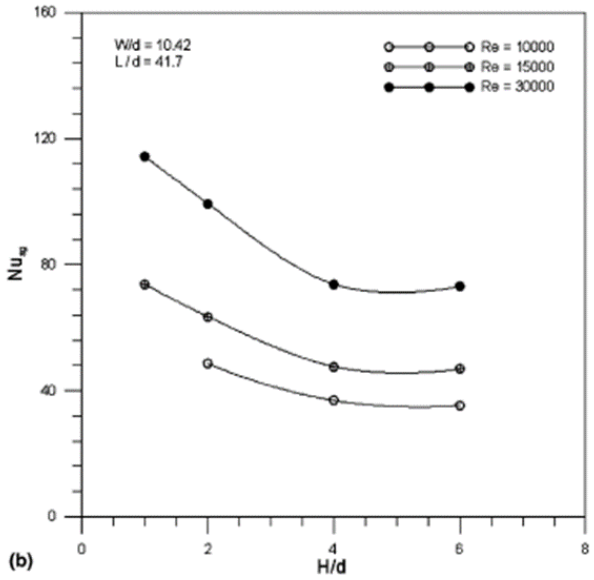

Figure 2-25: Experimental results of stagnation Nusselt number with nozzle to target spacing, H/D = 1, 2, 4 and 6 [53]

San and Lai [70] investigated experimentally the effect of the spacing between staggered jet arrays and the local Nusselt number, for Re = 10000, 20000, and 30000. As part of their experiment, they also varied the normalized jet to target separation (H/D=2, 3, 4 and 5). A correlation function relating stagnation Nusselt number was established based on jet Reynolds number, jet to jet spacing and jet-target separation. Figure 2-26 presents the experimentally measured Nusselt number in the stagnation region, with the jet to jet spacing from 4.0 to 16.0 for H/D from 2.0 to 5.0. At each value of H/D, a peak Nusselt number was found which is considered as the optimal design for the jet to jet spacing parameter. At larger values of H/D, such optimal jet to the jet spacing requirement is reduced. At smaller values of H/D, the optimal design allows the larger jet to jet spacing. The decrease of heat transfer performance with continuous increasing jet to jet spacing at a given H/D is called the jet fountain effect.

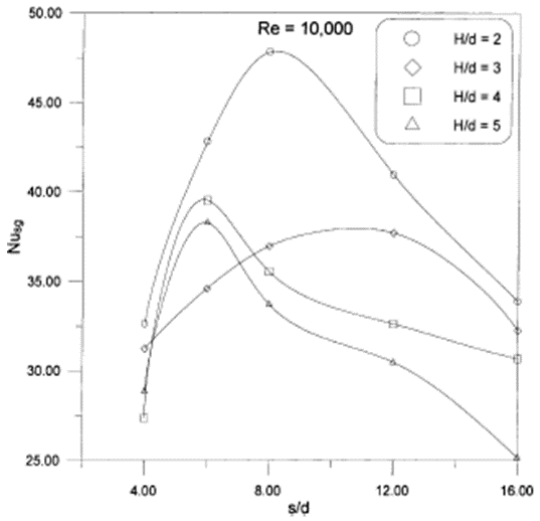

Figure 2-26: Experimentally measured stagnation Nusselt number variation with jet-to-jet spacing at different H/D [70]

The jet to target spacing is also found to vary the recovery factor although such recovery factor is independent of the jet Reynolds number. Goldstein, et al., [49] arrived at this conclusions based on experimentally testing circular air jet impingement. They demonstrated that the maximum stagnation Nusselt number occurs at H/D =8, see Figure 2-27. At small H/D, the recovery factor in the stagnation region has a minimum value at around r/D=2. Such minimum is deemed due to flow separation in the vortex ring region in the shear layer. At higher values of H/D, jet flow “pulls in” ambient air due to greater flow recirculation and mixing. For all H/D, it was determined that the correlation of $Nu/Re^{0.76}$ was valid.

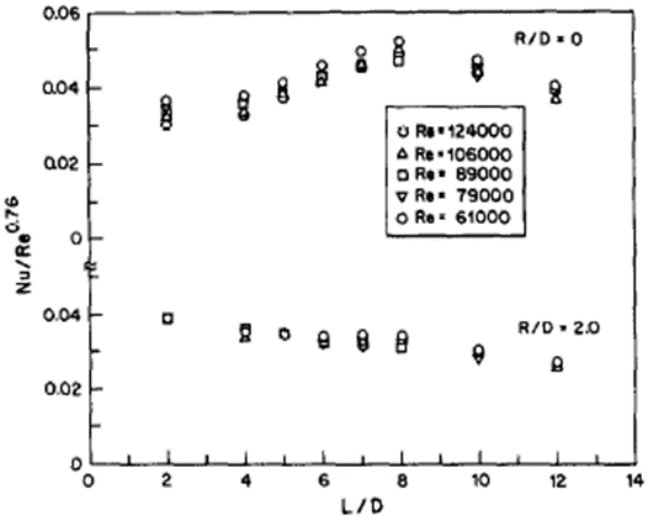

Figure 2-27: Experimental measured Nusselt number versus different jet height [49]

II. Large jet to target spacing (H/D≥2)

Bouchez, and Goldstein [45] investigated experimentally how different jet cross-flow rates interacted with the impingement surface around the stagnation point at large H/D. It was found that with a lower cross-flows no flow recirculation occurred and both mixing zone and stagnation point moved further downstream of the jet than for higher cross-flows. In addition, the jet pattern with a lower cross-flow was deflected from the jet centreline. Figure 2-28 shows smoke flow visualization using dry ice submerged in liquid water with a low cross-flow rate but the large value of H/D. Turbulence flow separation near the jet impingement region was clearly captured. Such turbulent flow has insufficient momentum to penetrate into axial jet centreline flow and so there was very little impingement on the tunnel floor

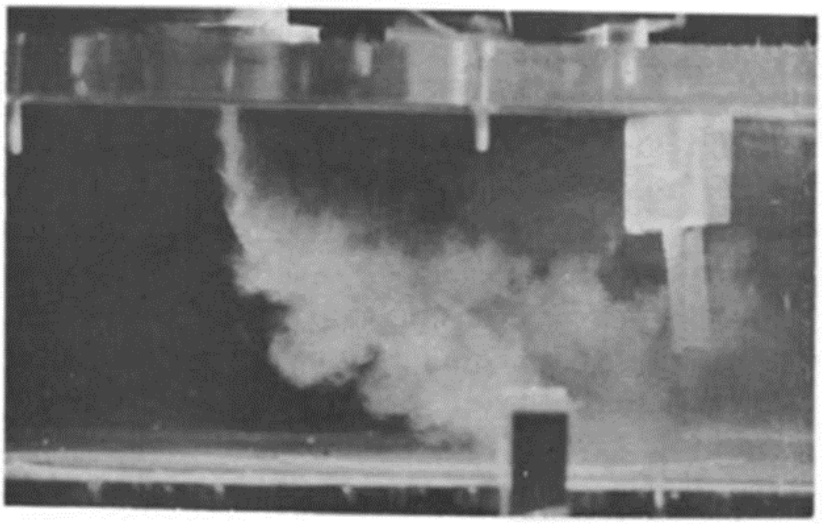

Figure 2-28: Experimental smoke visualization with large jet to target spacing and cross-flow [45]

Donadlson and Snedeker [71],[72] studied free jet impingement flow for both normal and oblique conditions with different surface shapes at H/D=39. The radial velocity distribution around stagnation point was determined from surface pressure probe measurements on the plate. When the jet impinged normally, the radial velocity gradients were found to correlate well with the centreline velocity of the jet and 0.5D from the same axial location. As jet inclination angle was gradually moved away from the normal position, the correlation became weaker. Several combinations of jet flow intensity and jet to target spacings were tested to investigate stagnation pressure for different plate shapes. Figure 2-29 shows the stagnation pressure distribution at a H/D=39. The convex hemisphere shape showed the steepest decline in stagnation pressure with radial distance. In contrast, a concave hemisphere has the least change in stagnation pressure with radial distance.

Figure 2-29:

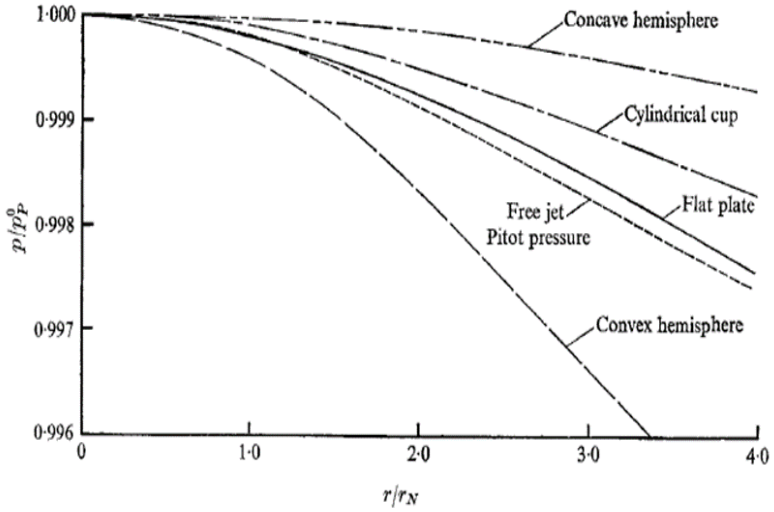

Experimental measured pressure distribution at the stagnation point with different jet impingement target surface shapes at H/D=39 [72]

Robinson and Schnitzler [73] studied a liquid water, free jet array impingement at H/D ratios between 2 to 30. They reported a good correlation of heat transfer and pressure drop with both H/D and jet to jet spacing parameters. With the increase in H/D from 5 to 20, it was found that the heat transfer performance deteriorated monotonically with increased jet to target spacing. At a given jet Reynolds number, increasing H/D also had a detrimental effect on the heat transfer performance. For large values of H/D, the heat transfer performance shows less sensitivity to the jet to jet spacing compared to small values of H/D. At H/D>10, it was observed that the thermal performance was better due to the free jet formation of the submerged jet.

Table 2-4 below summaries and compares all experimental and numerical studies gathered in this section

Table 2-4: Summary of the jet configurations identified in the present section of the literature review

First author	Date	Fluid	Nozzle geometry	Nozzle diameter (width) (mm)	Re (jet velocity) (m/s)	H/D (H/W)	Jet angle (α˚)	Data	Other Data	Measurement technique
Kuraan, A.	2017	Water	circular	6.65	4,000-8,000	0.08-1	90	temperature		thermocouple
Zhou, T.	2016	Air	circular	10	4,000-12,000	2	90	Nu	h	CFD
Huang, L.	1994	Air	circular	6.2	6,000-60,000	1-12	90	temperature		thermocouple
Lytle, D.	1994	Air	circular	7.8	3600-27600	0.1-1	90	velocity	pressure	infrared camera
Guo, Q.	2011	Air	circular	12	24,300-53,900	0.5-1	75-90	velocity	temperature	LCT
Behnia, M.	1999	Air	circular	10.9	10,000-30,000	0.1-2	90	Nu		CFD
Wang, B.	2013	Air	circular	2.5-15	(5-20)	10-80	30-90	Nu		CFD
Wae-Hayee, M.	2014	Air	circular	13.2	13,400	2	90	Nu		CFD/LCT
Jensen, M.	2013	Gas	circular	50	110,000-664,000	2	90	Nu		CFD
San, J.	2007	Air	circular	6	5,000-15,000	1-4	90	temperature		thermocouple
Choo, K.	2016	Air/Water	circular	4	5,000-25,000	0.1-40	90	temperature		thermocouple
Dutta, R.	2016	Air	slot	(9.2)	20,000	4	90	Nu		Fluent
Yong, C.	2015	Air	circular	2	5,000-25,000	2-4	90	temperature		thermocouple
San, J.	2001	Air	circular	3	10,000-30,000	2-5	90	temperature		LCT/infrared
Robinson,	2007	Water	circular	1	650-6500	2-30	90	temperature	Nu	thermocouple

2.3 Enhancement techniques

2.3.1 Nozzle geometry

Jet nozzle geometry is considered to play a primary role in heat transfer performance of the jet impingement. Various past research studies have suggested that the differences of reported performance results may be due to slightly different geometries tested. To gain a better understanding of such differences, research on the effect of nozzle geometry has been widely conducted by academic institutes. One aspect of nozzle performance was whether the nozzle was confined. A confined nozzle is when there is, around the nozzle some form of blockage, which may or may not totally enclose the nozzle: it may be semi-confined or fully-confined. For example, the blockage could depend on how the nozzle is machined into a back-plate.

Brignoni and Garimella [48] conducted experiments studying various nozzle geometries and shapes and their impact on pressure drop and local heat transfer distribution for confined air jet impingement, see Section 2.1.1. Their tested nozzle geometries include chamfered and unchamfered (square-edged) nozzles. Different jet impingement configurations were tested including different chamfer lengths, different chamfer angles, and different nozzle-to-target distances. They claimed that a 31% heat transfer enhancement was achieved by using a chamfered nozzle with a narrow-angle. Figure 2-30 shows different nozzle geometries with different chamfer depths and chamfer angles.

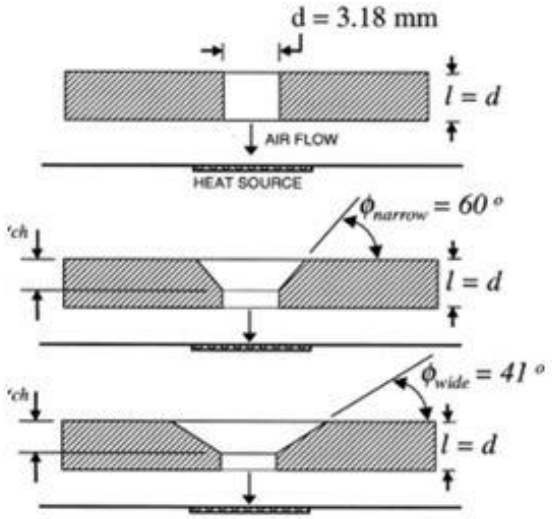

Figure 2-30: Nozzle chamfer depth and chamfer angle [48]

Colucci and Viskanta [47] reported on heat transfer using a nozzle with a hyperbolic shape for a confined jet impingement configuration. They concluded that as the nozzle radius increased, the distance of the second maxima from the centreline jet axis increased. Compared to an orifice nozzle, local Nusselt numbers for a hyperbolic shaped nozzle exhibited higher values. With reduced nozzle-to-plate spacing, the impact of the confinement plate on the local heat transfer is increased. The first and second maxima were found to be more obvious in the confined condition. Depending on the exit clearance, using hyperbolic nozzles that were specially constructed and based on contoured and diverging shapes, the different jet exit flows created varied from acceleration/deceleration to constant flow.

The nozzle exit geometry design also played a critical role in determining the heat transfer enhancement and therefore has been useful for many passive control applications. Lee and Lee [54] see Section 2.1.2, experimentally investigated nozzle geometry impact based on axisymmetric submerged air jet impingement using different three different nozzle exit configurations. They established a correlation of stagnation Nusselt number with jet Reynolds number for different H/D ratios. Orifice geometry could produce higher turbulence and non-uniform velocity gradients that contributed much of the heat transfer enhancement.

Change of nozzle exit configurations also impacted on upstream flow structure which indicated the characteristics of downstream flow and therefore the heat transfer of the impingement region.

Lee et al used vane-type swirl generators to produce highly swirling jet flow impingement for a rounded nozzle configuration. Figure 2-31 shows four different swirl generators, based on the swirl numbers S=0, 0.21, 0.44 and 0.77, and vane angles θ=0, 15, 30 and 45^0. Figure 2-32 shows the averaged Nusselt number decreased with increasing swirl flow for all values of H/D. For H/D > 2, the Nusselt number decreased steadily with the increase in H/D. At H/D=2, swirl flow did achieve a Nusselt number 35% higher compared to non-swirling flow. The vanes divide the flow into multiple jets when passing through the swirl generators. Such divided jets have a very low spreading rate and therefore result in a higher Nusselt number at lower values of H/D. Larger nozzle-to-plate spacing gives a higher spreading rate with smaller flow momentum in the tangential direction when using swirl generators and the heat transfer with swirl generators is less than for the jet with no swirl generator.

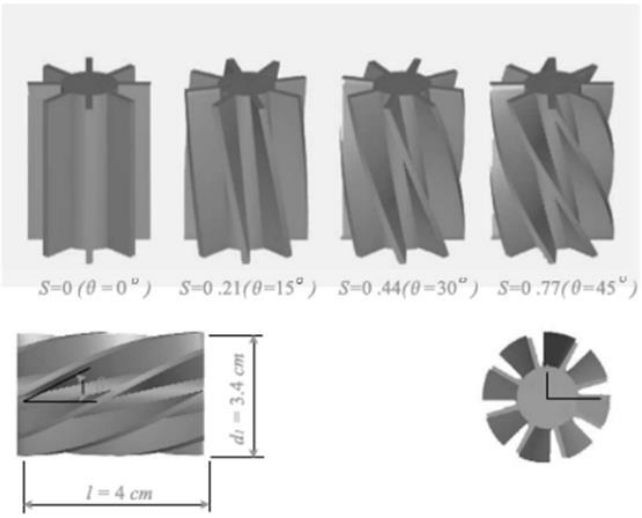

Figure 2-31: Various vane-type swirl generators geometries [74]

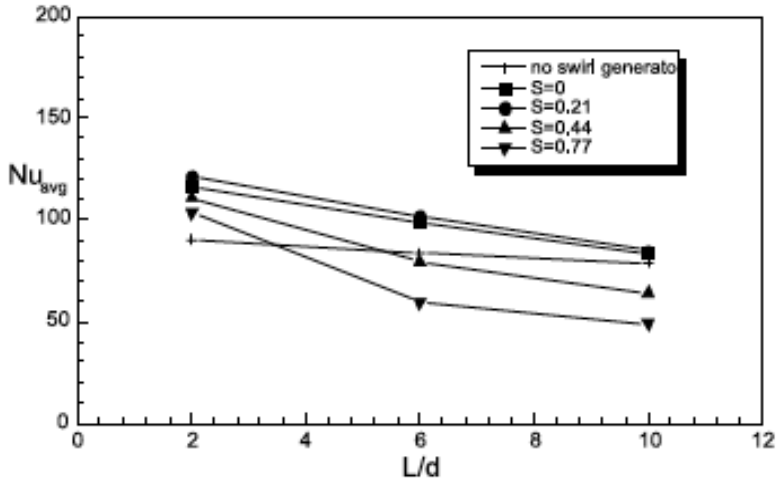

Figure 2-32: Experimental Nusselt number versus nozzle-to-plate spacing (H/D) at different swirl number [74]

Another swirl flow study using a circular jet was conducted by Wen and Jang [75]. They used swirling flow jets with jet Reynolds number from 500 to 27,000. The nozzle geometry was a smooth open tube, with a longitudinal swirling-strip (LSS) and a crossed swirling-strip (CSS). The nozzle-to-plate spacing was from H/D=3 to 16. Flow visualizations were analyzed in detail, including flow mixing, flow vortex formation, and jet flow entrainment from ambient air. The CSS configuration was found to have the highest averaged Nusselt number compared to the LSS and smooth open tube. Heat transfer was enhanced by 9-14% using the CSS and LSS. As with previous findings, their experimental results showed higher heat transfer with smaller values of H/D due to the reduction of the region covered by impingement.

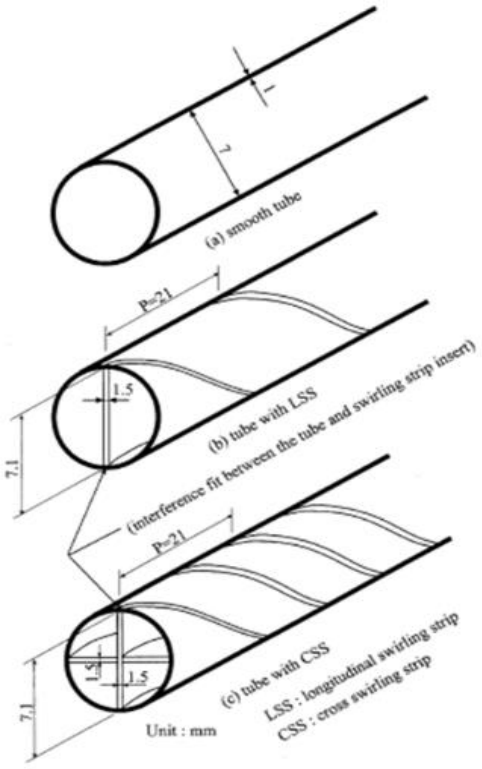

Figure 2-33: Experimental nozzle geometry based on smooth open tube, tube with LSS, tube with CSS [75]

Singh, et. al. [76] investigated experimentally and numerically the effect of an unconfined nozzle geometry on heat transfer characteristics for a jet ejected from a circular cylinder. The isoflux heated cylinder surface was impinged by a cold fluid (air) ejected from a circular, square and rectangular nozzle with equal hydraulic diameters under the influence of a Re range between 10,000 and 25,000 and H/D between 4 and 16. Figure 2-34 shows types of geometries used in Singh study. The author used a modified Re to show his results based on fixing the mass flow rate for all nozzle geometries as this is the case in in cooling of thermal systems.

$$\overline{Re_{hyd}} = \frac{\rho V_{avg.} D_{avg.}}{\mu} = \frac{D_{hyd.}\dot{m}}{\mu A_n}$$

The main key findings of Singh's study are as follow:

- For a certain Re, the rectangular nozzle geometry shows higher stagnation region Nu compared to other geometries due to higher mass flow rate. However, for the modified Nu (i.e. constant mass flow rate), the circular nozzle provides higher heat transfer rate.

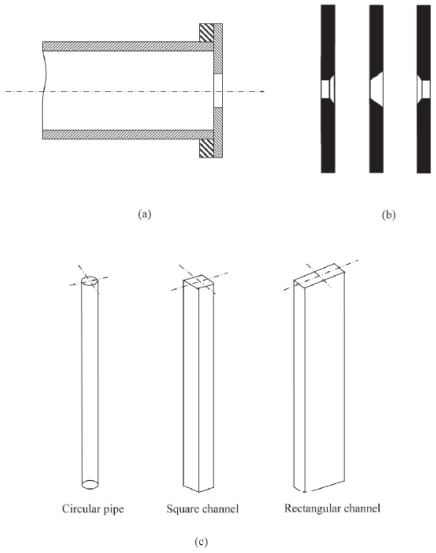

Figure 2-34: Types of nozzle geometries used. a) an orifice nozzle, (b) types of orifices and (c) long pipe nozzle [76]

- For both hydraulic Re and modified Re, shape geometry has a significant effect on stagnation region Nu up to a radial distance r/D=2. Beyond this radial distance, the nozzle geometry has a negligible effect.
- Due the ambient entrainment with the jet, the lower jet to target distance (H/D), the less stagnation point Nu.

Lee, et al., [77] investigated the effects of different nozzle diameters on fluid flow and jet impingement heat transfer. Various nozzle diameters were tested, from 13.6-34.0 mm. The nozzle-to-plate spacing tested was from H/D 2 to 14. Increasing nozzle diameter increases potential core length, and with increasing potential core length comes large mean flow velocity and momentum. For all jet diameters tested, maximum Nusselt number occurs at H/D=7 due to maximum turbulence intensity of jet impingement as shown in Figure 2-35 As the nozzle-to-plate spacing increases beyond H/D>7, the Nusselt number decreases monotonically with H/D.

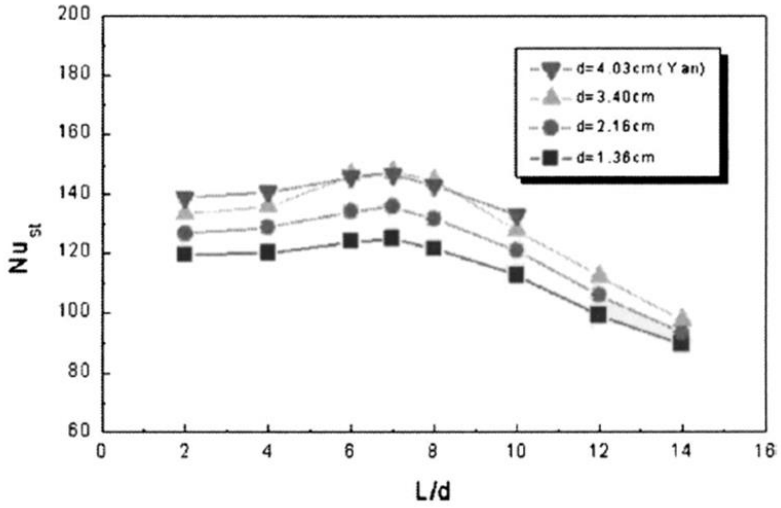

Figure 2-35: Experimental stagnation Nusselt number versus nozzle-to-plate spacing for different nozzle diameters [77]

Koseoglu and Baskaya [78] investigated, both experimentally and numerically, nine different jet exit geometries including rectangular, elliptic and circular jets. Various aspect ratios were tested with jet-to-plate spacings, H/D = 2, 6 and 12. Higher heat transfer rate in the stagnation region was achieved using large aspect ratio rectangular and elliptical jets. The influence of aspect ratio on heat transfer reduces with increasing nozzle to plate distance. Increasing cross-section area of a rectangular jet also reduces mean flow velocity at the exit and therefore heat transfer performance.

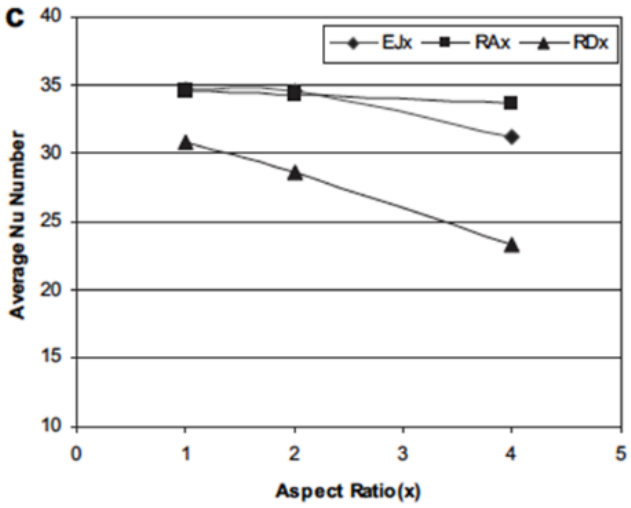

Figure 2-36: Experimental averaged Nusselt number at various aspect ratio at H/D=12 [78]

Behnia, et al., [62] conducted a numerical study using the v^2f turbulence model for heat transfer performance of confined and unconfined circular jet impingement. Good agreement between numerical results and experimental data was achieved for different jet Reynolds numbers and jet-to-target spacings. The averaged heat transfer was less for the confined jet compared to the unconfined jet, however, the stagnation heat transfer rate remained unchanged. At smaller nozzle-to-plate spacing, H/D<0.25, the model predicted that the effect of confinement would become significant. The predicted effects of mean flow velocity and turbulent intensity on Nusselt number also correlated well with the experimental results.

Garimella, and Nenaydykh [41] conducted an experimental study of different nozzle diameters and aspect ratio for an axisymmetric submerged confined liquid jet. The highest heat transfer coefficient was achieved with the smallest nozzle aspect ratio (l/d<1). The experimental results showed a significant decline of heat transfer performance with larger nozzle aspect ratio up to l/d=4. However, improvement of heat transfer occurs from l/d=8-12. This effect was found to be more pronounced with smaller nozzle-to-plate spacing.

The aspect ratio of the jet had a significant influence on the liquid flow at the nozzle exit location and this influence could be considered as a mean flow velocity and flow separation due to turbulence. By varying the jet Reynolds number, the very little effect of aspect ratio on the heat transfer coefficients was found. The impact of nozzle diameter on local Nusselt number was found to be more significant in the region nearest the jet for small values of H/D ~ 1. Jet flow turbulent intensity was considered a key factor for the Nusselt number and increasing nozzle diameter increased turbulent intensity for a given jet Reynolds number.

Both pressure drop and heat transfer performance are important for jet impingement. Different nozzle geometries have been found to effect these parameters one way or another. The experimental study by Whelan, et al., [79]

showed that chamfering and contouring the nozzle exit surface could moderately improve the average Nusselt number on the liquid jet array impingement. Figure 2-37 shows various nozzle geometry configuration tested in their experiment. However, neither chamfering nor contouring the same nozzle inlet surface was found to significantly reduce pressure drop across the nozzle plate. This test has identified the best individual performer for heat transfer for both confined-sub-merged and free-surface cases.

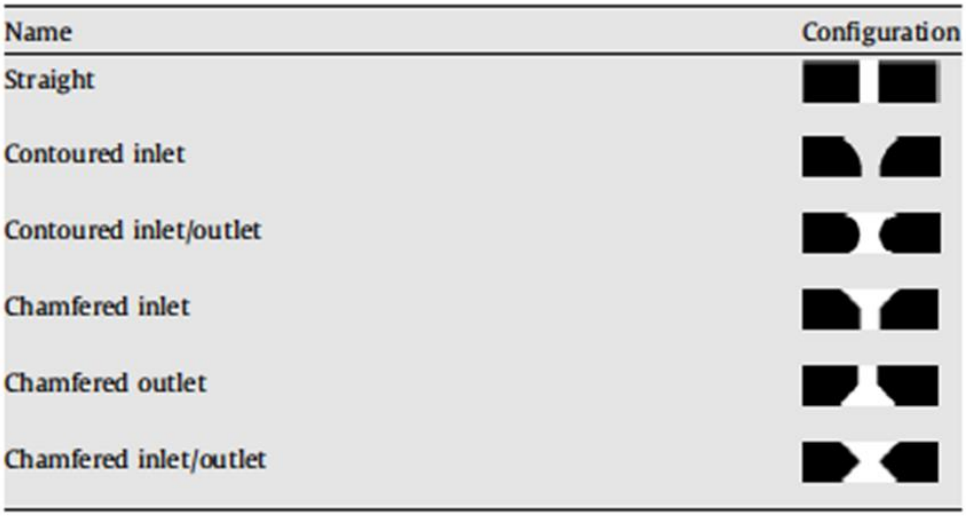

Figure 2-37: Different nozzle geometries [79]

Yang, et al., [80] studied the effect of nozzle configuration and curvature on slot jet impingement on a concave surface. Three different slot jet geometries were tested: rectangular shape, round shape and 2D contoured shape see Figure 2-38. Various flow and set-up conditions were tested including a different nozzle to concave surface spacings (H/D=1/2-20) and different jet Reynolds numbers (Re=6000-25000). It was concluded that the curvature shape drastically improved the heat transfer performance compared to the non-curved shape . Increasing nozzle-to-concave surface spacing creates a larger stagnation region before the Nusselt number reached its maximum. This pattern is considered as due to higher turbulence intensity of the flow inside the potential core region

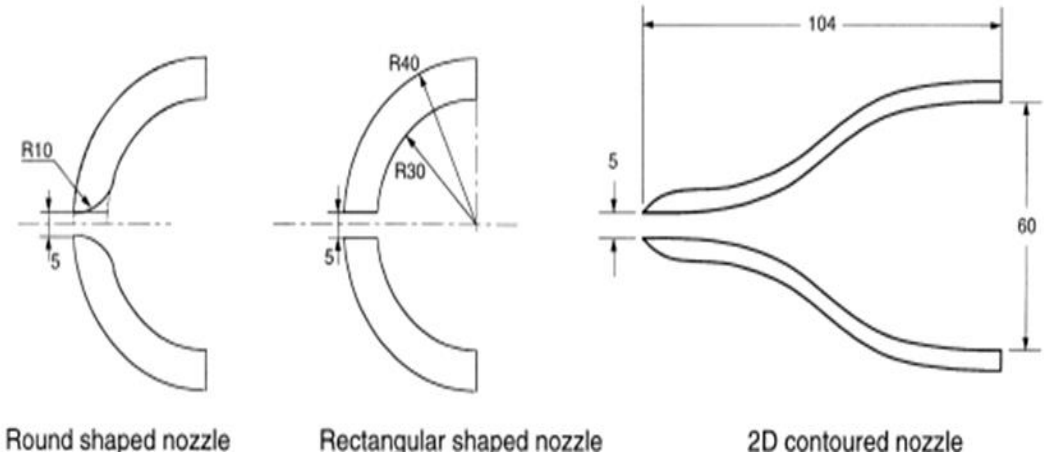

Figure 2-38: Different experimental nozzle geometries [80]

Attalla and Salem [81] investigated both square edges (unchamfered) and chamfered edge nozzle geometries for local and average heat transfer, based on circular air jet impingement. The experimental set-up was created to test various nozzle chamfered lengths, jet Reynolds number and nozzle-to-plate spacing. It was concluded that a chamfered edge nozzle did not change local Nusselt number distribution in the stream-wise direction. An unchamfered nozzle produced higher average Nusselt number than other nozzle geometries. Based on the measured data, a new correlation of Nusselt number was obtained based on jet Reynolds number, nozzle-to-plate spacing and chamfered length to diameter ratio. Figure 2-39 shows the experimental averaged Nusselt number versus jet Reynolds number of square-edge and chamfered edge shaped nozzles.

.

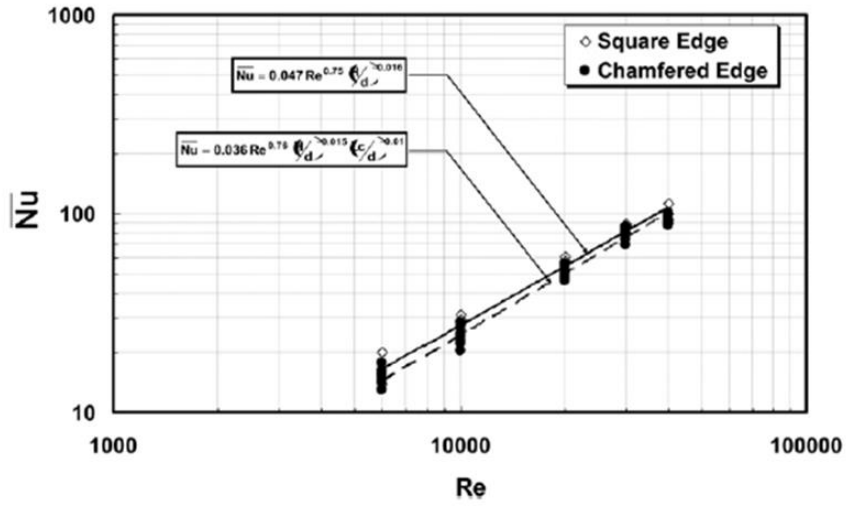

Figure 2-39: Experimental averaged Nusselt number versus jet Reynolds number of square-edge and chamfered edge shaped nozzle[81]

Gulati, et al., [82] investigated three different nozzle geometries with square, circular and rectangular cross-sections for different Reynolds number and jet-to-plate distance conditions. The results of their experiments showed that the average Nusselt number distribution of the plate was insensitive to the nozzle shapes tested. Both circular and square jets showed much the same heat transfer behavior though there were some small differences with the rectangular jet. As Reynolds number increased, the heat transfer rate increased. For the rectangular jet, it was found that the Nusselt number distribution along the major axis was different from minor axis. At jet to plate spacing below H/D=6, the stagnation Nusselt number distribution along the horizontal axis for the rectangular jet is higher than for the square and circular jets. Figure 2-40 below shows the pressure loss coefficient for the different jet to plate spacing. The circular nozzle had the lowest coefficient due to the smooth exit mean flow.

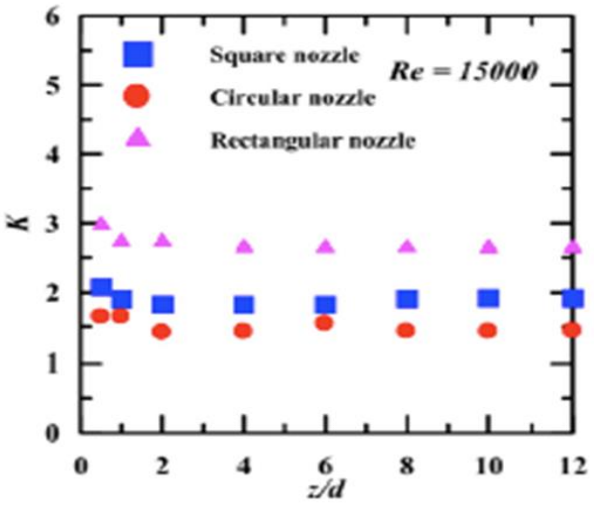

Figure 2-40: Experimental variation of K with different nozzle-to-plate spacing at Re 15000 for different nozzle shapes[82]

A mechanical tab, see Figure 2-41, can act as a vortex generator and usefully increase jet mixing. Hui et al. [83] performed an experimental study on the effects of a mechanical tab on turbulent flow structures for jet mixing flow. The device was found to induce a pair of counter-rotating streamwise vortices when installing into a jet as shown in the figure. Detailed flow visualization revealed that the Kelvin-Hemlmholtz vortex was accelerated when the mechanical tab was installed and that the small-scaled jet eddies appeared earlier than in natural jet flow. In addition, large-scale flow structures were found around the jet flow and exhibited helical and coherent behavior.

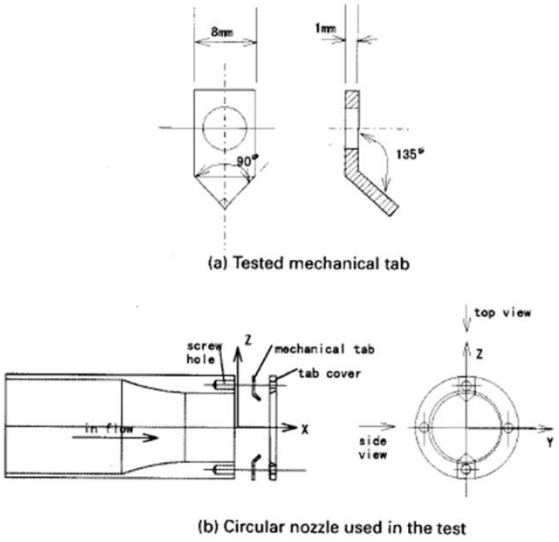

Figure 2-41: Experimental test set-up for mechanical tab used for jet flow mixing [83]

Table 2-5 below summaries and compares all experimental and numerical studies gathered in this section

Table 2-5: Summary of the jet configurations identified in the present section of the literature review

First author	Date	Fluid	Nozzle geome-try	Hydrualoc diameter (width) (mm)	Re (jet velocity) (m/s)	H/D (H/W)	Jet angle (α˚)	Data	Other Data	Measurement technique
Lee, J.	2000	Air	Standard, square -edged and sharp-edged orifice	0.25 (5)	10,000-30,000	2-10	90	temperature	Nu	LCT
Wen, M.	2003	Air	circular	7	500-27,000	3-16	90	temperature		thermocouples
Singh, D.	2015	Air	circular/slot	10.5 (10.5x10.5) (17.5x7.5)	10,000-25,000	4-16	90	temperature	Nu	Thermocou-ples/CFD
Lee, D.	2004	Air	circular	63	23,000	13.6-34		temperature		thermocouples
Koseoglu,	2010	Air	Circular, elliptic and rectangular	8-10	$(m = 0.\dot{0}01455)$	2-12	90	temperature	Nu	CFD/LCT
Behnia, M.	1999	Air	circular	-	10,000-30,000	0.1-2	90	Nu		CFD
Garimella	1995	Air	circular	0.79-6.35	4000-23,000	1-14	90	temperature	h	thermocouples
Whelan, B.	2008	Air	several	31.5	800-10,000	2-20	90	temperature	Nu	thermocouples
Yang, G.	1999	Air	slot	5	5920-22,500	0.5-20		temperature		thermocouples
Attalla, M.	2013	Air	Square-edge	5	6,000-40,000	1-6		temperature		infrared camera
Gulati, P.	2007	Air	Circular, square and rectangular	20	5000-15,000	0.5-12		temperature	Nu	infrared camera

2.3.2 Intermittency

Intermittency phenomena occur when periodical flows (usually cross-flows) disturb an otherwise steady axi-symmetric flow. Camci and Herr [84] studied a self-oscillating jet impinging on a flat plate to determine whether such a phenomenon could enhance gas turbine blade heat transfer. Here the term “oscillation” refers to induced periodic cross-flow of the jet. Compared to a conventional stationary jet, self-oscillating impingement provided greater heat transfer for heat removal. The inherent transient sweeping motion of the self-oscillating jet significantly increased the area of the impingement region. Improvement of the stagnation Nusselt number by up to 70% was claimed for a jet to plate distance of H/D=24. Detailed flow structures due to the oscillation were captured during jet impingement showing increased convection and diffusion rates.

Goppert, et al., [85] have studied intermittent periodicity of jet flows in order to identify whether unsteady motion imposed on the jet impingement would enhance heat transfer. They speculated that the thickness of the boundary layer would vary rather than remain fixed. In addition, the unsteadiness would also increase mixing which could reduce maximum velocity which is critical for local heat transfer enhancement. They demonstrated that a stable self-sustaining periodic flow could be achieved easily without having to install additional moving parts or energy sources. However, they concluded that the drawback of enhanced mixing was that it drastically reduced the maximum velocity and overrode any benefits arising from variations obtained in the permanent boundary layer on the plate surface. These experiments were unable to define a threshold-frequency consistently identified by past experiment studies and acts as the cut-off frequency for heat transfer enhancement.

Table 2-6 below summaries and compares all experimental and numerical studies gathered in this section.

Table 2-6: Summary of the jet configurations identified in the present section of the literature review

First author	Date	Fluid	Nozzle geome-try	Hydrualoc diameter (width) (mm)	Re (jet velocity) (m/s)	H/D (H/W)	Jet angle (α˚)	Data	Other Data	Measurement technique
Camci, C.	2002	Air	circular	5	7,500-14,000	24-60	90	temperature		LCT
Goppert,	2004	Air	circular	2-10	26,000-160,000	20-80		temperature		thermocouples

2.3.3 Surface Finish

Kanokjaruvijit, and Martinez-botas [86] and [87] added dimples to the surface of the target plate to examine the effect of jet impingement on a surface with a staggered array of dimples. They tested two dimpled geometries: cusped elliptical shape and hemispherical shape, see Figure 2-42. The combined coupling effect of jet impingement and channel flow with the presence of cross-flow provided the highest heat transfer performance of the dimpled plate at large jet to plate spacing. At moderate cross-flow, either the channel flow or jet impingement could dominate the heat transfer rate. At low cross-flow, jet impingement was found to be the dominant heat transfer mechanism. With the presence of dimples, flow circulation inside the concave dimples reduced heat transfer, especially with the smaller jet to plate spacing. The channel flow formed under moderate and high cross-flow conditions helped compensate for this penalty compared to low cross-flow condition. No difference was found in the heat transfer performance of hemispherical and cusped elliptical shapes so, from an economic point of view, it is more cost effective to use the hemispherical shape.

.

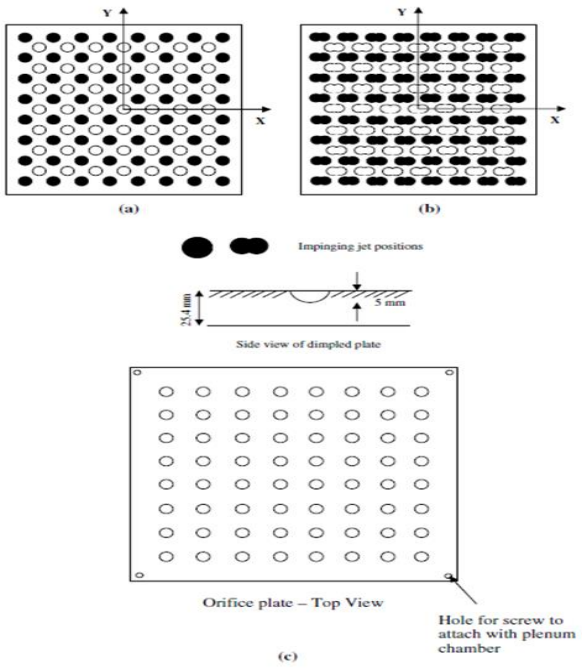

Figure 2-42: Experimental set-up of different dimpled plates including cusped elliptical and hemispherical shapes [87]

Zhang, et. al. [88] in his experiemntal and numerical studies emplyed an orthogonal single jet on a protrusion heated surface (constant heat flux). The protrusion took a shape of spherical pin-fin with height (δ) and diamater (D). Results were reported for local Nu distributions for Re 5000, 10,000 and 23000 and for normalized protrusion heights (δ/D) of 0.1,0.2 and 0.3 as shown in Figure 2-43.

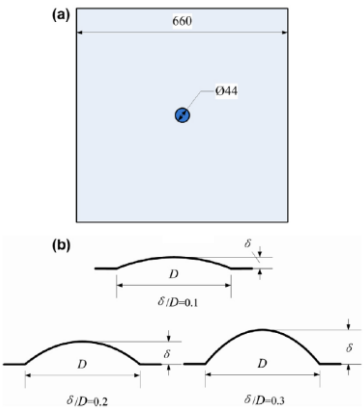

Figure 2-43: Dimensions of the target plate and protrusion [88]**.**

In general, flow sturctures are not effected by both protusion depth or jet Reynols number. A diversion in flow direction occurs when the flow meets with the protrusion and low pressure wake area behind the rib occurs where its length depends on the prutrusion height. Overall, distributions of local Nu show higher magnitude for roughened surface when compared to smooth surface. However, the higher protrusion, the lower local Nu distribtion. The effect or protrusion is limitied to a certain radial distance (r/D). As fot the stagnation Nu, it increases as protrusion height increases giving an overall higher values when compared to the smooth slat plate.

Kim, and Lee [89] conducted an experimental study of heat transfer and fluid flow characteristics of water drop impingement on a heated porous surface. They tested four different porous surfaces based on permeability and surface roughness obtained by using different sizes of small glass beads. Their test demonstrated two primary regions of impingement: contact and non-contact regions. The contact region is considered as water drop evaporation or boiling when in contact with the surface. The non-contact region is a surface film boiling regime where the drop was suspended in the air. The effects of wall temperature, impact velocity and particle size of the porous substrate on thermal and fluid flow performances were investigated.

Beitelmal, et al., [90] investigated the effect of surface roughness on heat transfer behavior based on an impinging air jet. They concluded from their experiments that the presence of surface roughness disrupted the boundary layer on the plate and caused the jet flow to be more turbulence and therefore increase heat transfer. The measured heat transfer enhancement due to surface roughness was up to 6%, based on the entire surface. A more pronounced effect due to surface roughness was an increase in turbulent intensity found at Reynolds numbers between 14000-34000, at H/D=4-8. Two correlations for averaged Nusselt number based on smooth and roughed plates were established.

Celik [91] compared a smoothed and roughened the heated surface with co-axial jet impingement. The co-axial jet was a double pipe arrangement. This

study concluded that the co-axial jet gave higher heat transfer than a single circular jet and that rough surface promoted better heat transfer due to interruption of the boundary layer over the roughened plate. The roughened surface achieved up to 27% higher averaged Nusselt number using the co-axial jet compared to a single circular jet configuration.

Xing and Weigand [92] investigated experimentally jet impingement on both smoothed and dimpled surfaces under various cross-flow conditions. The highest heat transfer rate was achieved using the jet to plate spacing of H/D=3 for all cross-flow conditions. The presence of dimples consistently increased maximum heat transfer rate by up to 12% more than for the smooth plate. With increased Reynolds number, heat transfer also increased.

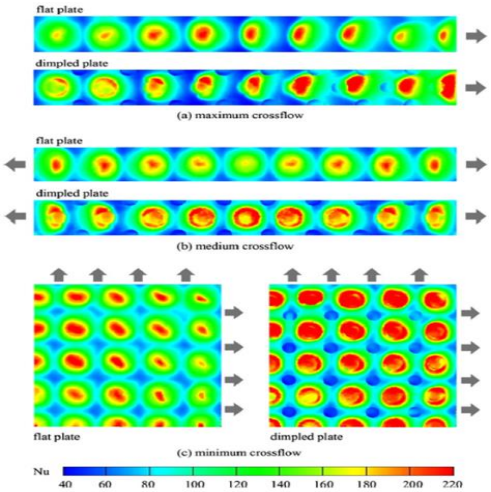

Figure 2-44: Experimental local Nusselt number distribution for smoothed and dimpled plates at H/D=3, Re=35,000 under various crossflow conditions [92]

El-Gabry and Kaminski [93] used roughened surfaces to increase heat transfer. They found that by using a roughened surface overall non-uniformity of the impingement plate was reduced significantly. Practically, such modification helped reduce thermal stress for a better life cycle of the product. They also tested inclined jets and have found this reduced peak in Nusselt number while yielding a more uniform heat transfer distribution. The maximum overall heat transfer coefficient was achieved at an optimal jet angle. The combined effect of

surface roughness, Reynolds number, jet angle, jet to plate spacing were studied to determine thermal and pressure drop performance.

Kanokjaruvikit, et., al., [87] h investigated experimentally the effects of an array of dimples on combined with an in-line array of circular jets on thermal heat transfer rate and pressure drop performance. Cross-flow was also included in the study to account for the effects of channel flow combined with jet impingement flow to determine which dominates the heat transfer rate. Under the cross-flow condition, dimples performed well as the channel flow created allowed flow separation from the dimple edges in the presence of the boundary layer. With strong cross-flow, jet flow is deflected by the channel flow and deviated towards downstream dimple edges. Compared to cusped elliptical, the hemispherical shaped dimples yielded higher heat transfer coefficients due to higher local flow circulation. Compared to deep dimples, shallow dimples yielded higher heat transfer coefficients as results of higher flow turbulence and more severe flow circulation. Maximum pressure at the stagnation point increased with dimples compare to the no dimple case.

Sharif, et., al., [94] simulated the effects of surface roughness on heat transfer using CFD to model circular jet turbulent flow impingement on a convex hemispherical surface. The different turbulent models considered were: RNG k-e model, SST k-w model, realizable k-e model and standard k-w model. However, only the SST k-w model was selected to study heat transfer performance as a function of surface roughness. Figure 2-45 shows the Nusselt number variations with surface roughness as a function of s/D. Different roughness parameters were used in the numerical modeling and all the roughness values gave higher heat transfer coefficients than the smooth surface. This heat transfer enhancement is deemed to be the result of surface protrusions penetrating the thermal boundary layer on the plate surface.

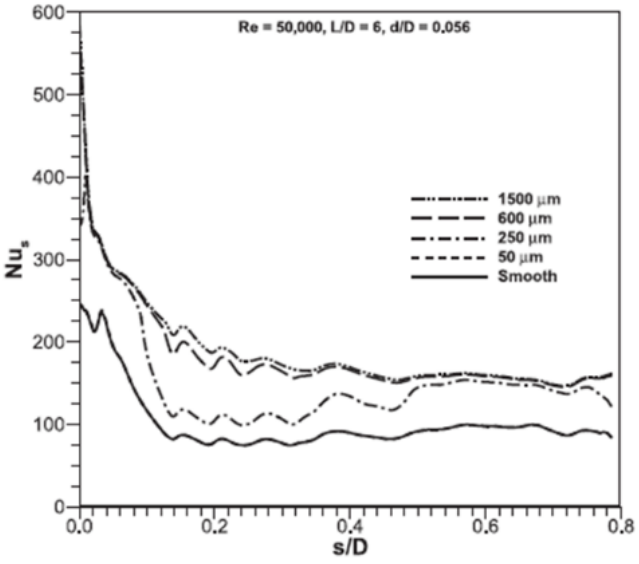

Figure 2-45: Numerical Nusselt number versus plate impingement location in radial direction[94]

Table 2-7 below summarises and compares all the jet configurations gathered in this section of the literature review.

Table 2-7: Summary of the jet configurations identified in the present section of the literature review

First author	Date	Fluid	Nozzle geome-try	Hydrualoc diameter (width) (mm)	Re (jet velocity) (m/s)	H/D (H/W)	Jet angle (α˚)	Data	Other Data	Measurement technique
Kanokjaruvijit, K.	2004	Air	circular	10	11,500	2-8	90	temperature		LCT
Zhang, D.	2013	Air	circular	44	5,000-23,000	2	90		Nu	CFD/PIV[1]
Kim, W.	2014	Water	circular	0.4	(0.8-2.3)	2-6	90	temperature	Nu	Thermocouples
Beitelmal, A.	2000	Air	circular	6.85	9600-38.5000	1-10	90	temperature		Thermocouples
Celik, N.	2011	Air	circular	6.85	10,000-40,000	1-10	90	temperature		Thermocouples
Xing, Y.	2010	Air	circular	15	10,000-40,000	3-5	90	temperature		Thermocouples
El-Gabry, L.	2005	Air	circular	1.75	10,000-35,000	1-2	30-90	temperature		Thermocouples
Sharif, M.	2013	Air	Circular	13-34	11,000-50,000	2-10	90	Nu		CFD

2.3.4 Turbulence Promoters

Spring et al., [95] conducted both an experimental and a numerical study of the use of a rib-roughened surface to enhance heat transfer for an array of jet impingements. Two different set-ups were studied; one with ribs and jets arranged parallel but perpendicular to any cross-flow, and the other with ribs and jets aligned in parallel with the cross-flow. For the inline set-up, the added roughness features (ribs) did not demonstrate any increase in Nusselt number compared to the unribbed plate. The middle section of the flow passage had much lower heat transfer coefficients than the unribbed plate. The majority of the flow was directed through the ribs, and such flow deflection significantly lowered the heat transfer rate in the region between the ribs. Further downstream of the jet where cross-flow occurred the heat transfer rate was reduced even further. For the staggered case the ribs helped to recover large flow separation due to cross-flow effects at downstream and therefore enhance heat transfer. Good flow attachment was found in the middle region of the flow field. In the meanwhile, the presence of ribs has kept the spanwise jet spreading minimal. Andrews, et al., [96] investigated heat transfer for jet impingement for an array of tiny rectangular pin-fins (ribs) which provided 50% blockage of the cross-flow. Up to 15% heat, transfer enhancement was achieved with rib arrays at a spacing of 3.0. The key factor with such a rib array was its reduction of heat loss due to the cross-flow. With the use of interrupted ribs, it was found that the heat transfer increases with distance

Xing, et al., [97] studied both experimentally and numerically micro-rib roughened plates with jet impingement under different cross-flow regimes. High Reynolds number flow was employed, Re = 15,000 to 35,000. With minimal cross-flow, the micro-rib roughened plate consistently gave a higher heat transfer distribution compared to a smooth flat plate. Here, both achieved a maximum Nusselt number at the jet to plate spacing of H/D=3.0. Similar to other studies, these results showed increasing heat transfer with increased Reynolds number.

For the worst cross-flow scenario, it was found that the presence of micro-ribs could enhance heat transfer by up to 10%.

Caliskan, [98] studied experimentally the effect of using roughened plate on flow heat transfer characteristics. The protrusion elements took the shape of ribs which was organised in to three different configurations. The ribs were also manufactured to either have a solid rib surface (SRS) or perforated rib surface (PRS) as shown in Figure 2-46. The measurements of flow and heat transfer on the heated surface which was located at H/D 2,4 and 8 with Re=10,000 were taken using LDA system. The average Nu for impingement plate with PRS configurations shows higher value when compared to SRS impingement plate due the higher flow turbulence resulting from the holes. The holes disturb the flow boundary layer creating higher turbulence when the flow separates and reattaches with the impingement jet. The maximum enhancement percentage in average Nu reported by the author is 48% when using configuration 3 and H/D=2.

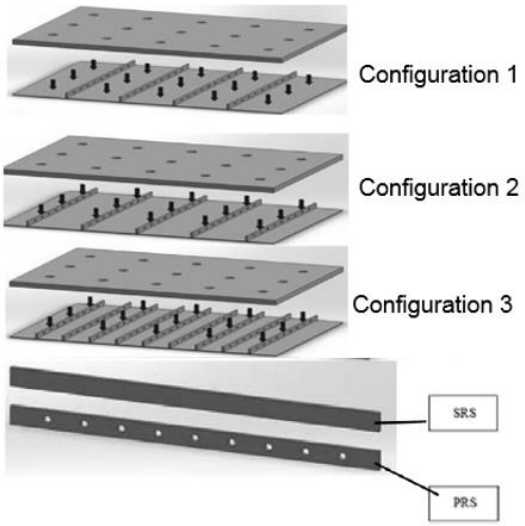

Figure 2-46: Geometry of rib configurations [98]

Nuntadusit, et. al., [99] performed an experemental/numerical study to investigate the effect of adapting different types of transvere perforated ribs inside a channel on the heat transfer and flow characterestics. The effect of perforation height (h=0.2H ,0.5H, 0.8H) and inclination angle (θ=15º and 30º) was examenied

under the influence of a constant Re=60,000 using thermochromic liquid crystal sheet. All configurations details are shown in Figure 2-47 below. Overall, the maximim heat transfer was achieved by the use of straight perforated rib with hole height of h=0.2H (Case b) due to the jet-like flow behind the protrusion when compared to other rib configurations which showed insignificant heat transfer enhancement. The inclined perforated ribs (case e and case f) showed significant increase in Nu when compared to the straigh and solid cases, especially at θ=30º which was reported in this study to be the best configuration in enhancing heat transfer.

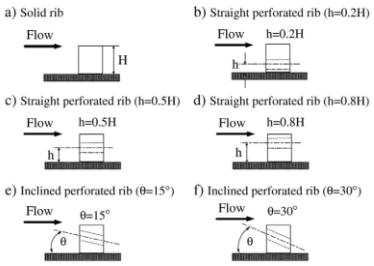

Figure 2-47: Details of rib geometry

Wan, et al., [100] studied numerically a square pin-fin configuration on a flat plate with jet impingement. Two configurations were used; inline and staggered. The numerical predictions were in good agreement with the experimental data for both heat transfer and pressure drop for Reynolds number in the range 15,000 to 35,000. Their results demonstrated the significant benefits to be obtained from using pin-fins on the target plate. Compared to the staggered array, the in-line arrangement achieved 35% higher heat transfer rate, but with a 3% reduction of discharge coefficient. The flow field represented by velocity vector contours are shown in Figure 2-48 comparing flat plate, in-line pin-fin and staggered pin-fin configurations. It is seen that the local flow, re-directed by the pin-fins, created vortex rings around the stagnation point on the surface. The large-scale coherent flow structures of the jet and cross-flow also promoted the heat transfer for the pin-fin roughened plate.

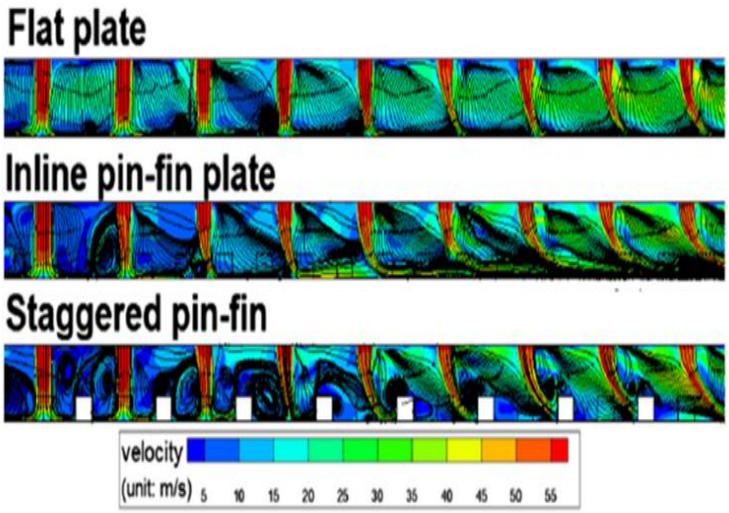

Figure 2-48: Numerical velocity flow field with flat plate, inline pin-fin plate, and staggered pin-fin comparisons using CFD method [100]

Choi, et. al. [101] in his experimental/numerical study, adapted the effect of both angled ribs and dimples on heat transfer coefficient inside channel using the transient liquid crystal technique. The rib angle and pitch are 60 and 6mm where dimple pitch (centre-to-centre) and diameter were 7.2mm and 6mm respectively. Three surface geometries were adapted in this study, ribbed channel, dimpled channel and rib-dimpled compound channel and Reynolds number was ranged between 10,000 and 30,000 based on the channel hydraulic diameter. The author reported that, for all configurations, the higher Re, the better heat transfer. For the rib case only, the endwall shows lower Nu than areas where the flow meets with the rib, this is due to the vortices occurred when the flow separated and re-attached with the heated surface. As for the dimple case only, higher heat transfer is observed at the region where the flow reattach with the heated surface inside and downstream of the dimples. Finally, using both roughness elements, although same Nu distribution pattern is observed in the case of ribs only but an overall higher heat transfer is observed due the contribution of dimple in inducing flow phenomena on the endwall.

Table 2-8 summarises and compares all the jet configurations gathered in this section of the literature review.

Table 2-8: Summary of the jet configurations identified in the present section of the literature review

First author	Date	Fluid	Nozzle geometry	Hydrualoc diameter (width) (mm)	Re (jet velocity) (m/s)	H/D (H/W)	Jet angle (α˚)	Data	Other Data	Measurement technique
Spring, S.	2012	Air	circular		35,000	3	90	temperature	Nu	TLC/CFD
Andrews, G.	2006									
Xing, Y.	2011	Air	circular	10	35,555	3	90	temperature	Nu	TLC/CFD
Caliskan, S.	2013	Air	circular	5	2,000-12,000	2-8	90	temperature		LDA
Nuntadusit, C.	2012	Air	circular	10	60,000	6	30-90	temperature		thermocouples
Wan, C	2015	Air	circular	10	15,000-35,000	3	90	temperature	Nu	Thermocouples/CFD
Choi, E.	2013	Air	circular	40-60	30,000-50,000	-	90	temperature		LCT

2.3.5 Jet angle

Akansu, et al., [102] studied oblique slot jet impingement on a flat plate to better understand the effects of jet inclination on heat transfer performance. This experiment study included measurement of local Nusselt number and surface pressure distribution for various jet angles, jet Reynolds number, and jet to plate spacing. It was demonstrated that there was a correlation between maximum heat transfer and jet angle. At 0^0 jet angle, normal impingement. The heat transfer is symmetrically distributed around the stagnation point on the plate. With increased jet angle, the maximum Nusselt number shifted upstream. At 45^0 jet angle, the maximum heat transfer was found to have shifted downstream. At small jet to plate spacings, increasing the jet angle also increased maximum Nusselt number. At a larger jet to plate spacing of H/D=6.0, the increase slowed down.

Wang, et al., [25] reported on different jet impingement angles from 0^0 to 45^0 at a Reynolds number of 20,000 on a curved surface with cross-flow. The important role played by the potential core in stagnation heat transfer for an inclined jet was identified. Both a convex surface and jet inclination were found to produce a thick boundary layer and thus reduced local heat transfer. Depending on the target surface location relative to the potential core distance, there is a transitional response of the primary peak corresponding to the stagnation point for jet inclination. Regardless of the degree of convexity of the curved surface, increasing inclination angle showed an increase in the primary peak at the stagnation point when the plate was inserted inside the potential core region. Outside of the potential core region, increased jet angle decreased the primary peak regardless of the convexity. At 0^0 jet angle, a second peak occurred, but only when the plate was inserted inside the potential core. At higher inclination angles, this secondary peak disappeared. Inside the potential core, increasing jet angle decreased the second peak.

A recent numerical study made by Bhagwat, et. al. [103] on the effect of three parameters, jet inclination, Re and H/D on the heat transfer characteristics over a heated flat plate. The inclination angle (θ) has two values of 30º and 60º, the azimuthal angle (α) (see Figure 2-49) was adjusted between 0 º and 180 º. The author adapted the V2F turbulence model in his simulation where Re was changed between 16680 and 41722 under the influence of 4≤H/D≤10. His results on the location of the stagnation point in the case of inclination jet matched other results reported by many researches where its location is no more coincide with the geometric centre of the domain. The shift in stagnation point is related proportionally to the jet inclination angle (θ). The author also reported that the Nu in the uphill direction has a dramatic decrease due lack of momentum while the Nu decreases slowly in the downhill direction due to regular loss of momentum. At a constant Re, the shallower inclination angle, the lower Nu where at constant θ, Nu shows a decrease in its magnitude when decreasing Re. Finally, the author stated that, an important role jet to target distance plays in the distribution of Nu as θ decreases.

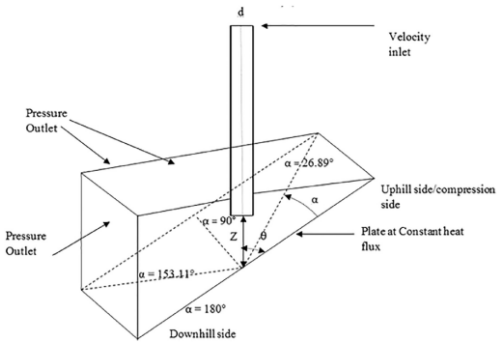

Figure 2-49: Computational domain of Bhagwat study [103]**.**

Tong [104] presented a numerical study of oblique free liquid jet impingement based on CFD. Detailed numerical flow fields were calculated representing free surface contours and pressure plots. Both parabolic and uniform jet configurations were investigated and simulations showed that with increasing jet angle, the maximum Nusselt number and pressure shifted upstream from the jet impingement point. The heat transfer was found to be influenced by the jet mean

flow velocity profile. For uniform jet flow, increased jet inclination angle also increased maximum Nusselt number. However, when a parabolic jet was used, the maximum Nusselt number initially dropped before rising as the jet angle increased.

Ingole, et. al., [105] in his recent experimental study, investigated the effect of a circular jet inclination angle (θ) on the heat transfer characteristics over a heated flat surface. The jet angle was varied (θ =15º,45º and 75º) where Re values were ranged between 2000 and 20,000 and jet to target distance H/D was between 0.5 and 6.8. Figure 2-50 shows all details of the experimental layout. Correlations between average Nu, jet to target distance (H/D), and angle ratio AR ($\frac{\theta_a}{\theta_p}$), which is the ratio between the actual inclination on the jet to the jet inclination of perpendicular jet, was presented in this study.

$$Nu_{avg} = 0.0151.Re^{0.908}\left(\frac{\theta_a}{\theta_p}\right)^{0.363}\left(\frac{H}{D}\right)^{-0.181}\text{Kuraan}$$

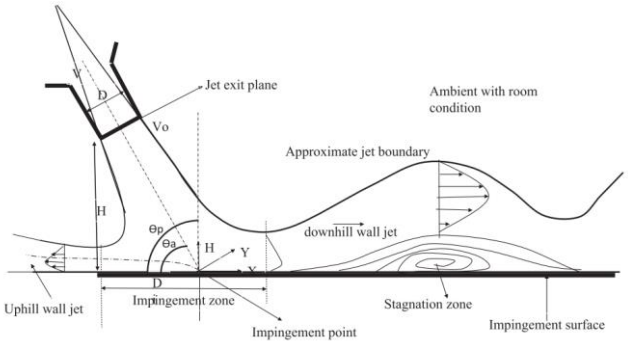

Figure 2-50: Nomenclature of inclined jet

Parida, et al., [106] combined both experimental and numerical approaches to investigate confined oblique jet impingement. The commercial CFD package Ansys-CFX was used for the numerical modeling. Three different jet configurations with jet angles 90^0 and 70^0 were studied. A higher averaged Nusselt number was achieved for 70^0 impingement compared to the 90^0 jet angle.

For the jet flow the CFD computed flow-fields replicated details of the flow entering an elliptical shaped inlet, the inlet flow then making a 90^0 turn and entering the circular jet before becoming fully developed inside the holes of the nozzle. The formation of two secondary vortices was identified near and far from the 90^0 bend. These secondary vortices accelerated the bulk flow from the jet and therefore provided higher impingement, resulting in a higher heat transfer rate. Furthermore, the swirling due to flow momentum kept the velocity high enough to sustain a high heat transfer rate over a long distance.

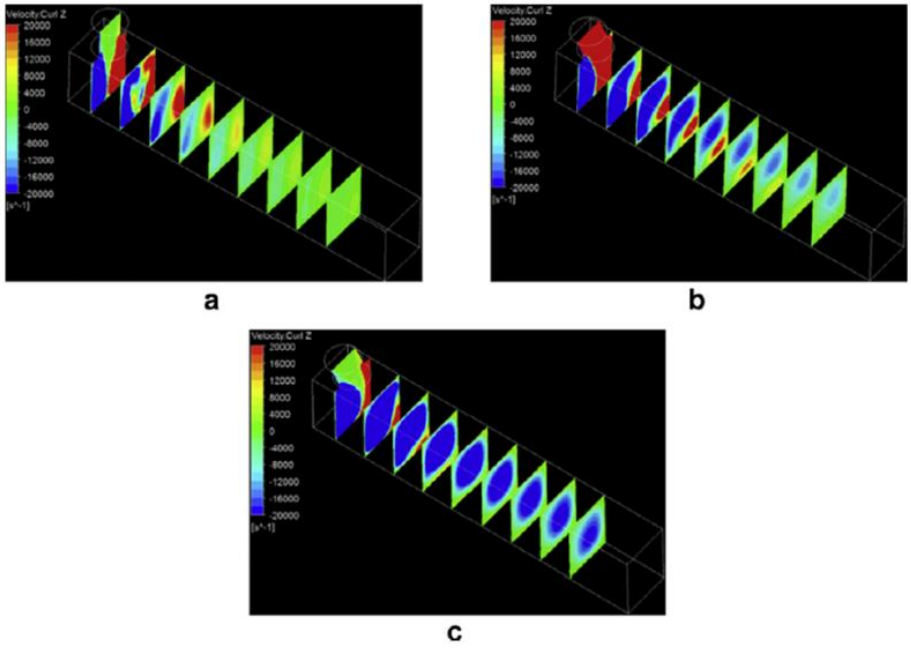

Figure 2-51: CFD Numerical vorticity contours for (a) 90^0 impingement with inlet flow normal to the inlet face (b) 70^0 jet angle with inlet flow normal to the inlet face (c) 70^0 jet angle with inlet flow parallel to the jet axis [106]

Table 2-9 below summarises and compares all the experimental set ups encountered in this section of the literature review.

Table 2-9: Summary of experimental set ups identified in the literature review

First author	Date	Fluid	Nozzle geometry	Hydrualoc diameter (width) (mm)	Re (jet velocity) (m/s)	H/D (H/W)	Jet angle (α˚)	Data	Other Data	Measurement technique
Akansu, Y.	2008	Air	slot	7.3	2500-7500	0.5-10	0-45	temperature		thermocouples
WANG B.	2013	Air	circular	2.5,5,10,15	(5,10,15,20)		30-90	velocity	pressure	CFD
Bhagwat, A.	2016	Air	circular	7.35	16,680-41,722	4-10	30-60	Nu		CFD
Tong, A.	2003	Air	slot	(2)	10,000	3	45-90	Nu		CFD
Ingole, S.	2016	Air	circular	25	2,000-20,000	0.5-6.8	15-75	temperature		Infrared camera
Parida, P.	2011	Air	circular	25	5000	2	90			thermocouples/CFD

Table 2-10 below Summarises the advantages and disadvantages of each heat removal method.

Table 2-10: Summary of advantages and disadvantages of the highlighted heat removal methods

Heat removal method	Advantages	Disadvantages
Nozzle geometry	- High heat transfer coefficient	- Manufacturing - Pressure drop - Mass flow rate - System dependent - Pumping/ Compressor power
Intermittency	- Enhancement of jet turbulence intensity - Enhancement of heat transfer coefficient up to 100%	- Pressure drop - Reducing arrival velocity - Sensitive to the amplitude and frequency of the oscillation
Surface finish	- Enhancement of local and average heat transfer coefficient	- Cost
Turbulence promoters	- Enhancement of heat transfer coefficient up to 60%	- Manufacturing - Cost - Weight - Stress concentration
Jet angle	- Used when geometry restrictions apply	- Uneven heat transfer in both uphill and downhill direction - Heat transfer reaches zero after a certain radial distance in the uphill direction - The narrower jet angle, the less average heat transfer

2.4 Closing Remarks

The literature review has shown that the heat transfer in jet impingement applications is highly sensitive to a number of parameters. The shape of the distribution of heat transfer, for example, depends significantly on jet-to-target distance (H/D). The literature reporting the magnitude and location of secondary peaks in the heat transfer that appear with an increase in turbulence in the wall jet region gives few details of the possible heat transfer mechanism that causes such peaks.

Recently, research has focused more on enhancing heat transfer by using the vortices within an impinging jet flow. These vortices can be generated by introducing an artificial excitation that, depending on its excitation frequency, can enhance flow energy separation. Finally, it is clear that surface roughness has a major effect on the overall heat transfer because of the turbulence induced by the surface roughness itself. The literature to date has reported the use of different types and shapes of turbulators such as ribs and other turbulence promotors. However, in the reviewed literature, there has been significant research into the steady and unsteady convective heat transfer from smooth and roughened surfaces, most of these studies were for jets ejected from a nozzle that is perpendicular to the heated surface. However, few studies have been compared the effect of using different roughness elements on the fluid flow and heat transfer characteristics of impingement on the heated surfaces for inclined jets. Some applications due to geometry restrictions must use a nozzle that it not perpendicular to the heated surface (inclined), such as cooling of HPT seal segments (see Figure 1-12). In addition, almost the majority of these studies used turbulators that have uniform shapes with fixed dimension and location on the heated surface.

This research aims to improve the overall heat transfer on a flat plate by investigating different types of turbulators shapes including non-uniform ones

with variable dimensions and locations based on a deep pre-study of flow contours over the heated surface. In addition, the ribs added to the baseplate will have a more random character which is different from the reports in the literature which focused on patterns of discrete dimples, pins or ribs.

3 Development of the CFD model

3.1 Introduction

This chapter is divided into four sections, first validation of the 3D- the axisymmetric model used for the orthogonal jet, second validation of the 3-D model for the cases of inclined jets. The third section demonstrates deep numerical study on the flow physics. Finally, will conclude all key findings in this chapter. All validations were made against the experimental results of O'Donovan and Murray [107] and [108] . All validations were made for Re=10,000 , H/D=2 and 6, and jet angles (α) of 90º,60º and 45º.

This chapter should help to understand the detailed numerical procedure including boundary conditions, selecting the suitable grid size, employing the appropriate turbulence model, and finally applying the right boundary conditions for all simulated cases.

3.2 The orthogonal impingement jet

3.2.1 Experimental Methodology

Figure 3-1 shows the experiment test facility used in the experimental study in [107] . An unconfined jet impinges steadily an isothermal flat surface using air as working fluid. The air jet leaves a circular brass nozzle with a diameter of D=13.5 mm and 20 diameters long in order to ensure fully developed flow. The filtered air, supplied by a compressor, flows to the nozzle pipe at ambient temperature and passes through a dehumidification system via a gas flow meter to measure both air volume flow rate and temperature.

The flow (air) enters the domain and impinges on the isothermally heated wall. represented by the bottom surface, while the both top and right-side surfaces were pressure outlets set to ambient pressure. The top surface contained the jet nozzle jet where a relatively cold jet at 25ºC left the nozzle at velocity (U)

obtained from the given jet Reynolds number of 10,000. In order to monitor and control the air temperature and flow volume, a gas flow meter was installed in the compressor line keeping the flow temperature within 0.5^0 of ambient. The target plate is made of a flat copper size (425 mm x 550 mm, and 5 mm thick). The plate is on a silicon rubber heated mat (15 kW/m^2) which was set to provide a constant plate temperature of 60ºC. The mat was insulated underneath. To monitor and measure the surface heat flux and temperatures a Rdf Micro-foil and a Synflex hot film sensor were flush mounted on the target surface along with T-type thermocouples.

To measure the flow velocity close to the target surface, two laser techniques were used, Practical Image Velocimetry (PIV) which measures the time averaged cross-section of the velocity flow and the Laser Doppler Anemometry (LDA) to measure the velocity at specific locations.

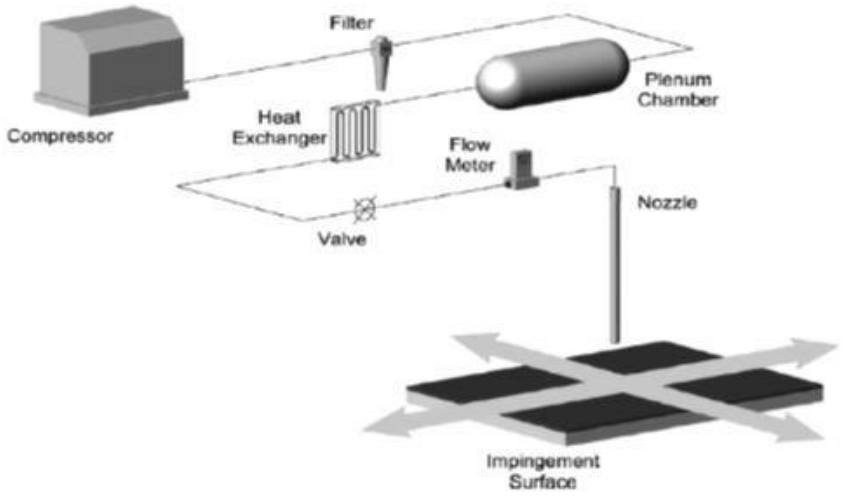

Figure 3-1: Experimental test rig [107]

3.2.2 Numerical Methodology

A schematic representation of circular jet impingement is shown in Figure 3-2. An orthogonal jet impinges on an isothermal flat plate kept at a constant temperature of 60 ºC, where the nozzle exit velocity is obtained from the jet exit Reynolds number. All geometry dimensions are normalized by the nozzle hydraulic diameter (D=13.5 mm). The flow parameters in this simulation are; the jet exit Reynolds number, Re, obtained from jet hydraulic diameter (D), the jet exit velocity (U), the normalised jet-to-target distance (H/D), and finally the normalised vertical distance between the flat plate and the nozzle exit, (H/D). The chosen values of these parameters are Re=10,000, H/D = 2 and 6 and, the angle of impingement is 90º (orthogonal).

An axisymmetric simulation of jet impingement was carried out using one of the latest versions of the commercial tool ANSYS v 16.2. An initial grid independence study was carried out adapting three different grid sizes in order to find the most suitable grid size that saves computational time and cost. A study was also conducted of the flow and thermal fields employing RNG k-ε, SST k-ω and RSM turbulence models to investigate their performance. The choice of these models where based on the results reported by other researchers in the literature. The results of the simulations were validated against the experimental data in [107] as mentioned above.

The turbulence models including the RNG k-ε, which will be used more frequently in this study, give good results by using a y+ value less than 5 in the boundary layer region employing 5-30 nodes within this region [109]. Where y+ is defined as a dimensionless quantity related to the distance between the wall and the first mesh node above it. It is important that the first cell should be fine enough to avoid positioning it in the buffer layer. The y+ is a function of both free stream properties and velocity (U_t) as shown in Equation 3.1.

$$y^+ = {\rho U_t \mathrm{y}}/{\mu} \qquad 3.1$$

- **Computational domain: geometry and boundary Conditions.**

Figure 3-2 shows the axisymmetric computational domain and boundary conditions used in this simulation. The domain diameter which includes the heated impingement surface (also referred to in the literature as “wall”) is 20D. An axisymmetric assumption is made in order to save computational time and cost; thus, we need to consider only the right half of the domain shown in the figure. A separate simulation was carried out to provide the velocity profile on the domain inlet in order to ensure a fully developed flow based on the Reynolds number used in this simulation.

A turbulence model study was conducted to help find the appropriate model to be employed for simulations. Also, a comparison was made between the use of a uniform velocity profile (constant jet velocity) and the use of a fully developed profile to see the impact of both profiles on the heat transfer rate. Finally, a study of the inlet turbulence intensity was also made in order to estimate the actual values was used in the experimental study. All simulations were performed using conditions mentioned in section 3.2.1.

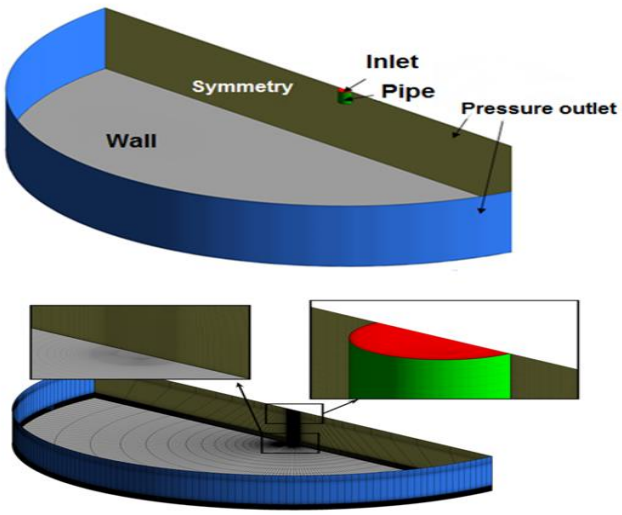

Figure 3-2 : Geometry, boundary conditions, and grid for an orthogonal jet impingement

- **Mesh generation, turbulence modeling and fluid properties**

The mesh was designed using grid refinement to resolve the wall boundary layer. A structured hexahedral mesh was employed to maintain domain orthogonality; afterward, it was further refined in regions of large temperature, pressure, velocity and turbulence gradients to attain a stable numerical solution. The value of y+ was kept as unity for the near-wall cells with at least 10 nodes inside the boundary layer as recommended by [109]. The regions close to the impingement wall and where the flow leaves the nozzle exit to have a larger concentration of nodes as shown in Figure 3-2. A non-uniform finite volume mesh with collocated variable locations is used for the computations where Mesh density was carefully scaled to investigate the sensitivity of the number of grid nodes to the predicted results. A rectangular mesh gathered toward both top and bottom walls with a bias factor of 70 is used in the z-direction where Finer computational meshes were adapted near the heated surface and the nozzle to obtain accurate velocity and thermal boundary layer. The grid size adapted in this study is approximately one million cells based on a systematic grid independence study as shown in the next section.

In jet impingement applications, the three flow regimes, laminar, transition and turbulent, exist in different regions. The laminar flow can be resolved numerically using a suitable grid and solving the momentum and continuity equations. On the other hand, the resolution of transition and turbulent flow require a suitable turbulence model, such as transition SST. It is essential to accurately resolve the flow turbulence as it powerfully effects the flow features. The appropriate model for simulation of turbulence in the domain usually depends on the accuracy required and the necessary grid that has to be generated to achieve that accuracy

According to Hadziabdic [110] , the wall function is not a suitable method to resolve the boundary layer which needs to be solved directly for more accurate results. This can be reached by creating a suitable fine mesh near the wall to resolve the viscous laminar sublayer.

As for the fluid properties, at low Mach number (<0.2), the compressibility of the fluid can be neglected [109] .Table 3-1 shows the air properties used in this simulation

Table 3-1: Air properties at 25ºC [111]

Property of Air	Value
Density (ρ)	1.177 kg/m^3
Dynamic viscosity (μ)	1.846E-5 kg/m.s
Thermal conductivity (k)	0.026 W
Specific heat Cp	1004.9 Nm/Kg.K
Corresponding Prantl No. Pr	0.0706

- **Results and discussion**
  - **a) Grid refinement study**

A grid analysis was used in this study to certify that the solution is independent of the computational grid. Generally, both numerical solution accuracy and computational time depend primarily on mesh refinement. In this work, a suitable grid is one which has an acceptable run-time and good accuracy. Three grid cases were used in the grid refinement study, see Table 3-2.

Table 3-2: Mesh sizes

№	Size, cells	Y+
Mesh 1	400 000	0.5
Mesh 2	986 000	0.5
Mesh 3	1 783 000	0.5

The commercial tool Ansys Fluent 16.2 was employed in this study to simulate the jet impingement. Extra attention was taken on the near-wall region since it plays an important role for convective heat transfer. The SIMPLEC scheme and Green-Gauss Cell Based gradient for spatial discretization were employed in this study using second order discretization schemes energy and momentum equations to produce more accurate results for heat transfer where first order schemes were used for other equations. Several steps were used before finalizing the choice of the appropriate solution: first, the use of the entire domain initialized by the inlet flow conditions employing first order upwind discretization to reach a convergence criteria at 10^{-6} for energy equation and 10^{-4} for the rest. The second step is seeking the solution by mixing up different orders of discretization schemes. Figure 3-3 shows a residual convergence example where convergence criteria at 10^{-6} for energy equation and 10^{-4} for the rest as mention above. As shown in the figure, the solution converges after approximately 1400 iterations

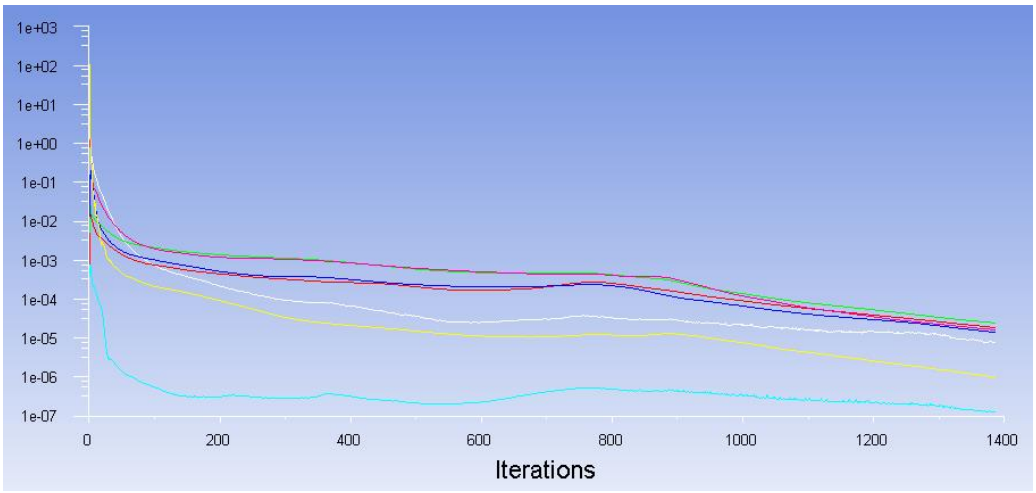

Figure 3-3 : Example of residual convergence

Figure 3-4 shows how, for H/D=6 and jet angle 90º, the simulated Nusselt number varied with the radial distance (r/D) using the RNG k-ε turbulence model, for different grids. Also included are the experimental results. It is notable, that both experimental and the numerical local Nusselt number values are close to all grid cases and therefore, grid 2 was adopted for the remaining numerical calculations to further proceed with all simulated cases in this study.

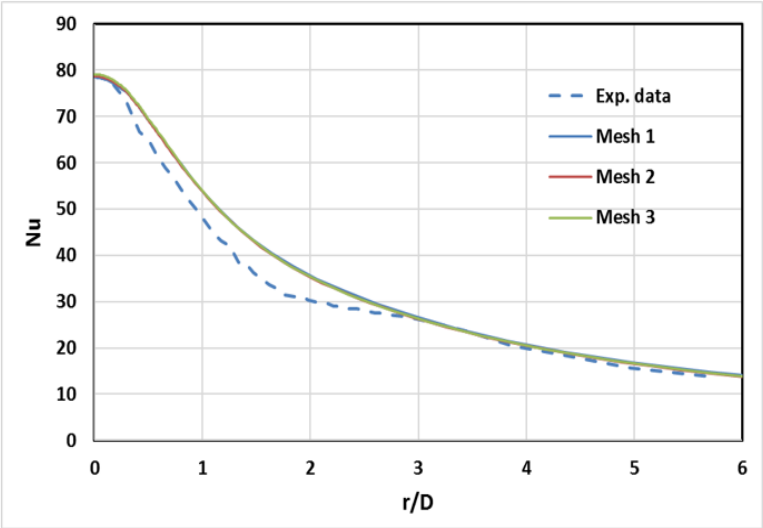

Figure 3-4: Nusselt number distribution for three grids, H/D=6, Re=10,000

For the sake of comparison ,the results of this investigation were also compared to another numerical study made by Alimohammadi, et al. [112] for the same experiment as shown in Figure 3-5. The figure shows that the simulation made by this investigation gives more accurate results when comparing to their numerical data.

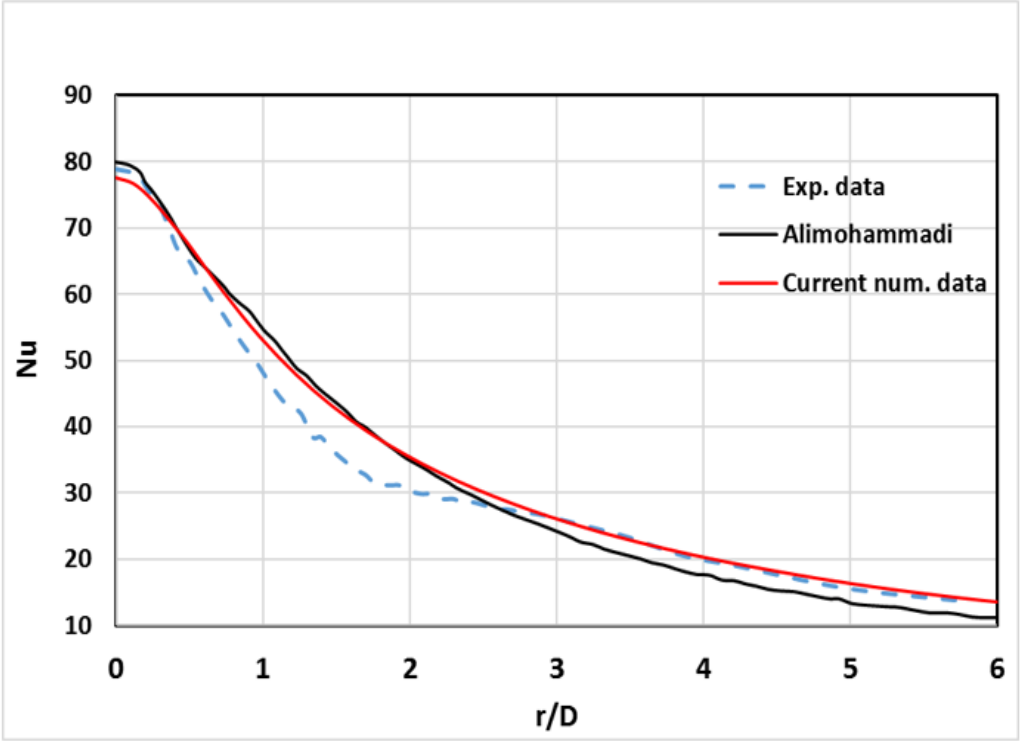

Figure 3-5 Results comparison, H/D=6, Re=10,000

b) Turbulence model

In the past years, two types of turbulence models have been developed to predict the turbulent flow; the eddy-viscosity model and the Reynolds stress transport model. This numerical study uses the eddy-viscosity model. Fluent AN-SYS v16.2 has both RNG k-ε and SST k-ω variations of this turbulence model, both of which have been found to be accurate in predicting results for this type of numerical investigation. Thus, an initial test run was performed using these two models and the RSM turbulence model to evaluate their relative prediction ability. The distribution of the local Nusselt number along the pre-heated impingement surface was compared with the experimental data of O'Donovan and Murray [107] for H/D=6 and α =90º, see Figure 3-6 The RNG k-ε turbulence model shows better overall agreement with the experimental data, and succeeded in predicting the local stagnation point Nusselt number (Nu_{stag}) with an error of only about 1.7% . However, both SST k- ω and RSM models overestimated Nu_{stag} by an error of 18 % and 21% respectively. Moving in the radial direction, the RNG k-ω

turbulence model gives, overall, a more accurate prediction of local Nu values. Unfortunately, none of the models discerned the slight trough in the experimental results at r/D ~ 2, which gave rise to the small maximum at r/D ~ 3. Based on this evaluation, this turbulence model was selected to be used for this parametric study.

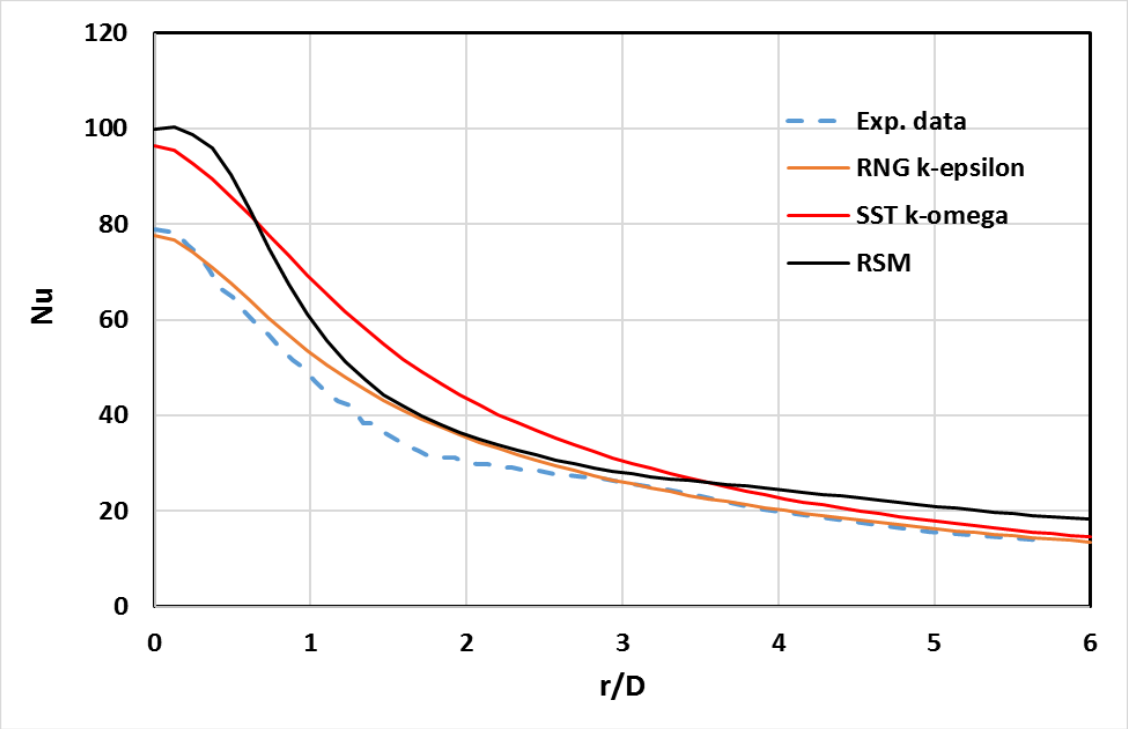

Figure 3-6 : Turbulence model study. H/D=6, Re=10,000

c) Inlet velocity profile

Inlet conditions such as velocity profile and turbulence intensity play a big role in the prediction of the heat transfer rate [113]. Figure 3-7 shows the distributions of fully developed, mass flow and uniform velocity profiles at the nozzle exit respectively (computational domain inlet) . As shown in the figure, the fully developed profile takes the shape of a hat while the other profiles show a flat curve (constant velocity magnitude values along the nozzle exit). The flat curve causes more interaction between the ambient and the jet resulting an overestimation of the jet turbulence intensity and might also overestimate the stagnation

point Nusselt number. Thus, the shape of the profile plays a key role in determining the flow turbulence due to the interaction with the ambient which has an impact on heat transfer rate.

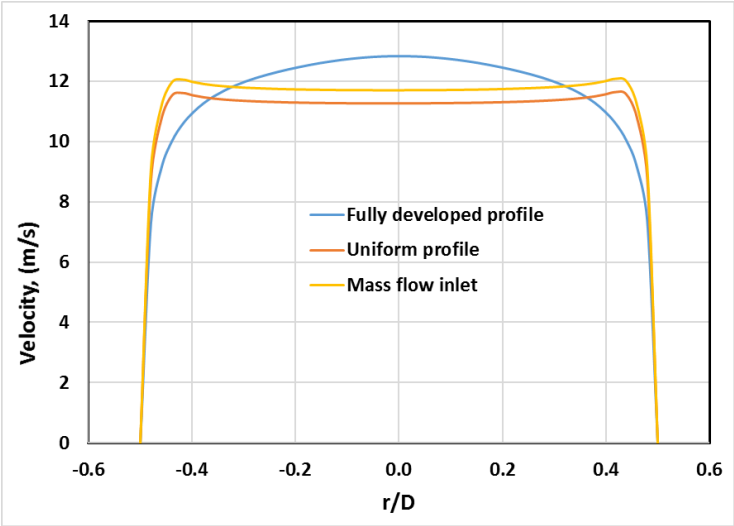

Figure 3-7: Distribution of three different inlet velocity profiles

Figure 3-8 demonstrates and compares the predicted local Nusselt number (Nu) obtained using the RNG k-ε turbulence model for two different velocity profiles at the nozzle exit: a uniform velocity profile which was calculated based on pre-specified Reynolds number, and a fully developed velocity profile which was simulated separately before applying it as an inlet condition. In addition, mass flow inlet profile was also simulated to compare with the other two velocity profiles. All profiles were for the same Reynolds number, Re=10,000, and jet-to-target distances of H/D = 6. The figure shows that the fully developed velocity profile gives more accurate results when compared to the experimental data. This is due to the fact that the uniform profile gives a higher flow momentum in the center of the jet than does the fully developed profile. According to Shadlseky [114], this results in higher Nu values in the stagnation region due to the steeper radial velocity gradient.

The fully developed profile succeeded in predicting the values of Nu more accurately than the uniform velocity profile for all values of r/D tested. At r/D = 0,

the uniform profile gave a noticeable higher Nu_{stag} than the fully developed profile which succeeded in predicting Nu_{stag} to an accuracy of 98%, where the error in Nu_{stag} estimated by the use of the uniform profile and mass flow inlet condition is approximately 6.7% and 10% respectively. However, the maximum error for the fully developed and the uniform profiles was 16% and 25% at a radial distance of about at r/D ~ 1.5. Starting from a radial distance r/D ≥ 3 all profiles start to predict an accurate results comparing to the experimental data, where both uniform profile and mass flow inlet condition keep overestimating the local values of Nu.

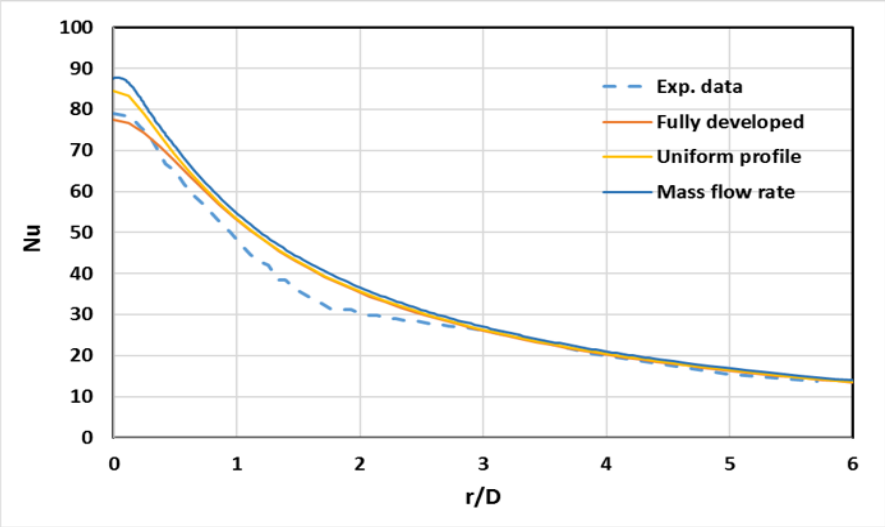

Figure 3-8: Inlet velocity profile study. H/D=6 , Re=10,000

d) Inlet turbulence intensity effect

The magnitude of the nozzle inlet turbulence intensity should be accurately estimated before simulating jet impingement as the turbulence intensity profile can be easily affected by the variance of the inlet turbulence which will affect the surface heat transfer prediction, especially for low H/D. Since the inlet turbulence intensity was not calculated in the experiment, a study was carried out to find the inlet turbulence intensity for H/D=6 and Re=10,000.

Two studies, one by Viskanta [115] have demonstrated that for larger jet-to-target distances (H/D=6), the nozzle inlet turbulence intensity has only a minor influence on the distribution of local Nu because of the domination of the turbulence created in the shear layer. Results shown in Figure 3-9 below agree with their finding except for the case with the lowest turbulence intensity the difference of Nu_{stag} is approximately 14% higher.

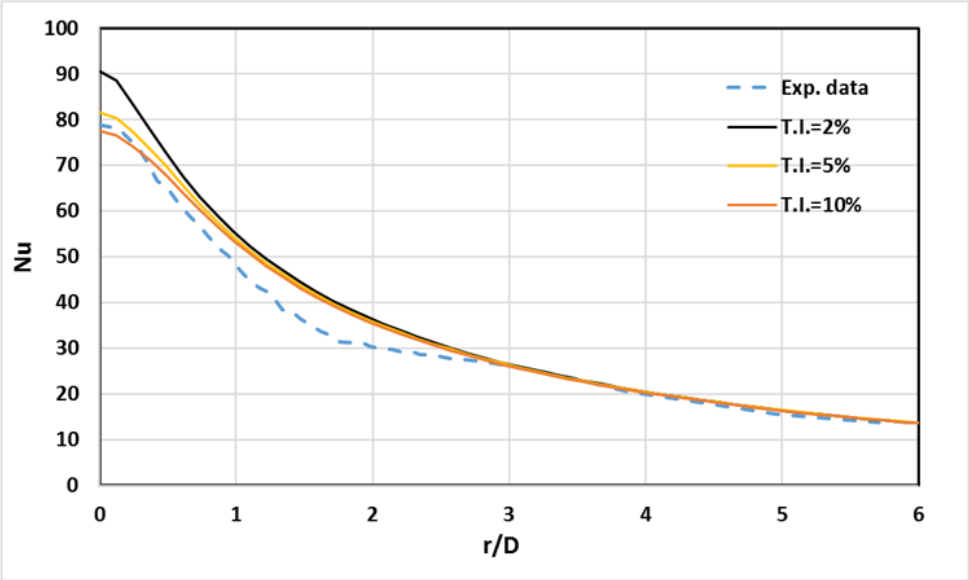

Figure 3-9: Inlet turbulence intensity comparison study, H/D=6 , Re=10,000

Based on the results in Figure 3-10, nozzle turbulence intensity of 10% will be used for all simulations. In the case of 10% inlet turbulence intensity, although the flow leaves the nozzle with high turbulence but its arrival velocity (the velocity arrives at the target plate) is the lowest comparing to the other two cases giving lowest Nu_{stag} as shown in Figure 3-10.

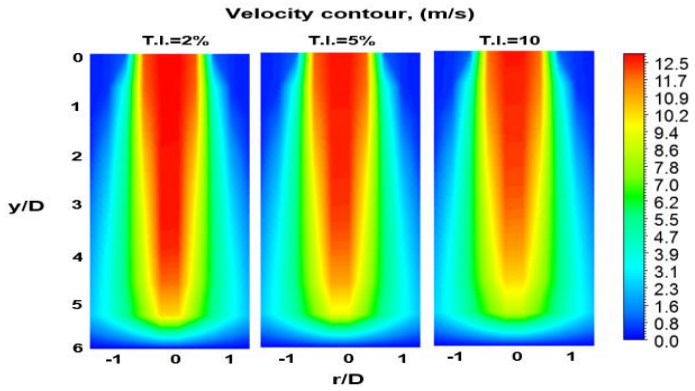

Figure 3-10 : Velocity contours of three different turbulence intensities

3.3 The Inclined Jet

3.3.1 Experimental test rig

Figure 3-11 shows the schematic diagram of the experimental rig. An inclined jet nozzle impinges on a flat plate with an angle (α) which can be inclined between 0^0 to 90^0 (orthogonal) in 15^0 increments. The experimental apparatus and the flow physics details were as described in Section 3.2.2.

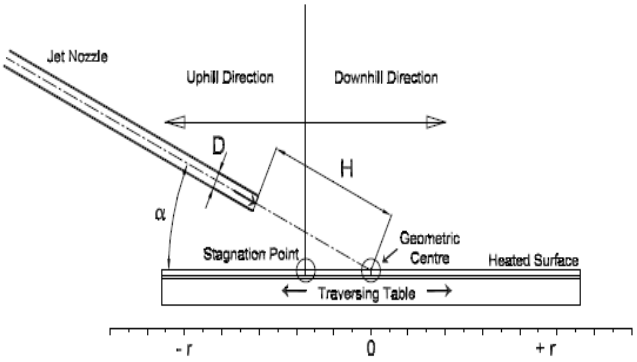

Figure 3-11 : Schematic diagram of the experimental rig [108]

3.3.2 Numerical Methodology

I. The computational domain

Previously only half the actual computational domain was used because of the natural symmetry of the arrangement, see Figure 3-2. The same procedure was followed in the inclined jet simulations with same details of geometry, grid size and boundary conditions for the orthogonal jet. The maximum aspect ratio for all grids is 1.15, and the distance of the first node from the flat heated plate was about 0.005 mm for all grids, giving a y^+ value ≤ 0.5 for the whole wall surface. In addition, approximately 20 nodes were applied within the boundary layer to ensure full resolution of this critical thin layer. Figure 3-12 shows base grid for grid No. 2.

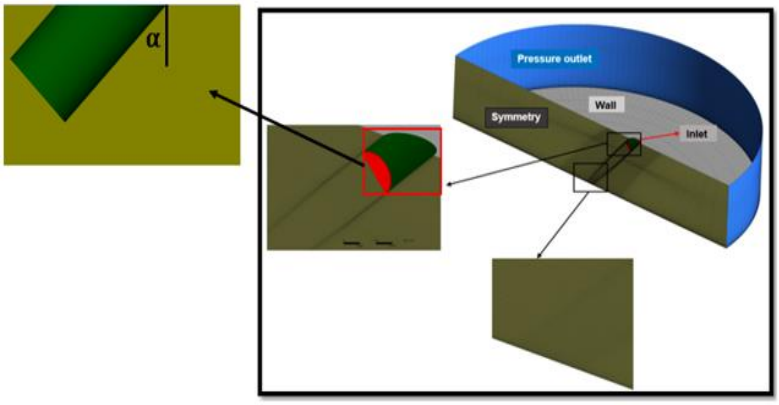

Figure 3-12 : Geometry, boundary conditions, and grid for an inclined jet impingement, H/D=6 and α = 45º

Two geometries were simulated and validated against the benchmark work of O'Donovan and Murray [108]. The nozzle to plate distance was fixed at H/D = 6 and the angle of inclination, α = 45^0 and 60^0 as shown in Table 3-3

Table 3-3: Geometry parameters

Case	H/D	α, °
1	6	45
2	6	60

3.3.3 Results and discussion

To validate the numerical results, the simulated local Nusselt number (Nu) was compared to the benchmark experimental data of O'Donovan and Murray [108]**.** In the case of inclined jets, the nature of the flow differs than it is for the orthogonal jet, so turbulence model study was also conducted seeking the suitable turbulence model as shown in Figure 3-13. As shown in the figure, the RNG k-ε failed to predict accurate results of the local Nu in both directions and to locate both the magnitude and location of $\boldsymbol{Nu_{stag}}$. In addition, the model did not predict the secondary peak of Nu in the downhill direction. On the other hand, the SST k-ω turbulence model succeeded to give reasonable results comparing to the experimental data. So, the SST k-ω turbulence model will be used for all inclined jet geometries. All boundary conditions, solution parameters and convergence criteria used in this section were the same as the ones used in section 3.2.2.

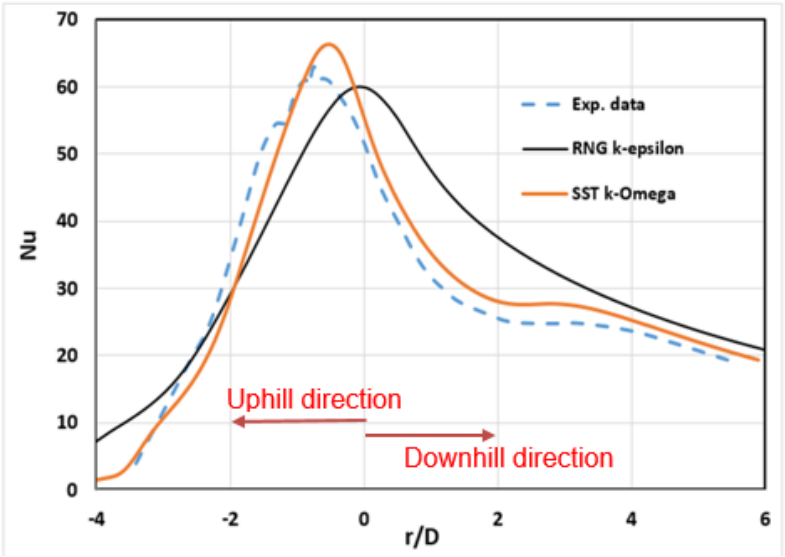

Figure 3-13 : Local Nu values for two different turbulence models, H/D= 6 and α = 45º, Re=10,000

This section includes a total of two cases that were simulated and validated using the SST k-ω turbulence model for the jet to target distance H/D=6 and two different jet angles (α) 45^0 and 60^0 are presented in, Figure 3-14 and Figure 3-15 respectively.

Starting with Figure 3-14 for H/D=6 and α=45^0, the numerical data gave overall good agreement with the experimental data in both directions. In the downhill direction (see Figure 3-11), the numerical results, however, overestimated the peak value of Nu_{stag} by about 5% with a maximum percentage error for local Nu values of 10% at r/D~3. In the uphill direction, the numerical data also had good agreement with the experimental data with some minor underestimation of local Nu up to about r/D ~ -3. Numerical data were also shifted to the right comparing to the experimental results.

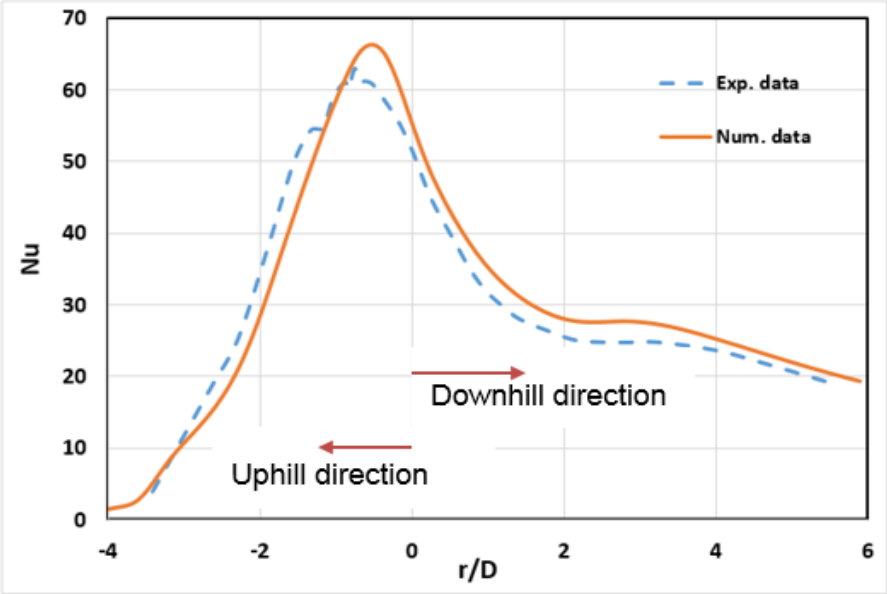

Figure 3-14: Local Nu values for H/D= 6, Re=10,000 and α = 45º

Figure 3-15 shows Nu as a function of r/D for H/D=6 and α =60^0. Much the same patterns can be seen as for α=45^0. The simulated data generally showed good agreement with the measured local Nu values in both the downhill and uphill directions. All local values of Nu were shifted to the right by a maximum offset of r/D ~ 0.65 where the peak value of Nu_{stag} was overestimated by about 1.9%. In the downhill direction, or radial distances, 1.75 < r/D <3, higher local Nu values were simulated with a maximum error of about 17% due to the turbulence model used.

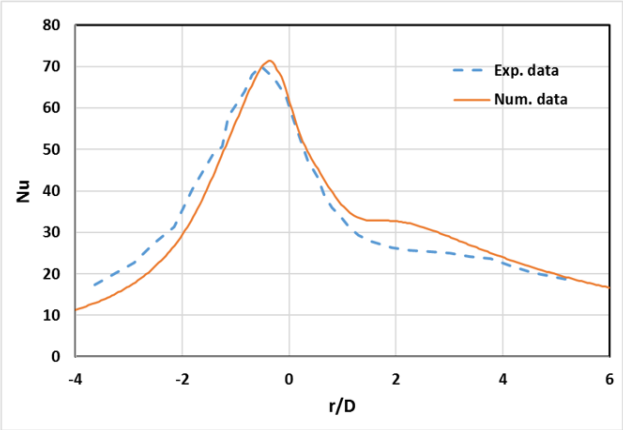

Figure 3-15 : Local Nu values for H/D= 6, Re=10,000 and α = 60º

3.4 CFD flow field data

3.4.1 Free jet configuration

According to Gardon and Akfirat [24], the analysis of the behavior of a free jet is very important in characterizing and comparing flow heat transfer for different configurations of a jet impinging on a flat plate. These researchers concluded that there exists a correlation between free jet flow behavior and the rate at which heat is transferred to the impinging jet, but there is a need to include the influence of the impinged surfaces. Gardon and Akfirat reported that there is a reasonable agreement between the flow characteristics of the free jet and the heat transfer to the impinging jet with the existence of the impingement surface. Hence, in this thesis, flow measurements for the jet were analyzed.

The typical fully turbulent jet flow was assumed throughout the heat transfer studies. The flow used was separately and independently simulated and the results so obtained were used as inlet boundary conditions in the ANSYS v 16.2 simulation software. Since, fundamentally, the jet flow turbulence is a function of only its Reynolds number and the diameter of the jet flow nozzle, heat transfer correlations do not depend on the turbulence intensity parameters. Nonetheless, different nozzle configurations and turbulence promoters have been used in an effort to improve the rate of heat transfer from impingement surface to jet flow.

To standardize the jet flow, one specific nozzle was selected and used to approximate the standard jet flow condition. The theoretical background and numerical equations of free jet flow are well established in the literature, hence, in this thesis, a numerical flow field was simulated with Reynolds numbers of 10,000 based on the desired free jet as shown in Figure 3-16. The figure presents the fundamental structure of the free jet flow providing a reasonable approximation of the desired flow.

Obviously, Figure 3-16 shows that the flow spreads due the ambient entrainment, thus increases the width of the mixing region as the flow travels from the nozzle. The velocity of the nozzle exit is maximum at the centreline which remains constant until the ambient starts to penetrates announcing the end of the potential core. The turbulence intensity (defined in equation 3.2) is maximum at the jet mixing region and increases as the jet travels away from the nozzle where it is minimum at the nozzle centreline as shown in the figure. This is due the momentum exchange between the jet and the ambient leading to a noticeable increase in jet turbulence.

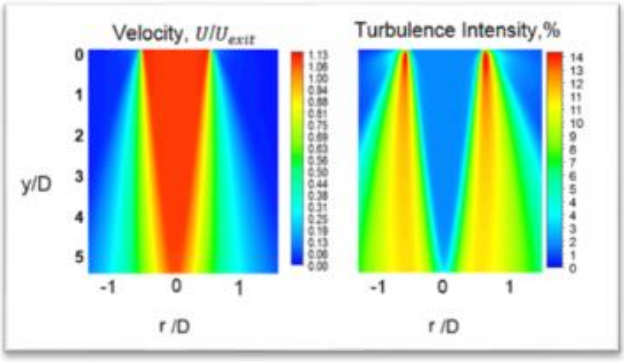

Figure 3-16 Free jet flow field, Re=10,000, H/D=6

Equation 3.2 defines the turbulence intensity (T_i) as the ratio between the local rms velocity to the mean jet exit velocity. Turbulence intensity is minimum within the jet core where the its maximum value occurs in the jet mixing region.

$$T_i = \frac{\sqrt{\frac{2}{3}k}}{U_{jet,exit}} * 100 \qquad 3.2$$

Where k is the turbulent energy, and $U_{jet,,exit}$ is the averaged mean jet velocity at the jet exit.

Figure 3-17 shows the turbulent intensity and the normalised local mean velocity (as U/U_{max}) along the jet centreline where Figure 3-18 presents the axial distributions of the two parameters along five different axial locations with respect to the nozzle exit (y=0). The turbulence intensity profile of the jet flow is dumb-bell shaped. The core region is where the velocity is conserved and maintained relatively constant at about 95% of the jet exit velocity. At a jet Reynolds number of 10,000, the core length is 3 jet diameters from the nozzle exit as shown in Figure 3-17. However, the turbulent intensity is a minimum of the jet centerline and a maximum where shear forces are a maximum, that is within the mixing layer surrounding the jet. Outside of the mixing layer the turbulence and turbulence intensity dies away quite rapidly.

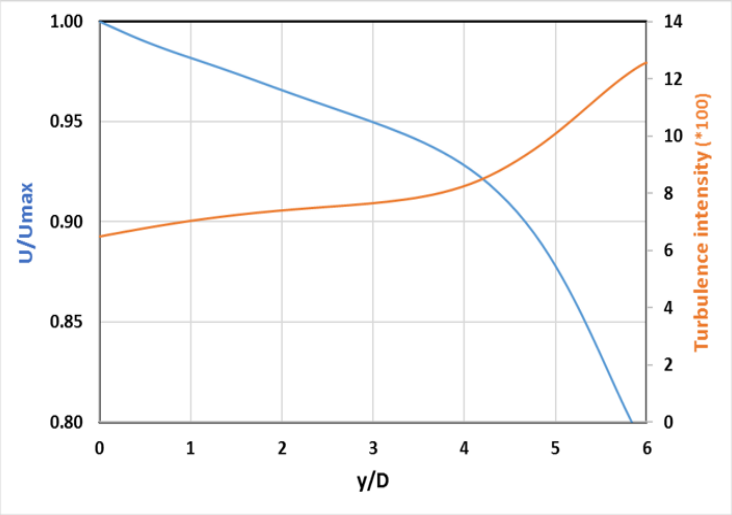

Figure 3-17 Free jet centreline velocity and turbulence intensity, Re= 10,000 and H/D = 6

Figure 3-18 also shows that as the flow travels away from the nozzle its centreline velocity decreases while its turbulence intensity increases due the entrainment of the ambient as mentioned before. The centreline flow velocity decreases approximately 10% of its exit velocity by travelling from the nozzle exit to an axial distance y/D=5 where its turbulence intensity increases of about 14%.

This shows the influence of jet to target distance (H/D) on both jet velocity and turbulence intensity. As the jet travels more distance from the jet exit, the hat shape of the free velocity curve is getting narrower announcing a change in the velocity profile where the opposite observation occurs for turbulence intensity curves. Again, Figure 3-18 shows that the length of the potential core for free jet flow is located at an axial distance of 3D from the nozzle exit where the flow speed is about 95% of the centreline speed (U_{max}) as shown in the figure.

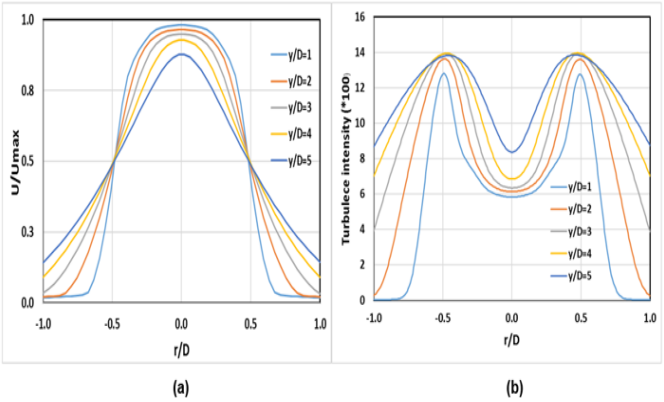

Figure 3-18 (a) Free jet velocity and (b) turbulence intensity as functions of normalised radial distance at H/D = 6 and Re=10,000.

3.4.1.1 Normal jet impingement

Figure 3-19 shows typical results obtained from simulation of a normally impinging jet with H/D =2. Thus, the impingement surface is situated within the jet core potential region. There exists a stagnation region at or close to the geometric centre within which the local velocity normal to the plate is negligible, and the surrounding flow moves radially outwards over impingement surface. It can be seen also that the jet velocity has minimal reduction as it remains almost constant even at the edges during all the travelled distance due to the minimal contribution of the ambient for such short H/D. The figure also shows the field turbulence intensity profile with a maximum value at the shear layer outer edge. Moving outwards from the stagnation region close to the jet flow wall are local regions of high turbulence intensity.

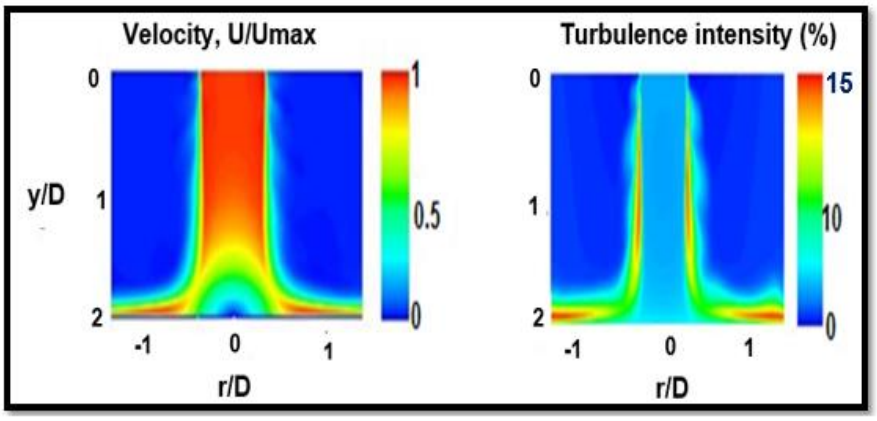

Figure 3-19 Velocity and turbulence intensity contours for Re=10,000 and H/D=2

In order to investigate the effect of the impingent surface on the jet leaving the nozzle, a comparison of normalized jet velocity for both free and impinging jet is shown in Figure 3-20. According to Gardon and Akfirat [24], at distances greater than 1.5 jet diameters above the impingement surface, the free jet is predominantly not disturbed. The figure demonstrates that the jet remains undisturbed from leaving the nozzle (at y/D=0) to an axial distance y/D≈1.5 agreeing with the above study. A noticeable drop in jet velocity then occurs between y/D=1.5 to y/D=2 from its maximum to zero due to no slip condition. On this basis, if H/D = 2, the differences between a free jet and an impinging jet will be in the region 1.5<y/D<2. Hence, for the current studies, a numerical simulation was obtained for the region 0.5 < y/D < 2 and this is shown in Figure 3-20.

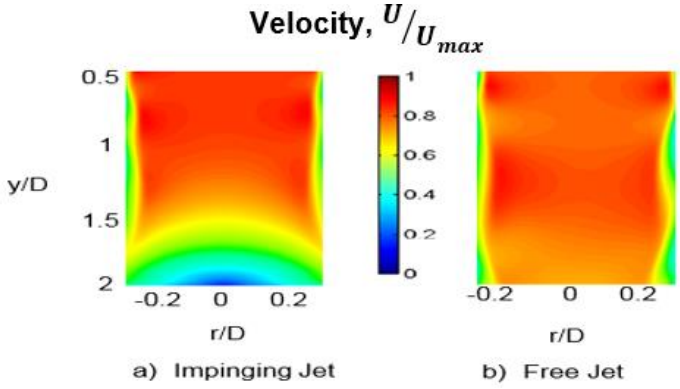

Figure 3-20 Comparison of a free jet flow with an impinging jet flow, Re=10,000, H/D=2

The similarity between the two jet flows shown in Figure 3-20 is defined by Equation 3.3, and this quantity is plotted in Figure 3-21

$$\boldsymbol{Similarity}, [\%] = \frac{\boldsymbol{U_{impingement\ jet}}}{\boldsymbol{U_{freejet}}} \boldsymbol{X\ 100} \qquad \boldsymbol{3.3}$$

Figure 3-22 shows the similarity of H/D=2 and 6 along the axil distance (y/D), measured from the nozzle exit at y/D=0. For H/D=2, from the figure , it is obvious that the jet centreline velocity is undisturbed beyond the 1D axial distance from impinging surface (the impingement surface is located at y/D=2), this is shown by the unity ratio between the velocity of the impingement jet to the velocity of the free jet. As for the case of H/D=6, the centreline velocity maintains constant till an axial distance of 4.5D from the nozzle exit and then starts to diminish as a result of the existence of the impingement surface. agreeing with results reported by Gardon and Akfirat [24]. In conclusion, the impingement surface located at H/D=2 is placed within the potential core where in the case of H/D=6, it is located beyond the potential core.

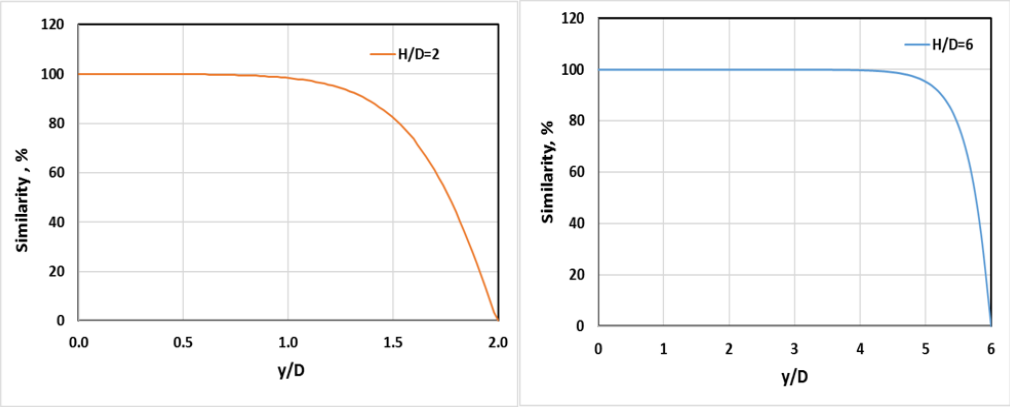

Figure 3-21 Centreline similarity of free and impinging jet flows, Re=10,000, H/D=2 and H/D=6

Among the important investigations conducted into the flow field was the relation between the stagnation zone and wall jet. Simulated mean velocities and turbulence intensities were obtained for jet-to-plate distances of H/D = 2 and 6 , and are shown in Figure 3-22. The Impinging jet flow varies with H/D. The larger

the value of H/D the more developed the flow. At low values of H/D (say ~2 diameters) there is a downward pressure on the impingement plate by the free jet. This downward pressure decreases the turbulence intensity in the stagnation region. The velocity at the centreline is significantly reduced while the surrounding air flow develops more or freely, which leads to the velocity profile having a uniform magnitude. Figure 3-22 also shows flow field turbulence intensity. High turbulence corresponds to strong shear in the surface boundary layer, and this is indicated by how the impinging jet flow spreads outwards. The influence of the shear layer is significant and increases with increasing H/D and extends over large radial distances before rapidly decreasing and fading away. However, close examination of Figure 3-22 shows that very close to the impingement plate, the turbulence intensity is small due to the no-slip condition. At the stagnation region, as explained before, low values of H/D correspond to a zone of low turbulence, and high values of H/D correspond to a zone of high turbulence.

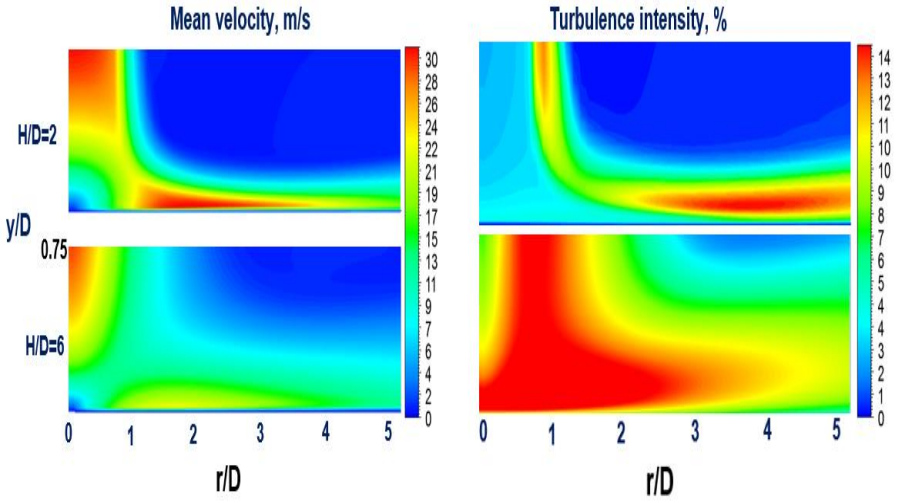

Figure 3-22 Impinging jet mean flow velocity and turbulence intensity with r/D, for Re=10,000, and two different values of H/D =2 and 6

3.4.1.2 Inclined Jet impingement

Results from inclined impinging jets were simulated and measured: Two values of H/D were selected: 2 and 6, which respectively are within and beyond the jet core potential region. Flow Reynolds number was 10,000 and angles of impingement 45^0, 60^0, 75^0 and 90^0 were used to simulate oblique flow. Figure 3-23, shows the simulated average flow field velocity for four angles of impingement. The location of the geometric centers is shown by the small black circles, and the stagnation points by the red circles. As α decreases the stagnation point moves away from the geometric center in an uphill direction.

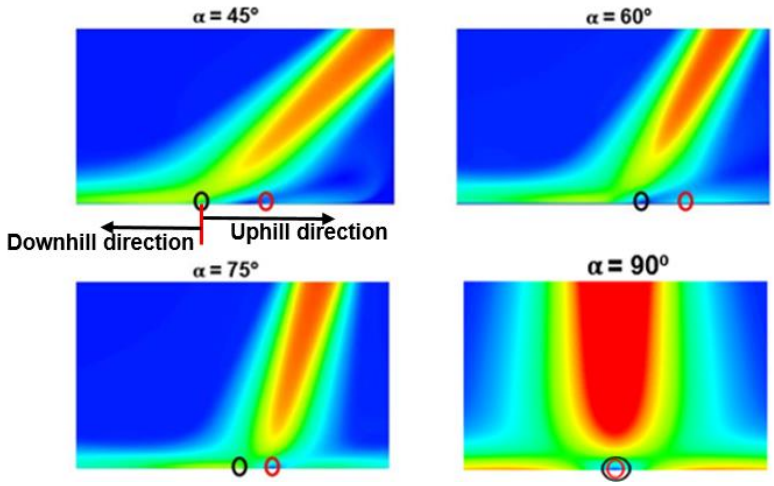

Figure 3-23 Velocity contours of inclines impinging jets, Re=10,000, H/D=6

Goldstein and Franchetti [116], investigated displacement of the stagnation point relative to the jet flow geometric center at $\alpha = 90^0$. Changes in stagnation point location with the angle of impingement was observed for H/D of 2 and 6, see Figure 3-24. It is obvious that location of the stagnation point is a function of impingement angle and largely independent of H/D. Goldstein and Franchetti [116], did not provide an analysis explaining why the stagnation point moved, but did develop an empirical correlation between H/D, α, and the resulting displacement. The measured movement of the displacement of the stagnation point with respect to the geometric center is shown in Figure 3-24 (b).

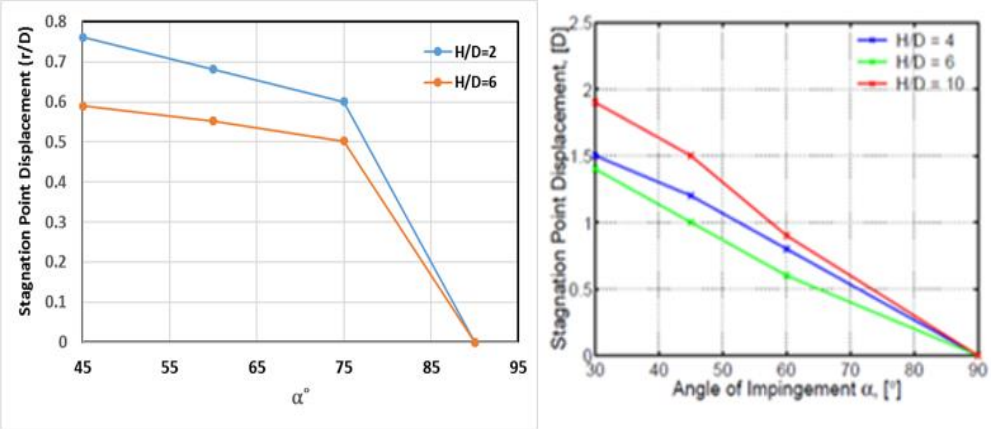

a) CFD data **b) Goldstein & Franchett** [116]

Figure 3-24 Displacement of stagnation point

In research by Beitelman, et. al., [117], the stagnation point displacement with α was discovered to be unaffected by Reynolds number (for a given H/D). and changes within about 3 jet diameters from the geometric center.

3.4.2 Heat Transfer Distributions

Surface heat transfer rate is a time averaged function of both mean and root mean square distribution of Nusselt number with respect to different jet impingement configurations. Fundamentally, Nu is a function of the difference in temperature, ΔT, between flow and impingement surface on the heat flux, q. Heat transfer data is presented in this section for a zone extending between geometric center and radial distance of 6 diameters

There are three factors that affect the rate of convective heat transfer in an impinging air jet; local velocity of the fluid, intensity of the turbulence and the temperature difference between the impinging surface and the jet fluid. Thus this section presents and explains the heat transfer distribution characteristics in these terms. The simulations are divided into normally and inclined impinging jets.

3.4.2.1 Normal jet impingement

The simulated heat transfer rate was found to depend significantly on H/D spacing, see Figure 3-25 for simulations at Re=10,000, H/D = 2 and 6 are within and beyond the jet core potential region. The figure shows good agreement between experimental and numerical data for both heights with an error of 1.7% of stagnation Nusselt number and maximum error of 12% over at r/D≈1.5 for H/D=6. For H/D=2, better overall agreement between experimental and numerical data at the stagnation point with maximum error of approximately 10% at r/D≈1.3.

At H/D = 6, there is penetration of the shear layer into the jet centreline which results in a reduced velocity at the centreline whilst the turbulence intensity sharply increases.

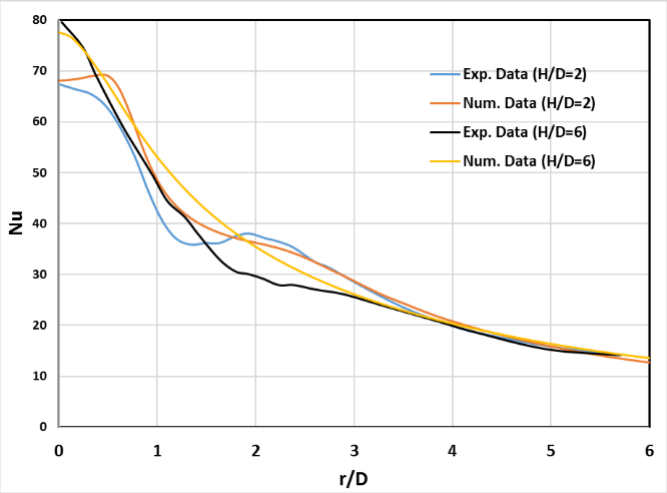

Figure 3-25 : Nu as a function of normalized radial distance for numerical and experimental data, for H/D = 2 and 6, Re=10,000 and α = 90º

Using the given parameters for the simulation, the Nusselt number at the stagnation point was predicted. At the stagnation point, the flow is not actually stationary since there is velocity fluctuation in a radial direction, but this flow is assumed stagnant based on average time considerations. As the flow is not stagnant per se, mixing is taking place on a continuous basis due to the influx of relatively cold fluid which maintains a temperature difference. Using time averaging reduces the contribution of these fluctuations. Hence, the heat transfer at the

stagnation point occurs due to the combined effects of both temperature difference and time varying velocity. It is seen that the simulated Nusselt number increases to a maximum at the stagnation point.

At H/D =2, Nu increases in a radial direction between the stagnation point and at radial distance of approximately r/D=0.5, though this value does depend on H/D and Reynolds number. A second maxima is observed at approximately r/D=2.5. Three causes have been proposed by the literate for these peaks, the peak at r/D=0.5 occurs due the change in the flow radial velocity as it travels radially from the stagnation point. When the jet deflects after hitting the surface, it accelerates rapidly but at greater distance the spreading of the jet causes its velocity to diminish. Golden and Akfirat [24], explained the increase in Nu at r/D=2.5 as a result of the change in flow boundary layer from laminar to turbulent as the jet speeding from the deflection zone. This mechanism does not apply at large H/D or impingement jets that are fully developed where a fully turbulent boundary layer flow exists in the stagnation region.

The position of the maximum at r/D = 2.5 coincides approximately with the point where toroidal vortices, which form in the shear region around the circumference of the jet, strike the plate as highlighted in the flow visualization carried out by Popiel and Trass [118] at y/D = 1.2 and 2. Popiel and Trass [119] suggested that the vortices cause a pulsation in the jet that is responsible for the synchronized appearance of the next toroidal vortex around the entire nozzle circumference. They also show that ring-shaped eddies are formed in the wall jet at approximately the point where the toroidal vortices reach the plate.

At low H/D, the magnitude of the secondary peak depends on the Reynolds number, increasing with increase in Re. This happens as a result of the fact that the potential core becomes longer. Livingood, et. al.,[120] stated that, At lower Re, three Nu maxima could be seen at radial distances of 0.5, 1.4 and 2.5 jet diameter from the stagnation point. However, As Re reaches 20,000 only two Nu maxima will be seen as the two outer maxima will merge. As the flow travels

downstream the wall region (r/D>0.5), the heat transfer diminishes with increasing radial displacement. That the jet boundary layer on the plate is fully turbulent for 0 < r/D < 0.5 follows from the existence of the maximum in Nu till r/D ~ 0.5. Within the stagnation zone, H/D =2, there is a pressure exerted by the free jet on the wall jet (the fluid flowing over the impingement plate) and this pressure assists in maintaining constant relatively low heat transfer fluctuating.

At H/D = 6, we also see from Figure 3-25 the maximum Nu occurs on the stagnation point due to the jet being penetrated by the shear layer at this distance of the nozzle above the heated surface. Hence, on the plate, the turbulent flow velocity profile is increased significant. The heat transfer diminishes with increasing radial displacement because the flow velocity at the plate decreases. It is obvious that as H/D increases the relative magnitude of the secondary peak in Nu decreases. This continues until the secondary peak ceases to exist. Schlunder et. al., [121] found that, the maximum $Nu_{stag.}$ And the maximum turbulence intensity occurring at H/D=7.5. Works presented in the literature specifically that of Goldstein and Behbahani [122] have highlighted the fact that, at the stagnation point, the value of Nu is a local minimum. However, this normally applies where nozzle to plate spacing is low, and/or Reynolds number is critically high and this is normally applicable only to jets of low turbulence. Finally, Figure 3-25 shows also that the distribution of local heat transfer is independent on H/D beyond radial distance r/D≥4 agreeing with results reported by Goldstein et al. [49] and [123].

3.4.2.2 Inclined jet impingement

Figure 3-26 a and b, present both experimental and simulated results for the oblique impingement of a circular jet on a flat plate in comparison with the orthogonal jet. In each case, the Nusselt number is plotted as a function of normalized radial distance (r/D) from the impingement point. Overall, the figure shows good agreement between experimental and numerical Nu values for all for

both H/D=2 and H/D=6 under the influence of three jet angles (α=90º,60º and 45º)

H/D = 2 and 6, for an obliquely impinging jet. It can be clearly seen that the peak heat transfer ceases to exist at the geometric center, and the profiles are asymmetric with distinct differences in the uphill and downhill directions, which increase as the impingement angle moves away from normal. When the angle between the impingement surface and the jet increases, the displacement is increased (note this is [90^0 - α). This is in agreement with the already described concept of stagnation point displacement as explained in Section 4.2.3. For large values of H/D the profile shows the maximum heat transfer moves in an uphill direction and, as would be expected, the displacement is greatest for smallest α. There is a rather rapid decrease in Nu in the downhill direction. At both spacings, secondary peaks occur in downhill directions for both inclined angles except for α=60º which has two peaks for lower H/D. For lower H/D=2, the lowest angle has better overall heat transfer especially in the uphill direction. This is not the case for H/D=6, where the highest inclined angle produces more overall heat transfer in the downhill direction.

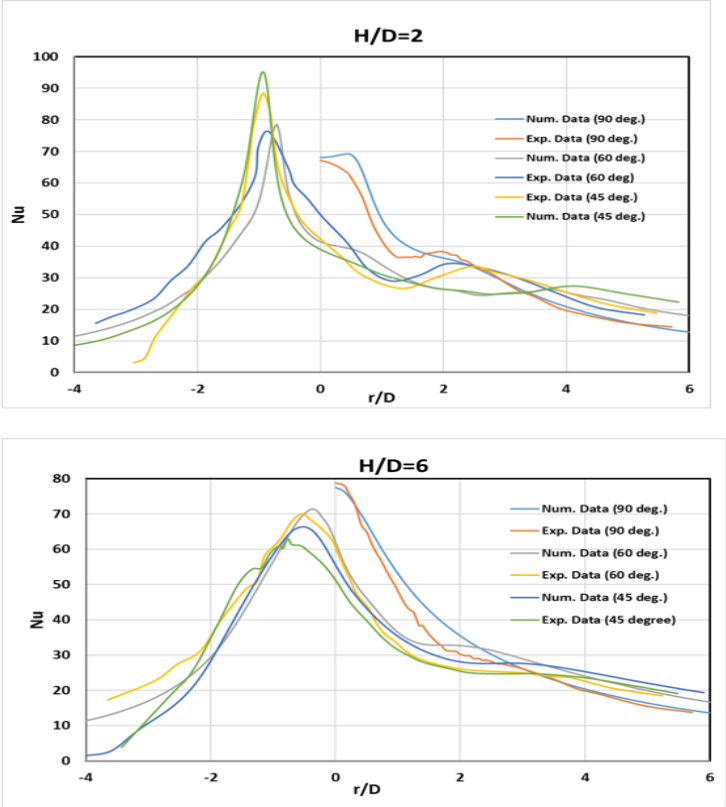

Figure 3-26: Nu as a function of r/D for an obliquely impinging jet for both numerical and experimental data; Re = 10000, H/D = 2 and 6 and α = 45º, 60º, and 90º

When the jet impingement is at an angle away from the normal a proportion of the jet flow transforms into a wall jet (flow parallel to the plate) some of which flows in the downhill direction. Hence, the wall jet boundary layer development usually takes the direction of the downhill pattern. In instances where the angle of impingements is smallest ($\alpha = 45^0$), the uphill direction jet wall is significantly reduced and hence, the heat transfer can be neglected for short radial displacements relative to the stagnation point.

3.5 Closing Remarks

This chapter presented details of computational models, produced using the CFD software package, ANSYS v 16.2 to simulate the behavior of an axisymmetric jet both orthogonal and inclined to the impingement surface. In all cases, jet impingement on a flat plate is discussed in detail, including the analysis of boundary layer, and the use of a mesh adapted turbulence model which was validated against an independent experimental study. All cases were validated against the experimental work done in [107] and [108]. In general, numerical data showed good agreement for both orthogonal and inclined jet with the experimental data. Two turbulence models were used in this validation due to the difference in flow nature between an orthogonal and inclined jet, the RNG k-ε model was used for orthogonal jet where SST k-ω model was used for all cases of inclined jets.

4 Average Nu obtained using different roughness elements

4.1 Introduction

Near-wall flow can be dramatically effected by wall roughness when the nature of the flow and its thermal behaviour are significantly different from those on a smooth surface. This effect depends on many parameters such as Reynolds number, type and size of any surface roughness and temperature differences [124]. In particular, surface roughness can disturb the stagnation region thermal sublayer, increasing the heat transfer [44]. Previous studies such as [90] and [125] reported that the local Nusselt number can be increased by as much as 50% to 60% for rough plates compared with a smooth wall. This claimed dramatic increase of heat transfer inspired the study made in this chapter.

The purpose of this investigation is to study the effect of simulated surface roughness on heat transfer. This was achieved by investigating the heat transfer features in two cases: a smooth, horizontal surface (the baseline case) and the same surface with three different roughness elements, square cross-sectional continuous rib, spherical pin-fin and cubical pin-fin added to it. Results are presented in the form of average Nusselt number $\overline{N_u}$ within and beyond the stagnation region. All roughness elements were considered to be an adiabatic wall where no heat transfer occurs to or from them. Each roughness element was tested for six different heights (e) from 0.25 mm to 1.5 mm in incremental steps of 0.25 mm for three different jet angles (α) of 90º, 60º and 45º. A total of 54 simulated cases (3 x 6 x 3) were investigated in this chapter.

This chapter investigates not only the effect of each roughness type but also how the roughness geometry impacted on the average Nusselt number. Each roughness element was arranged in a circle concentric with the geometric centre (i.e. centre of jet) with a radius of one and a half jet diameters (R/D = 1.5) in order

to keep it within the stagnation region. The jet diameter kept constant for all simulations (D=13.5mm) where the plane was located at H/D = 6 below the jet, for all the tests with a jet Reynolds number of 20,000 and jet temperature is 20°. The chapter is divided into two main sections, normal jet impingement and inclined jet impingement, each section contains the effect of roughness type and rib height on the average Nusselt number.

4.1.1 Thermal and Velocity boundary layer calculations

Temperature gradient plays the main rule in determining heat transfer which also determined by the thermal boundary layer thickness where the thinner boundary layer thickness the better heat transfer [126]. For turbulent thermal boundary layer most of the changes in velocity and temperature take place across the inner region, the buffer layer and the viscous sub-layer [127].

The temperature distribution along various locations including the centreline on the heated wall is shown in Figure 4-1 below for Re=20,000 and H/D=6. The x-axes represent the vertical distance from plate surface (y/D=6) to half diameter above it. The figure shows that as the jet flow travels more distance from the geometric centre, it accumulates more heat which raises its temperature. Thus, the thermal boundary layer thickness (δ_T) increases causing less convective heat transfer.

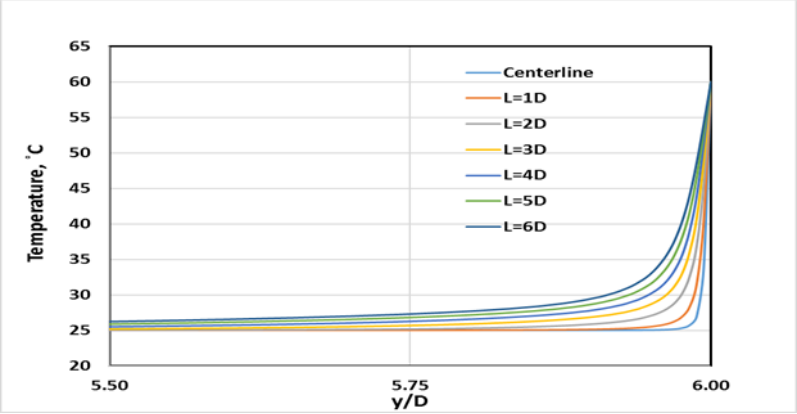

Figure 4-1: Temperature distribution along various locations on the heated wall for Re=20,000 and H/D=6

However, the flow velocity increase after impinging till it reaches its maximum at radial distance of approximately r/D=0.97 then start to as the flow travels away as shown in Figure 4-2.

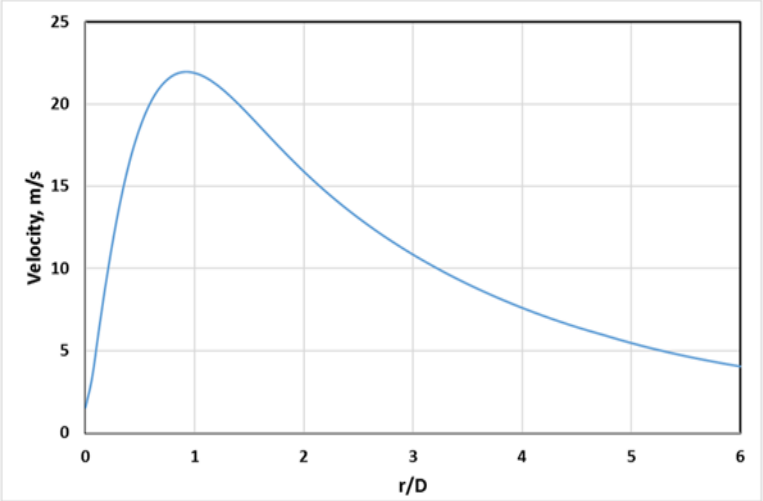

Figure 4-2: Velocity distribution along radial distance for Re=20,000 and H/D=6

Using the definition of the thermal boundary layer thickness (δ_T)in equation (1.11), which can be estimated at about 99% of the free stream temperature. As for velocity boundary layer thickness (δ) ,it has been estimated in the literature [128] by one tenth of the hydraulic diameter (0.01D) for stagnation zone where for wall jet region it can be estimated at about 95% of the free stream velocity. Table 4.1 below shows δ_T and δ for each location shown in the figure above,

Table 4-1: Thermal and velocity boundary layer thickness over a heated wall

Location, L (mm)	1D	1.5D	2D	3D
$\boldsymbol{\delta_T}$ $\boldsymbol{(mm)}$	0.81	1.59	2.43	5.11
$\boldsymbol{\delta}$ $\boldsymbol{(mm)}$	0.135	0.22	0.56	0.73

4.1.2 Normal jet impingement – Smooth flat plate (the baseline case)

As mentioned above, the study in this chapter will be for Re=20,000, jet to target distance (H/D) =6 and jet temperature 20° for both orthogonal and inclined jets, thus requires to first realise the effect of Re=20,000 on heat transfer for smooth flat plate configuration in order to further investigate. First will start with Figure 4-3 which demonstrates local Nu values along the radial distance on the heated surface for H/D=6 and Re=20,000. As shown in the figure, Nu is maximum as expected at the stagnation point (r/D=0) where noticeable degradation in its values as the flow travels downstream losing about 53% of its maximum value at a radial distance H/D=2.5.

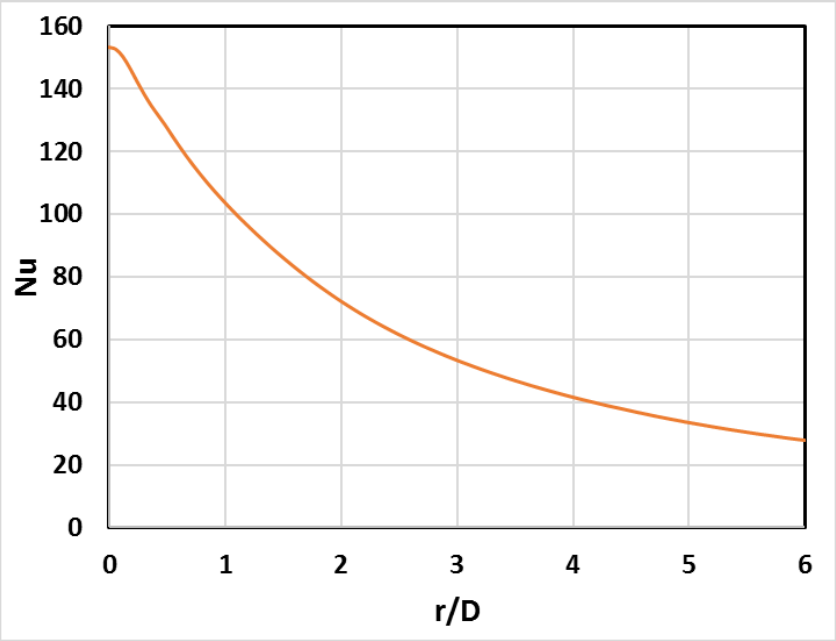

Figure 4-3: Local Nu distribution for Re=20,000, H/D=6 and α=90º

The concept of area averaged heat transfer can be better understood with the wider range of plots. Generally, the higher the Reynolds number the higher the area averaged heat transfer. We also see from the figure the maximum Nu occurs on the stagnation point due to the jet being penetrated by the shear layer at this distance of the nozzle above the heated surface. Hence, on the plate, the turbulent flow velocity profile is

increased significant. The heat transfer diminishes with increasing radial displacement because the flow velocity at the plate decreases.

Schlunder et. al., [121] found that, the maximum $Nu_{stag.}$ And the maximum turbulence intensity occurring at H/D=7.5. Works presented in the literature specifically that of Goldstein and Behbahani [122] have highlighted the fact that, at the stagnation point, the value of Nu is a local minimum. However, this normally applies where nozzle to plate spacing is low, and/or Reynolds number is critically high and this is normally applicable only to jets of low turbulence.

4.1.3 Inclined jet impingement – Smooth flat plate (the baseline case)

As for the effect of Re on heat transfer for inclined jets (α=45º and 60 º), Figure 4-4 presents simulated results for Nu with H/D = 6, respectively, for Reynolds number, Re = 20,000 and α = 45^0 and 60^0 respectively shows that the magnitude of Nu increases with increase in jet inclination angle. As for the position of the stagnation point, the close jet angle to normal jet, the close the stagnation point to the geometric centre. The secondary peak become more pronounced at higher inclination angle. This phenomenon is also similar for normal jet impingements which are characterized by the fact that the jet is accumulatively delayed thereby building large Reynolds number. Therefore, for a particular H/D setting there will be variations in heat transfer distribution over the impingement plate with change in geometric and jet flow parameters.

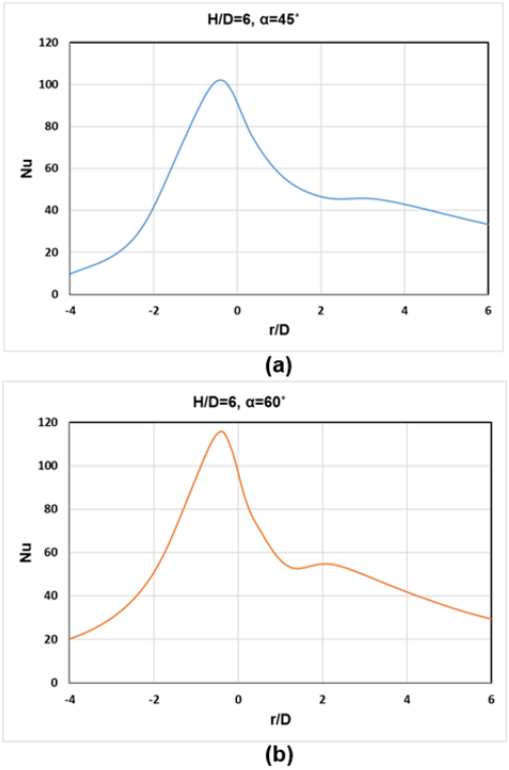

Figure 4-4: Local Nu distribution for Re=20,000, H/D=6 , (a) α=45º and (b) 60º

4.2 Normal jet impingement

Three different roughness elements were tested for a normally impinging jet, α=90º as shown in Figure 4-5. The arrangement of each set of pins, the rib and the cubical elements have same width, depth and height (e), where the spherical cap has a width of 2e. Each element was tested for six different heights of e = 0.25, 0.5, 0.75, 1, 1.25 and 1.5 mm in order to find the optimum value of each.

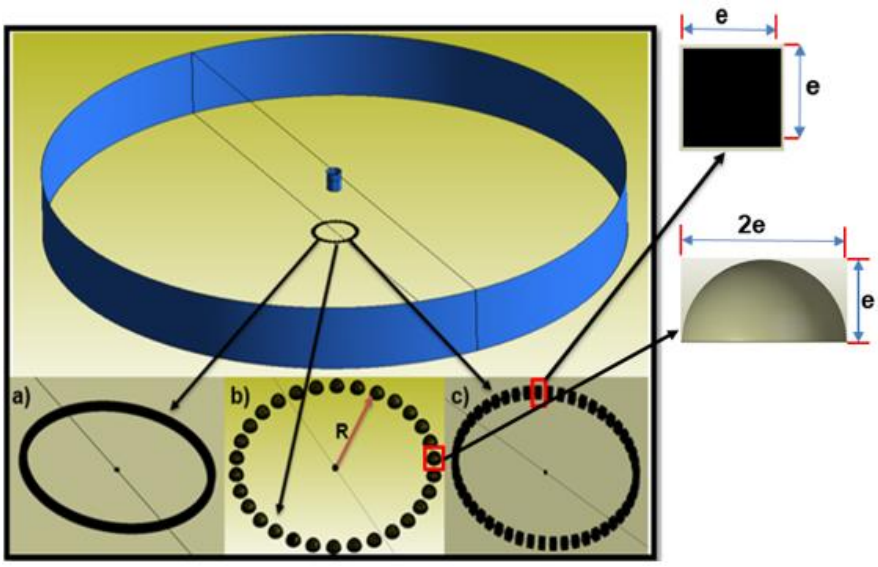

Figure 4-5: Roughness elements geometries a) Rib, b) Spherical pin-fin and c) Square pin-fin

4.2.1 Roughness element – continuous rib

Figure 4-6 illustrates the meshing strategy used in this simulation. It is well known from the literature that the near wall regions have a large impact in the solution variables and momentum [129], thus, extra care is taken with near-wall meshing in this type of problem in order to get accurate results. Mesh generation was done using ANSYS ICEMCFD v16.2. Hexahedral elements were used by block-structured grids using spatial discretization of the domain. A very fine mesh was applied in the direction normal to the heated surface as well as the roughness elements to ensure a proper functionality of the turbulence model especially low Reynolds number models which require a dimensionless distance between the wall and the first nose less than 1. The growth rate of the cell near the heated surface where all heat transfer takes place was no greater than 1.2in the direction normal to the heated surface. O-grid strategy was applied within and bear the round nozzle to ensure high cell orthogonality. A total grid size was approximately 1.2 million for the whole computational domain.

The maximum increase percentage in total surface area due adding this roughness element is approximately 0.2%.

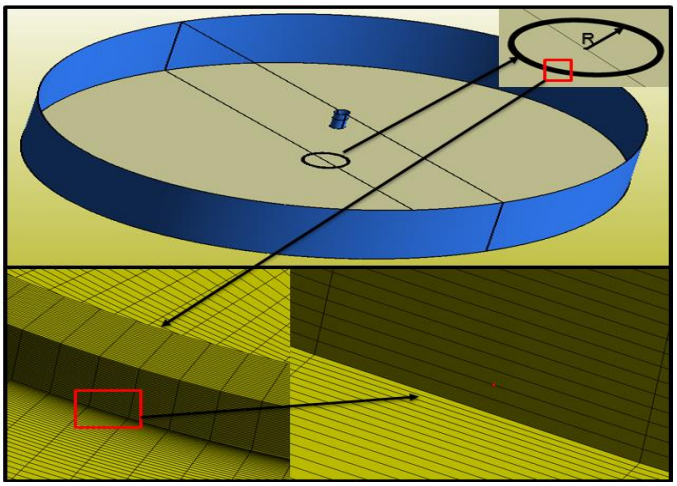

Figure 4-6: Meshing used for continues rib

Figure 4-7 shows the effect of rib height on the local Nusselt number distribution for a circular jet impinging on a flat plate without a rib (baseline case) and with a continuous rib, forming a circle of radius one and a half times the diameter of the jet and with its centre coincident with the centre of the jet (i.e. the stagnation point). The rib had a square cross-section.

For the flat, undisturbed plate the simulated Nu values gradually and smoothly decrease with increasing distance from the centre. Once a rib has been inserted the shape of the Nu curve, as would be expected, undergoes a sudden and very sharp change in the shape of a large zigzag imposed on the curve at the position of the rib. The minimum of the zigzag coincides with the rib's downstream edge.

This figure indicates that as the rib height increases so does the distance over which the heat transfer is enhanced (the re-attachment length), where Nu is increased which confirms the work of other researchers such as [124], [130], [131], and [132] . The figure was split into two in order to see more clearly the effect of rib height on local Nu. Generally, for rib heights (e) of 0.25mm, 0.5mm and 0.75mm, the local heat transfer shows an increase compared to the no rib case due to the increase in turbulence before and after the rib. This increase appears in the form of a peak around the re-attachment point. The re-attachment

point is where the flow hits the heated surface after passing the rib, the velocity at which flow hits the surface at this point is defined as the “arrival velocity”.

However, for e ≥ 0.75 mm, another Nu peak occurs just before the rib at (r/D≈ 1.4) due to the flow recirculation in front of the rib which enhances heat transfer rate in this region (see Figure 4-8). For 1≤ e ≤1.5 mm, the rib height starts to have a dramatic effect on the local Nu distributions where overall results give a lower local heat transfer than for the no rib case. This is due to the increase in rib height becoming so large that in the physical distance the flow travels before reaching the re-attachment point the turbulence in the turbulent shear layer reduces substantially. The figure also demonstrates that, for e=1.5mm, the stagnation Nusselt number $N_{u_{stag}}$ starts to be noticeably effected by the rib height showing lower value of baseline case (smooth).

It follows that must be an optimal rib height that balances both the flow arrival velocity and its turbulence at the re-attachment point resulting in maximum total heat transfer. Confirming the existence of this optimal height and finding its value is especially important in the design of cooling mechanisms for GT vanes.

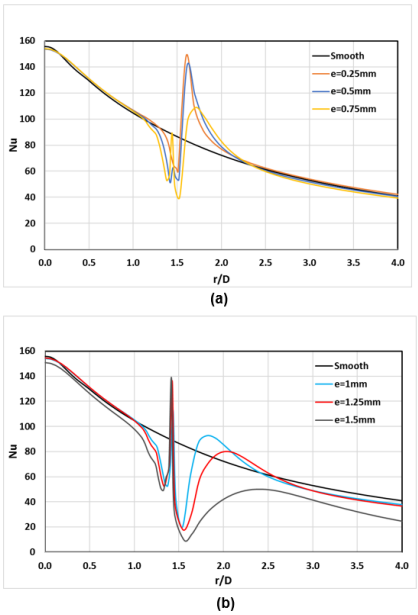

Figure 4-7 : Effect of rib height on local Nusselt number for Re= 20,000, H/D=6 and α = 90º.

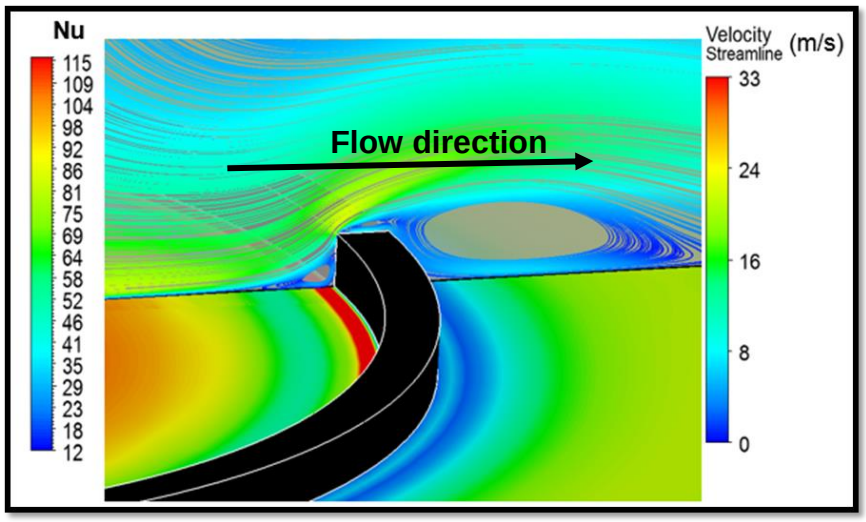

Figure 4-8 : Velocity streamlines and local Nu contours for e=1.25mm, Re= 20,000, H/D=6 and α = 90º.

It is suggested that as rib height increases the low-pressure region behind the rib becomes larger, and the forces pushing the separated flow toward the wall weaken, and that one factor in that process might be the increasing distance from impingement surface to the separation point at the upper edge of the rib.

Figure 4-9 shows contours of local Nu distributions for all rib heights for the circular rib which is represented by the black circle. The low-pressure (wake) region, where there is flow recirculation, is shown by the blue area behind the rib. As can be seen from the figure, as the rib height increases, so the extent of the low-pressure region behind the rib increases. This process continues as the rib height increases until it actually reduces the heat transfer in this region. as shown for rib height 1.5 mm. The optimum rib height is 0.25 mm, this is illustrated in Figure 4-9 by the dominance of the red colour.

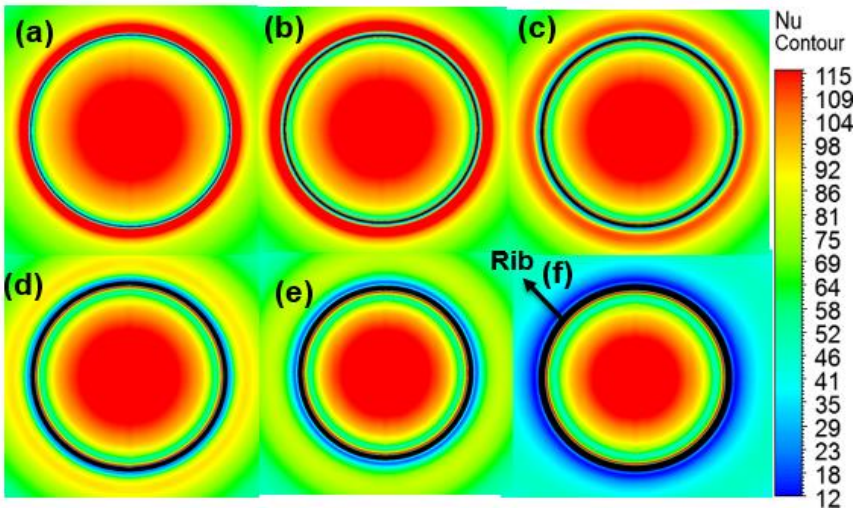

Figure 4-9 : Nu contours for different rib heights, Re= 20,000, H/D=6 and α = 90º., (a) 0.25 mm, (b) 0.5 mm, (c) 0.75 mm, (d) 1 mm, (e) 1.25mm and (f) 1.5 mm

Figure 4-10 shows the streamwise average value of the Nu for all six rib heights. The average was obtained by numerically integrating the local Nu using equation (1.10) between 0 ≤ R/D ≤ 2.5 as beyond this the effect of roughness height is negligible (see Figure 4-7. Where R is the distance downstream from jet centreline and D is the hydraulic diameter of the jet downstream of the ribs.

The optimal rib height is e=0.25 mm, above this value the averaged Nu decreased with further increase in rib height as shown. A relative improvement of the averaged Nu ($\overline{N_u}$) compared to the no rib case of about 4.5%, 3.8%, 1.4% for heights e=0.25 mm, e=0.5mm and e=0.75mm where lower $\overline{N_u}$ values is shown of -2%, -22%, and -47% for heights 0.75mm, 1 m,1.25 and 1.5 mm respectively.

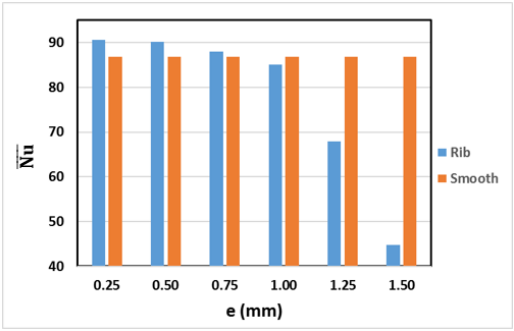

Figure 4-10 : Effect of rib height on average Nusselt number over 0≤r/D≤4, Re=20,000, H/D=6 and α = 90º.

This is due to the fact that the flow is travelling a very long distance before it hits the surface with low arrival velocity, leading to an-enlarge the low-pressure region causing a decrease in the arrival velocity resulting low local Nu values as shown in Figure 4-11 . Further investigation of this effect will be presented in the next chapter.

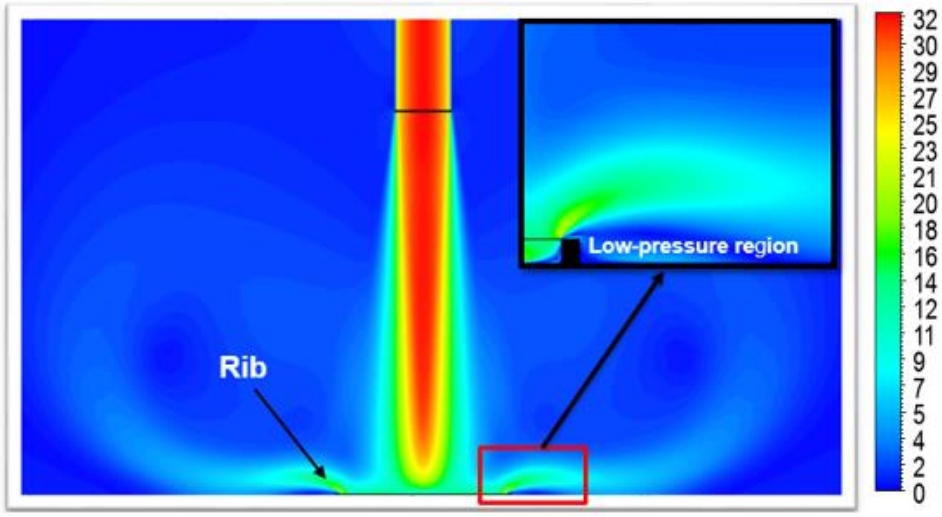

Figure 4-11 : Velocity contour for rib height of e= 1.5 mm, Re=20,000, H/D=6 and α = 90º. Roughness element – spherical pin-fin

4.2.2 Roughness element – Spherical pin-fins

In this section, an array pin-fin with spherical cap shape were used to roughen the smooth surface to investigate their impact on $\overline{N_u}$. The roughness height (e) is varied between 0.25 mm and 1.5 mm with an increment of 0.25 mm. The heat transfer rate can be enhanced not only due to the change of the physics of the flow but also due to enlarging the total surface area [133]. Here is the maximum increase is approximately 0.4% of the total surface area was due to adding these roughness elements. However, in the current research, the rib is considered to be an adiabatic wall which means the effect of the extended area on the flow physics will only be discussed in this research. Figure 4-12 below shows meshing strategy used for this type of roughness; the y+ value is 0.5, as recommended by the literature. The number of roughness elements is and the distance between them (pitch) change as the size of the element changes (see Table 4-2).

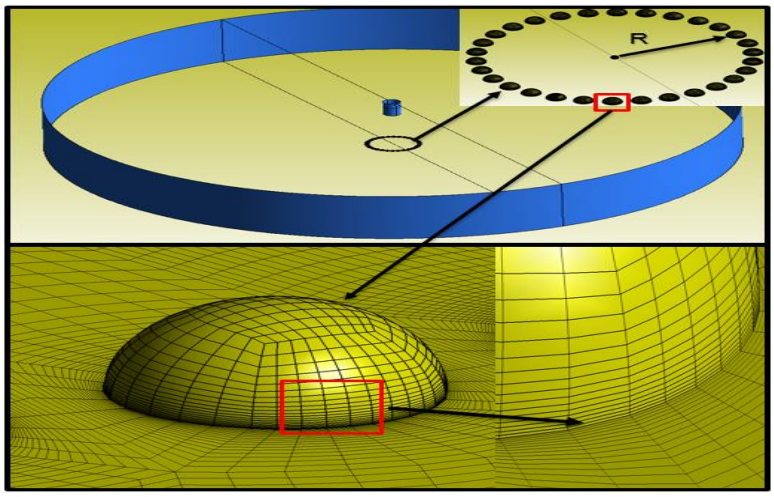

Figure 4-12 : Computational mesh for a single spherical pin-fin element on a plane wall

Table 4-2 : Geometry details of the spherical pin-fins

Height e (mm)	Area (mm^2)	Pitch (mm)	No. of roughness elements
0.25	0.393	2.04	50
0.5	1.57	3.25	30
0.75	3.54	2.75	30
1	6.29	0.55	50
1.25	9.82	1.75	30
1.5	14.14	1.25	30

Figure 4-13 shows the effect of sphere height on the local Nusselt number distribution for a circular jet impinging on a flat plate. The sphere had a radius e and a width of 2e. Overall, local Nu curves show a moderate increase comparing to the rib case discussed above for 0.25≤e≤1 mm. However, for e=0.75mm, the curve of local Nu shows higher values comparing to the baseline case due to the increase in turbulence within the stagnation region. Unlike this rib-roughened surface, the two Nu peaks occur before and after the roughness element for all heights due to the flow recirculation happens in these two regions. The effect of sphere height on local Nu starts to diminish at r/D=2mm for e≤0.75mm.

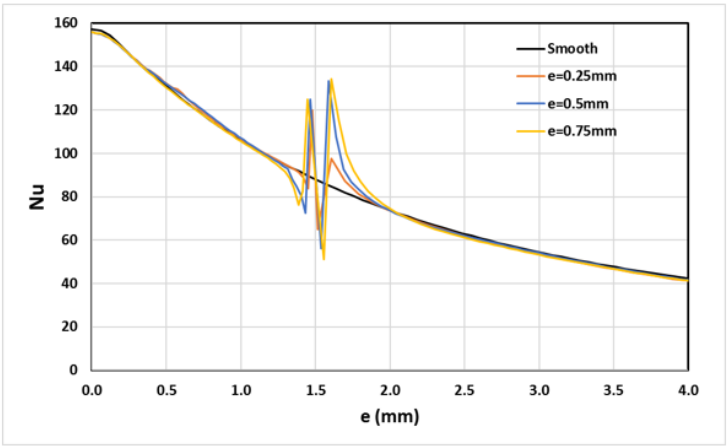

(a)

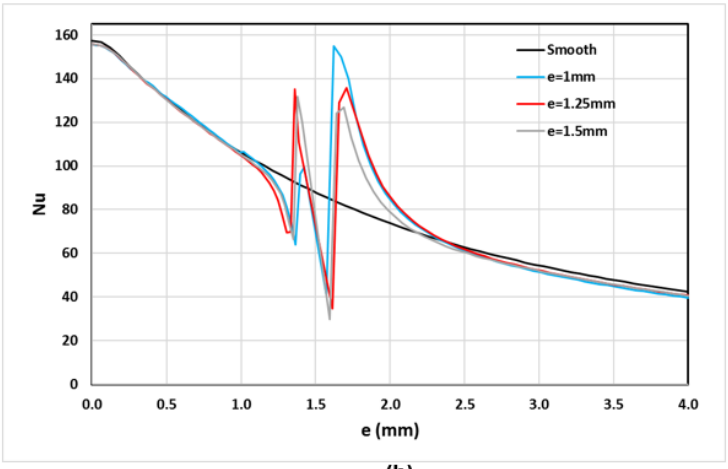

(b)

Figure 4-13: Effect of spherical pin-fin height on local Nusselt number for Re= 20,000, H/D=6 and α = 90º.

In order to investigate the effect of each roughness element on its neighbour as the size changes, the distribution of local Nu and flow velocity between two selected elements were drawn on (line 1) between two neighbouring elements, as shown in Figure 4-14.

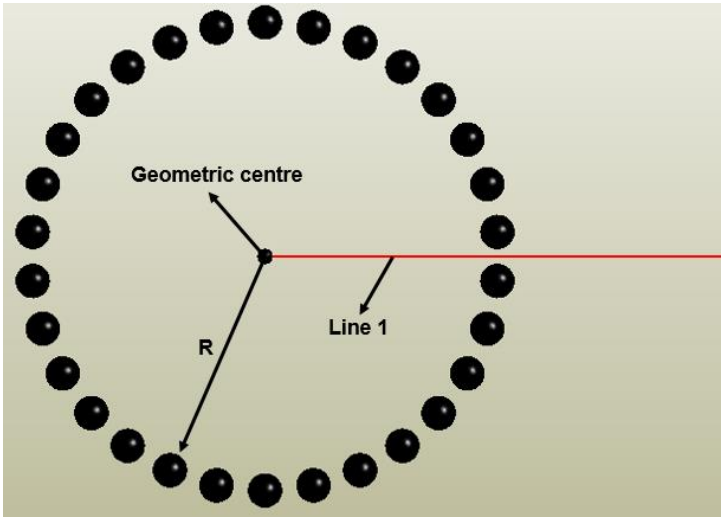

Figure 4-14: Top view of roughness element with height e=1.5mm

Figure 4-15 demonstrates the distribution of local Nu and flow velocity of three roughness heights compared to the baseline case. The figure shows, both the distribution of local Nu and flow velocity of two neighbouring roughness elements with heights 1mm and 1.5mm were noticeably declined comparing the baseline case. This is due to the wake region between the two neighbouring roughness elements caused by flow deflection where both local Nu and flow velocity rapidly decreases in this region as shown in Figure 4-16

For e=1.5mm, a decrease percentage of approximately 50% and 90% in local Nu and flow velocity respectively between the two neighing roughness elements. However, the height 0.5mm seems to have a negligible effect on local Nu and flow velocity distribution when compared to the baseline case. Thus, selecting the right roughness element size should prevent a considerable amount of heat transfer loss.

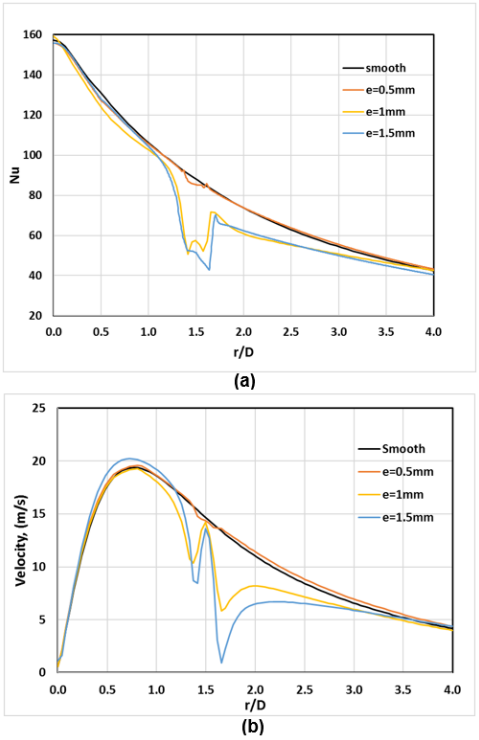

Figure 4-15 : Local distributions of three roughness elements heights for Re= 20,000, H/D=6 and α = 90º, (a) Nu, (b) Velocity

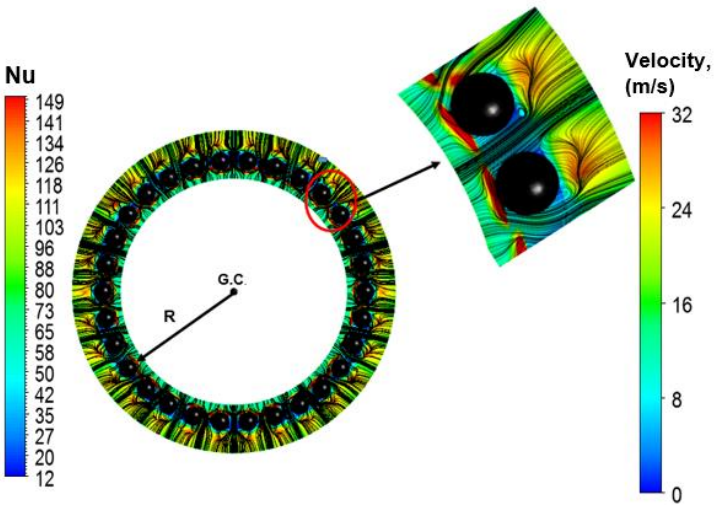

Figure 4-16: Local Nu and streamlines velocity for e=1.5mm

Overall, $\overline{N_u}$ shows an improvement for all spherical pin fins heights comparing to the no rib case, see Figure 4-17 with the percentage increases between

0.6% to 6%. The improvement was greatest at e=0.75 mm and decreased gradually as rib height increases till it reached a minimum at e=1.5 mm, where improvement was about 0.6%. Beitelmal et. al. [90] investigated the same surface roughness configuration, though with different details in the geometry, and reported an increase in $\overline{N_u}$ of about 6%. The difference between the two sets of results is explained by Beitelmal's roughness element being higher, producing a greater degree of radial vortices recirculation, lowering heat transfer [133] . However, generally, Unlike the rib case, with this type of roughness configuration, average Nu improves for all heights. Finally, changing the size of this type of roughness element seems have a big impact on $\overline{N_u}$. More details on studies made to enhance heat transfer using hemispherical roughness elements can be found [134], [135].

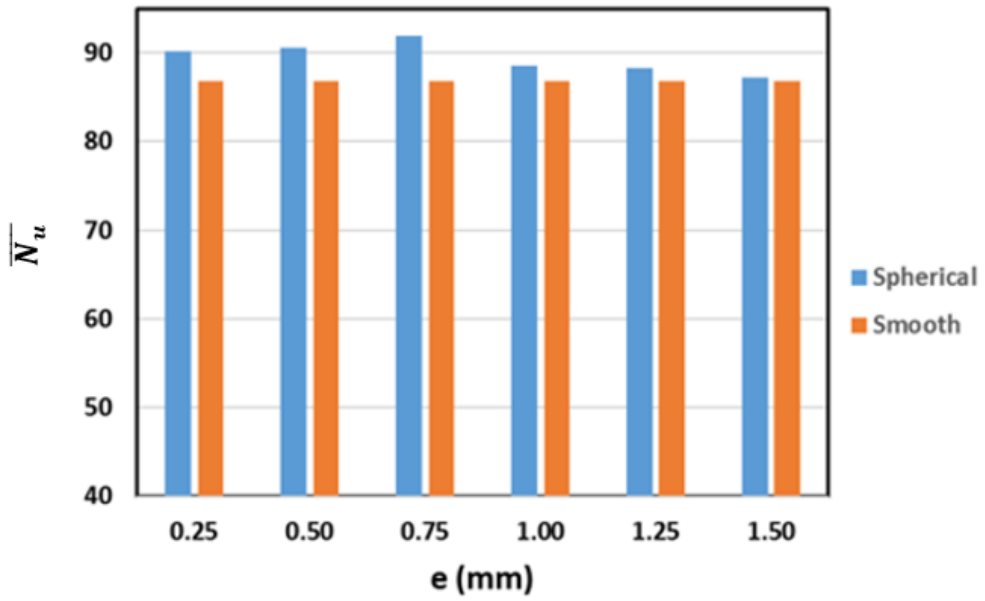

Figure 4-17 : Effect of spherical pin-fin height on average Nusselt number over 0≤r/D≤4, Re= 20,000, H/D=6 and α = 90º.

The velocity contour of the flow for rib height e=1.5 mm is shown in Figure 4-18. Unlike the contours for ribs of square cross-section, the flow travelled a shorter distance before it re-attached with the heated surface resulting in higher $\overline{N_u}$ at the same nominal height. This is due to the nature of the rib geometry; the hemispherical shape provides less resistance to the incoming flow.

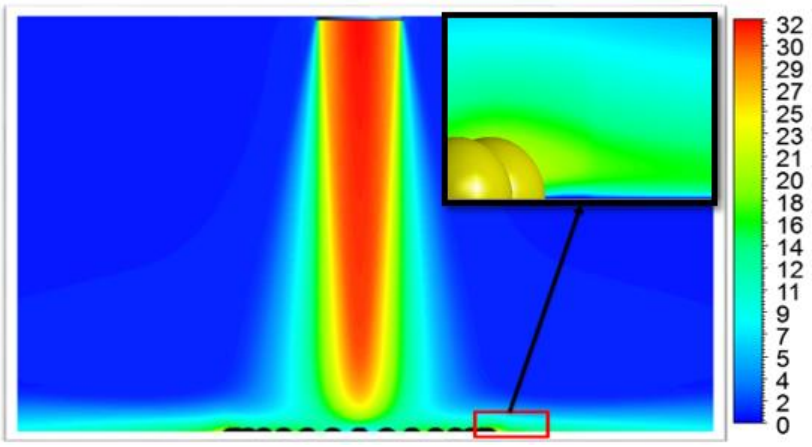

Figure 4-18:Velocity contour for spherical pin-fin roughness element for e=1.5 mm, Re=20,000, H/D=6 and α = 90º.

Local Nu contours are shown in Figure 4-19 below. A close look at the figure, shows that the height of the roughness element effects the stagnation region. The higher the rib, the narrower the stagnation region. On the other hand, for 0.25 ≤ e ≤ 0.75, the height of the roughness element has an opposite impact on the local Nu values in the region just behind the protrusion where an enhancement of local Nu is more noticeable as the height increases. This is because as e increases, the low-pressure region, into which the flow was pushed, increased, resulting in higher heat transfer. However, an opposite observation is shown for e≥1.

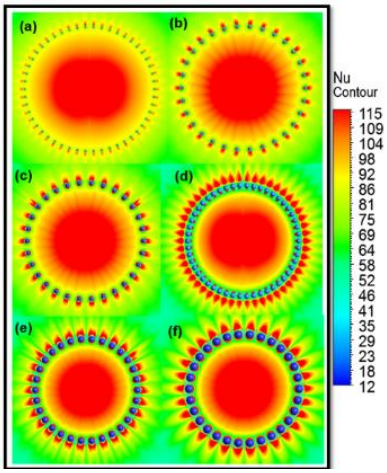

Figure 4-19: Local Nu contours for roughness heights of (a) 0.25 mm, (b) 0.5 mm, (c) 0.75 mm, (d) 1mm, (e) 1.25mm and (f) 1.5 mm, Re= 20,000, H/D=6 and α = 90º.

In order to identify the low-pressure zone behind the roughness element, contours of velocity vectors of three spherical pin fins heights are shown in Figure 4-20 below. The vertical red line shows where the flow separation starts above the hemispherical element. As shown in the figure, the lower the hemispherical height, the earlier flow separation, the earlier the low-pressure region forms above the protrusion. As for the low pressure region behind the roughness element, this region is wider as the height increases causing more heat transfer in that region.

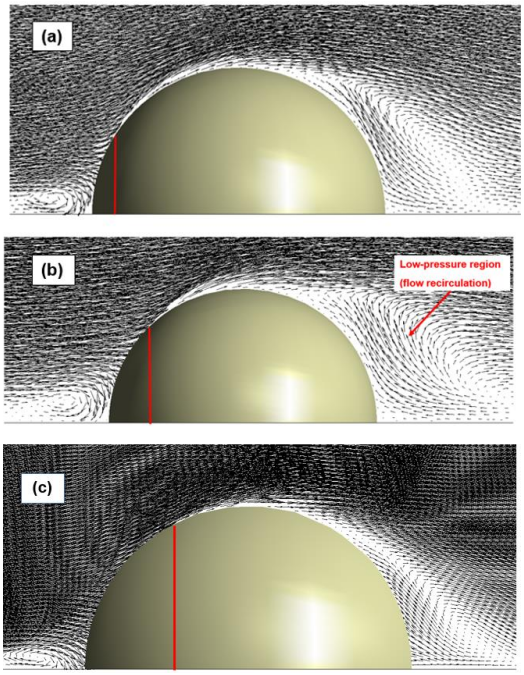

Figure 4-20: contours of velocity vectors for heights (a) e=0.25mm, (b) e=0.75mm and (c) e=1.5mm, Re=20,000, H/D=6 and α = 90º.

To investigate the effect of roughened element height on $\overline{N_u}$ in more details, simulated contours of turbulence kinetic energy (TKE), local Nusselt number (Nu) are shown in Figure 4-21 for three rib heights of 0.25 mm, 0.75 mm and 1.5 mm. In general, as the height increased, TKE increased causing the flow to be more turbulent which then enhanced the local Nu. However, at larger heights (e.g. e=1.5 mm), the roughness elements start to have an effect on each other which results in an obvious decrease in TKE as shown in the figure.

below for three heights of 0.25 mm, 0.75 mm and 1.5 mm. In general, as the height increases, turbulence kinetic energy increases causing the flow to be more turbulent due to the recirculation vortices generated which then enhances local Nu [136]. However, for larger height (i.e. e=1.5mm), the roughness elements are getting closer to each other which effects the individual kinetic turbulence energy resulting an obvious decrease in T.K.E. as shown in the figure.

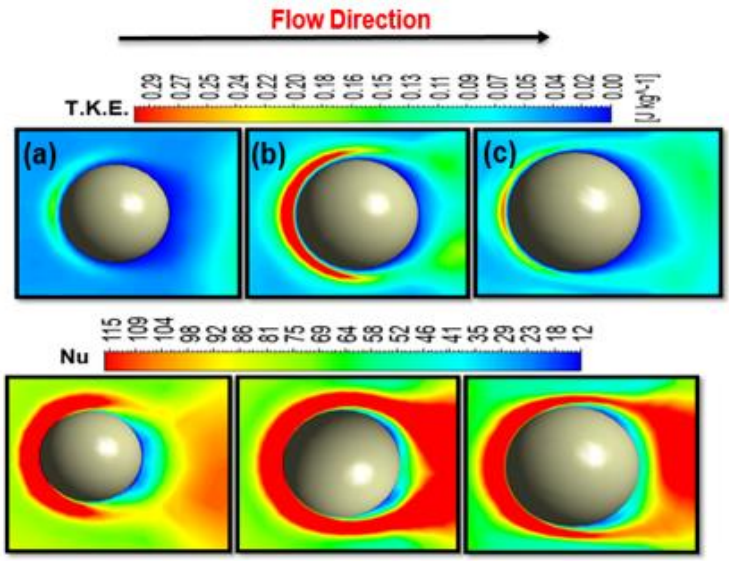

Figure 4-21 : Contours of turbulence kinetic energy (T.K.E.) and local Nu distributions for (a) e=0.25 mm, (b) e=0.75mm and (c) e=1.5mm, Re=20,000, H/D=6 and α = 90º.

4.2.3 Roughness element – cubical pin-fin

Figure 4-22 below shows an array of cubical pin-fins with detailed mesh for one of them. The array has also radius R of 1.5D measured from the geometric centre. The same as the case of spherical pin fin, a fixed distance of 1.3mm kept between all elements with varying their number to a maximum of 50 roughness elements when e=0.25mm, all have same width and height of e. The maximum percent increase in total surface area by using cubical pin-fin is 0.5%

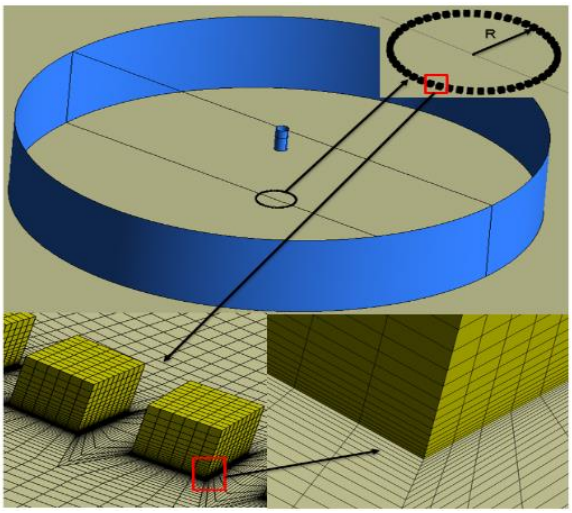

Figure 4-22: Computational mesh for a square cross-sectional pin-fin roughness element on a plane wall

The detailed geometry of all cubical pin-fins is shown in **Table 4-3** below

Table 4-3: Detailed geometry for cubical pin-fin

Height e (mm)	Area (mm^2) (5 faces)	Pitch (mm)	No. of roughness elements
0.25	0.3125	2.3	30
0.5	1.25	2.05	30
0.75	2.8125	1.79	30
1	5	1.55	30
1.25	7.8125	1.3	30
1.5	11.25	1.05	30

Figure 4-23 shows the effect of cubical height on the local Nusselt number distribution for a circular jet impinging on a flat plate. The cubical roughness element has a length and a width of e. Overall, two peaks of local Nu are shown for all heights due the flow recirculation occurs in front and after the roughness elements. Both peaks increase as the height increases so the drop in local Nu which occurs in the region attached to the roughness wall. At r/D≈2.25, and e≤0.75mm, all local Nu curves starts to match as the height variation is no more affects the heat transfer rate. However, for e≥1mm, curves of roughened surfaces show a slight lower value of local Nu than the smooth case.

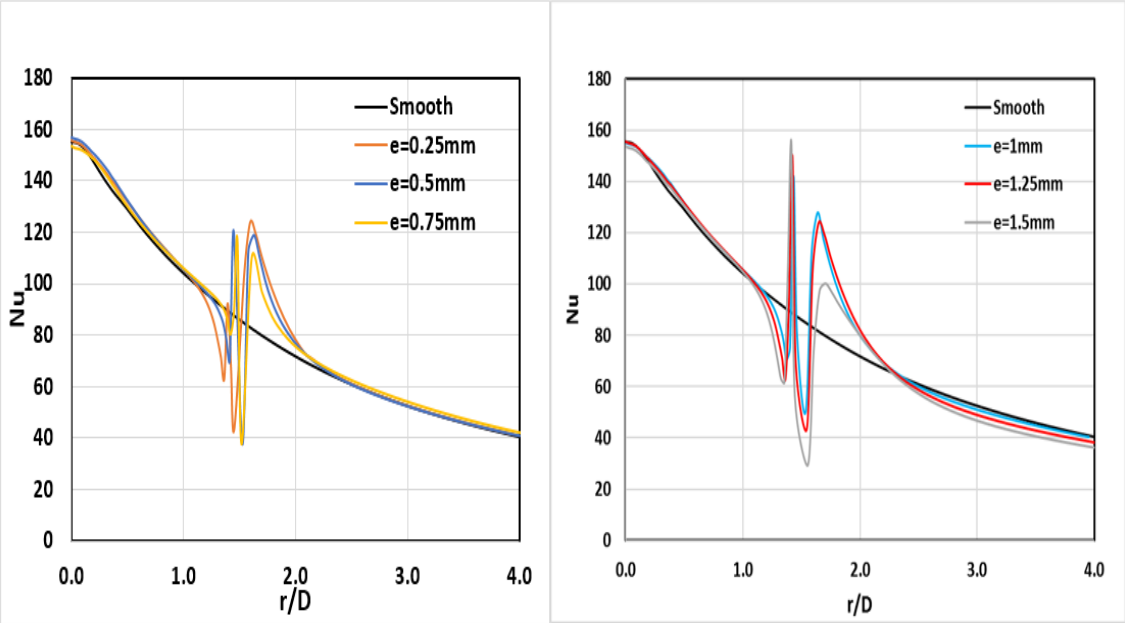

Figure 4-23: Effect of cubical pin-fin height on local Nusselt number for Re=20,000, H/D=6 and α = 90º.

Figure 4-24 shows the effect of using a cubical pin-fin on $\overline{N_u}$. The figure shows that, $\overline{N_u}$ can vary by up to about 7.2% of the value of the smooth surface, for the smaller pin heights (0.25 mm and 0.5 mm) but gradually decreasing to about -1.4% for e=1.5 mm. The rate of heat transfer increases as the tip of the square pin-fin gets closer to the jet exit since the surface area is increased. However, as the fin height further increases, both velocity and pressure of the jet decreases causing the average Nu over the surface area to diminish but the local Nu which is based only on the local value may increase [137].

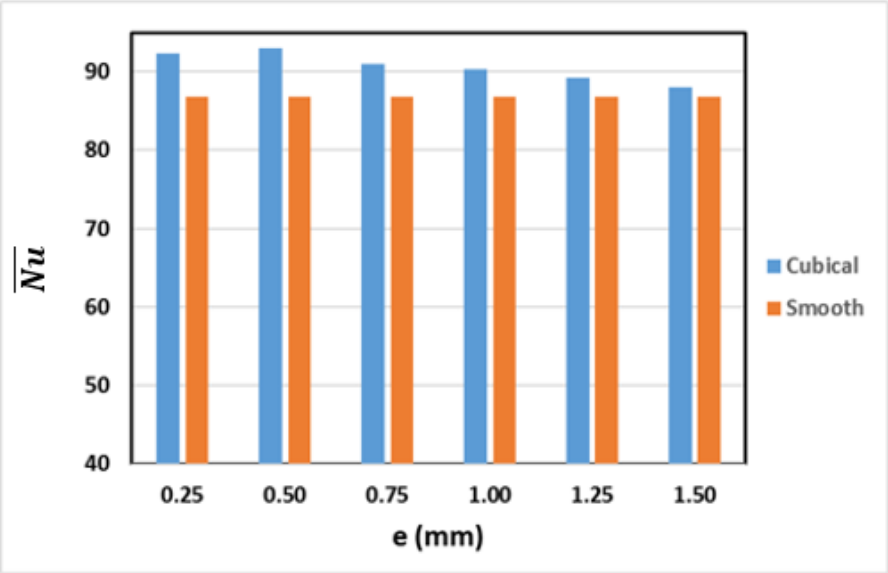

Figure 4-24: Effect of cubical pin-fin height on average Nusselt number over 1≤r/D≤4, Re=20,000, H/D=6 and α = 90º.

Local distributions of Nu are shown in Figure 4-25 below, overall, cubical pin-fins show higher local heat transfer distributions for all heights. As e increases, so does the local heat transfer rate, this is obvious for 0.25mm≤e≤1.25mm. However, for e=1.5mm, Nu starts to fall down due to the increase of the wake region behind the roughness element. This low pressure region forces the flow to recirculate within it which effects the main flow velocity by reducing it. This reduction causes heat transfer rate to diminish.

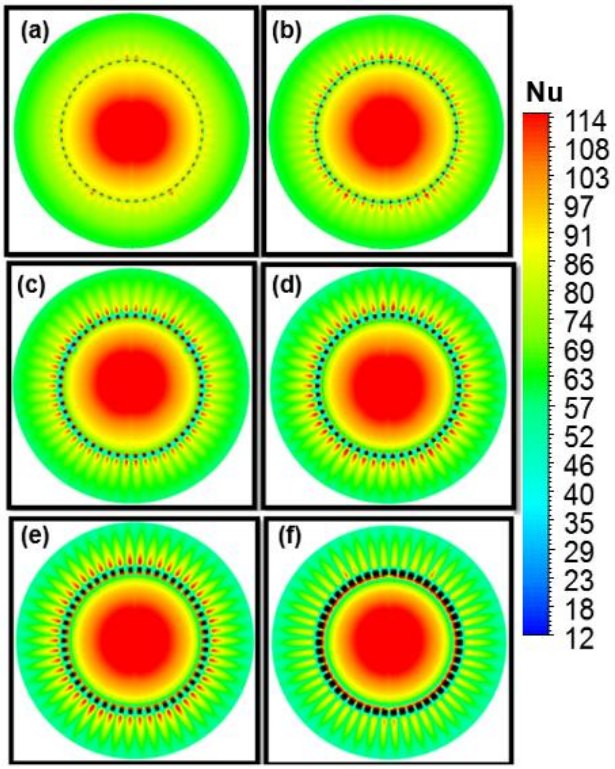

Figure 4-25: Local Nu contours for roughness heights of (a) 0.25 mm, (b) 0.5 mm, (c) 0.75 mm, (d) 1mm, (e) 1.25mm and (f) 1.5 mm, Re=20,000, H/D=6 and α = 90º.

Figure 4-26 shows velocity vector contours for three pin heights; 0.25 mm, 0.75 mm and 1.5 mm. As shown in the figure, the higher the pin, the larger the separation region (the region above the fin top edge), the larger the low-pressure region, and the higher the local Nu. However, for e=1.5 mm, flow starts to recirculate above the top edge of fin, as shown in the figure, causing the main jet to travel a longer distance and reducing its arrival velocity before it hits the heated surface resulting lowest increase in $\overline{N_u}$.

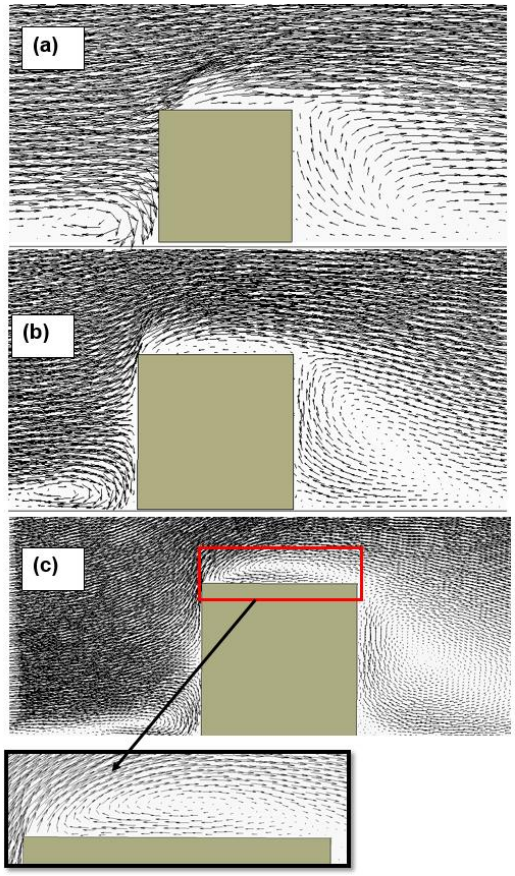

Figure 4-26: contours of velocity vectors for heights, (a) e=0.25mm, (b) e=0.75mm and (c) e=1.5mm, Re=20,000, H/D=6 and α = 90º.

Flow properties such as turbulence kinetic energy (TKE) could also affect the heat transfer characteristics in such applications. The TKE in front of the pin-fin increase with increasing pin height as shown in Figure 4-27 due to flow recirculation occur in this region. This should increase the local Nu but not necessarily increase $\overline{N_u}$ as discussed above. Neighbouring protrusions start to effect each other for bigger pin-fins due to their influence on the jet flow properties. This is shown in local Nu distribution for e=0.25mm and 0.75 mm where an enhancement arises on both sides of the rib, however, for e=1.5mm, this enhancement disappears due to the change in flow properties (i.e. TKE) caused by the neighbouring roughness element.

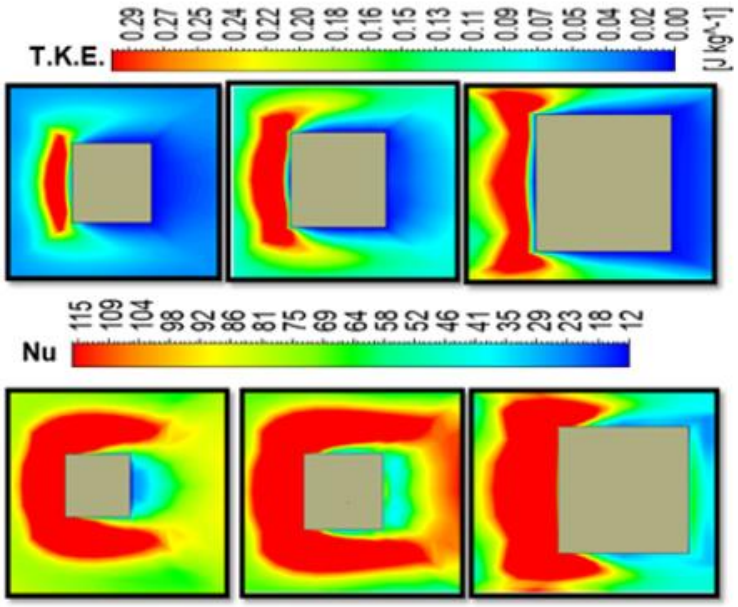

Figure 4-27: Contours of turbulence kinetic energy (T.K.E.) and local Nu distributions for (a) e=0.25 mm, (b) e=0.75mm and (c) e=1.5mm, Re=20,000, H/D=6 and α = 90º.

4.2.4 Comparison of Results

The percentage increases in simulated $\overline{N_u}$ might be modest, but it has the potential to significantly improve heat transfer by simple surface modification. An increase in $\overline{N_u}$ is achieved by overcoming a reduction in flow velocity by increasing flow turbulence.

Figure 4-28 compares $\overline{N_u}$ for three different roughness elements, continuous rib, cubical pin-fin and spherical pin-fin. In general, the cubical roughness element showed a more stable percentage increase compared to the other roughness geometries. All roughness types showed close maximum percentage increases and these occurred for the lowest pin heights of 0.25 and 0.50 mm. However, the cubical pin-fin showed a better heat transfer rate for all heights. This due to the fact that by employing cubical pin-fins, this balances the increase in the total surface area and the pressure loss penalty comparing to em-

ploying spherical pin-fins and rib where both either lack of total surface area increase or pressure loss penalty. The bigger total surface area, The less the pressure drop the higher heat transfer coefficient.[138].

At e=1.5 mm, the rib surface configuration showed an average Nu lower than the base case (i.e. smooth plane) due to the fact that at this height, flow recirculation occurs at the top edge of the rib preventing the flow re-attachment with the heated surface [see Figure 4-26 (c)].

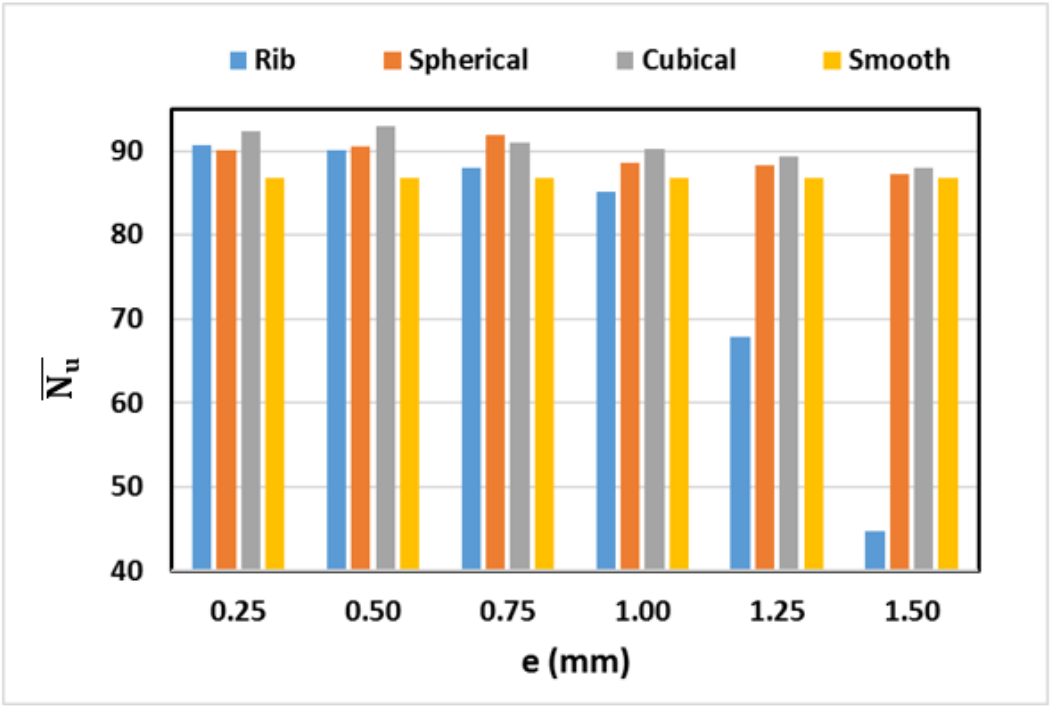

Figure 4-28 : Comparison of average Nu of three different roughness elements, Re=20,000, H/D=6 and α = 90º.

A close look at Figure 4-28 shows that both the spherical and the cubical pin-fin roughness elements gave an overall higher heat transfer rate than the square cross-section rib. Table 4-4 shows the percentage increase in $\overline{N_u}$ for the three types of roughness elements for all six different heights at jet nozzle Re=20,000, H/D = 6, R/D = 1.5 and α=90º. A close look to the table shows that, the increase percentage of the average heat transfer varies up to 7.2% for e= 0.5 mm by using cubical pin-fin. Both spherical and ribbed roughness elements showed an increase percentage in average Nu between 0.6% to 6% by selecting

the right roughness element height. The latter observation agreed well with results reported by the experimental work of [90] and [91] as both reported an enhancement of about 6% could be achieved by employing one array of spherical protrusions. For the case of rib-roughened, this percentage starts to decline for higher e. especially for e=1.5mm where the average Nu was lower than the baseline case of about -47%

Table 4-4 : Average Nu for different roughness elements, $\alpha = 90^{o}$, Re=20,000 and H/D=6

No.	Rib height (mm)	Rib		Spherical pin-fin		Cubical pin-fin	
		$\overline{N_u}$	% increase	$\overline{N_u}$	% increase	$\overline{N_u}$	% increase
1	0.25	90.7	4.5%	90.1	3.8%	92.3	6.4%
2	0.5	90.1	3.8%	90.6	4.4%	93	7.2%
3	0.75	88	1.4%	91.9	6%	91	4.9%
4	1	85	-2%	88.6	2.1%	90.3	4.1%
5	1.25	68	-22%	88.2	1.7%	89.3	2.9%
6	1.5	45	-47%	87.3	0.6%	88	1.4%

Impingement cooling on roughened plates has been the focus of recent research since the heat transfer could be improved by roughened elements. Three popular easy to manufacture roughening element geometries have been chosen in this study based on the literature review and due to their impact on heat transfer rate in jet impingement applications, continues rib, square pin fin and spherical pin-fin. This variation of roughness element geometries chosen in this study should give a clear idea of the protrusion impact on the flow physics and heat transfer rate.

Even though roughening the plates can improve the heat transfer rate mostly due to both enlarging the surface area and increasing flow turbulence, the protrusions can also change the flow characteristics causing bigger pressure loss and then decreases heat transfer rate [139] [97] . In addition, despite the increase in the object weight due to enlarging surface area, thermal stresses could be an issue when employing roughness elements especially those with sharp edges.

Temperature at sharp edges remains high due to the heat diffusion which was blocked at such small area allied with this region [140] [141], this could lead to a thermal failure (creep) of the roughness element which can be reduced by manufacturing roughness elements with round edges.

4.3 Inclined jet impingement

The distribution of local Nu over the smooth flat plate (the baseline case) is shown in Figure 4-29 below

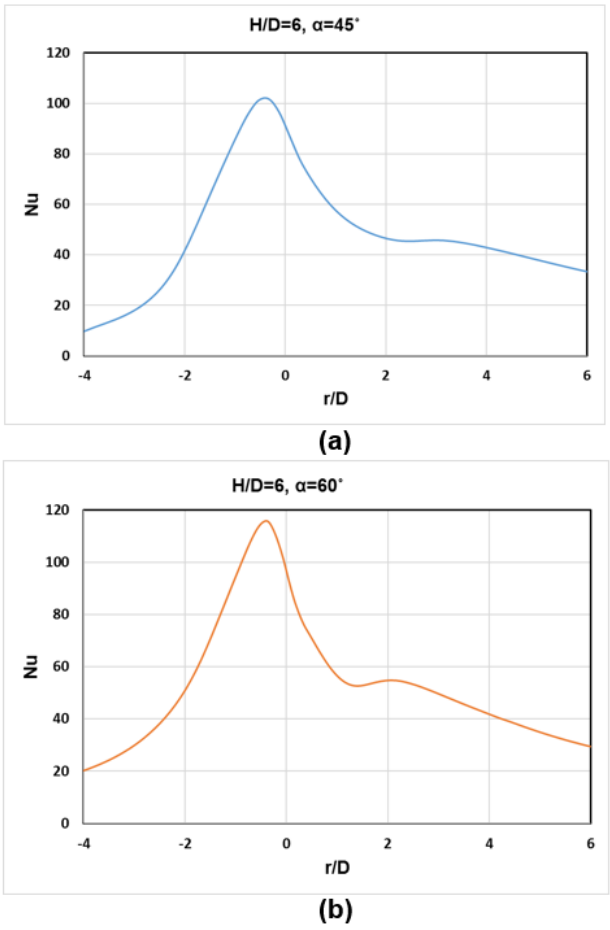

Figure 4-29: Distributions of local Nu for Re=20,000, H/D=6, (a) α=45º and (b) α=60º

Over the past decades, there has been significant research into the steady and unsteady convective heat transfer from smooth and roughened surfaces, most of these studies were for jets ejected from a nozzle that was perpendicular to the heated surface. However, few studies [142], [143] and [144] have studied the effect of roughness elements on the heat transfer rate under the influence of inclined jets. This section will help cover this gap in the literature. Figure 4-30 shows geometry of the inclined jet with the three different types of roughness elements described in section 4.1.

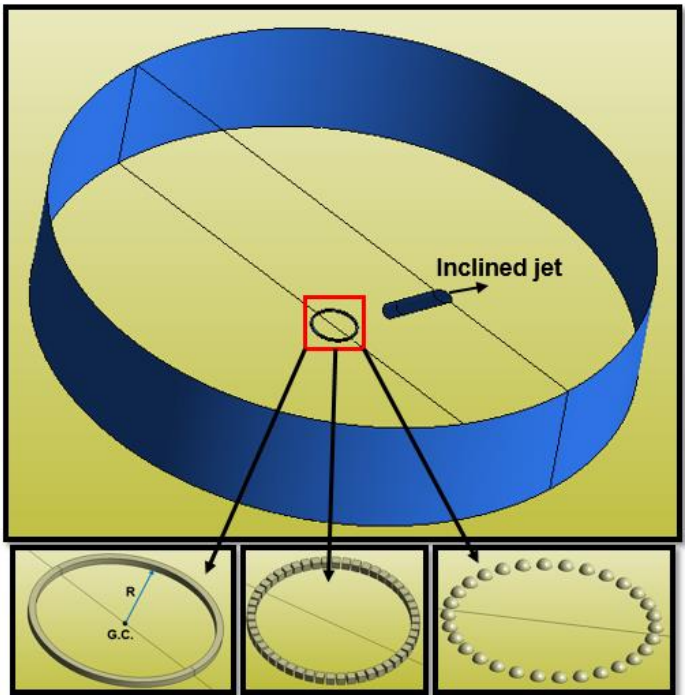

Figure 4-30 : Roughness elements geometries for inclined jet Re, 20,000, H/D=6, α = 60º and α = 45º., a) Rib, b) Spherical pin-fin and c) Square pin-fin

4.3.1 Roughness element – continues rib

Figure 4-31 shows the effect of adding a circular rib of square cross-section, centred on the jet axis and of radius R = 1.5D, for α= 45º and 60º. As previously, the rib was tested with six heights, e = 0.25 to 1.5 mm in steps of 0.25 mm. The inclined jet shows an expected lack of symmetry which makes the distributions of local Nu uneven. For the sake of comparison, a line was taken on the geometric centre line for -4≤r/D≤4. Note that the area under this line does not represent the

average Nu. The figure clearly shows that for α= 45º and 60º the cases where rib height is between 0.25 mm and 0.75 mm, there is a significantly higher local Nu than the baseline case (smooth case) in the downstream, or downhill, direction. However, close inspection of the data also shows that the stagnation Nu is lowered compared to the baseline case. The increase in local Nu values in the radial direction (0 ≤ r/D ≤ ~1.5) are between 3-15% compared to the smooth case with maximum increase percentage where e=0.25mm. Downstream r/D=1.5, where the rib is located, its effect represented by a peak in local Nu, again the maximum peak at the lowest height. At r/D≥3, both curves of e=0.75mm start to fall down underneath the baseline curve giving lower Nu values.

When the jet meets the rib, it separates from the wall forming a low pressure region where flow recirculation occurs. The length of this separation depends on several parameters but mostly on rib height [145]. As rib height increases above 1mm, the local Nu starts to fall below the value for the unobstructed wall due to the long distance the flow travels, which lowers its velocity and turbulence levels, before it re-attaches with the wall. This observation was also reported in the experiments made by [146] and [147].

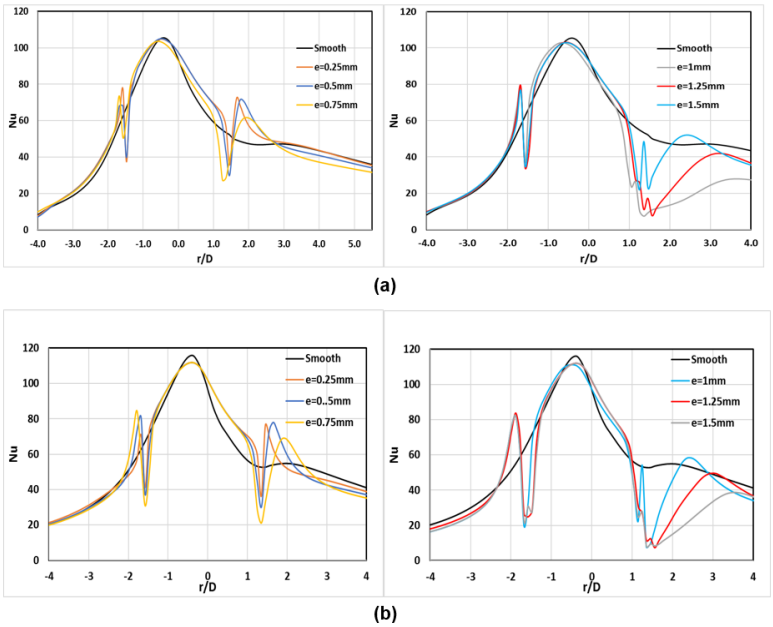

Figure 4-31 : Effect of rib height on local Nusselt number for Re= 20,000 and H/D=6 and (a) α = 45º and (b)= α = 60º

Figure 4-32 shows top view of local Nu contours for all six rib heights at angles of impingement of 45º and 60º for various radial distances. When the flow hit the heated surface most of the streamlines flow downhill exchanging momentum with the wall. Generally, an enhancement of local Nu occurs behind the rib in both directions (downhill and uphill) due to the obstruction caused by the rib as shown in the figure. This obstruction can cause cavities to form behind the rib where the impinging jet penetrates into the cavity and recirculates inside causing high levels of heat transfer. Due to jet inclination, the shape of the vortices formed behind the rib is not uniform around the circular rib and their size depends on the roughness element height (see Figure 4-33). However, the heat transfer enhancement due to these vortices is limited to e≤0.75mm. Above this height, local Nu values start to fall down below the baseline local Nu values.

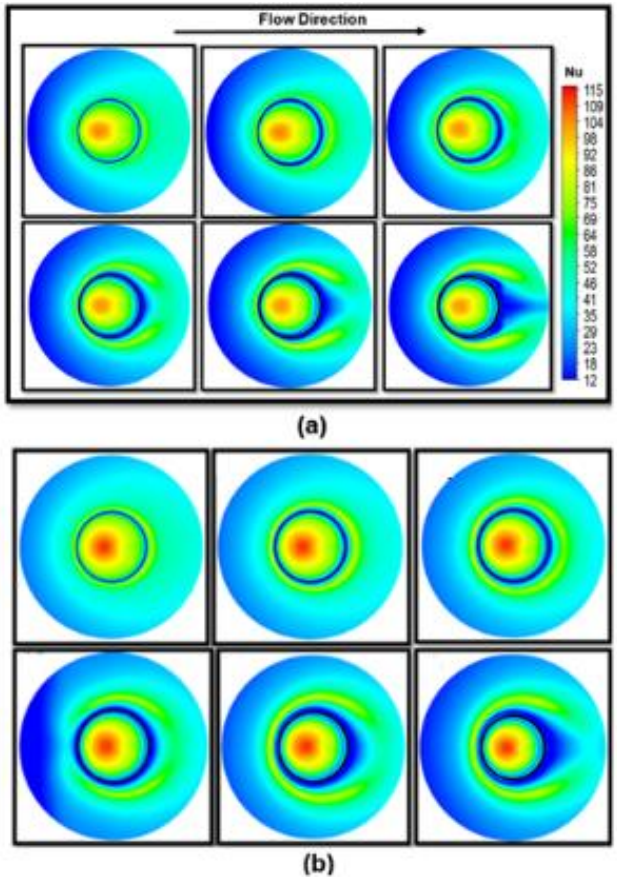

Figure 4-32 : Nu contours for all rib heights for (a) α=45º and (b) α=60º, Re=20,000 and H/D=6

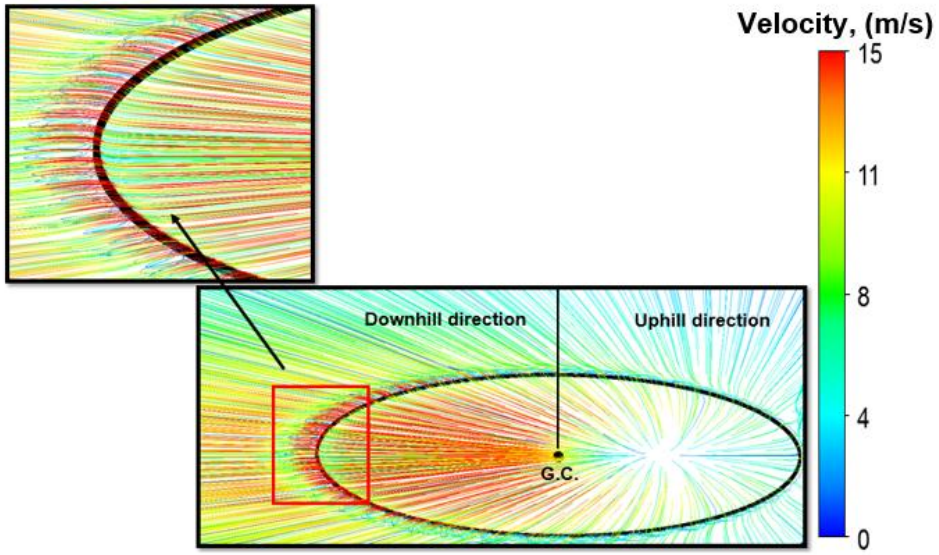

Figure 4-33: Velocity streamlines for e=0.25mm, α=45º Re= 20,000 and H/D=6

Comparing the values of average Nu in Figure 4-34 we see that, in general, $\overline{N_u}$ Increases as the angle made between the jet and the impingement surface increases. This is because, as the jet angle decreases so the flow rate in the downhill direction increases, assisting in the development of a boundary layer in the direction where majority of the flow goes. The heat transfer in the uphill direction will reduce to close to zero after a short distance, due to the decreasing flow in this direction as the jet angle decreases. This will reduce the overall $\overline{N_u}$ calculated in both directions. The plot of $\overline{N_u}$ in Figure 4-34 indicates that, for both angles, the maximum value of $\overline{N_u}$ again occurs at e=0.25 mm. The enhancement in $\overline{N_u}$ in percentage terms gradually decreases as the rib height increases. The maximum percentages increase for the circular rib of square cross-section, both for e=0.25 mm, were 4.8% and 3.8% for α=45º and α=60º respectively. For e=0.5mm and 0.75mm, this enhancement starts to diminish to 4.3% and 2.9% for the lower angel, and to 2.9% and 1.7% for α=60º.

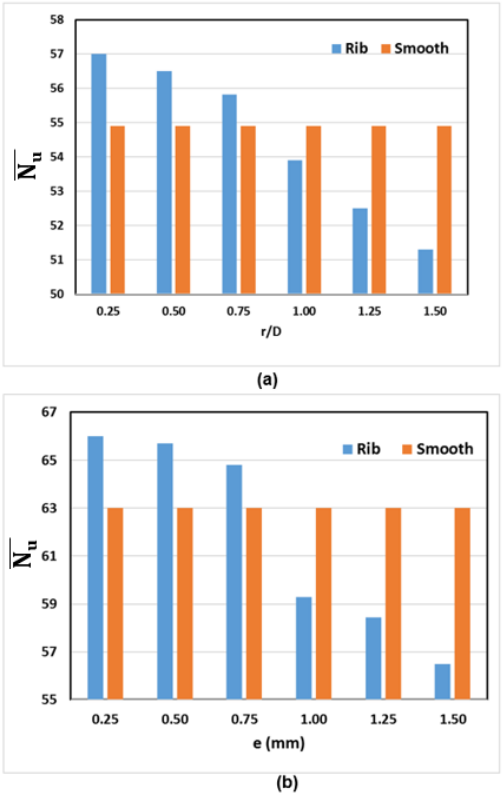

Figure 4-34: Effect of square rib height on average Nusselt number for H/D=6, Re=20,000 over -4≤r/D≤4, (a) α=45º, (b) α=60º

4.3.2 Roughness element – spherical pin-fins

As explained above, depending on the shape of the roughness element, the separation distance and pressure loss would vary giving different average heat transfer rates.

Generally, spherical pin-fins roughened surface seem to improve heat transfer rate regardless of the height. This is due to the relative low pressure loss penalty of this type of roughness elements when compared to the cubical pin-fins [148],[133]. Figure 4-35 below compares the pressure distributions of cubical and spherical roughness element. It is shown in the figure that the spherical pin-fin has lower pressure loss of about 18% before and after the protrusion when compared to the cubical pin-fin.

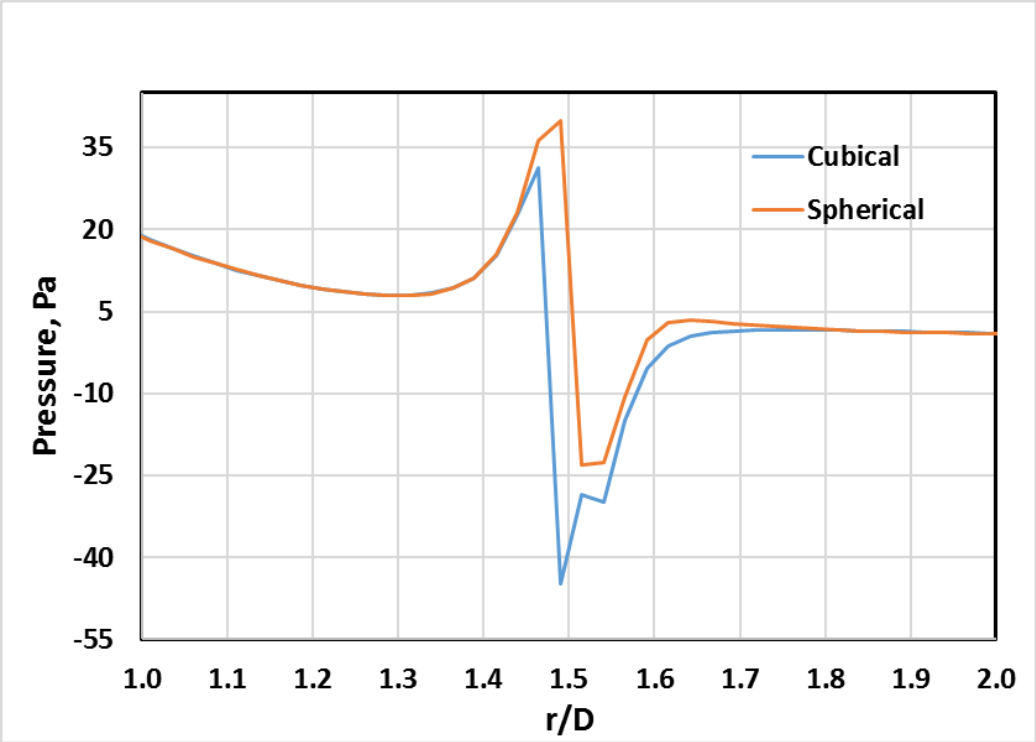

Figure 4-35: Pressure distribution of spherical and cubical pin-fins at e=0.5mm. Re= 20,000 and H/D=6, α=45º

Figure 4-36 demonstrates this using local Nu contours for spherical pin-fins with six heights. It can be seen that for all heights, there is an enhancement of heat transfer rate, this enhancement depends on both roughness element's height and number and it is most clearly shown for heights of 1.25 mm and 1.5 mm.

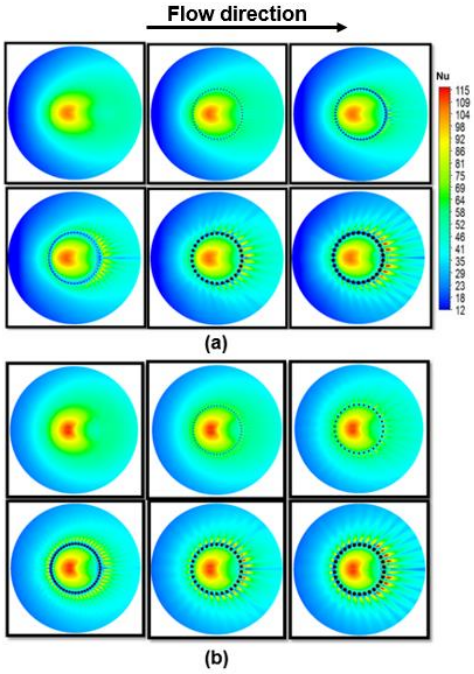

Figure 4-36 :Top view of Nu contours for all hemispherical heights for (a) α=45º and (b) α=60º, Re, 20,000 and H/D=6

Figure **4-37** shows this average for two angles of impingement (α=45º and 60º) for the six heights of the spherical pin-fins. The figure shows, the average Nu increase percentages show a no-uniform pattern as the height changes due to the fact that the number of roughness elements for the two case of e=0.25mm and 1mm is 50 where for the rest of heights it is 30. Varying the number of roughness elements will also expand the knowledge the impact of this variation to heat transfer rate in addition to the impact of changing height. In analysing Figure 4-37, the improvement is maximum for the height of 1.5mm where increase percentages of 5.7% and 6.4 are achieved for α=45º and 60º respectively. However, lower heights show also a considerable enhancement in the average Nu especially at e=0.25mm and 1mm where more roughness elements were employed (see Table 4-2). The enhancement percentages are between 1%, and 4.4% for the rest of heights at α=45º and between where it is between 2.5% and 5% for the bigger angle.

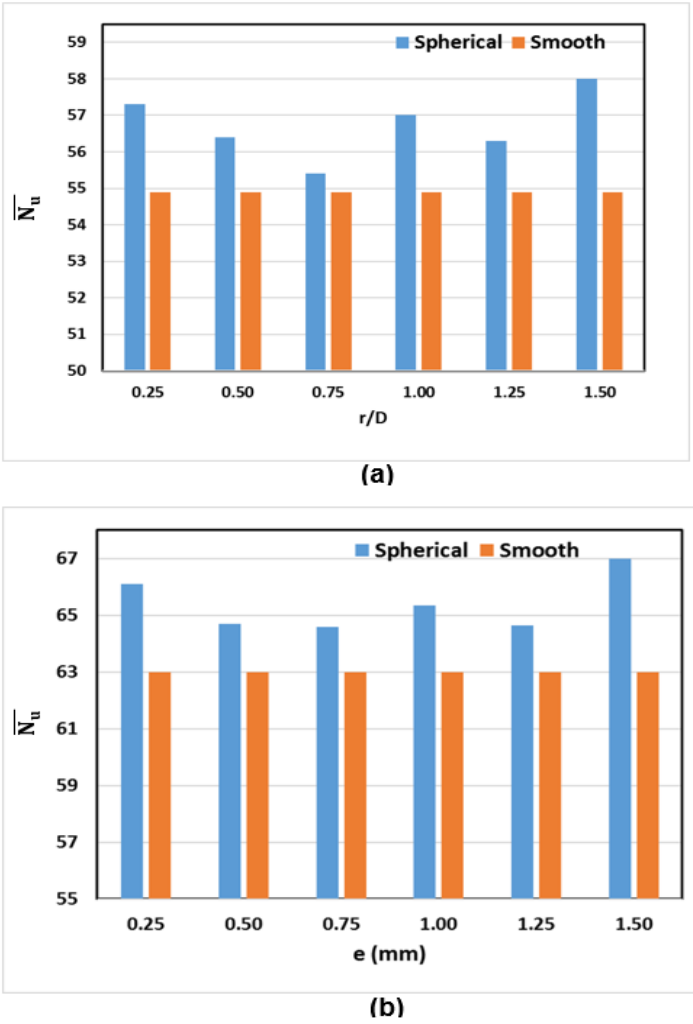

Figure 4-37 : Effect of spherical pin-fin height on average Nusselt number for H/D=6, Re=20,000 over -4≤r/D≤4, (a) α=45º, (b) α=60º

4.3.3 Roughness element – cubical pin–fin

Figure 4-38 shows the effect of using a cubical pin-fin roughness element with different height on $\overline{N_u}$ for angles of inclination α=45º and 60º. Again, the optimum rib height which gives the maximum average heat transfer for this type on configuration is e=0.25mm. A percentage increase of about 4% and for both angles. As the rib height increased, the value of $\overline{N_u}$decreased for both impingement angles, although the rate of decrease was less for the larger angle. Roughness elements between 0.75mm and 1.5mm seems to fail improving the heat transfer

rate with maximum decrease percentage of -12% and -20% for α=45º and 60º respectively. In general, regardless of the jet inclination, both angles seem to give same behaviour, the only roughness element that enhances the heat transfer is e=0.25mm.

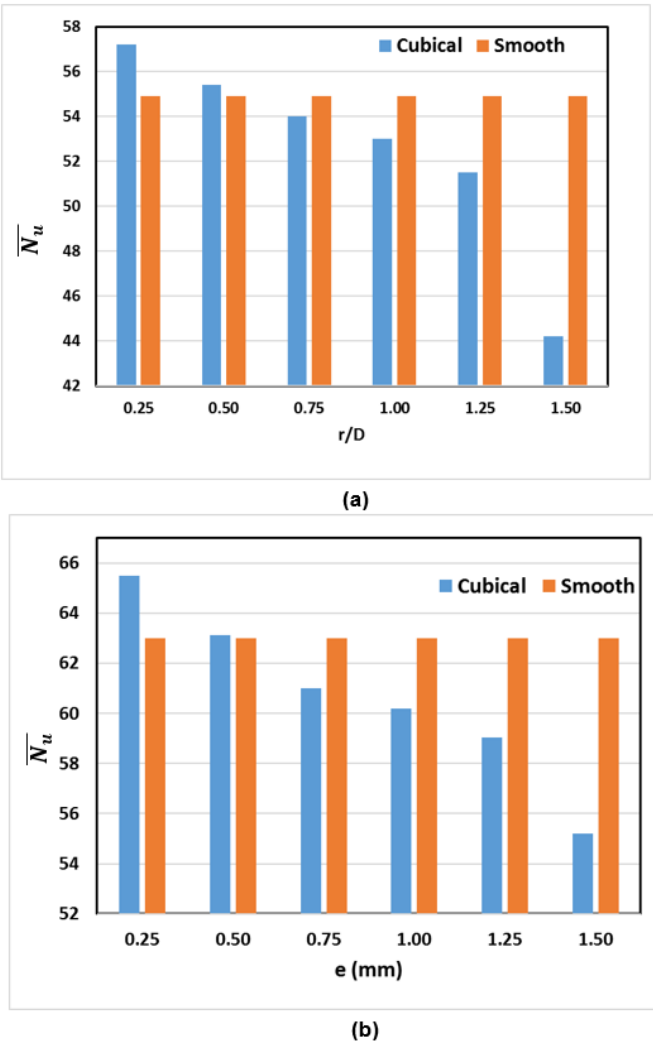

Figure 4-38: Effect of square pin-fin heights on average Nusselt number for H/D=6, Re=20,000 over -4≤r/D≤4, (a) α=45º, (b) α=60º

Figure 4-39 shows, local Nu contours for three heights. shows that starting from e=0.75 mm, the height of the roughness element starts to have a noticeable impact on local Nu in the downhill direction. This impact is shown in the figure in the form of the zigzag lines which come clearer as the height increases. However,

an obvious drop-off of local Nu is shown in the case of α=45º and e=1.5 mm which also explains the result discussed above.

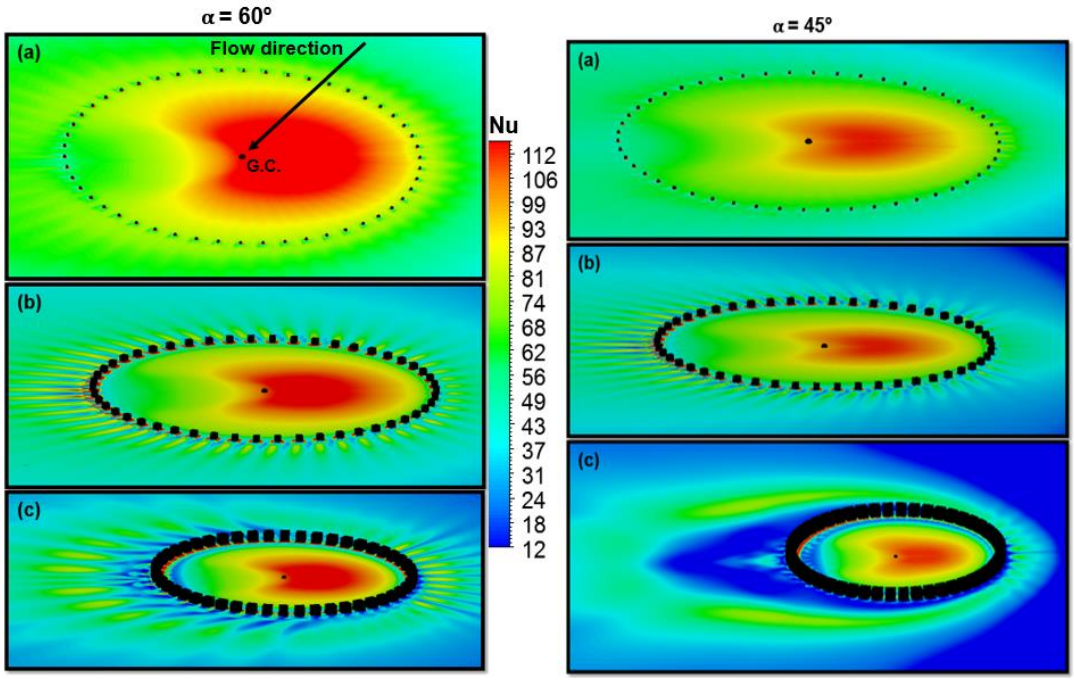

Figure 4-39: Nu contours for square pin-fin α=60º and α=45º, Re=20,000 and H/D=6, (a) e=0.25mm, (b) e=0.75mm and (c) e=1.5mm

4.3.4 Comparison of results

Figure 4-40 presents the $\overline{N_u}$ for the three types roughness element, six heights and two inclined angles. Overall, spherical pin-fins show higher $\overline{N_u}$ values compared to the other roughness elements. The maximum percentages increase was by employing a spherical pin-fin with heights of e=0.25mm and 1.5mm for both inclined angles of impingement. Overall, both angles of inclination showed same pattern for the three types of roughness element.

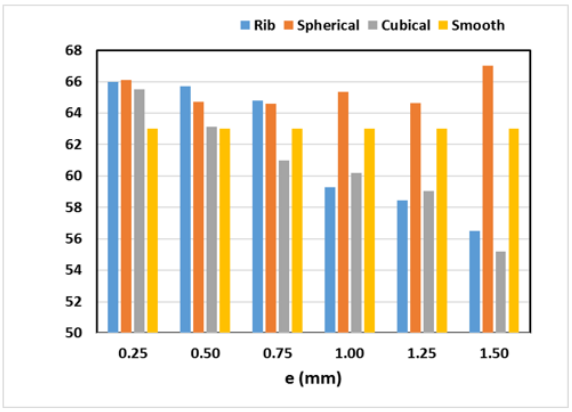

(a)

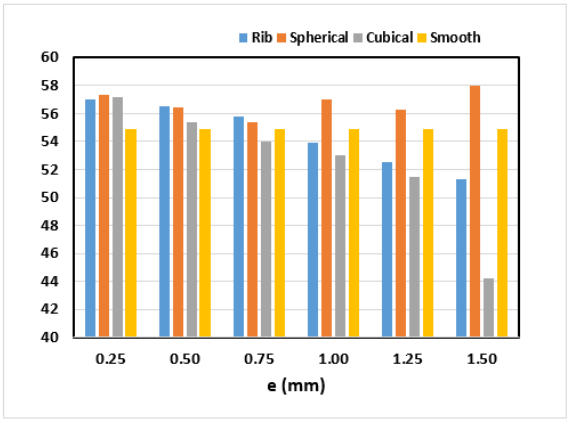

(b)

Figure 4-40: Comparison of average Nu of three different roughness elements and six heights (e), H/D=6, Re=20,000, for (a) α= 60º and (b) α= 45º

Three parameters govern the heat transfer rate over a rib roughened surface, the quality of flow mixing behind the rib, the pressure drop and increase in surface area. The convex hemispheres seem to have the lowest pressure drop of the roughness elements tested. This may be because of the additional flow mixing that occurs behind it between the deflected flow and the flow between the protrusions. However, regardless of the higher pressure drop of the square pin-fin compared to spherical pin-fin, it has a larger overall surface area which helps overcome the loss in heat transfer rate due to this drop. The continues rib however provides the largest surface area compared to the other two roughness elements, but the lack of deflected flow and the high pressure drop, resulting lower heat transfer rate than the spherical pin-fins for e≥1mm.

The mixing that occurs before and behind the three different roughness elements is demonstrated by their velocity vectors, see Figure 4-41. A close look to this figure, shows that the flow smoothly passes over the hemisphere before re-attaching with the plane wall, resulting in the smallest low-pressure region and pressure drop. However, both rib and pin-fin roughness elements have a higher pressure drop penalty, though the less deflected flow for the rib element makes it the lowest heat transfer enhancer. The shape of the vortices behind the rib is controlled by flow mixing quality and it is these vortices that are responsible for higher local heat transfer rate.

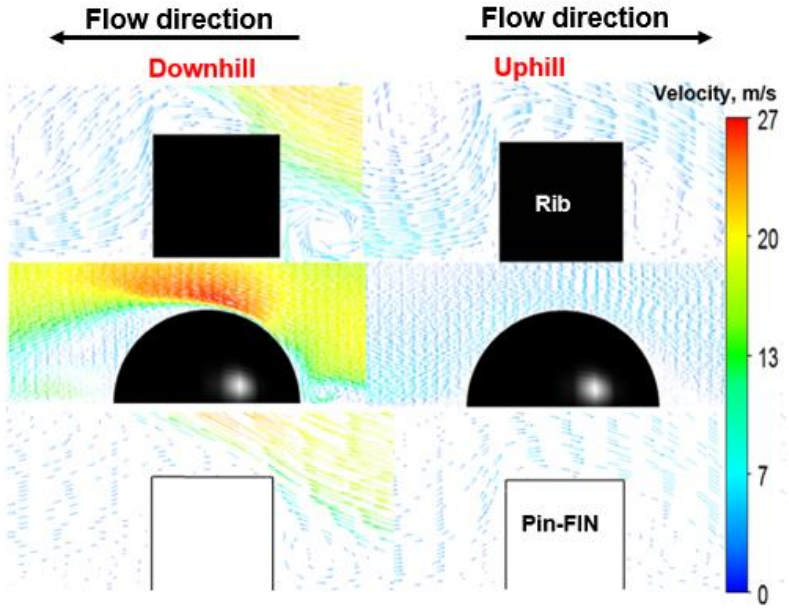

Figure 4-41: Velocity vectors in both downhill and uphill direction for the three roughness geometries for e=1.5 mm, α=45º.

Table 4-5 summarises the results obtained from this section. Generally, the average Nu seems to be very sensitive to the variation of both roughness heights and their number. The table shows the simulated $\overline{N_u}$ for the three roughened surfaces, six heights and two angles of inclination of the jet used in this chapter. The average Nu for baseline cases over the same averaged area are 54.9 and 63 for α=45º and α=60º respectively. It can be seen that, for α = 45º and 60º, the optimum height is e= 1.5mm where the percentages increase in $\overline{N_u}$ could

reach between 5.7 and 6.4%, by employing a spherical pin-fin roughness element. However, roughness elements with certain heights and shapes could give lower heat transfer rate when compared to the baseline case.

Table 4-5 Average Nu for different roughness elements, (a) α = 45º, (b) α = 60º Re=20,000 and H/D=6

No.	Height (mm)	Rib		Spherical pin-fin		Cubical pin-fin	
		$\overline{N_u}$	% Increase	$\overline{N_u}$	% Increase	$\overline{N_u}$	% Increase
1	0.25	57	3.8%	57.3	4.4%	57.2	4.2%
2	0.5	56.5	2.9%	56.4	2.7%	55.4	1%
3	0.75	55.8	1.7%	55.4	1%	54	-1.64%
4	1	54	-1.8%	57	3.8%	53	-3.5%
5	1.25	53	-4.4%	56.3	2.6%	51.5	-6%
6	1.5	51.3	-6.5%	58	5.7%	44.2	-19.5%

(a)

No.	Height (mm)	Rib		Spherical pin-fin		Cubical pin-fin	
		$\overline{N_u}$	% Increase	$\overline{N_u}$	% Increase	$\overline{N_u}$	% Increase
1	0.25	66	4.8%	66.1	5%	65.5	4%
2	0.5	65.7	4.3%	64.7	2.7%	63.1	0.2%
3	0.75	64.8	2.9%	64.6	2.5%	61	-3.8%
4	1	59.3	-5.9%	65.4	3.7%	60.2	-4.5%
5	1.25	58.4	-7.3%	64.6	2.6%	59	-6.3%
6	1.5	56.5	-10.3%	67	6.4%	55.2	-12%

(b)

4.4 Closing remarks

This chapter reports the results of using simulation to investigate the effects on the average predicted Nu, of three differently shaped roughening elements (a continuous circular rib of square cross-section normal to the flow, cubical pin-fins and spherical pin-fins) imposed on a flat, horizontal plane (the wall) subject to flow of hot fluid from a nozzle of diameter 13.5mm. All roughness elements were located at the same radial distance measured from the geometric centre, R/D=1.5 on a plane located H/D=6.

The optimum height of the roughening ribs was investigated using six rib heights; 0.25 mm to 1.50 mm in increments of 0.25 mm, for each of three impingement angles; α= 45º, 60º and 90º.

For α=90º impingement configuration, maximum enhancement of $\overline{\boldsymbol{N_u}}$ was obtained by the use of cubical pin-fin roughness element. For e=0.5 mm cubical pin-fin percentage increase of about 7.2% compared to the baseline case. However, for a rib-roughened wall of side 1.5 mm there was a dramatic decrease in $\overline{\boldsymbol{N_u}}$ of 47%. At e=0.25 mm rib roughness elements gave a close increase in $\overline{\boldsymbol{N_u}}$ where cubical and spherical pin-fins gives the maximum heat transfer rate at e=0.5mm and 0.75mm respectively.

For both α=45º and 60º configurations the optimum rib height was varying depending on the roughness type. While significant improvement was found for all the roughening elements the best performing, adding about 5% and 4.4% to the $\overline{\boldsymbol{N_u}}$ compared to the baseline case, was the spherical pin-fin for 45º and 60º respectively. This was closely followed by the cubical pin-fin and rib roughened surface (4%).

The next two chapters will further investigate enhancing heat transfer for inclined jet flows for impingement angles 45º and 60º, with H/D=6 and Re=20,000 for four different radial locations; r/D = 1.0, 1.5, 2.0 and 3.0. The rib heights will again range from 0.25 to 1.5 mm in incremental steps of 0.25 mm, but various non-uniform shapes will be introduced.

5 Average Nu obtained using a uniform roughness element

5.1 Introduction

The jet flow impinging orthogonally on a flat, smooth horizontal plate starts to accelerate in the radial direction after it hits the plate. Thus, its velocity initially increases in the downstream direction but soon starts to fall off with further increase in radial distance. Placing a roughening element at a downstream location could enhance heat transfer but placing it an appropriate radial location could maximise this enhancement. The suitable choice of roughness element location and height depends on both local flow velocity and turbulence intensity.

Rough surfaces are often used with jet impinging cooling because surface roughness can increase the heat transfer rate in the stagnation region by piercing the thermal sublayer [44]. It is well known that a significantly high local heat transfer coefficient is reached over the stagnation region of jet impingement, but the local heat transfer coefficient shows a rapid degradation with radial distance downstream. One possible remedial action is the use of multiple jet impingements, but this requires a greater mass flow rate. However, the use of turbulators such as ribs attached to the plane to enhance the overall heat transfer rate is a less expensive alternative technique.

In this chapter, the effect of using a roughness element in the shape of a circle with square cross section, and with the same centre as the jet (see Figure 5-1) on the average Nu will be investigated. The effectiveness of the roughness element will be tested for four different radii (R) and six heights (e).

The chapter is divided into two main sections: normal jet impingement (α=90º) and Inclined jet impingement (α=45º and α=60º). The jet Reynolds Number was 20,000 in each case. Each section will include the testing of rib location and rib height on the average Nu ($\overline{N_u}$). The rib will be tested for four different

locations, R= 1D, 1.5D, 2D and 3D, where D is the jet hydraulic diameter, and for each location it will be tested for six different rib heights (e) between 0.25 mm and 1.5 mm in increments of 0.25 mm to ascertain the optimum height for each location. This range of rib locations should extend from within to outside the stagnation region. Figure 5-1 shows the geometry of the uniform circular rib. The total number of simulated cases is 48, (4 x 6 x 2).

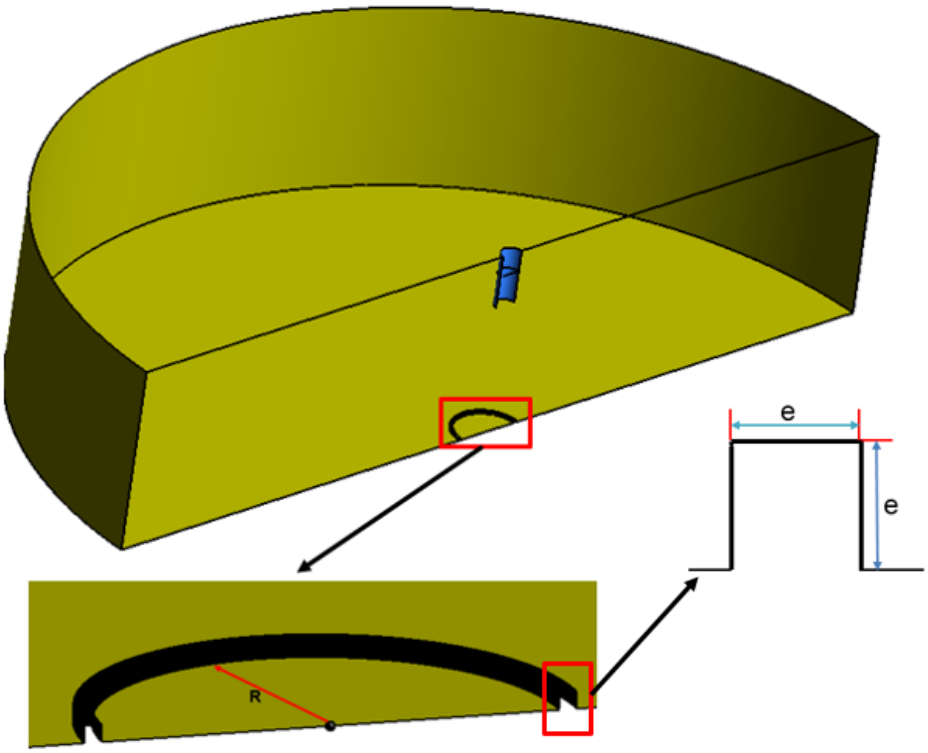

Figure 5-1 :Geometry of Uniform (circular) rib with square cross-section

5.2 Normal jet impingement

5.2.1 Rib location – R=1D

Placing the rib at a radial distance R = 1D, places it within the stagnation region [27]. As mentioned above, the rib height (e) will be varied to find the optimum rib geometry that gives maximum average Nu. The Nu was averaged over

the surface area from 0≤r/D≤4, where r is the distance downstream from jet centreline and D is the hydraulic diameter of the jet. We can start at r/D=0 due to the symmetrical nature of the flow. The range r/D ≤ 4 where the major amount of heat transfer occurs in this region as shown in Figure 5-2 so it is this region that is important in determining ($\overline{N_u}$).

Figure 5-2 shows the effect of rib height on the local distribution of Nu for a circular jet impinging normally on a flat plate. As shown in the figure, the local value of Nu directly behind the rib is increased because of rib induced flow separation and reattachment. In very simple terms, it disturbs the stagnation layer which acts to insulate the surface. Depending on geometry and circumstances, the ribs may also increase heat transfer by increasing the effective area of the surface [14]. The figure also shows that, for rib heights of 0.25, 0.50 and 0.75 mm, an enhancement of heat transfer rate can be achieved. However, the increase in the drag resulting from the presence of the ribs causes the impinging jet to decelerate and disperse more rapidly, such that the value of Nu decreased far from the stagnation point as shown in the figure for e≥1 mm.

Also for e≥1 mm, all the rib heights caused a subsiduary peak in the local Nu immediately in front of the rib due the flow recirculation that occurs before the protrusion. For the peak in Nu behind the rib, the higher the rib, the more flow recirculation, the higher the peak in Nu.

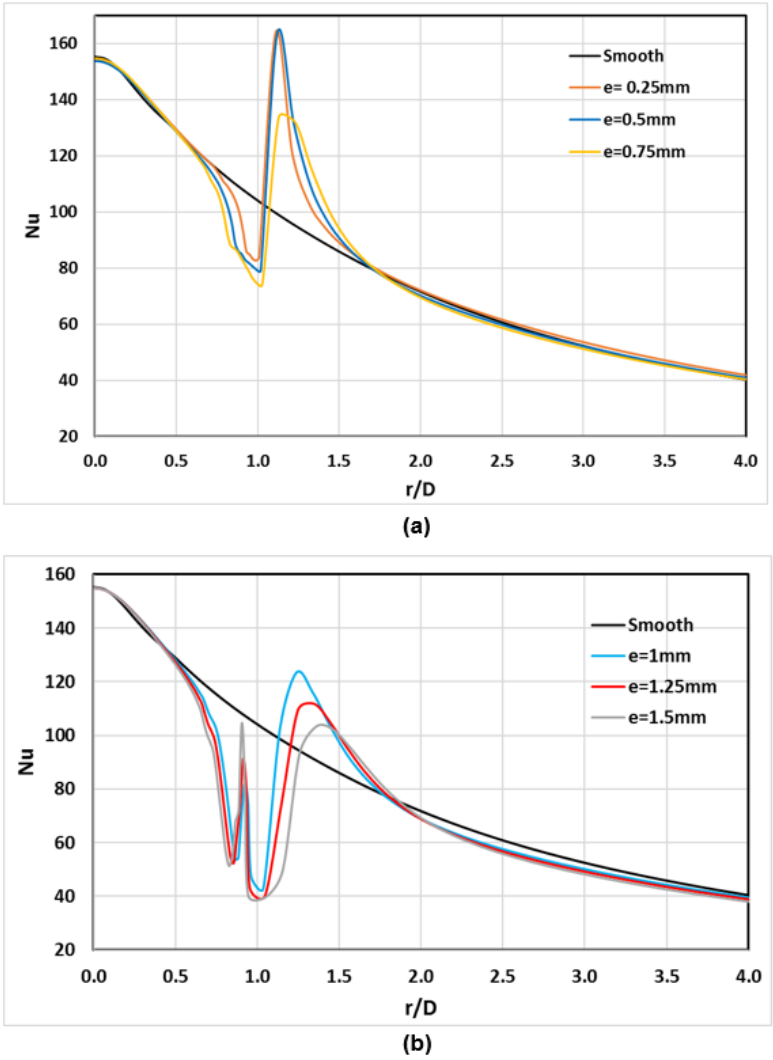

Figure 5-2 : Local Nu distributions for six rib heights, e, Re, 20,000, H/D=6, R/D=1 and α = 90º.

Gau, et., al., [131] have reported on this phenomenon for a slot (2-D) air jet impinging on a flat rectangular surface with straight ribs of different heights attached perpendicular to the flow. They explained that the shear layer, while separated from the surface, experiences turbulence effects which enhance momentum and mass (heat) transfer so that its re-attachment to the surface behind the rib results in an increase in heat transfer. Subsequent to this impingement, the turbulent free shear layer reattaches itself to the surface and a new boundary layer develops. Thus, placing ribs normal to the flow of the wall jet is an effective

means for disrupting the rather rapid decrease in convective heat transferred to/from the wall and enhancing total heat transfer rate to/from the wall.

Thus, it is well known that the addition of ribs to a surface will disturb the flow of the impinging jet over that surface and increase turbulence. The rib protrudes from the surface and the fluid flow over the rib generates a low-pressure area immediately behind it. The separated flow generated by the rib is pushed into this region by the higher pressure above it and it re-attaches to the surface.

Figure 5-3 indicates that a flow separation happens in front of the rib resulting a small separation region followed by a larger after-rib recirculation vortex. The figure indicates that as the rib height increases so does the distance over which the heat transfer is enhanced (the re-attachment length, r_2), where Nu is increased. This confirms the above analysis and the work of other researchers such as [130]. It is suggested that, as shown in Figure 6-3, as rib height increases so the low-pressure region length (r_2) behind the rib becomes larger (also in the front of the rib r_1), and the forces pushing the separated flow toward the wall weaken. One factor contributing to this effect could well be that the distance from impingement surface to the separation point at the upper edge of the rib increases.

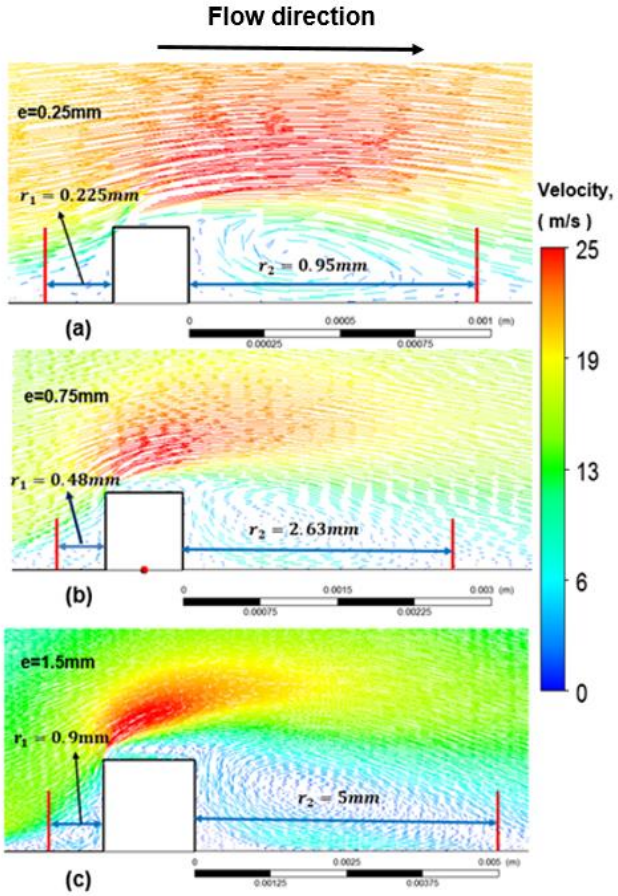

Figure 5-3 : Velocity vector contours for three selected rib heights, (a) e=0.25 mm, (b) e=0.75 mm and (c) e=1.5 mm, Re, 20,000, H/D=6 and α = 90º.

The contours local Nu distribution is shown in Figure 5-4, which indicates that at e=0.25 mm a noticeable enhancement in heat transfer occurs after the rib due to higher arrival flow velocity compared to the other two rib heights. The higher the rib, the lower the arrival velocity. The figure also shows for ribs of e≥0.75 mm, an enhancement of the local high heat transfer occurs just before the rib due to vortices in this area.

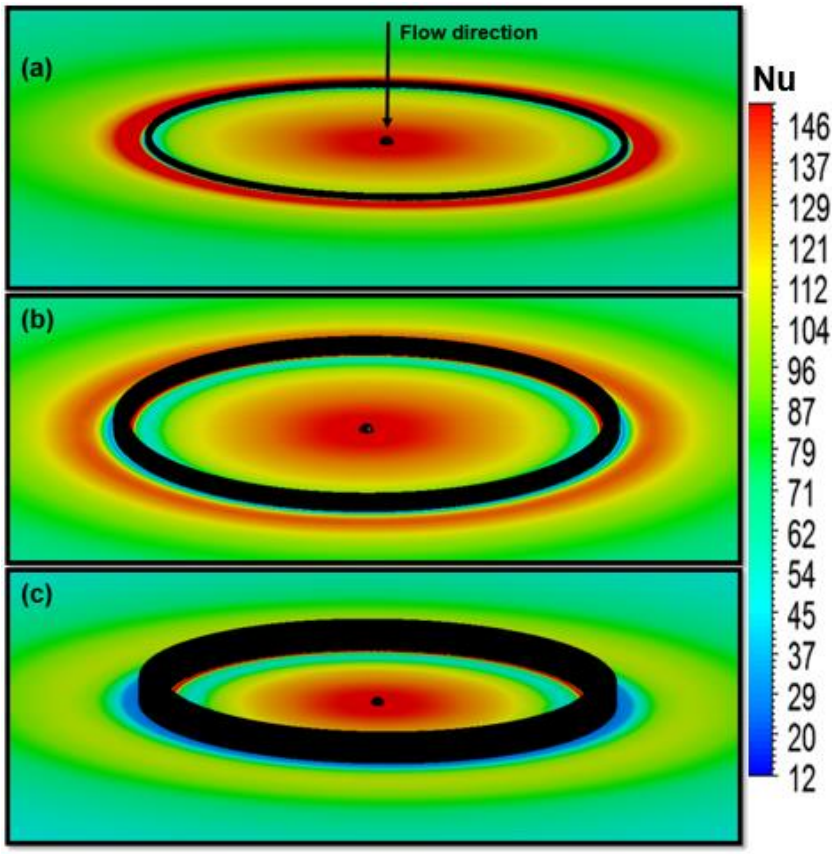

Figure 5-4: Local Nu contours for three heights, (a) 0.25mm, (b) 0.75mm and (c) 1.5mm

To show the effect of rib height on the average Nu of the heated surface, Figure 5-4 presents the average Nu ($\overline{N_u}$) normalized to the baseline value (smooth surface) $\overline{N_{u_o}}$. The average was obtained by numerically integrating the local Nu between 0 ≤ r/D ≤ 4, in a downstream direction. It should be noted, for completeness sake, that the local heat transfer is, in fact, slightly affected at distances further downstream than r/D ≥ 4 for rib heights 0.25≤e≤0.75 mm (see Figure 5-2).

The optimal rib height, of those tested, is e = 0.25 mm with an increase in relative ($\overline{N_u}$) of 3.5% compared to the case of a smooth surface. This increase reduces to 2.1% and 0.6% for e=0.5 mm and 0.75 mm respectively. However,

the average Nu value decreases to lower than the baseline case with further increase in rib height. At e=1.5 mm, a decrease of approximately -10.5% was observed compared to the baseline value.

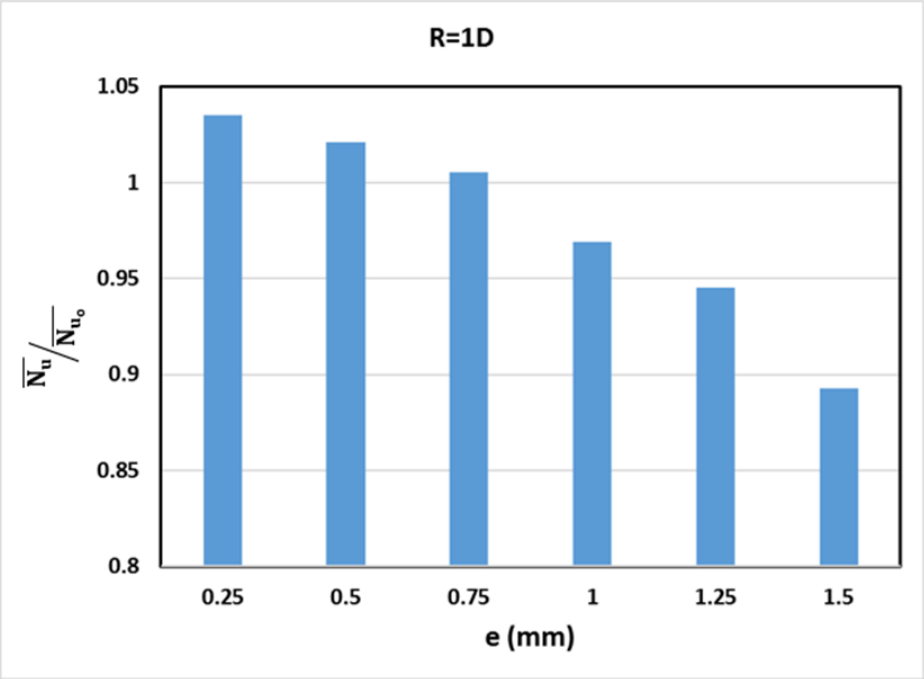

Figure 5-5: Effect of rib height on normalized Nu, R=1D, Re, 20,000, H/D=6 and α = 90º.

5.2.2 Rib location – R=1.5 D

It has been shown in Section 5.2.1 that an overall heat transfer enhancement could be achieved by employing a circular rib with radius 1.5D and height e=0.25 mm. The increase in Nu averaged over the total surface area between 0 ≤ r/D ≤ 4 was 4.5%. However, deploying a circular rib at this location with heights 1.00 ≤ e ≤1.50 mm leads to a lower value of $\overline{N_u}$ by -2%, -22%, and -47% for e=1.0, 1.25, and 1.50 mm, respectively.

Figure 5-6 below shows velocity vector contours for three selected rib heights of e=0.25, 0.75 and 1.50 mm. The rib height at this radial location effects the re-attachment length (r2). Increasing rib height by 0.50 mm, from 0.25 to 0.75 mm, increases r2 by almost four times. The longer r_2, the more flow recirculation,

the more turbulent kinetic energy and the better the heat transfer rate. However, for e=1.50 mm, two separate flow recirculation can be seen before flow re-attachment with the heated surface. In addition, the flow recirculation above the roughness element is such that it could prevent the incoming jet from re-attaching with the heated surface. Indeed, this is the case for e=1.50 mm. Also, at e=1.50 mm, it can be seen that a small recirculation region occurs on top of the rib lowering the main flow velocity and increasing the wake are behind the rib causing lower heat transfer.

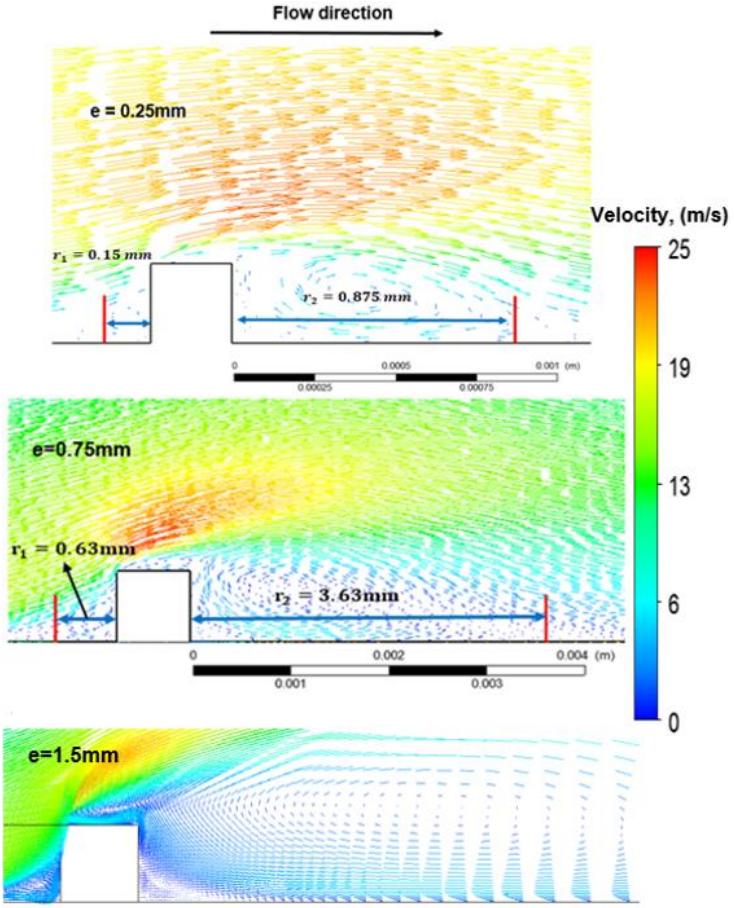

Figure 5-6: Velocity vectors contours for three selected rib heights, (a) e=0.25mm, (b) e=0.75mm and (c) e=1.5mm, Re, 20,000, H/D=6, R/D=1.5 and α = 90º.

The local Nu contours are shown in Figure 5-7 below. The heat transfer rate shows an obvious enhancement for e=0.25 mm and e=0.75 mm compared to the baseline case. This enhancement is more obvious at e=0.25 mm. However,

for e=1.50 mm, the flow fails to reattach with the heated surface causing lower heat transfer which is shown in the figure as a blue area. For e=1.50 mm, most of the heat transfer occurs only within the rib, beyond the rib the heat transfer is diminished due the lack of contact between the jet and the heated surface

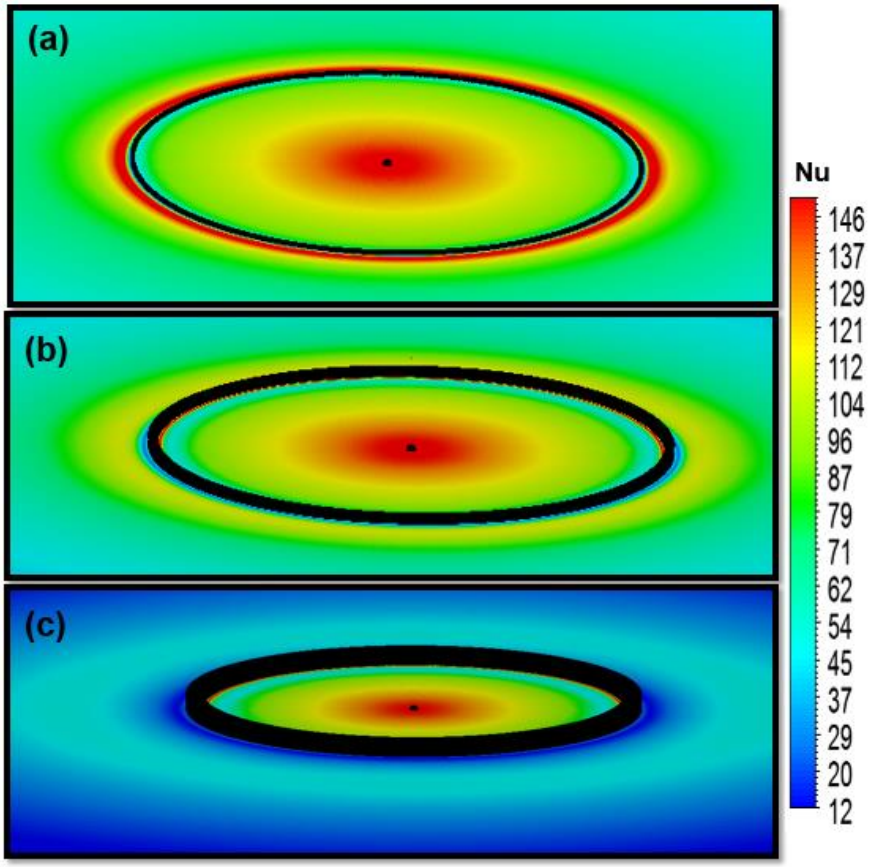

Figure 5-7: Local Nu contours, (a) e=0.25mm, (b) e=0.75mm, (c) e=1.5, Re, 20,000, H/D=6 and α = 90º.

Normalized average Nusselt number ($\overline{N_u}/\overline{N_{u_o}}$) obtained when the rib is at a radial distance R=1.5D is shown in Figure 5-8. It can be seen that when e=0.25 mm, maximum $\overline{N_u}$ is achieved. For e=0.25 mm and 0.50 mm there are increases of 6.0% and 5.3% respectively with respect to the baseline value. However, the increase gradually decreases as the rib height increases till it reaches 2.7% at e=0.75 mm. For e≥0.75 mm, the baseline smooth surface gives a better average

value for Nu. For e=1.0, 1.25, and 1.50 mm the respective values of average Nu are -0.5%, -20% and -42% below the baseline value for the smooth surface.

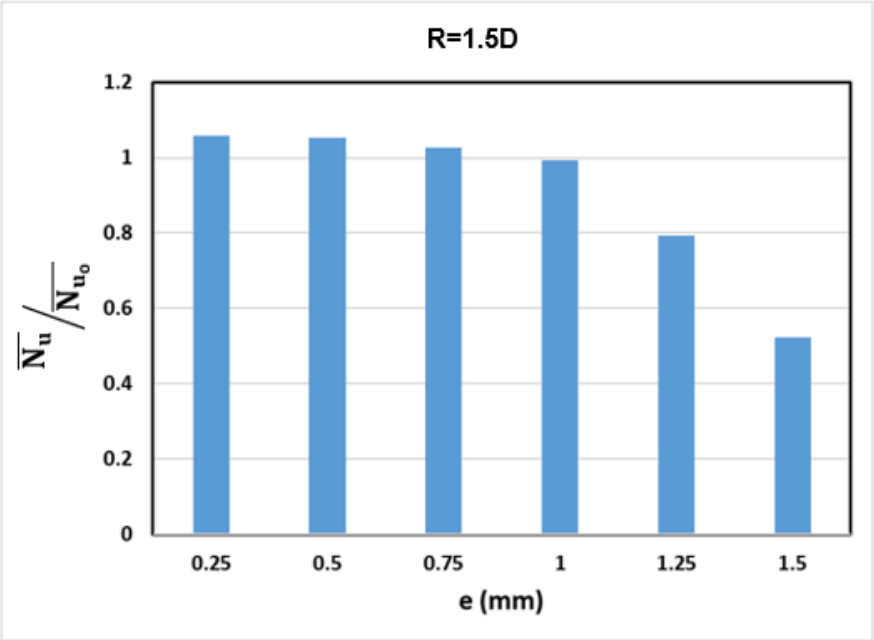

Figure 5-8: Effect of rib height on normalized Nu, R=1.5D, Re, 20,000, H/D=6 and α = 90º.

5.2.3 Rib location – R=2D

By comparison with the baseline case, placing the circular rib at R=2D improves the local Nu significantly, see Figure 5-9. This enhancement is a result of the high turbulence level induced by the flow recirculation before and after the rib. As rib height increases, the distance between the heated wall and the upper edge of the rib - where flow separation occurs - also increases causing the flow to travel a greater distance before it re-attaches with the wall. This shifts the re-attachment point to the right, as shown in the figure. Unlike the two locations previously discussed, the average Nu enhancement lasts till rib height, e=1.00 mm with an optimum rib height of e=0.50 mm.

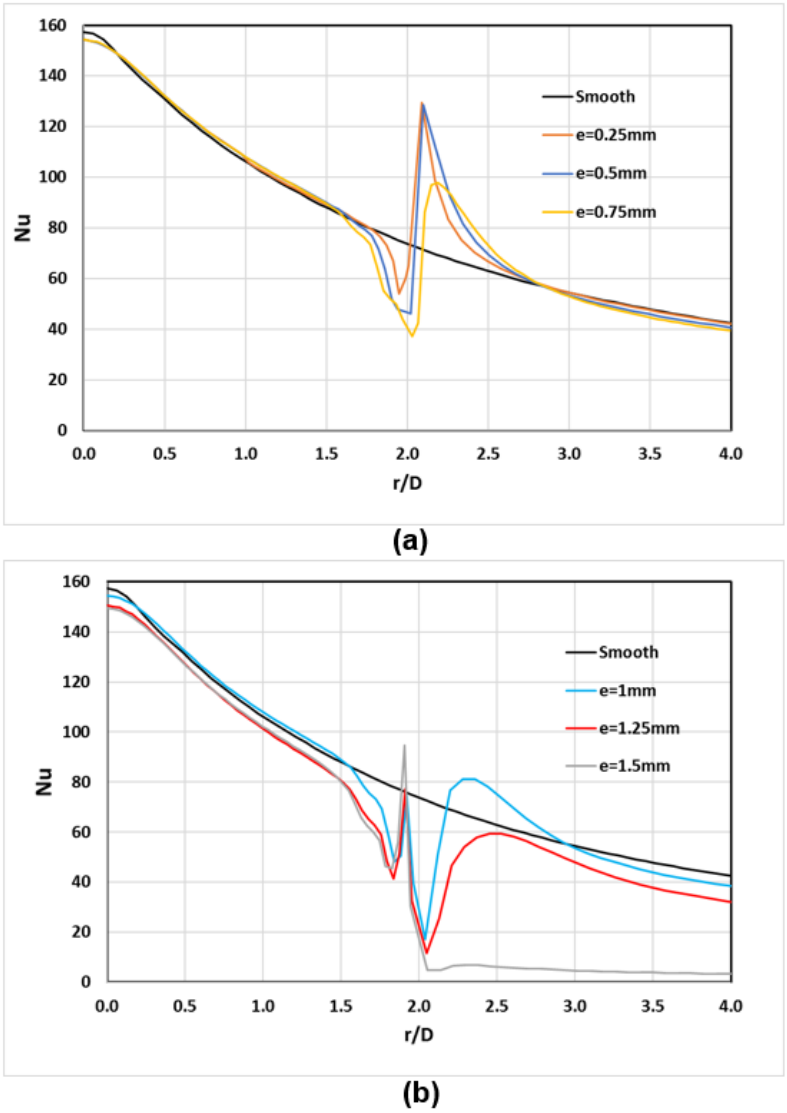

Figure 5-9: Local Nu distributions for six rib heights for Re, 20,000, H/D=6, R/D=2, and α = 90°

Figure 5-10 presents velocity contours for three heights of the rib at R =2D. The figure shows an enhanced re-attachment length compared to the previous locations (R= 1D and 1.5D) which indicates that the local flow has a higher velocity at this location. The re-attachment length (r_2), increases as the rib height increases, this is true up to a certain rib height where, above this height, the flow does not re-impinge on the heated surface and travels upward instead. For example, as shown in the figure below, with e=1.50 mm, the flow was not able to

resist the drag caused by the rib and instead of re-attaching it flows in the upward direction. This leads to no increase in heat transfer due to the presence of the rib.

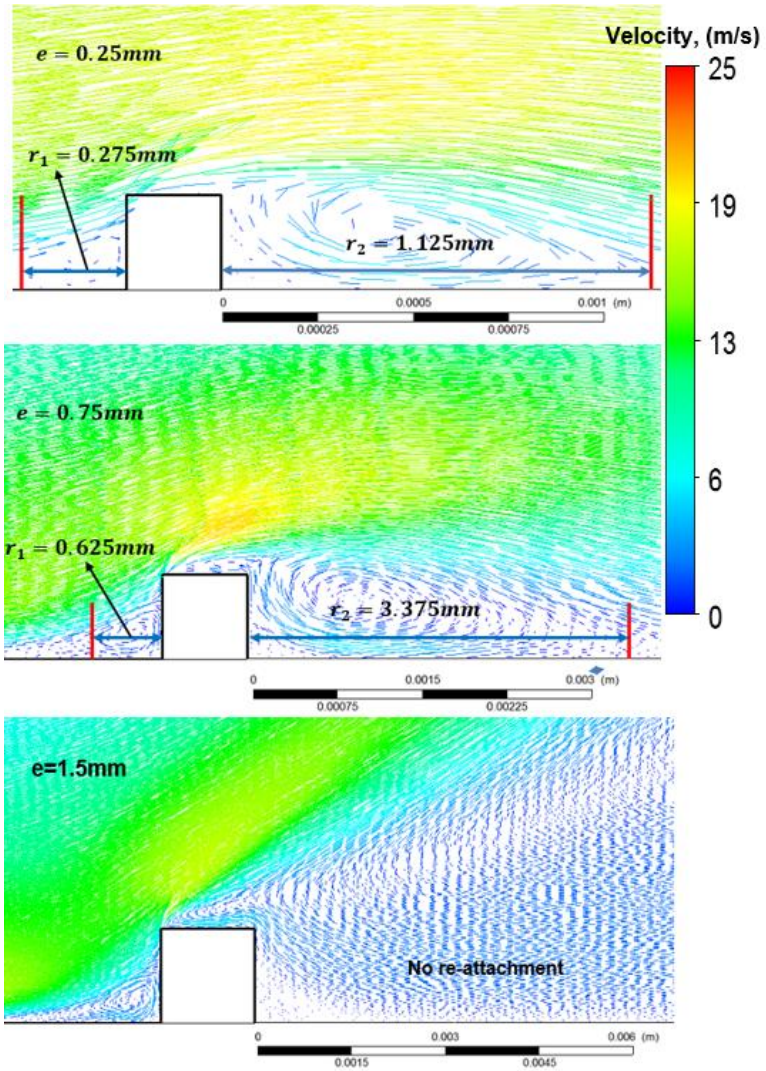

Figure 5-10: Velocity vector contours for three rib heights, (a) e=0.25 mm, (b) e=0.75 mm and (c) e=1.5 mm, Re, 20,000, H/D=6, R/D=2 and α = 90º.

Local Nu contours for four selected rib heights are shown in Figure 5-11, the maximum enhancement in heat transfer rate occurred at e=0.50 mm which is shown by the red area downstream of the rib. Both rib heights of 0.25 mm and 0.75 mm also show also a relative enhancement but the rib height of e=1.50 mm appears to actually reduce heat transfer as the flow was not able to re-attach with the heated surface due to the drag caused by the rib. It can be also seen that

changing rib height had no effect on the stagnation zone (the red circle in the middle).

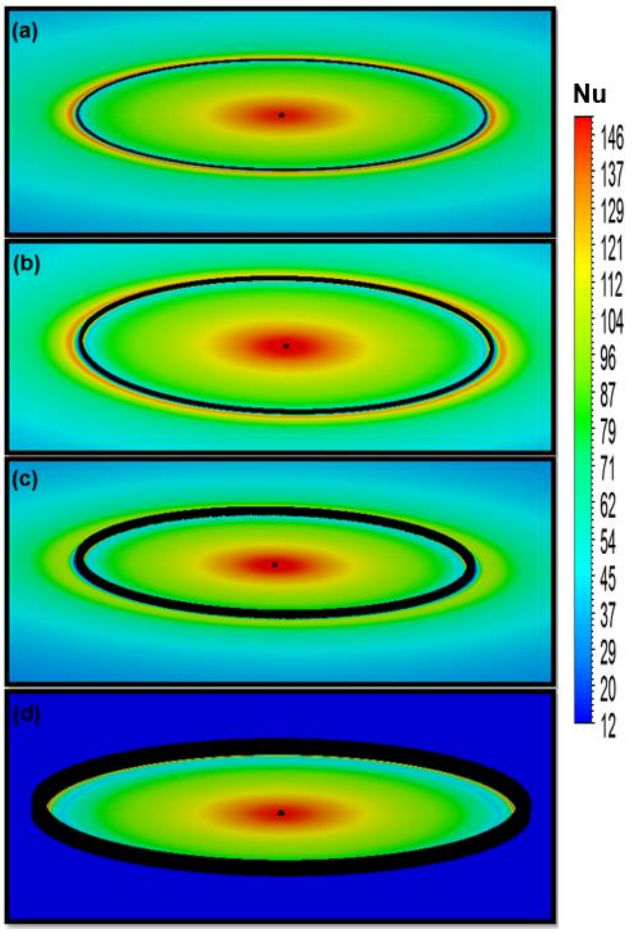

Figure 5-11: Local Nu contours, (a) e=0.25 mm, (b) e=0.5 mm, (c) e=0.75 mm, (d) e=1.5mm for Re, 20,000, H/D=6, R/D=2 and α = 90º.

Unlike the two locations at r=1D and 1.5D, discussed above, placing the rib at R=2D enhances heat transfer even for a rib of height, e=1.00 mm. For ribs in the range 0.25 ≤ e ≤ 1.00 mm, the enhancements with respect to the baseline are 10.5%, 15.6%, 12.7% and 10.7% respectively (see Figure 5-12). Thus there is a greater increase in heat transfer rate with the rib at this radial location compared to r=1D and 1.5D. The figure also shows as rib height further increases, e≥1.25 mm local Nu drops noticeably with a sharp negative impact on heat transfer before and after the rib due the enhanced drag generated.

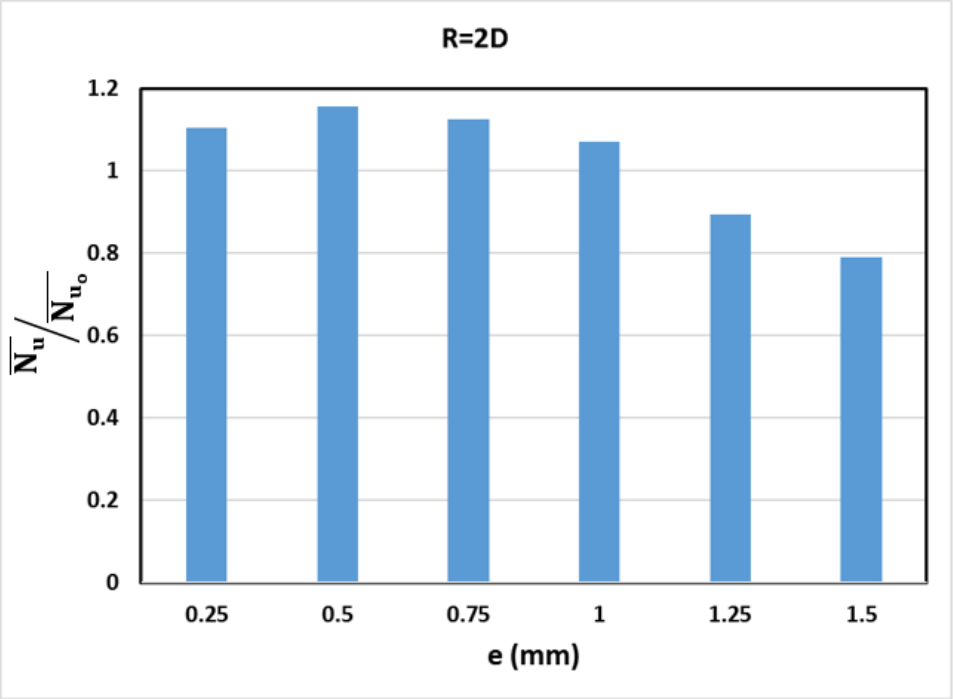

Figure 5-12: Effect of rib height on normalized Nu, for R/D=2, Re, 20,000, H/D=6 and α = 90º.

The location R=2D represents just after the beginning of the wall jet region [27] where the flow starts to exchange momentum with the wall. The formation of a boundary layer begins in the stagnation region with a thickness of no more than 1% of the jet hydraulic diameter [128]. The wall jet boundary layer thickness is influenced by both flow velocity gradients with respect to the no-slip wall and with respect to the stationery flow above the jet. The wall shearing layer thickness increases as the flow moves downstream, where its average velocity decreases due to momentum exchange with the wall. Depending on the velocity gradients, rib location could have a different impact on the flow physics and heat transfer rate.

Gaining a greater heat transfer rate by placing the rib away from the stagnation region encouraged the idea of placing the rib at R=3D which is discussed in the next section.

5.2.4 Rib location – R=3D

Figure 5-16 shows local Nu distribution for six heights of the roughening ribs for rib radius, R=3D. The figure clearly shows an enhancement of average Nu for rib height, e≤1.00 mm, However, for e≥1.25 mm the curves representing the local Nu distribution show lower values.

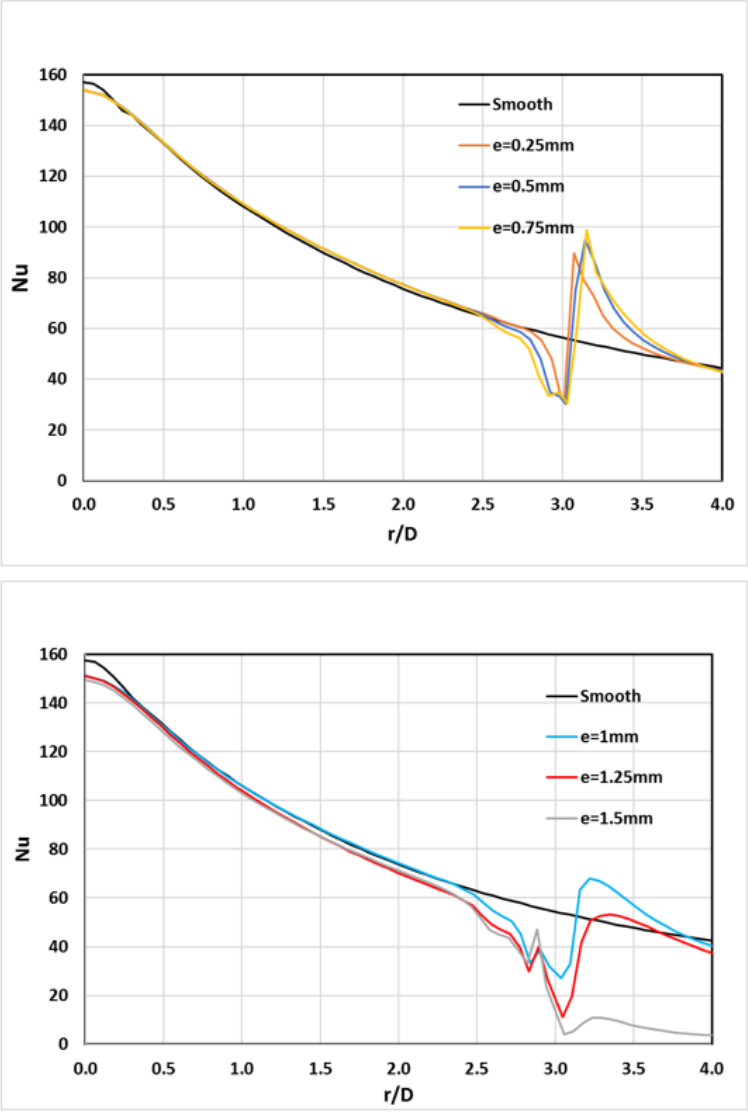

Figure 5-13: Local Nu distributions for six rib heights for Re, 20,000, H/D=6, R/D=3, and α = 90º

As mentioned above, the rib protrusion effects the flow properties; changing its velocity, pressure and kinetic energy due to the change of the flow patterns that occurs as a result of the rib's obstruction. The rib height e=0.75 mm provides the maximum heat transfer enhancement as it gives the maximum local Nu value at r/D≥3 At e=1.50 mm, however, the flow wasn't able to re-attach with the heated surface due to flow recirculation in different regions before and after the rib, see Figure 5-14.

Figure 5-14 shows that the highest flow velocity (green lines) is located above the top of the protrusion while the lowest velocity (blue lines) is found at the top and around the protrusions. It can be observed that the flow with highest velocity exists predominantly for protrusions with lower heights. A protrusion usually exerts drags on the flow, causing pressure build up and lowering velocity, after the flow passes the protrusion a low pressure region will occur behind the protrusion. Flow recirculation and higher turbulence will then occur in this low pressure region which enhances the heat transfer rate. However, depending on the height and shape of the protrusion, this low pressure region could be large enough to have a negative effect on heat transfer rate by preventing the main jet flow proceeding on its regular path. The figure demonstrates this fact as it shows that the higher the rib, the larger the low pressure region, and the longer distance the flow travels before it re-attaches to the heated surface. At e=1.50 mm it can be seen that the flow failed to reattach.

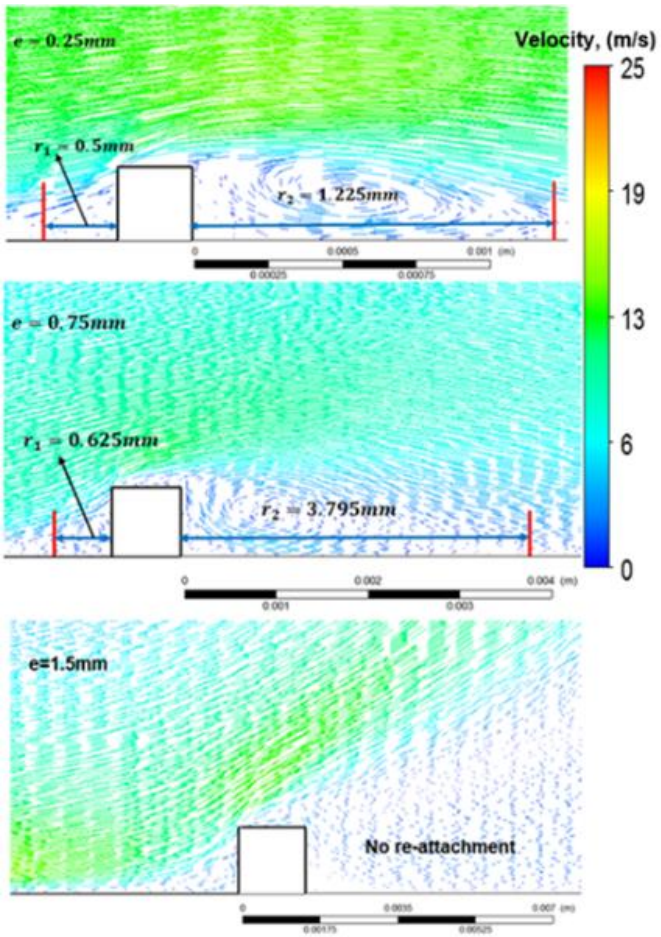

Figure 5-14: Velocity vectors contours for three selected rib heights, (a) e=0.25mm, (b) e=0.75mm and (c) e=1.5mm, Re, 20,000, H/D=6, R/D=3 and α = 90º.

Contours of local Nu are shown in Figure 5-15 , it can be seen that heat transfer enhancement is more obvious as the rib height increases. At e=0.75 mm in particular, a wider region of heat transfer enhancement occurs behind the rib compared to lower rib heights. As previously observed, a rib height of 1.50 mm provided sufficient drag that the flow travelled upward instead of re-attaching with the heated surface.

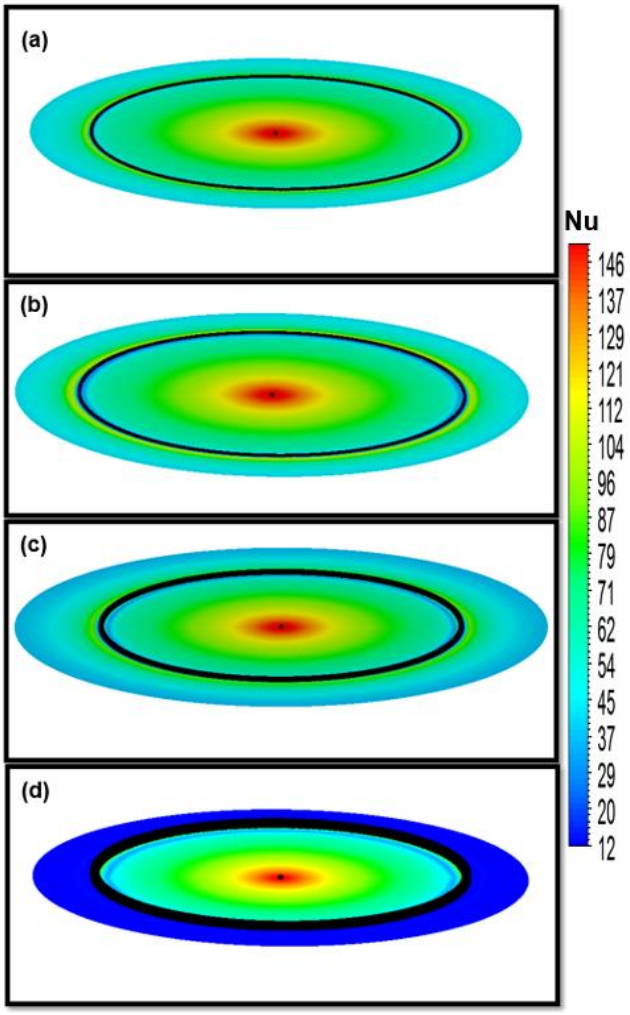

Figure 5-15: Local Nu contours, (a) e=0.25mm, (b) e=0.5mm, (c) e=0.75, (d) e=1.5mm, Re, 20,000, H/D=6, R/D=2 and α = 90º.

The normalised average Nu variation with respect to rib heights is shown in Figure 5-16. An enhancement in the average Nu of about 11.5% was achieved by introducing a rib with height 0.75 mm. For rib heights 0.25 mm, 0.50 mm and 1.00 mm, enhancement of average Nu was 6.2% ,8.7% and 4.5% respectively. A drop in heat transfer is noticeable as rib height increases above e≥1.00 mm. The use of inappropriate rib height, of e=1.50 mm say, could lead to a loss of heat transfer of over 55% compared to the baseline case.

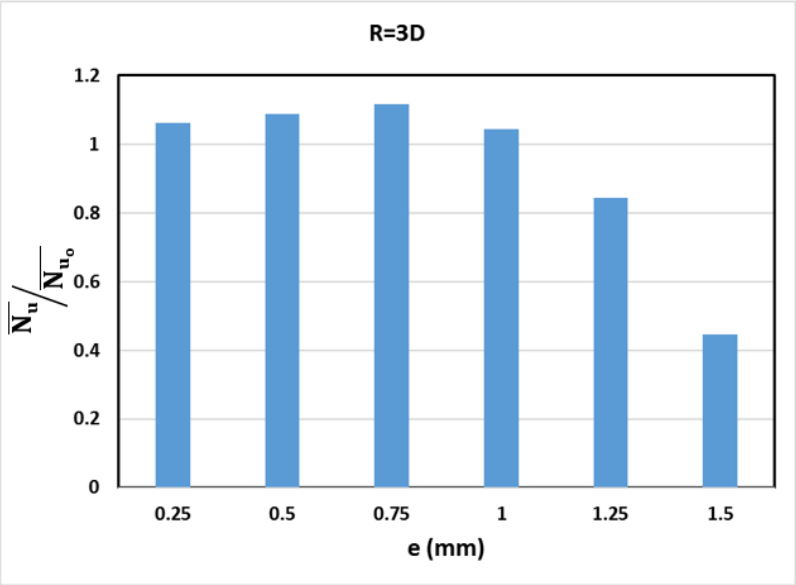

Figure 5-16: Effect of rib height on normalized average Nu, R=3D, Re= 20,000, H/D=6 and α = 90º.

5.2.5 Comparison of results

Figure 5-17 shows the effect on the local Nusselt number for ribs located at different radii from the centre of the jet. Here the range for R/D was 1,1.5,2 and 3 where most of heat transfer takes place in this region. For each rib location, the local Nu distribution determined the optimal rib height. As R/D increased, and the radial distance of the rib from the stagnation point increased the local maximum Nu associated with the presence of a rib decreased. This phenomenon is explained by the combined effects of the decrease in turbulent energy of the fluid as it moves away from the stagnation point and the rapid decrease in the velocity of the wall jet with radial distance from the impingement point. From Figure 5-17 it appears there could be an optimum rib height and location on the target surface for which the averaged Nu value is a maximum.

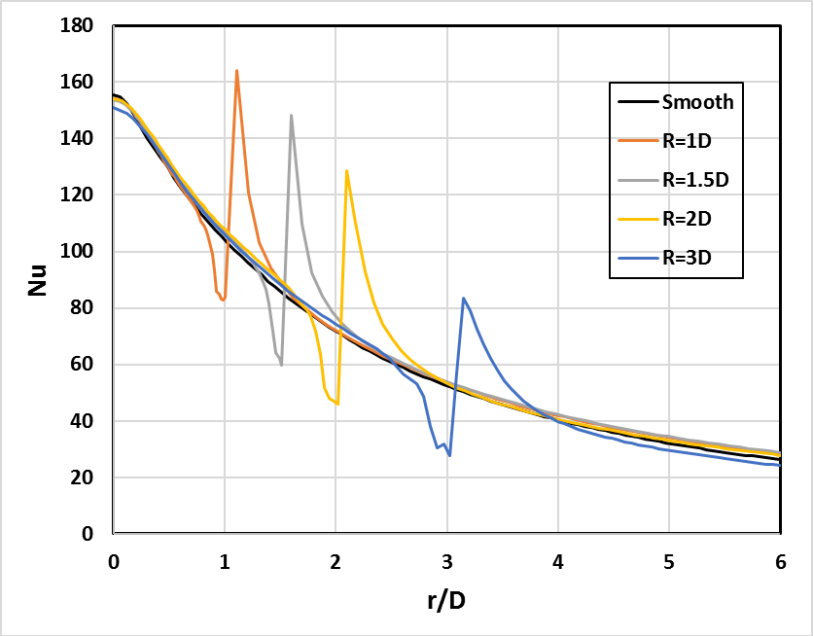

Figure 5-17: effect of rib location on local Nu

Figure 5-18 shows the normalized average Nusselt number for a circular rib on the target surface. The Nusselt number is normalized by dividing by the value for the averaged Nu over 0 ≤ r/D ≤ 4 when no rib is present. Clearly the most effective location for the rib is at R/D = 2 for which $\overline{N_u}/\overline{N_{u_o}}$ = 1.156. For R/D ≥ 2, the averaged Nusselt number initially decreases as R increases. It is argued that maximum enhancement of the heat transfer rate was obtained when the rib was installed at a location close to the boundary between the stagnation region and the wall jet region, at R/D = 2.

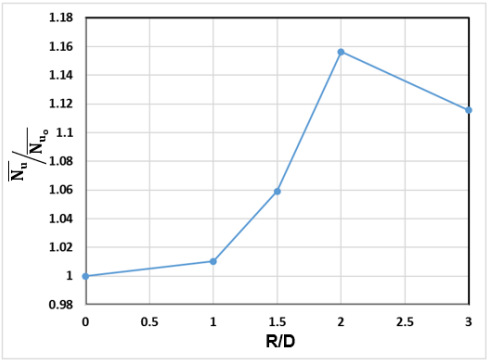

Figure 5-18: effect of rib location on normalized average Nu

5.3 Inclined jet impingement

Figure 5-19 shows the simulated radial velocity distribution for both angles of inclination for an impinging jet flow. For example, it can be seen that in the uphill direction, at r=-3D, the radial outward flow velocities are 2.7 m/s and 3.9 m/s for α=45º and α=60º, respectively. And in the downhill direction at r=3D, the corresponding radial outward flow velocities are 16.5 m/s and 14.5 m/s. The flow velocity in the uphill direction is lower about 16% and 27% of that in the downhill direction for α=45º and α=60º, respectively. The same considerations apply at other radial distances.

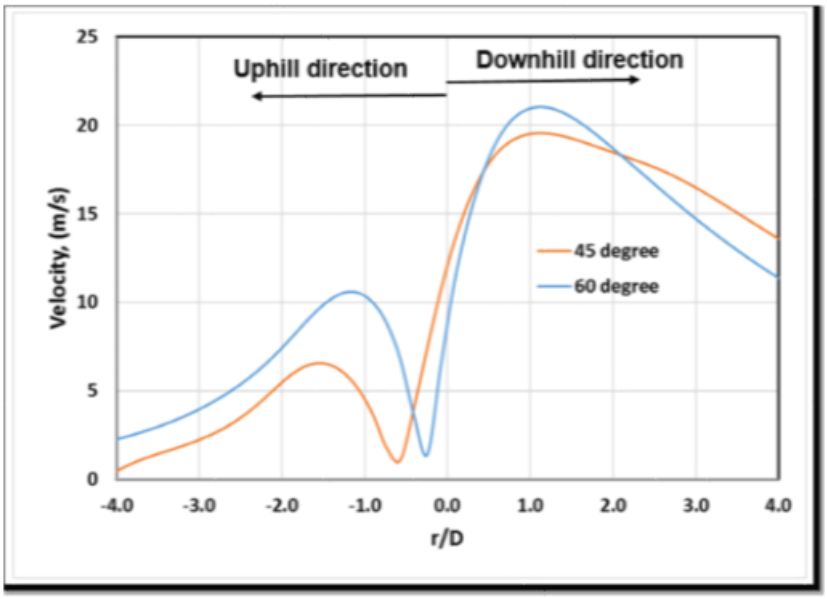

Figure 5-19 : Simulated velocity distribution for α=45º and α=60º, Re=20,000 and H/D=6

5.3.1 Rib location – R=1D

The effect of roughness element height on local Nu in both the uphill and downhill directions is shown in Figure 5-20. The figure is for two angles of inclination, 45º and 60º with the smooth surface and three rib heights of 0.25, 0.50 and 0.75 mm, as those heights had previously proved to be the most effective at R=1D, see Section 6.2.1. Measurements were also made for heights of 1, 1.25

and 1.5 mm and will be included only in obtaining the normalised average Nu later on this section.

For α=45º, the figure shows a noticeable heat transfer enhancement in the uphill direction for r≤1.5D for all three rib heights compared to the smooth wall case. In the downhill direction however, this enhancement continues till r/D≈3, after which, heights e=0.50 and 0.75 mm start to show lower Nu values than for the smooth wall case. However, for e=0.25 mm the Nu values continue to show enhanced heat transfer. Somewhat different behaviour is seen for α=60º, where the stagnation Nu has been moved to a radial distance of r/D~0.3 and the roughened surfaces show a lower value for the stagnation Nu, about 4.5% less than the stagnation Nu of the baseline case (smooth wall).

In the uphill direction, the rib roughened surfaces show lower values of local Nu until a radial distance of r≈-1D (the negative sign indicate uphill direction) is reached at which the presence of the rib causes a disturbance oscillation in the local value of Nu and after which all curves converged on the baseline local Nu. This is due to the roughened element at R=1D being within the stagnation region. Except for the recirculation region, the presence of a rib seems to have little or no effect on local Nu distributions on the uphill direction. For the downhill direction, local Nu distribution over the rib roughened surfaces show much the same behaviour as for α=45º where only the rib of height e=0.25 mm shows an overall enhancement of local Nu values compared to the baseline case.

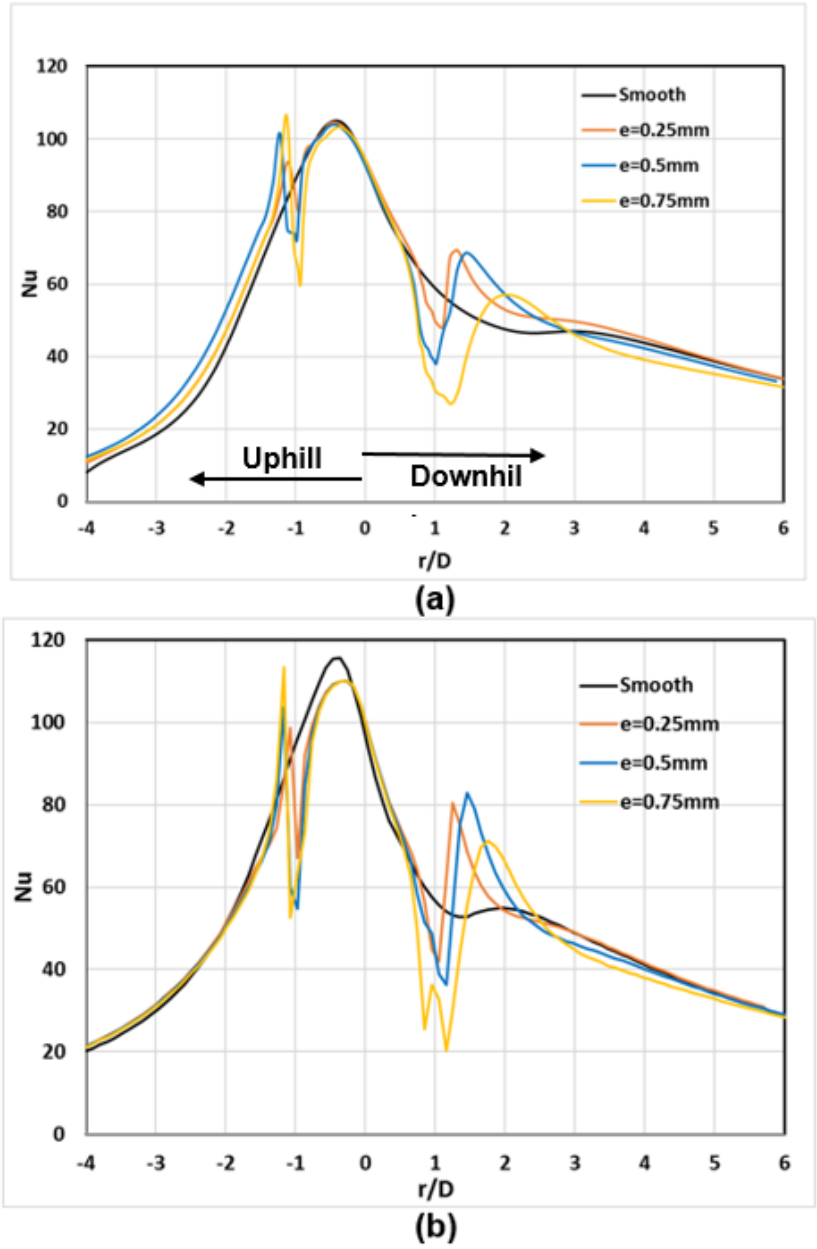

Figure 5-20 : local Nu distributions for three rib heights, R/D=1, (a) 45º and (b) 60º

A visual comparison of Local Nu distributions for α=45º and 60º is shown in Figure 5-21. The shape of the flow footprints shows that changing rib height can affect heat transfer in both directions but mainly in the uphill direction. The protrusion generates flow recirculation behind it in the uphill direction where a small change of the jet flow in this direction causing a noticeable enhancement in heat transfer. It can be observed from the figure that, in the case of α=45º, a

wider region of enhanced heat transfer occurs in the uphill direction owing to lower flow velocity compared to the larger angle of inclination.

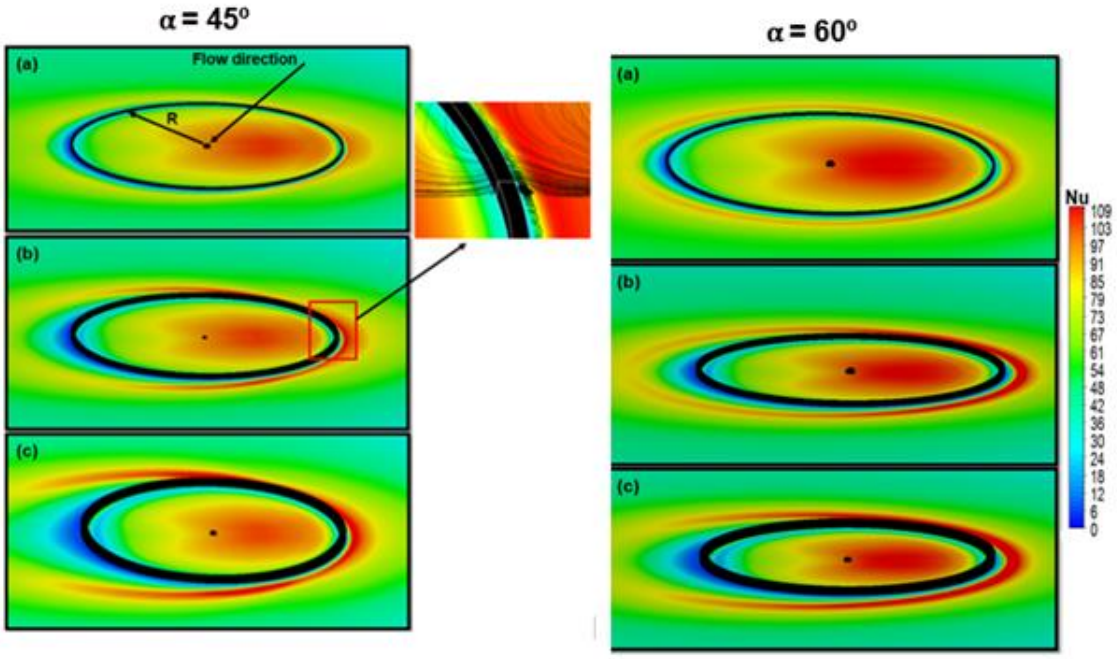

Figure 5-21: Local Nu contours for r/D=1, three heights, (a) 0.25mm, (b) 0.5mm and (c) 0.75mm

Figure 5-22 shows the normalized Nu averaged over a surface area between -4≤r/D≤4 with change of rib height. It can be seen that at α=45º the presence of a rib at r/D=1, enhanced average Nu for all rib heights tested, giving an increase of between 6.7% at e=0.25 mm to 2.3% at e=1.50 mm. However, at α=60º, the presence of a rib at r/D=1, regardless of the height had a negative impact on heat transfer.

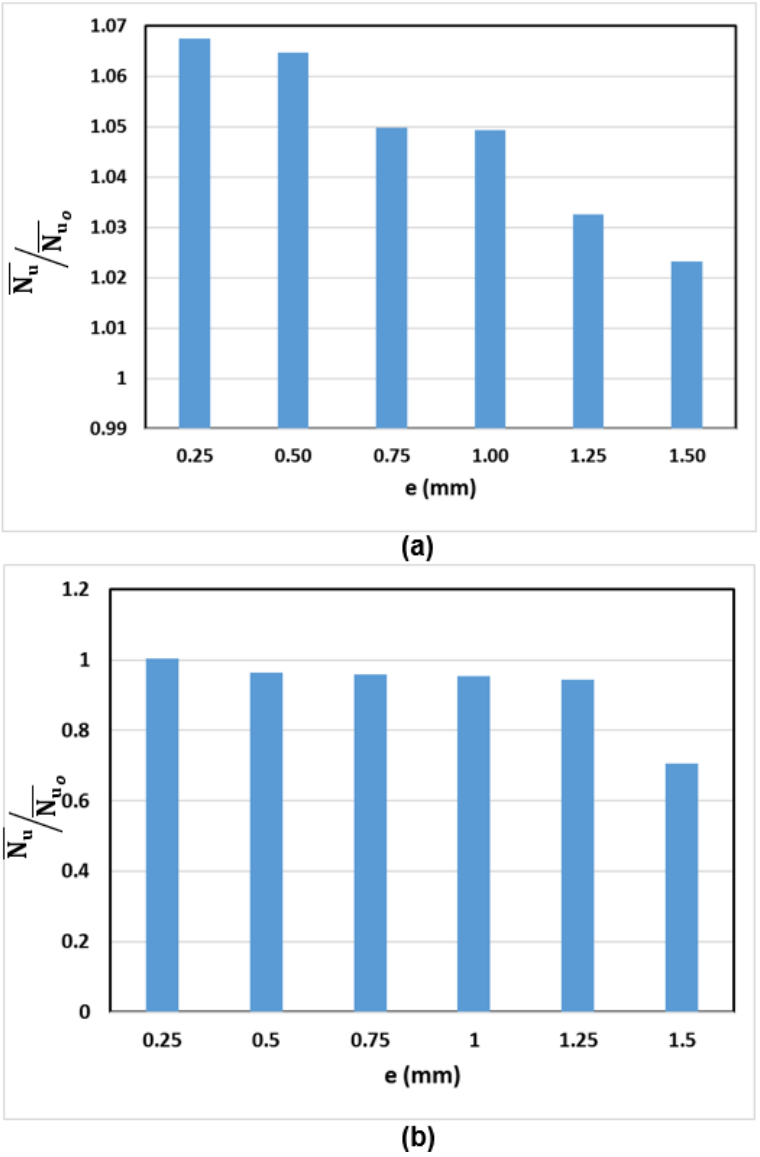

Figure 5-22: Effect of rib height on normalized average Nu, R=1D, Re= 20,000, H/D=6, (a) α = 45º and (b) α = 60º

5.3.2 Rib location – R=1.5D

The radius of the rib was increased to R=1.5D and its resulting impact on local heat transfer (Nu values) is shown in Figure 5-23. As can be seen, the rib roughened elements have a very noticeable effect on local Nu distributions, particularly in the downhill direction for both angles of inclination of the jet. For α=45º,

an enhancement of local Nu distribution can be seen for -4≤r/D≤3, while the same stagnation Nu value was maintained with respect to the baseline with a slight shift to the right in the case of α=60º. This enhancement is more noticeable between 0≤r/D≤1.25 with maximum enhancement of about 18% at r/D≈1. However, after the jet met the rib, except for height e=0.25 mm, the presence of a rib lowered local Nu values when compared to the baseline case. For rib heights e=0.5 and 0.75 mm, appear to enhance local Nu for 2≤r/D≤3, then they fall below the baseline for r/D > about 3.

As for α=60º, the stagnation Nu shows higher values for all three ribs compared to the baseline case, with maximum increase of about 3.6% for e=0.75 mm. Also, the location of the stagnation Nu was shifted slightly downhill. Unlike the case of α=45º, the enhancement occurs overwhelmingly in the downhill direction, with a very noticeable enhancement between 0≤r/D≤1.25 with maximum enhancement of approximately 30% at r/D≈1. In the uphill direction, except in their immediate vicinity all ribs, regardless of their height, seemed to have a negligible effect.

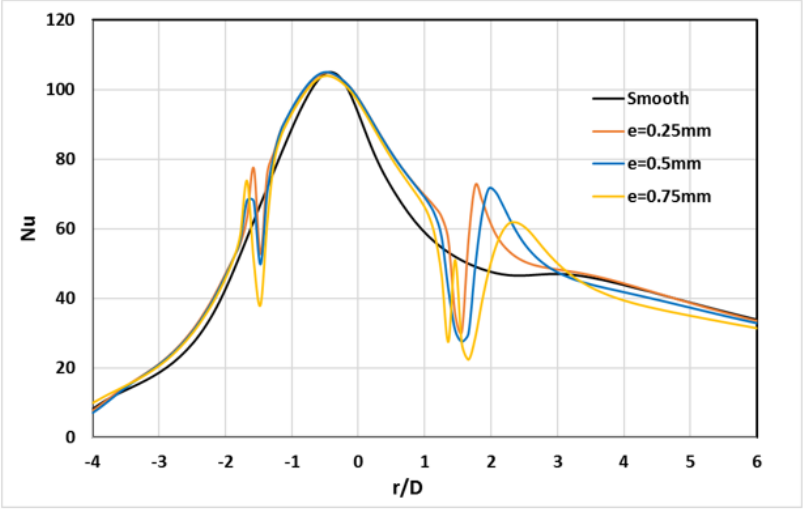

(a)

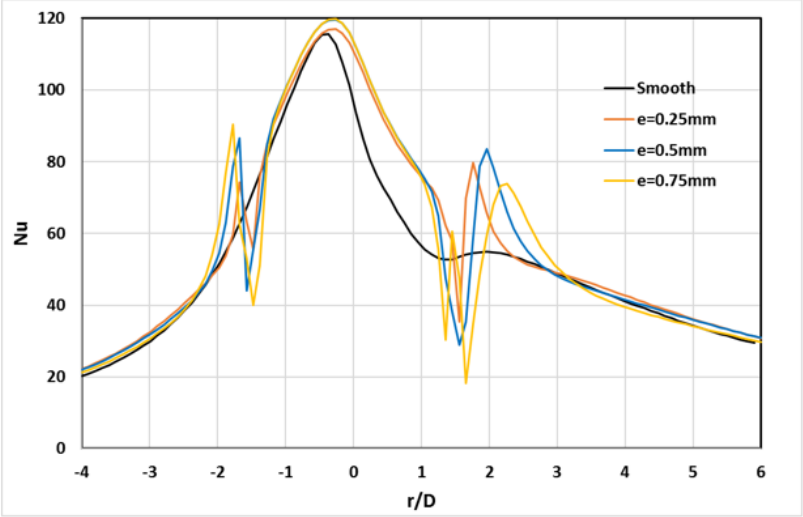

(b)

Figure 5-23: local Nu distributions for three rib heights, R/D=1.5, (a) 45º and (b) 60º for Re=20,000, H/D=6.

Studies made by Foss, et. al., Foss, el., al. [149],[150] have shown that the stagnation Nu for inclined jets is located where the maximum static pressure occurs. Because the rib affects the flow static pressure, so it will also affect the location of $N_{u_{stag.}}$. Their finding was confirmed in this research. This is what obviously happened for α=60º. When ribs were introduced into the flow they affected the value and the location of $N_{u_{stag.}}$ as shown in Figure 5-24. The same phenomenon will be observed in the results obtained for greater rib radii, see below.

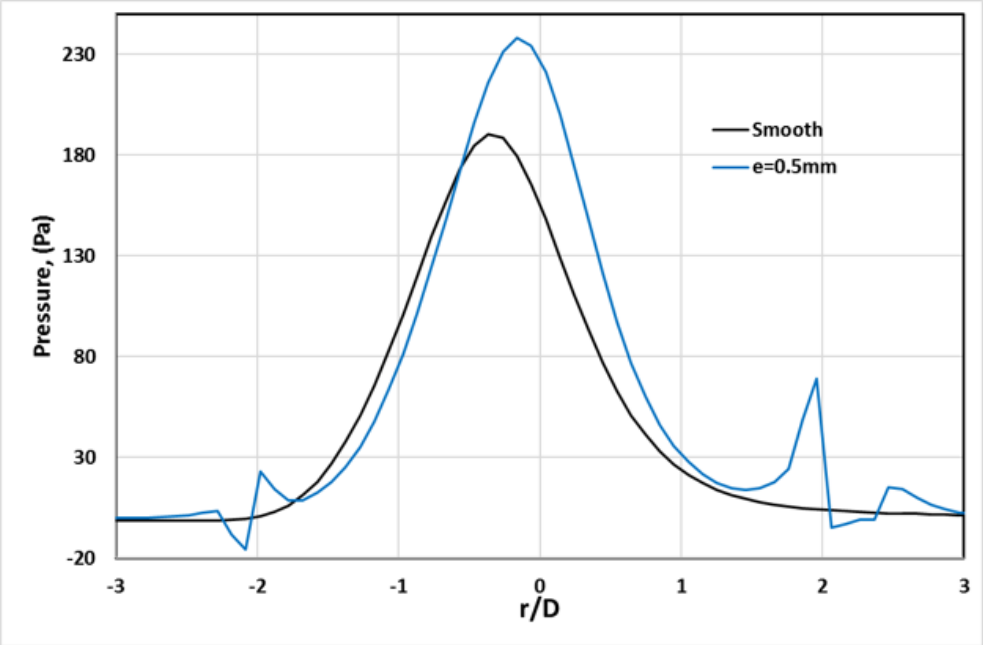

Figure 5-24: static pressure distribution for the baseline case and rib height e=0.5mm, α =60º

As the angle of inclination approaches orthogonality (α increasing), the mass flow rate in the uphill direction increases, transferring more heat from the heated surface. This can be seen in Figure 5-25 where, in the uphill direction, the heat transfer rate increased with angle of inclination. This enhancement is shown by the presence of the red area behind the rib for α=60º for rib heights of e=0.50 and 0.75 mm. This enhancement increased as the rib height increased except for the case where e=1.5mm. However, this observation was true only for the local Nu distribution and not necessarily true for the averaged Nu because the flow ejected from inclined jets lacks symmetry over the surface. In addition, although local heat transfer enhancement after the rib increases with increasing rib height so does the recirculation region where low Nu occurs due to the increase in the difference between the temperature of the recirculation flow and the heated surface. The figure also shows also shows that for the lower angle of inclination, the region of low Nu is larger in the downhill direction before and after the rib than for the larger angle. However, an opposite observation can be seen in the uphill direction.

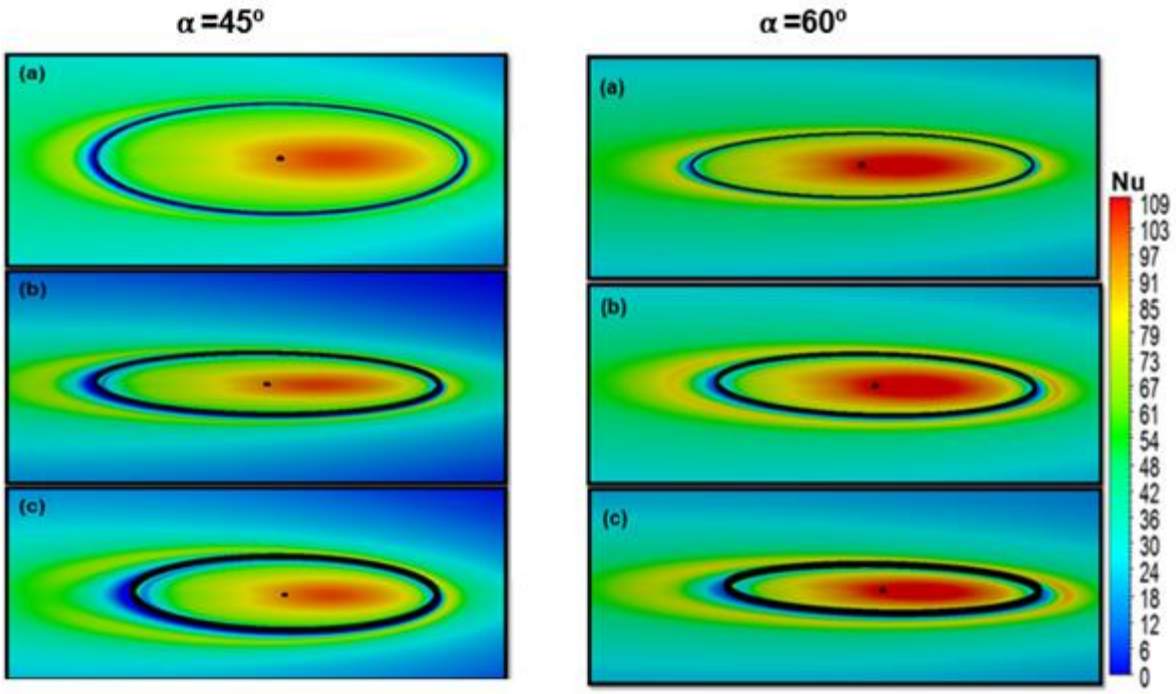

Figure 5-25: Local Nu contours for r/D=1.5, three heights, (a) 0.25mm, (b) 0.5mm and (c) 0.75mm for Re=20,000 and H/D=6

Normalised average Nu for both angles is shown in Figure 5-26 for six rib heights. Of the two angles of inclination with the lower (α=45º) the heat transfer is enhanced only for rib heights between 0.25≤e≤0.75 mm where enhancement was 6%, 3% and 1.8% for the three rib heights respectively. For e>1.00 mm there is no enhancement. For α=60º, there was enhanced heat transfer for rib heights between 0.25 mm and 0.75 mm, each with a similar enhancement of about 2.5%. However, for all rib heights e≥1 there was an overall lower heat transfer rate when compared to the baseline case.

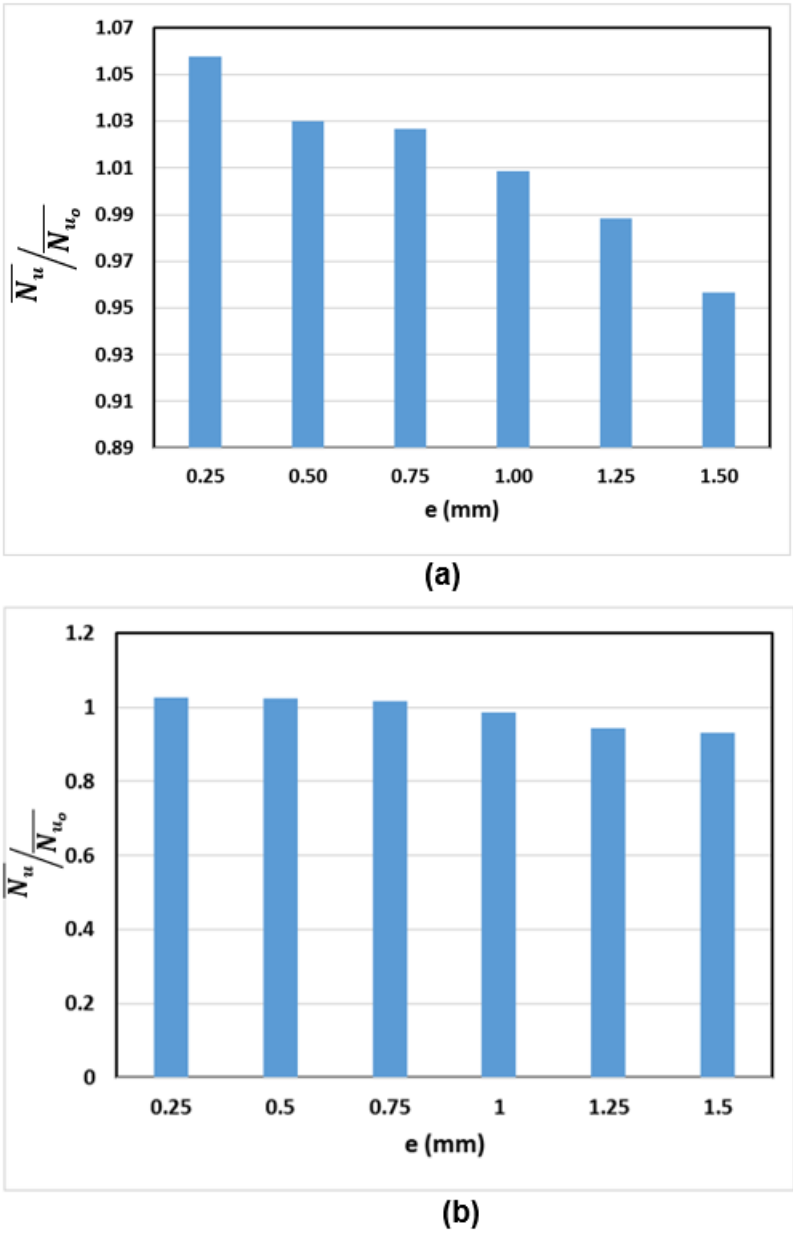

Figure 5-26: Effect of rib height on normalized average Nu, R=1.5D, Re, 20,000, H/D=6, (a) α = 45º and (b) α = 60º

5.3.3 Rib location – R=2D

The radius of the rib was increased to R=2D where the wall jet region takes place. The resulting impact on the local Nu values is shown in Figure 5-27. The local Nu distribution, especially in the uphill direction, appears very different with a rib placed at this radius. As the figure shows, by the sudden drop at r/D=-2, for

angle of inclination α=45º and all rib heights, the uphill flow suddenly stops transferring heat. It is suggested that at this angle the flow did not pass over the rib which acted as a physical barrier. However, for the larger angle of inclination (α=60º), the model predicted heat transfer from the wall in the uphill direction except for rib height, e=0.75 mm, where the flow was unable to pass over the rib. In general, it can be said that placing a rib uphill of an inclined jet flow, regardless of its height is not an effective means of enhancing heat transfer rate.

In the downhill directions the local Nu distribution followed more typical patterns.

For α=45º, enhancement of local Nu distribution can be seen for -2≤r/D≤3.5, with a small increase in the value of the stagnation Nu value for e=0.5 and 0.75mm. This enhancement is noticeable between 0≤r/D≤1.5 with maximum enhancement of about 9.5% at r/D≈1 for e=0.5mm. However, immediately after the rib there was a sudden and short-lived increase in local Nu compared to the baseline case. As for α=60º, the stagnation Nu shows higher values for the two lower ribs compared to the baseline case, with maximum increase of about 29% for e=0.25 mm at r/D≈1. Again, the location of the stagnation Nu was shifted slightly downhill, and again like the case of α=45º, the enhancement occurs overwhelmingly in the downhill direction, with a very noticeable enhancement between 0≤r/D≤1.75 with maximum enhancement of approximately 29% at r/D≈1. In the uphill direction, except in their immediate vicinity, all ribs, regardless of their height, seemed to have a negligible effect.

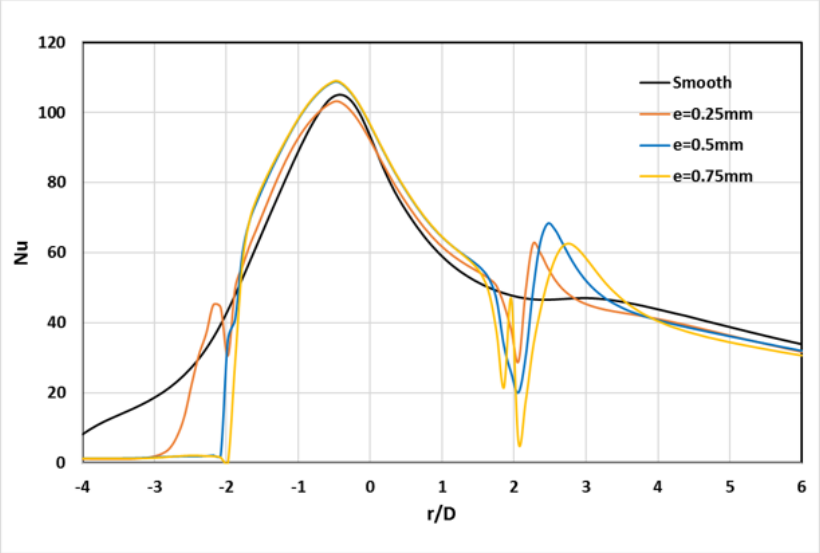

(a)

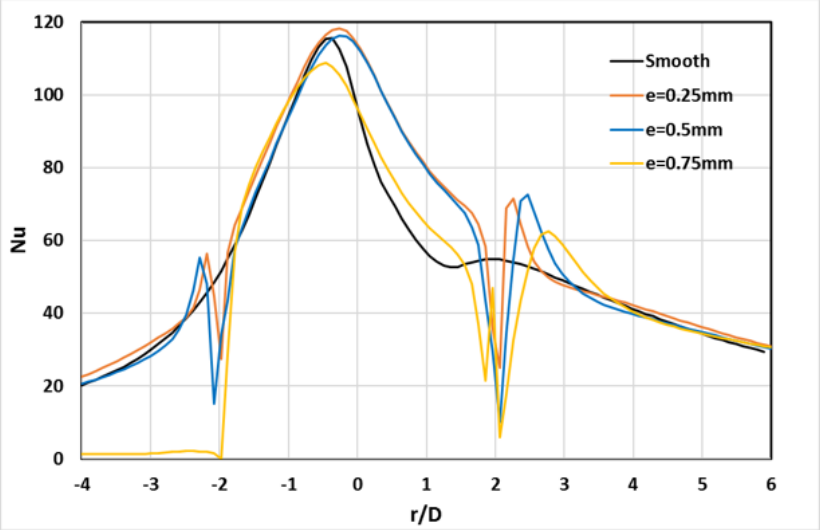

(b)

Figure 5-27: local Nu distributions for three rib heights, r/D=2, (a) α =45º and (b) α =60º

Local Nu contours for both angles of inclination and rib heights e = 0.25, 0.50 and 0.75 mm are shown in Figure 5-28. It is obvious that for α=45º, all rib heights appear to have a major adverse impact on flow in the uphill direction because the flow hasn't enough momentum to pass over the rib. However, this is not the case for the larger angle of inclination, where there is a greater mass flow rate in the uphill direction. It can also be seen that for α=60º, the stagnation region

is similar for the two rib heights e=0.25 and 0.50 mm, but the higher rib of e=0.75 mm shows a different Nu footprint.

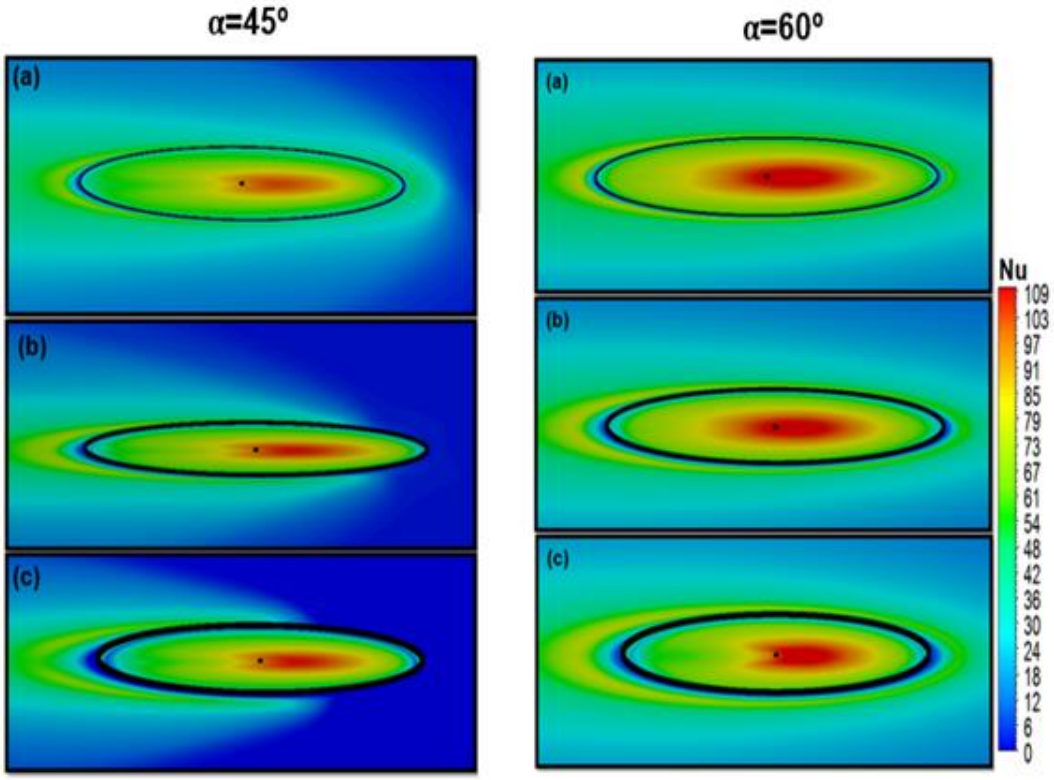

Figure 5-28: Local Nu contours for r/D=2, three heights, (a) 0.25 mm, (b) 0.5 mm and (c) 0.75 mm for Re=20,000 and H/D=6.

The effect on normalized average Nu of placing the rib at a radial distance r=2D, for six rib heights and two jet inclination angles is shown in Figure 5-29. For α=45º, except for e=0.25 mm which enhanced heat transfer by 3.4%, all ribs showed a lower heat transfer rate than the baseline case. For α=60º, the rib with height e=0.25 mm also shows an enhancement of the normalized average Nu of about 3%, the two ribs of heights 0.50 mm and 0.75 mm show a similar heat transfer rate to the baseline case. Overall, placing the rib at radial distances of R/D=1.5 and 2 does not seem to be an effective technique to enhance heat transfer for angles of inclination of 45º and 60º

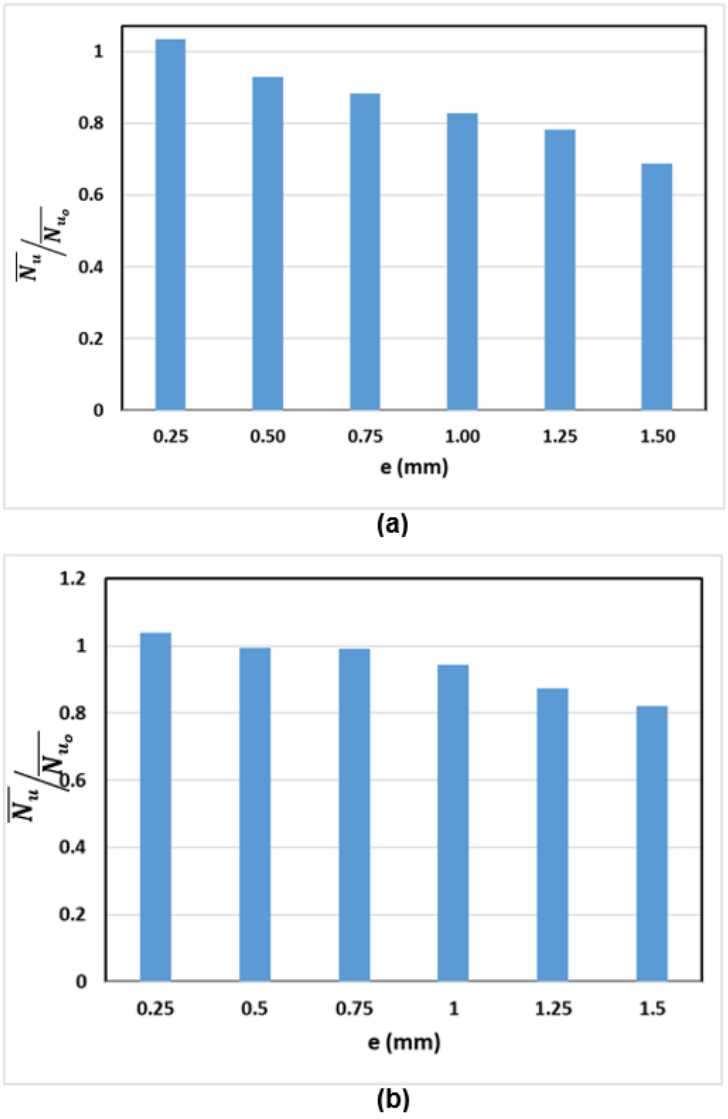

Figure 5-29: Effect of rib height on normalized average Nu, Re=1D, Re, 20,000, H/D=6, (a) α = 45º and (b) α = 60º

5.3.4 Rib location – R=3D

In Figure 5-30 shows the predicted curves of local Nu distribution for angles of inclination of α=45º and α=60º, with ribs of different heights positioned at r=3D. Compared to the previous rib locations (r/D = 1, 1.5 and 2), placing the rib at r/D=3 produces a number of changes in the detail. For α=45º in the uphill direction, the values of local Nu are much closer to the baseline case, but at R=3D the rib acted as a physical barrier to the flow. In the downhill direction, as previously, the presence of the ribs enhances heat transfer up to the rib at which a

perturbation occurs and after which the local value of Nu falls below the baseline case.

For α=60º, the flow rate in both uphill and downhill directions was sufficient to pass over all three ribs tested. The stagnation Nu did move slightly downhill and its magnitude was reduced slightly for all three rib heights. The local values of Nu were close to the baseline save in the immediate vicinity of the rib with the, by now, usual dip before the rib and the usual enhancement immediately after the rib.

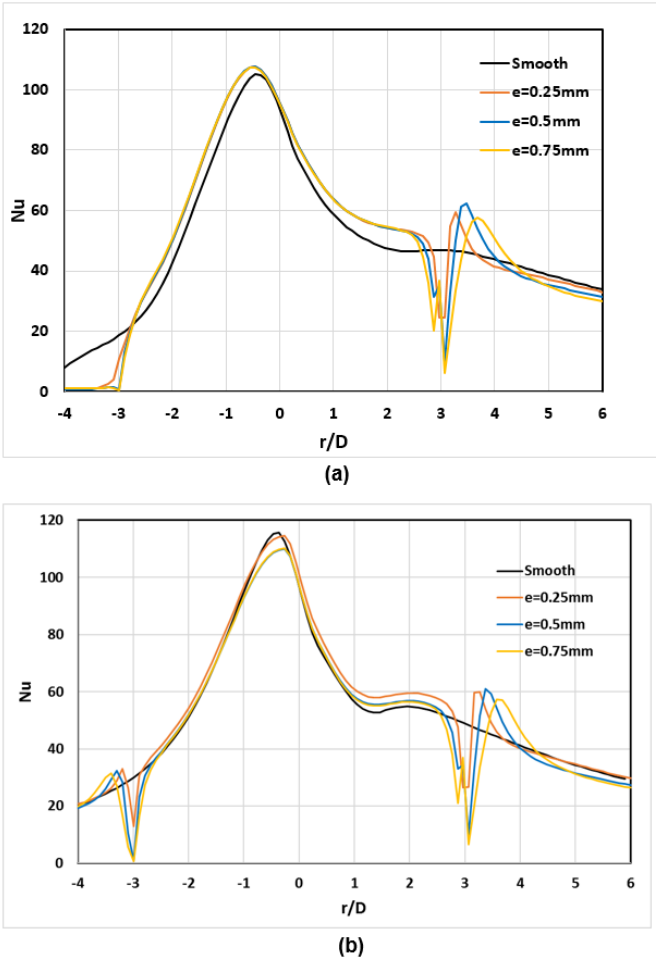

Figure 5-30: local Nu distributions for three rib heights, R/D=3, (a) α =45º and (b) α =60º for Re=20,000 and H/D=6.

Figure 5-31 shows the effects of using three different height circular ribs placed at R=3D, on the local Nu distribution for angles of jet inclination of α=45º and α=60º.

In the downhill direction, where the majority of the flow exists, for all three cases shown (e= 0.25, 0.50 and 0.75 mm) the local heat transfer increased. In the uphill direction, for α=45º however, the rib acted as a physical barrier to the flow and no heat transfer was predicted by the simulation. However with the angle of inclination 60º there was sufficient flow uphill to pass over the rib and some heat transfer took place

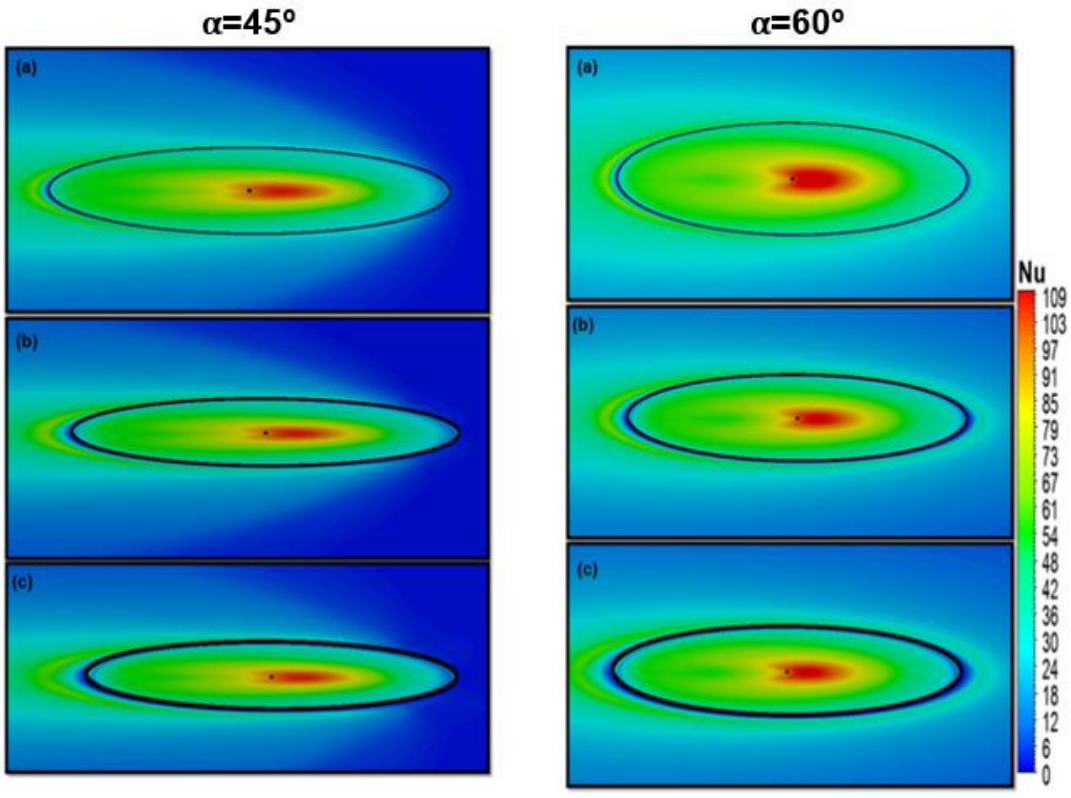

Figure 5-31: Local Nu contours for r/D=3, three heights, (a) 0.25mm, (b) 0.5mm and (c) 0.75mm

The normalised Nu, averaged over -4≤r/D≤4, for all the rib-roughened plates is shown in Figure 5-32. For α=45º the figure shows that rib heights of 0.25 and 0.50 mm give heat transfer enhancement of about 7.0% and 3.7%, respectively. For α=60º the figure shows that rib heights of 0.25 and 0.50 mm give heat

transfer enhancement of about 4.0% and 1.7%, respectively. However, ribs of a greater height (e > 0.75 mm) reduced the overall heat transfer below that of the baseline.

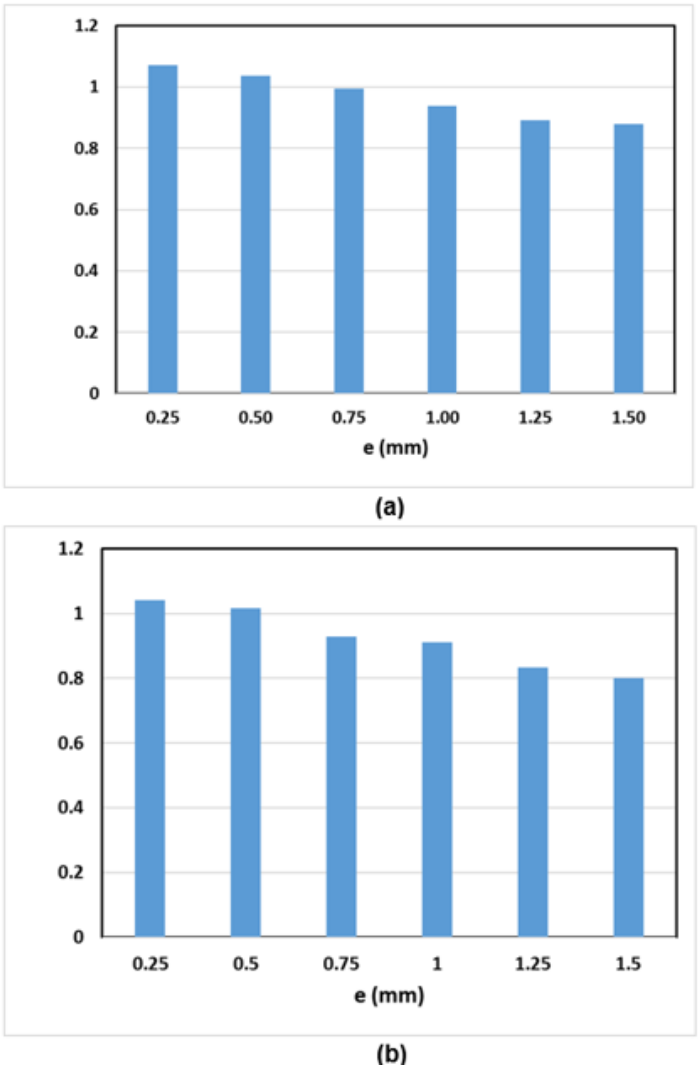

Figure 5-32: Effect of rib heights on normalized average Nu, R=3D, Re, 20,000, H/D=6, (a) α = 45º and (b) α = 60º

5.3.5 Comparison of results

An overall comparison of the effect of varying rib height and radial location on the normalized average Nu for two angles of jet inclination is shown Figure 5-33. As shown in the figure, for both angles of inclination, R/D=3 seems to be the most effective rib location for heat transfer enhancement. Gains of approximately 7% and 4% can be achieved for α= 45º and 60º respectively.

At R/D=1 for α=45º the presence of a rib increased the normalized average Nu by up to 6.7%. However, for α=60º, the presence of a rib, regardless of the height had a negative impact on heat transfer enhancement. When the rib location was at R/D=1.5 the maximum normalised average Nu for α=45º was 6% and for α=60º, the maximum enhanced heat transfer was 2.5%. At R/D=2 the lower angle of inclination gave a maximum enhancement of 3.4% and the higher angle of inclination. For r/D=3 and α=45º the maximum heat transfer enhancement was 7.0%. For α=60º the maximum heat transfer enhancement was 4.0%. When placing the rib at radial location R/D=3, although this location shows a maximum heat transfer enhancement for both angles of inclination, but this location is not the optimum location due to the fact that the rib does not play any role in the uphill direction where, under certain conditions, the flow in the uphill direction was unable to cross over the rib. Therefore, placing only a half circular rib in the downhill direction would be a more effective and less expensive alternative idea. Therefore, considering the current configurations, the optimum location of the rib for α=45° is R/D=1 where R/D=2 is the optimum rib location for α=60°.

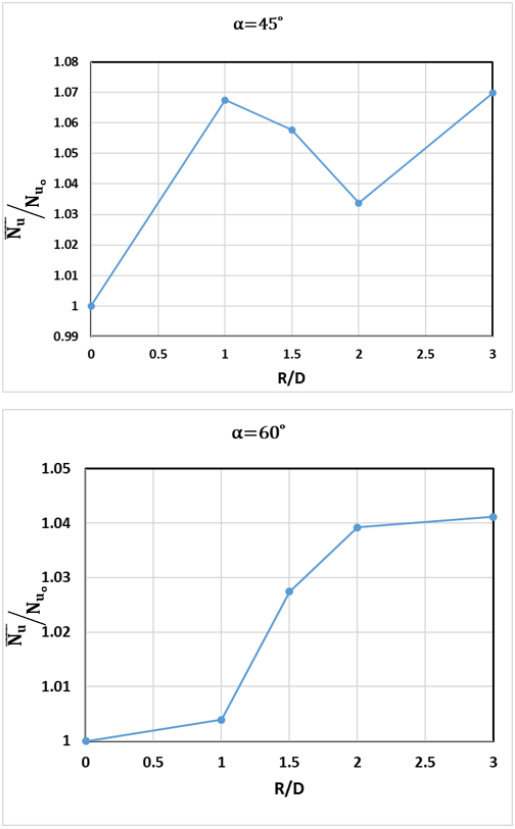

Figure 5-33: effect of rib location on normalized average Nu for two jet inclination angles

5.4 Closing Remarks

This chapter has presented the results of a simulation exercise on the effect of rib location and height on normalised Nu averaged over a surface area. The simulations were for circular ribs of six heights and square cross-section, centred on the jet with three angles of inclination, 90º, 60º and 45º. The radial locations tested should cover both the stagnation and wall jet regions.

In general, as the rib height increased so the low pressure region area behind the rib increased.

For α=90º, due to the symmetrical nature of the flow, the averaged surface area was 0≤r/D≤4. For this angle the rib height that matches the velocity boundary

layer thickness at the rib location seems to be the most effective height for enhancing heat transfer (see table 4.1). However, too high a rib, say 1.25 and 1.50 mm gave a lower heat transfer rate compared to the baseline.

Again for $\alpha=90^{o}$, the most effective rib radial location was at R/D=2 which, according to the available literature is the beginning of the wall jet region. Maximum heat transfer enhancement was approximately 15.6%. However, it was found that placing a rib in the stagnation region (R/D<1) did not enhance the heat transfer for any of the rib heights tested.

For inclined jets, the averaged surface area is $-4 \leq r/D \leq 4$ because the flow patterns were not symmetrical in the uphill and downhill directions. Also for inclined jets, the most effective rib height to enhance heat transfer was 0.25 mm regardless of the rib location.

For angle of inclination, $\alpha=45^{o}$, placing the rib at R/D=1.5 gives a heat transfer enhancement for all rib heights of between 1.8% and 6%. The maximum enhancement was 7% at R/D=3 with rib height e=0.25 mm. For $\alpha=60^{o}$, the maximum enhancement was 4% at R/D=3 with rib height e=0.25 mm

The next chapter will discuss the effect of a non-uniform rib geometry (teardrop shaped ribs) on the heat transfer rate. The rib will be tested for six heights and two radial locations.

6 Average Nu obtained using a non-uniform roughness element

6.1 Introduction

Results obtained in the last chapter demonstrated that using a circular rib of square cross-section could improve the average heat transfer rate between a jet and a plane surface by 2.1% to 15.6% for orthogonal impingement (α=90º), depending on rib height and location. Lower overall heat transfer enhancement was obtained for inclined jets where the flow distribution over the heated plate lacked symmetry. For α=60º, the use of a circular rib enhanced overall average Nu by a maximum of 4.0% when using a rib of height e=0.25 mm at r=3D. For α=45º, improved overall average Nu of about 6.7% was achieved for rib height of 0.25 mm at R=1D.

The effective rib locations in the case of the inclined jets were located either within the stagnation region at r=1D, or else well away from this region at r=3D where, under certain conditions, the flow in the uphill direction was unable to cross over the rib. This means using a rib uphill of the wall jet region can be useless because its presence stops the fluid flow, with no heat transfer beyond it.

In this chapter the roughness element used was of square cross-section but non-uniform in plan, so that enhanced heat transfer might be obtained when using an inclined jet because the rib would not act as a total barrier to the flow, either uphill or downhill. The non-uniform shape of the rib was designed to enhance heat transfer in the uphill direction especially for the lower inclined angle where less uphill flow takes place. The proposed non-uniform reversed dropped tear rib configuration adapted a design idea of narrowing the rib edges in the uphill direction when compared to the uniform circular rib, where the flow in this direction has much less momentum than the flow following the uphill direction. This design should help enhancing heat transfer rate in the uphill direction when

compared to the circular ribs. However, the same design idea was also conducted in the downhill direction to investigate the effect of narrowing rib edges in this direction by the use of dropped-tear rib configurations where the most of the flow follows this direction.

The square cross-section, circular ribs were replaced by square cross-section continuous ribs which had the shape of tear drops and reversed tear drops, see Figure 6-1.

Figure 6-1 shows the non-uniform shapes of the rib used. Each shape had six heights of between e=0.25 and 1.50 mm in increments of 0.25 mm. The ribs were tested with the geometric centre (G.C.) placed at two radial locations. Jet-to-plane distance was H/D=6, and Re=20,000. The geometric centre is where the flow meets with heated surface when ejected from the nozzle. Two angles of inclination for the jet were used α=45º and 60º. Thus a total of 48 simulations cases (4*6*2) were performed.

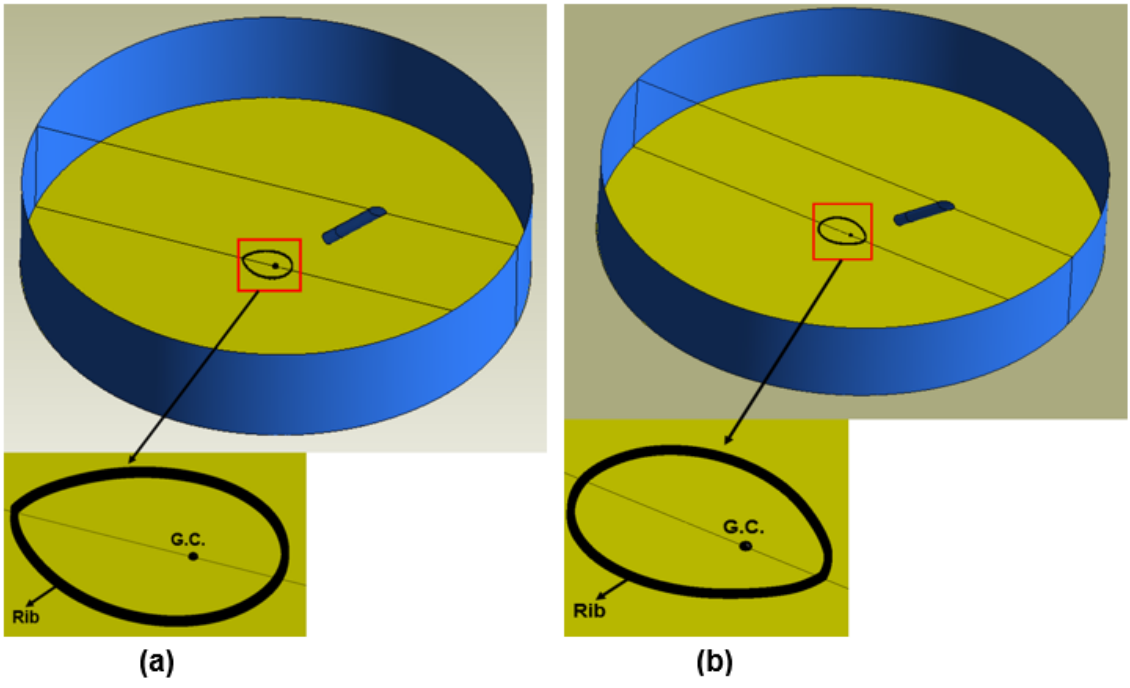

Figure 6-1: Geometry details of (a) Dropped tear, (b) Reversed dropped tear.

Figure 6-1 and Table 6-1 show the plan view of the two rib shapes used in this chapter. The orientation was made relative to the G.C. The downhill direction is in the direction of L_2 for the tear drop rib (the less sharp end is pointed downhill) and L_3 for the reversed tear drop rib (the sharper end is pointed downhill). This chapter is divided into two sections based on the tear drop shaped rib and the reversed tear drop rib. Each section includes the effect of varying rib height (e) and location (R) on the normalised average Nu.

Table 6-1 : Geometry details of dropped tear and reversed dropped tear ribs

Dropped Tear Rib	Dropped Tear Rib	Reversed Dropped Tear Rib	Reversed Dropped Tear Rib
Shape A	Shape B	Shape C	Shape D
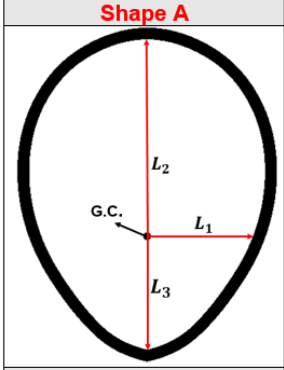	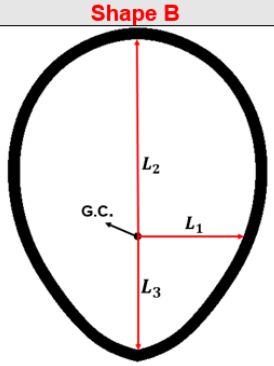	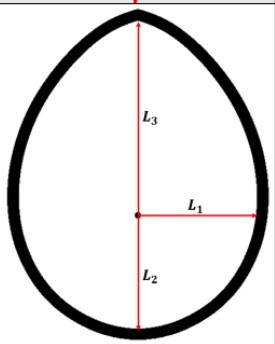	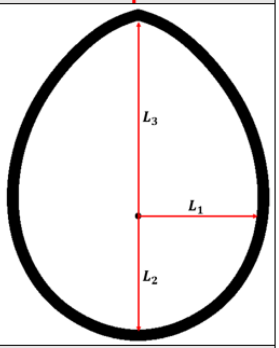
L1= 14 mm	L1= 17.5 mm	L1= 15 mm	L1= 17.5 mm
L2= 25.5 mm	L2= 36.5 mm	L2= 14 mm	L2= 17.5 mm
L3= 15 mm	L3= 17.5 mm	L3= 25.5 mm	L3= 36.5 mm

All detailed simulations will be presented for heights of e=0.25, 0.75, and 1.50 mm. However, Results for normalised average Nu will be presented for all the six rib heights.

6.1.1 The effect of using Tear Drop Rib

The minority of the flow from an inclined impinging jet travels in the uphill direction. Generally, the lower the jet angle, the lower the heat transfer in the uphill direction before it approaches zero at short radial distances from the G.C. However, the local heat transfer can be enhanced by the presence of a rib, but to maximise the heat transfer rate in the uphill direction, the rib should be appropriately designed and located.

I. Shape A

Figure 6-2 shows local Nu contours for tear drop rib for three rib heights e=0.25, 0.75 and 1.50 mm and two angles of inclination of the jet. The sharper end of the rib is located in the uphill direction at a radial distance L_3=15.0 mm (≈1.15D, since the nozzle is 13.5 mm diameter). The figure shows an obvious enhancement in heat transfer especially in the uphill direction. Some enhancement is also noticeable outside the rib due to flow recirculation. In the downhill direction the wake region behind the rib increases the heat transfer. In the uphill direction the wake region after the rib seems reduced and heat transfer is not enhanced so much. For α=45º, the wake region is minimum when rib height is e=0.25 mm and increases as the rib height increases. However, while the footprint of the wake shows symmetry, it is non-uniform.

For α=60º, overall the local Nu contours in the downhill direction show much the same behaviour as for α=45º. However, in the uphill direction, the figure shows that for rib heights of e=0.75 mm and e=1.50 mm while there is enhancement of local Nu it is not so great as for the lower angle of inclination.

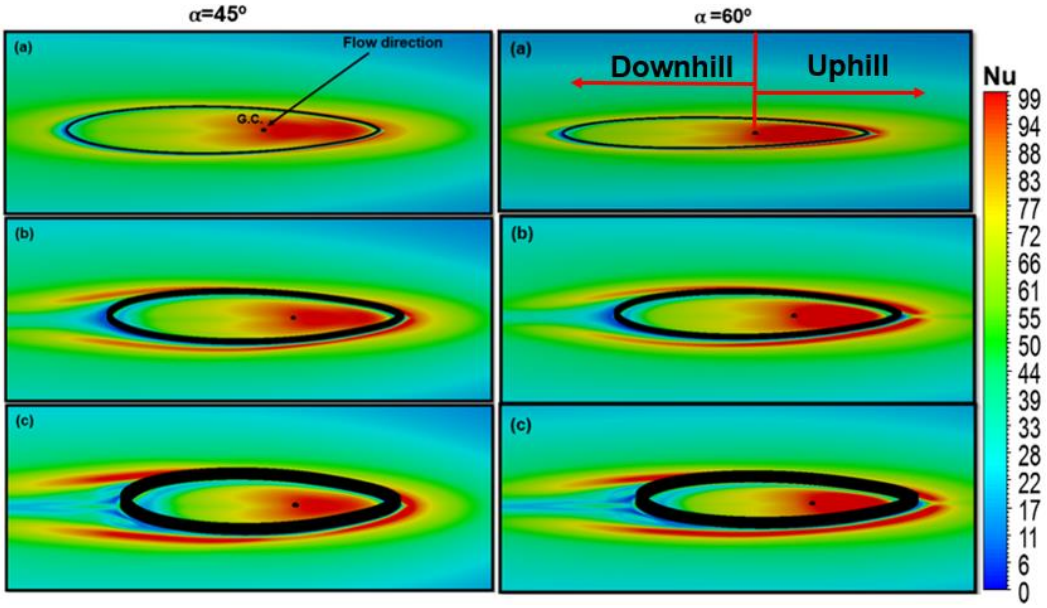

Figure 6-2: Local Nu contours, Shape A, Re=20,000, H/D=6, (a) e= 0.25 mm, (b) e= 0.75 mm and (c) e=1.50 mm.

The effect of this rib shape on the jet flow was further investigated. Figure 6-3 shows the turbulence kinetic energy (TKE) contours for three rib heights and two inclined jet angles. The figure shows that the flow turbulence increased in the uphill direction for both angles. This enhancement in flow turbulencs is shown by the red region where maximum enhancement can be seen for e=0.25 mm for both angles. In the uphill direction the flow TKE is more pronounced for α=45º than for α=60º. This is due to lower flow velocity in this direction for the lower angle. In the downhill direction, a noticeable enhancement in the flow turbulence is shown behind the roughness element for rib height e=0.75 mm, this is more pronounced for α=45º. For e=1.50 mm, the contour footprint shows a continuous wake region downstream the rib, commencing immediately behind the rib. This is due to differences in the flow pressure magnitudes in this region slowing the local flow velocity to almost zero.

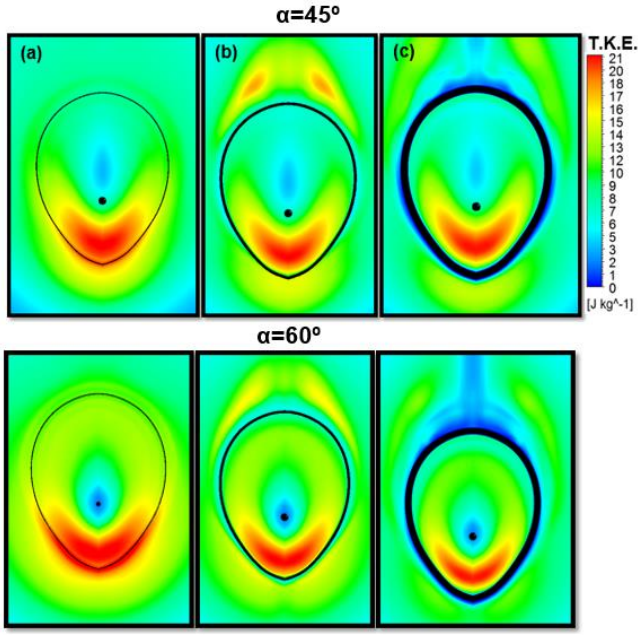

Figure 6-3: Plan view of flow turbulence kinetic energy contours for two angles of inclination, α=45º and α=60º. Re=20,000, H/D=6, (a) e= 0.25 mm, (b) e= 0.75 mm and (c) e=1.50 mm

The effect of rib height on the normalized average Nu for -4≤r/D≤4 for both inclined jet angles is shown Figure 6-4. Changing the plan shape of the rib from a circle to a tear drop gives, overall, a noticeably enhanced heat transfer, as

shown in the figure for both angles of inclination of the jet. The lower jet inclination angle shows an overall better average heat transfer enhancement than the higher. The maximum enhancements for α=45º and 60º are 9.5% and 5.5%, respectively and these occur at rib height e=0.25 mm. In addition, unlike the case of a circular rib, with a tear drop rib shape, all six rib heights show heat transfer enhancement. These are 9.5%, 8.6%, 8.4%, 8.1%, 7.6% and 6.3%, respectively for the six rib heights at α=45º. For α=60º, the enhancements are between 5.5% and 2.8% for rib heights between 0.25 mm and 1.50 mm, see Figure 6-4.

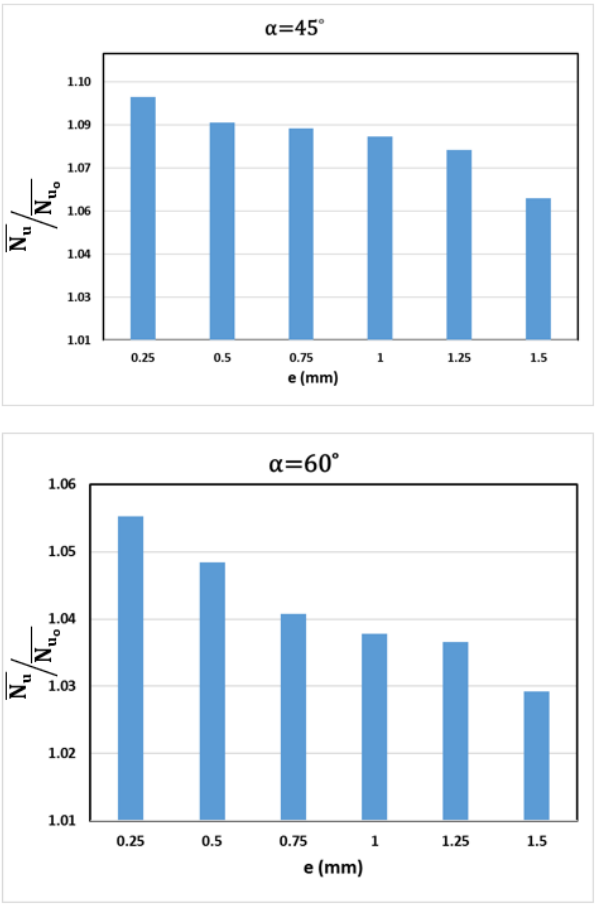

Figure 6-4 : Effect of rib height on normalized average Nu, Shape A, Re= 20,000, H/D=6.

II. Shape B

In order to investigate changing the rib shape and size on the normalised average Nu, the rib dimensions were changed for shape B as shown in Table 6-1. The rib was both enlarged so that L_1 = L_3 = 17.5 mm (=1.3D), and stretched in the downhill direction so that L_2 = 36.5 mm (=2.7D). This means that the rib was shifted downstream in all radial directions.

In general, the local Nu contours shown in Figure 6-5 show similar footprints to shape A, but with a lower heat transfer rate in all directions. This is due to the lower momentum the flow has when travelling a greater distance to the rib, particularly for α=45º in the uphill direction. The wake areas in the uphill directions are minimal for all rib heights. In the downhill direction they are maximums for e=0.75 mm and e=1.50 mm. The stagnation region (shown as the red area within the rib boundaries) does not appear to be significantly effected by rib height for α=45º, but for the larger angle of inclination, it appears that this region gets smaller with increasing rib height. Overall, for shape B the there is less heat transfer enhancement than for shape A.

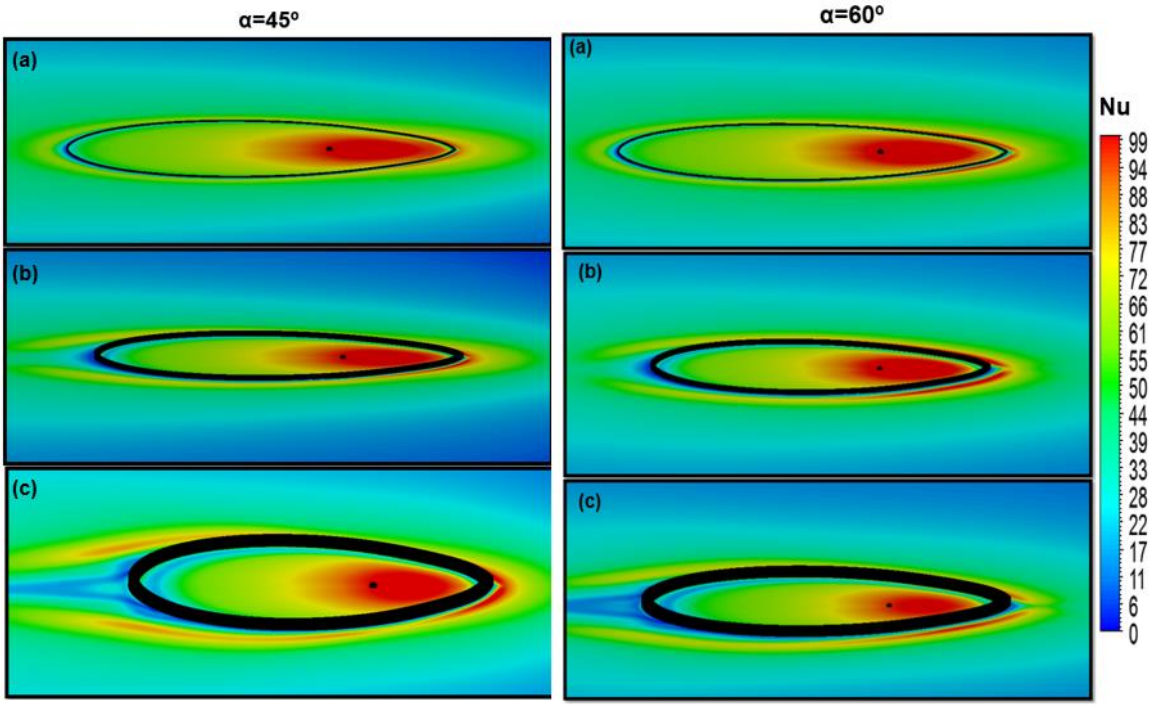

Figure 6-5: Local Nu contours for Shape B, Re=20,000, H/D=6, (a) e= 0.25 mm, (b) e= 0.75 mm and (c) e=1.5 mm.

Figure 6-6 shows the TKE distributions for the shape B rib for three heights. In general, as the rib height increases, flow turbulence increases as does the wake area behind the obstruction. The figure demonstrates this fact especially for e=1.50 mm where both the flow TKE and the wake areas are obvious for both angles of inclination. In the uphill direction, the rib with height e=0.25 mm seems to give better heat transfer enhancement for both angles when compared to the other two heights. In the downhill direction where the majority of the flow rate takes place, the figure shows that the flow present for α=45º has greater TKE than that for α=60º.

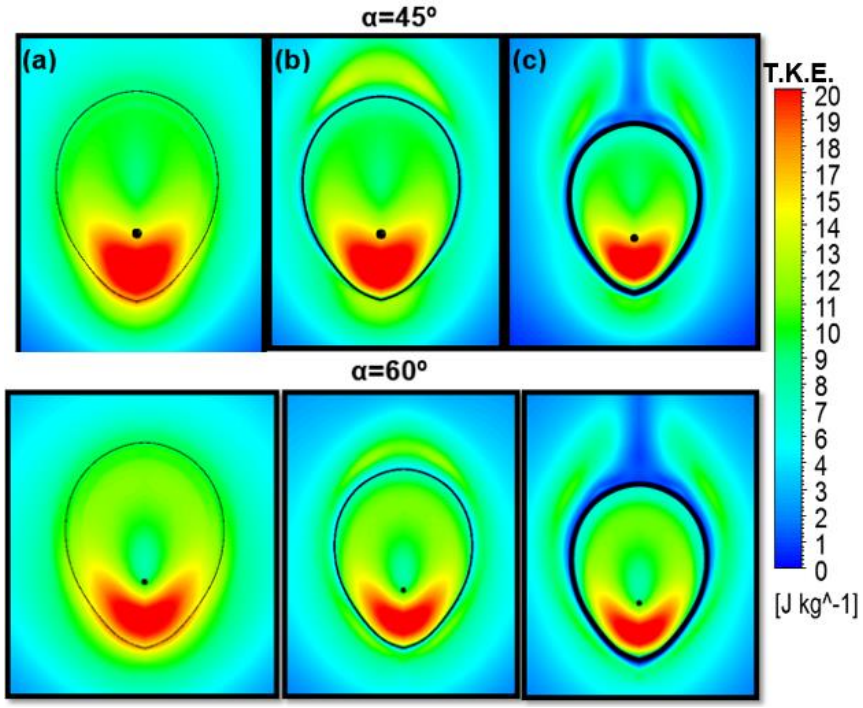

Figure 6-6: Top view of turbulence kinetic energy contours for shape B, Re=20,000, H/D=6, (a) e= 0.25 mm, (b) e= 0.75 mm and (c) e=1.5 mm

The impact of using shape B on the normalised Nu averaged over a surface area of -4≤r/D≤4 for six rib heights is shown in Figure 6-7 The impact of using shape B on the normalised Nu averaged over a surface area of -4≤r/D≤4 for six rib heights is shown in Figure 6-7. For α=45º, a noticeable improvement in heat transfer rate is seen when compared to shape A. Shape B gives an enhancement in heat transfer rate of 12.4% for e=0.25 mm which is about 25% extra compared to shape A with the same rib height This enhancement continues for all rib heights where the minimum enhancement was 8.0% for rib height e=1.50 mm, that is 20% more than for shape A. For α=60º, the heat transfer enhancement was limited to rib heights e≤0.75 mm with maximum enhancement of 4.2% at e=0.25 mm, with 3.1% and 2% for rib heights e= 0.50 mm and 0.75 mm respectively. When the rib height was greater than 1 mm, the average Nu shows a lower heat transfer rate compared to the baseline case. This is due to the large wake areas behind and both sides of the rib.

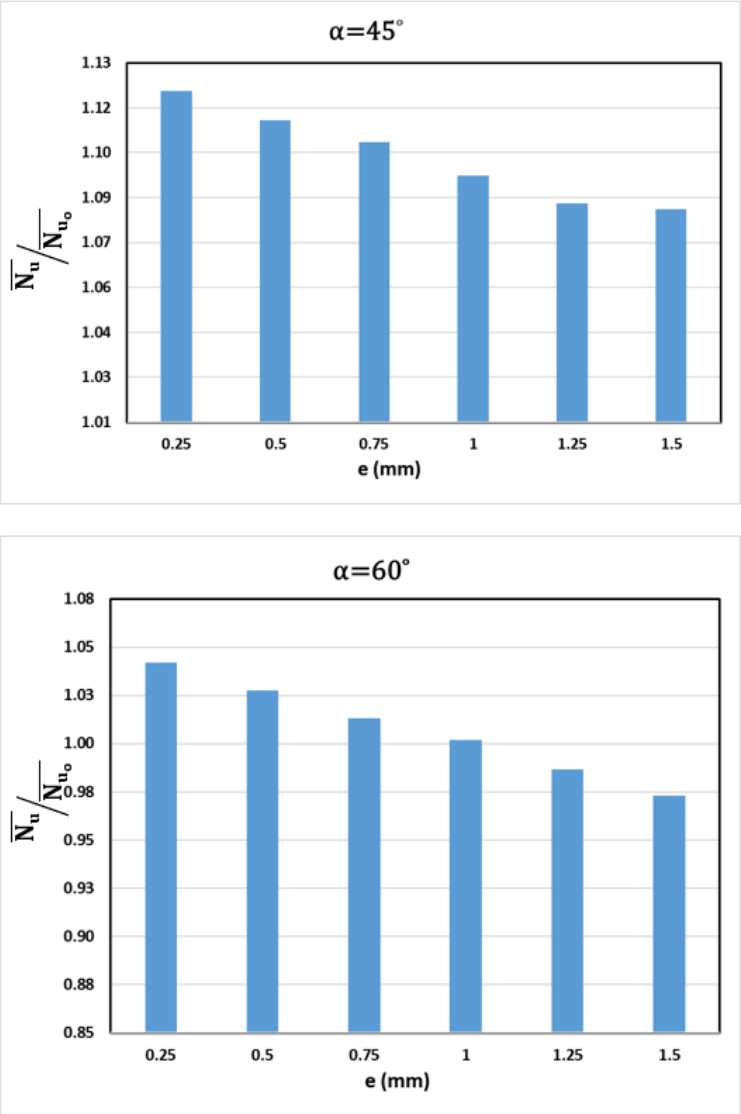

Figure 6-7 :Effect of rib height on normalized average Nu, Shape B, Re= 20,000, H/D=6

6.1.2 The effect of using Reversed Dropped Tear Rib

III. Shape C

As shown in Table 6-1 shape C was almost shape A rotated through 180^0. However there was one additional and important difference, the maximum width of shape A was 32.5 mm and this was located about 8.5 mm downhill from the G.C., shape C has a maximum width of 28.0 mm positioned at the G.C. This geometry provided a wider rib edge in the uphill direction which is of interest in terms of improving heat transfer in the direction of minority flow.

Figure 6-8 shows the Nu contours for shape C for three rib heights and two angles of inclination. A noticeable heat transfer enhancement can be seen in the uphill direction for both angles, but is more pronounced for the larger, 60^o angle. This enhancement exists on both sides of the rib but starts to diminish in the downhill direction. Turning the drop around so the sharper end points downhill seems to minimize the wake regions in the downhill direction where flow interactions occur in the area just behind the rib. The enhancement in Nu on the rib sides does not occur directly adjacent to the rib but a small distance away from it, and this distance increases as the rib height increases. This is due the curvature of the rib. Except for rib height e=1.50 mm, all rib heights seem to noticeably enhance the heat transfer rate in both uphill and downhill flow directions

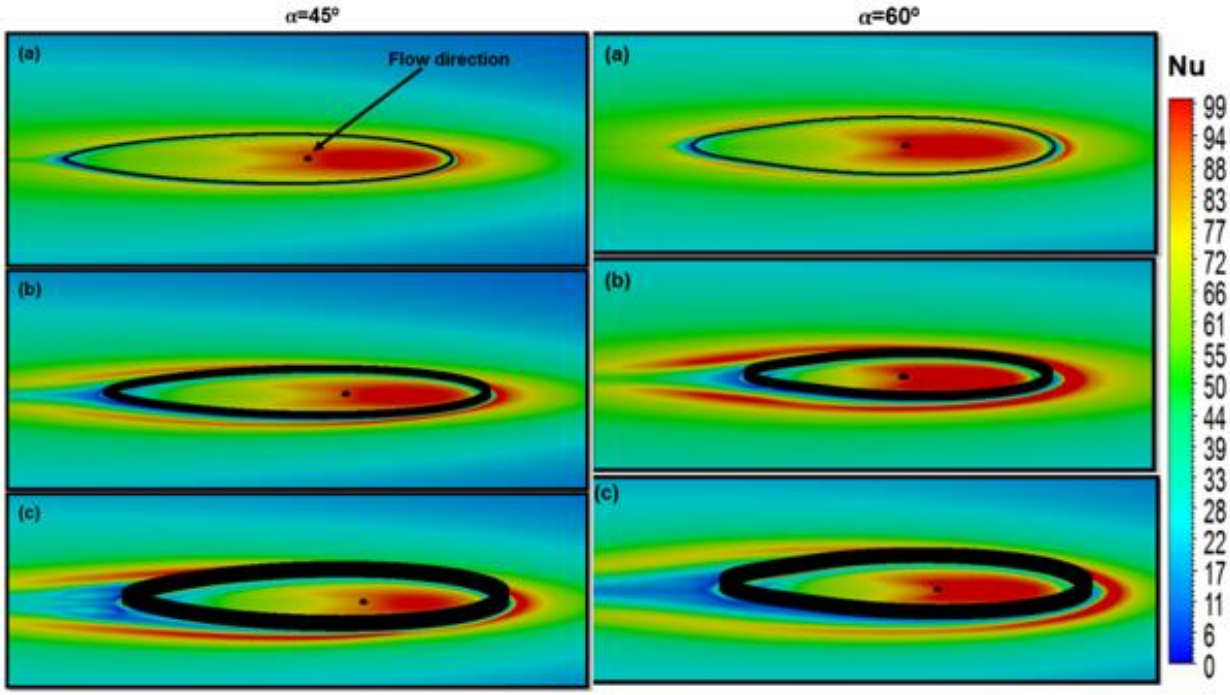

Figure 6-8: Local Nu contours for Shape C, Re=20,000, H/D=6, (a) e= 0.25 mm, (b) e= 0.75 mm and (c) e=1.5 mm.

The TKE contours of the flow for the reversed tear drop rib for two jet angles and three rib heights are shown in Figure 6-9.

The TKE of the flow is effected not only by the rib shape but also by the rib height, as shown by the assorted colours. The blue area shows low flow turbulence which commenced around the G.C. and extended in the uphill direction. When the flow meets the edge of the rib then, depending on the rib height, the flow can gain turbulence due to flow recirculation before and after the rib. Rib heights of 0.25 and 0.75 mm show an obvious flow turbulence enhancement for both angles of incidence. Overall, except for the rib height e=1.50 mm, all rib heights show an enhancement in the flow turbulence. For e=1.50 mm, the flow experiences significant drag due to the presence of the roughening elements which affects its turbulence, resulting in an obvious decrease which start from the geometric centre and grows in the downhill direction. The presence of the rib generates secondary flows with different physical properties such as pressure and velocity and which affect the flow turbulence especially for higher ribs.

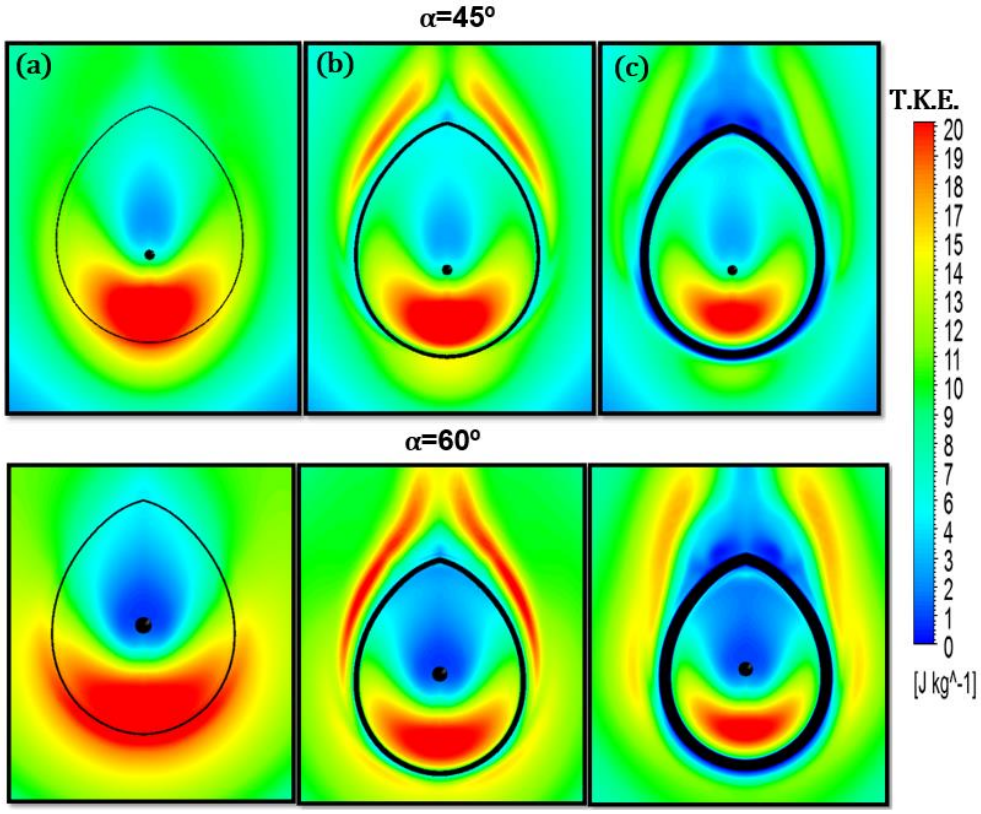

Figure 6-9: Top view of turbulence kinetic energy contours for shape C, Re=20,000, H/D=6, (a) e= 0.25 mm, (b) e= 0.75 mm and (c) e=1.5 mm

The effect of the rib height on the normalised average Nu for both angles of incidence is shown in Figure 6-10. For α=45º, all rib heights expect for e=1.50 mm, show greater heat transfer enhancement than tear drop shape A. The enhancement achieved by using a rib height of 0.25 mm reached approximately 11.0%, an increase of about 15% for the same rib height for shape A. The rib heights between 0.50 mm and 1.25 mm give heat transfer enhancement of between 9.3% and 8.3%. Overall, except for the rib height e=1.50 mm, the reversed tear drop rib shows an obvious improvement in heat transfer rate with α=45º. This is due the noticeable enhancement of Nu in the uphill direction as shown in Figure 6-8.

As for α=60º, the maximum heat transfer enhancement happens at rib height e=0.25 mm with an enhancement of 4.7%. This level of enhancement diminishes as e increases with values of 3%, 3.1% and 2.8% respectively for e= 0.50, 0.75 and 1.00 mm. For heights of 1.25 and 1.50 mm, the heat transfer rates fall below

the baseline case due to the drag caused by the ribs resulting in larger wake regions.

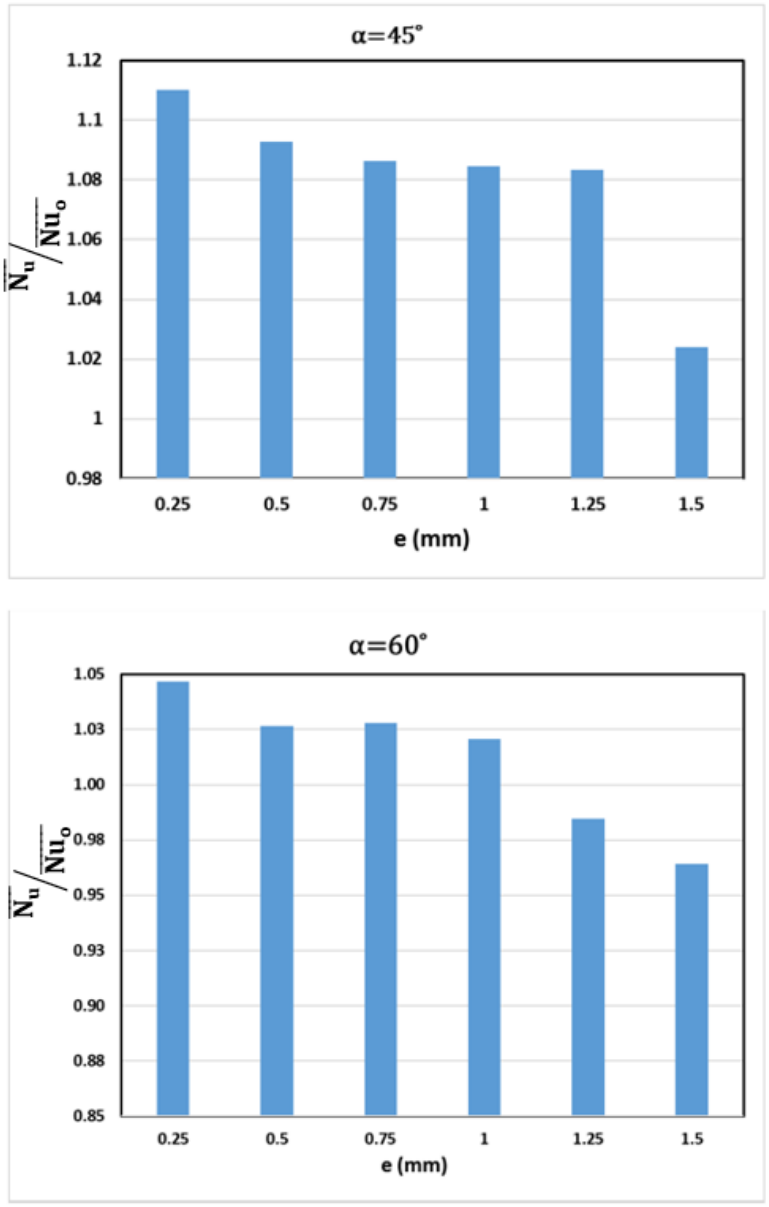

Figure 6-10: Effect of rib height on normalized average Nu, Shape C, Re= 20,000, H/D=6

IV. Shape D

As shown in Table 6-1 shape D was almost shape B rotated through 180^0. But, once again, there was one additional and important difference, the maximum width of shape B was 40.5 mm and this was about 8.5 mm downhill from the G.C. Shape B has a maximum width of 35.0 mm positioned at the G.C. This geometry placed the less narrow end in the uphill direction which is of interest for improving heat transfer in the direction of minority flow.

Contours of the local Nu footprint are shown in Figure 6-11. The figure demonstrates that, as the rib height increases so does the heat transfer rate for both angles of incidence, this is obvious in the uphill direction. Enhancement also occurs on both sides of the rib, but less in the downhill direction. The flow outside the rib continues to transfer heat as it moves forward in the downhill direction. Regardless of the angle of incidence, rib height e=0.25 mm shows the minimum heat transfer loss when compared to the other heights. Obvious wake regions can be seen for the higher ribs, mostly behind the sharper end of the rib in the downhill direction. The higher the rib, the larger the wake areas and the lower the average Nu.

For $\alpha=45^o$, a small region of heat transfer enhancement occurs within the wake region just behind the sharper end of the rib for e=1.50 mm. This enhancement is due to flow interactions that occur in this region. This is not the case for $\alpha=60^o$ where a long wake region occurs just behind the sharper end.

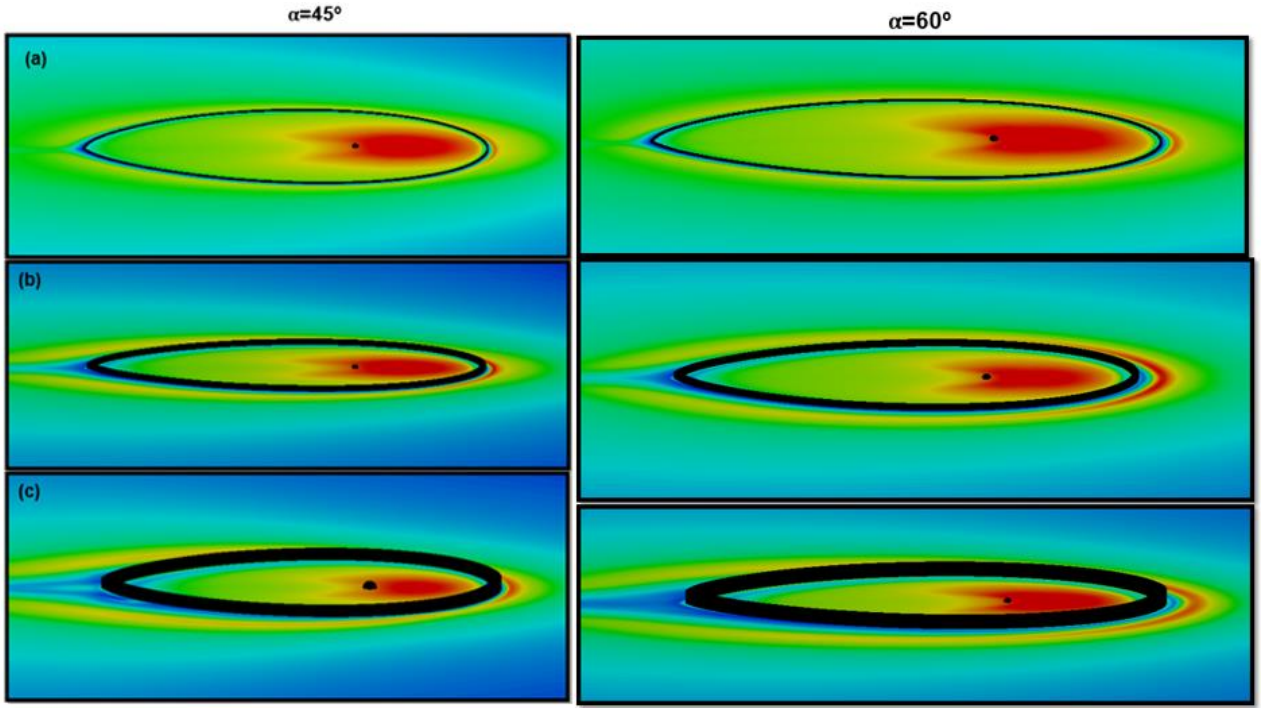

Figure 6-11: Local Nu contours for Shape D, Re=20,000, H/D=6, (a) e= 0.25 mm, (b) e= 0.75 mm and (c) e=1.5 mm.

The TKE of the flow plays a major role in enhancing the heat transfer rate, increasing this turbulence disturbs the flow boundary layer, thus enhancing the heat transfer between the heated wall and the fluid. Figure 6-12 shows the TKE of the flow for three different rib heights. The same general behaviour was seen as for shapes A, B and C: the presence of a rib increases the flow turbulence and the wake areas where flow turbulence is minimal.

Most of the flow turbulence enhancement happens in three main regions, within the rib, outside of the rib and downstream the rib in the downhill direction. It can also be seen that the rib of height e=1.50 mm, produced larger regions of low turbulence for both angles of incidence.

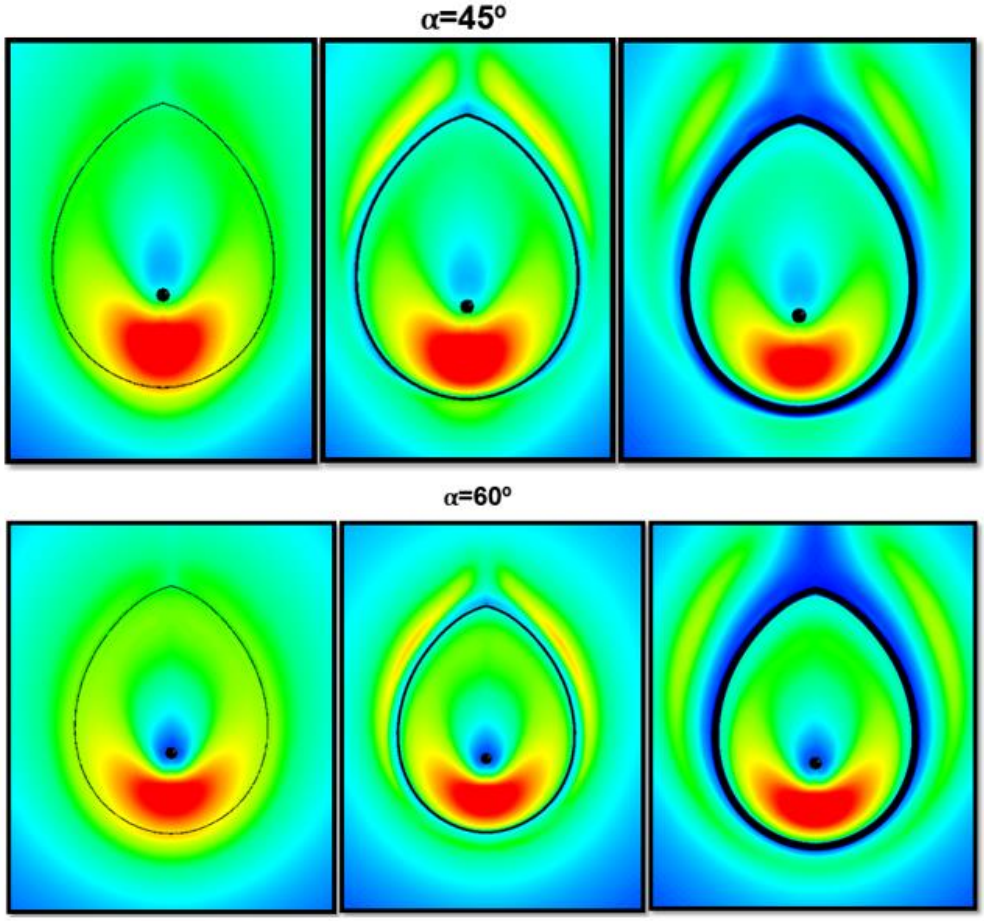

Figure 6-12: Top view of turbulence kinetic energy contours for shape D, Re=20,000, H/D=6, (a) e= 0.25 mm, (b) e= 0.75 mm and (c) e=1.5 mm

As shown in Figure 6-13, the normalised average Nu shows good enhancement for all rib heights, for angle of incidence α=45º. The maximum enhancements were 11.5% and 5.0% at e=0.25 mm for α=45º and α=60º respectively. This increase reduced as rib height increased; to 9.8%, 8.2%, 7.8%, and 6.7% for rib heights of 0.50, 0.75, 1.00, and 1.25 mm, respectively for α=45º. However, for α=60º, this rib shape enhances the heat transfer rate only for rib heights of 0.25 and 0.50 mm, 5.0% and 3.1%, respectively. Generally, shape D appears to be more efficient with less flow in the uphill direction (i.e. lower α).

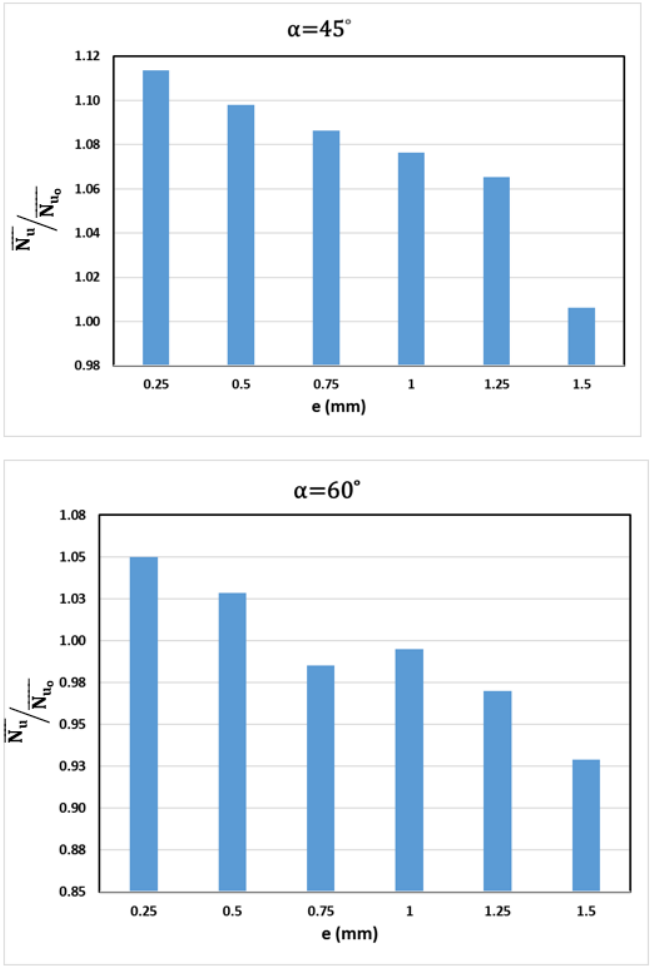

Figure 6-13: Effect of rib height on normalized average Nu, Shape D, Re= 20,000, H/D=6

Care should be taken when designing the rib as rib height should be taken into account.

6.1.3 Comparison of results

An overall comparison of the effect of using the non-uniform rib shapes for different rib heights and radial locations on the normalized average Nu for two angles of jet inclination is shown Table 6-2. As shown in the table, for both angles of inclination, all four rib geometries investigated showed enhanced heat transfer of between 4.2% to 12.4% by using the optimum rib height.

Table 6-2 summarises key findings in this chapter. In conclusion, the heat transfer rate could be significantly and noticeably enhanced using dropped-tear and reversed dropped-tear rib configurations. For α=45º, the optimum rib height is 0.25 mm giving a maximum heat transfer percentage of 12.4%by using shape B. However, for α=60º with same rib height (e), the use of shape A enhances the heat transfer rate by 5.5%

Table 6-2: Average Nu and optimum height for non-uniform rib shapes

Parameter	Shape A		Shape B		Shape C		Shape D	
α	45°	60°	45°	60°	45°	60°	45°	60°
e (mm)	0.25	0.25	0.25	0.25	0.25	0.25	0.25	0.25
$\overline{N_u}$	9.5%	5.5%	12.4%	4.2%	11%	4.7%	11.5	5%

6.2 Closing Remarks

The majority of flow ejected from inclined nozzles flows downhill, with less flow travelling in the opposite (uphill) direction. The flow in the uphill direction will become stationary at some radial distance, depending on the jet Reynold's number and the angle of inclination.

Designing a rib that maximises heat transfer rate in the uphill direction was the aim of this chapter. The rib design was based on two ideas, (i) placing a roughening element close to the stagnation point, and (ii) have the optimum rib height to maximize flow turbulence. Two rib geometries were tested in this chapter, the tear drop and the reverse tear drop. Each geometry was also tested in two different sizes.

The heat transfer rate was investigated by determining the normalised average Nusselt number over the surface area between $-4 \leq r/D \leq 4$, where most of the heat transfer enhancement occurs. The simulated Nu was normalized to the simulated average Nu in the case where no rib was used (the baseline case).

The simulation was carried out for two jet inclination angles, $\alpha=45^{o}$ and 60^{o}, Re=20,000, and jet-to-target distance (H/D) =6. Overall results show enhancement in heat transfer rate for both angles but this was more pronounced for $\alpha=45^{o}$ than for 60^{o}.

For $\alpha=45^{o}$, all four rib geometries investigated showed enhanced heat transfer of between 6.0% to 12.0%. In each case the maximum enhancement was for rib height e=0.25 mm; 9.5%, 12.4%, 11.0% and 11.5% respectively for shapes, A, B, C and D. For all rib shapes and heights examined there was an increase in heat transfer rate except for the one case of e=1.50 mm with shape D.

For $\alpha=60^{o}$, the maximum enhancements in heat transfer rate were all for e=0.25 mm and were 5.5%. 4.2%, 4.7% and 5.0% respectively for shapes, A, B, C and D. Enhanced heat transfer was consistently obtained only for $e \leq 0.50$ mm.

7 Conclusion

The purpose of this research was to investigate the effect of surface roughness on heat transfer using the commercial software package ANSYS 16.2. This was achieved by investigating the heat transfer in two cases: a smooth, horizontal surface (the baseline case) and the same surface with different roughness elements added to it. The roughness elements took the shapes of hemispherical pin-fins, square pin-fins and a continuous rib in the shape of a circle or tear drop. The rib roughness element was further investigated by varying its height and location to study its impact on the average Nu. Results are presented in the form of average Nusselt number $\overline{N_u}$ within and beyond the stagnation region.

All roughness elements were considered to be an adiabatic wall where no heat transfer either to or from them. Each roughness element was tested for six different heights (e) from 0.25 mm to 1.50 mm in incremental steps of 0.25 mm under the influence of different jet angles (α) of 90º, 60º and 45º. This research investigated not only the effect of each roughness type but also how the roughness geometry impacted on the average Nusselt number. The jet diameter kept constant for all simulations (D=13.5mm) where the flat, horizontal plane was located at H/D = 6 below the jet. For all the tests the jet Reynolds number was 20,000.

The investigation started with a deep study of the physics of jet flow without the presence of the impinging plate, as the behaviour of a free jet is very important in characterizing and comparing flow heat transfer for different configurations of a jet impinging on a flat plate. A study of potential core length revealed that the centreline velocity was constant till an axial distance of 1.5D above the impingement surface, confirming results previously reported in the literature. The potential core length ends when the jet centreline velocity has decreased to 0.95 of the jet exit centreline velocity and it plays an important role in determining the heat transfer rate.

The study also included jet velocity (Re), vertical distance between the heated surface and the nozzle (H/D) and, finally, the effect of the jet angle (α) on the local Nu over the heated surface. Results revealed that the heat transfer rate is sensitive to all three variables. In general, the lower surface-to-target distance (H/D) and the higher Re, the higher the heat transfer rate. The maximum heat transfer for high H/D occurs at the stagnation point where the flow velocity is zero (no-slip condition) and maximum static pressure occurs. However, for low H/D, the maximum local Nu occurs at a radial distance r/D=0.5, and a secondary Nu peak occurs downstream on the heated surface.

As for inclined jets, angles of impingement (α) 45^0, 60^0 and 75^0 were used to simulate oblique flow for Re=10,000 and 20,000, for H/D=2 and 6. Results showed that as α decreased the stagnation point moved away from the geometric center in an uphill direction to a location that was a function of impingement angle but largely independent of H/D.

Further investigations were carried out to examine the effect of simulated surface roughness on heat transfer. This was achieved by investigating the heat transfer features for the surface with three different roughness elements added: hemispherical pin-fins, cubical pin-fins and a square cross-sectional continuous rib. Results are presented in the form of average Nusselt number $\overline{N_u}$ within and beyond the stagnation region.

All roughness elements were considered to be an adiabatic wall where no heat transfer occurred to or from them. Each roughness element was tested for six different heights (e) from 0.25 mm to 1.50 mm in incremental steps of 0.25 mm for three different jet angles (α) of 90º, 60º and 45º. The first three roughness elements were arranged in a circle concentric with the geometric centre (i.e. centre of jet) with a radius of one and a half jet diameters (R/D = 1.5) in order to be within the stagnation region. Results for orthogonal impinging jet showed that both the hemispherical and the cubical pin-fin roughness elements gave an overall higher heat transfer rate than the square cross-section continuous rib. For an orthogonal jet, the increase of the average heat transfer was enhanced by up to

7.2% compared to the baseline case; this was for e=0.50 mm using cubical pin-fins. Both hemispherical and ribbed roughness elements showed an increase in average Nu of between 2.7% and 5.9% depending on roughness element height.

However, for Inclined jets, the average Nu seems to be very sensitive to both the height of the roughness element and their number. The study was made to show the simulated $\overline{N_u}$ for the three roughened surfaces, six heights and two angles of inclination of the jet used. The average Nu for baseline case over the same area are 54.9 and 63.0 for α=45º and α=60º, respectively. It can be seen that, for α = 45º and 60º, the optimum rib height is 1.50 mm where the increase in $\overline{N_u}$ could be between 5.7% and 6.4%, obtained by employing a hemispherical pin-fin roughness element. However, roughness elements with other heights and shapes could give lower heat transfer rate when compared to the baseline case.

The research continues to study the effect on the average Nu of using a continuous circular shape rib roughness element with square cross section, was further investigated. The circular roughness element was centred on the geometric centre and tested for four different radii (R= 1D, 1.5D, 2D and 3D) and six different heights (e) between 0.25 mm and 1.50 mm with an increment of 0.25 mm. The study was for an orthogonal jet and two inclined angles of jet impingement (α=45º and α=60º).

Starting with the orthogonal jet, rib heights of 1.25 and 1.50 mm reported lower heat transfer rates than the baseline case regardless of rib radius. It was also found that placing the rib, regardless of its height, in the stagnation region was ineffective when seeking to enhance heat transfer. The most effective rib location for α=90º was at R/D=2 which, based on the literature is the beginning of the wall jet region. The results showed that when using the right rib height, e=0.25 mm a maximum heat transfer enhancement of 15.6% was achieved. The range of heat transfer enhancement for the rib at R/D=2, was between 10.7% and 15.6% for rib heights e≤1.00 mm.

For jet ejected from an inclined nozzle, the most effective rib height is e=0.25 mm regardless of rib location. For α=45º, the maximum heat transfer enhancement percentage is 7.0% obtained by placing a 0.25 mm rib at a radial location of R/D=3. However, the location R/D=1 shows enhanced average Nu for all rib heights tested, giving an increase of between 6.7% at e=0.25 mm to 2.3% at e=1.50 mm as for α=60º, the maximum heat transfer enhancement reached 4.0% by placing a rib with height e=0.25 mm, at R/D=3. Ribs of height e > 0.75 mm reduced the overall heat transfer to below that of the baseline.

The investigation proceeded by considering using specially design ribs to improve the heat transfer rate for jets inclined at α=45º and 60º to the horizontal. The new rib geometries were designed after an intensive study of the flow velocity contours for inclined jets in order to come up with a design that maximises the heat transfer between the flow and the heated surface, especially in the uphill direction where the minority of the flow goes.

The rib took the shape of tear drop, see Table 6-1, whose geometric centre was located close to the stagnation point in the uphill direction. Overall results show enhancement of heat transfer rate for both angles but the improvement was more pronounced for α=45º. At this angle, all four shapes gave enhanced heat transfer of between 6% to 12% for all rib heights. As for α=60º, the enhancement in heat transfer rate was limited to rib height e≤0.50 mm. The maximum heat transfer enhancement between 4.2% and 5.5%, was for rib height e=0.25 mm. The heat transfer rate was noticeably and consistently enhanced by the use of the tear drop shaped ribs with height 0.25 mm.

Future work

This research highlighted several topics on which further researches would be useful. Several adaptions have been left for future work due to lack of time. Future work can be made to investigate the following ideas:

- The use of lower jet inclination angles ($15 \leq \alpha < 45$) for different jet to target distances (H/D)
- The use of mist cooling with different mist percentages (less than 1% and between 1% and 5%.
- The use of different non-uniform rib geometries with different rib locations for single and multiple jets.
- The use of curvature surfaces including wavy surfaces instead of flat surface.
- The use of swirling jets.
- The above suggested ideas should consider minimising the pressure loss due to the use of roughness elements.
- The roughness element should be designed to reduce the thermal stress on the edges, avoid ribs with sharp edges.
- The use of roughness element should not considerably increase the overall object weight.

Yet, every doctoral dissertation should have an end. So I rest my case!

References

1. Rolls-Royce. The jet engine. 1996. p. 292.

2. Heat transfer and cooling in gas turbines. The Propulsion and Energetics Panel 80th Symposium. Turkey: AGARD; 1993.

3. Yahya, S. M. Turbines Compressors and Fans. 2011. 430-433 p.

4. Saravanamutto, HIH. Cohen, H., Rogers G. Gas Turbine Theory. 2006.

5. Han, B., Goldstien, R. J. Jet-Impingement Heat Transfer in Gas Turbine Systems. Annals of the New York Academy of Sciences. 2001. pp. 147–161.

6. Goldstein, R. J. Film cooling. Advan Heat Transfer. 1971. pp. 321–379.

7. Almutairi, A.,S. Computation of Conjugate Heat Transfer in Impinging Flows. (Master's thesis, The University of Manchester, Manchester, UK). 2010;

8. Flack, R. D. Fundamentals of Jet Propulsion with Applications. Cambridge University Press; 2005.

9. Krewinkel, R. A review of gas turbine effusion cooling studies. International Journal of Heat and Mass Transfer. Elsevier Ltd; 2013; 66: 706–722.

10. Armellini, A., Casarsa, L., Giannatta P. Low Reynolds number flow in rectangular cooling channels provided with low aspect ratio pin fins. International Journal of Heat and Fluid Flow. Elsevier Inc.; 2010; 31(4): 689–701.

11. Jambunathan, K., Lai, E., Moss, M., A., Button, B. L. A review of heat-transfer data for single circular jet impingement. International Journal of Heat and Fluid Flow. 1992; 13(2): 106–115.

12. Sushil, S., G., Sonawane , C. R. Numerical Simulation of Gas Turbine Blade Cooling for Enhancement of Heat Transfer of the Blade Tip.

International Journal of Research in Engineering and Technology. 2014; Vol. 03(9): 35–41.

13. Sporer D., Refke A., Dratwinski M., Dorfman M., Metco S., Giovannetti I., et al. New high-temperature seal system for increased efficiency of gas turbines. Sealing Technology. 2008; 2008(10): 9–11.

14. Zuckerman, N., Lior N. Jet impingement heat transfer: Physics, correlations, and numerical modeling. Advances in Heat Transfer. 2006; 39(C): 565–631.

15. Cziesla T., Biswas G., Chattopadhyay H., Mitra NK. Large-eddy simulation of flow and heat transfer in an impinging slot jet. International Journal of Heat and Fluid Flow. 2001; 22(5): 500–508. Available at: DOI:10.1016/S0142-727X(01)00105-9

16. Chen, C. J. and Jaw SY. Fundamentals of Turbulence Modeling. Taylor&Francis. 1998;

17. Craft TJ., Graham LJW., Launder BE. Impinging jet studies for turbulence model assessment-II. An examination of the performance of four turbulence models. International Journal of Heat and Mass Transfer. 1993; 36(10): 2685–2697.

18. Cooper D., Jackson DC., Launder BE., Liao GX. Impinging jet studies for turbulence model assessment-I. Flow-field experiments. International Journal of Heat and Mass Transfer. 1993; 36(10): 2675–2684.

19. Heyerichs K., Pollard A. Heat transfer in separated and impinging turbulent flows. International Journal of Heat and Mass Transfer. 1996; 39(12): 2385–2400.

20. Craft TJ., Launder BE., Suga K. Development and application of a cubic eddy-viscosity model of turbulence. International Journal of Heat and Fluid Flow. 1996; 17(2): 108–115.

21. Wilcox DC. Turbulence Modeling For CFD. DCW Industries, La Can˜ada,

CA. 2002;

22. Park TH., Choi HG., Yoo JY., Kim SJ. Streamline upwind numerical simulation of two-dimensional confined impinging slot jets. International Journal of Heat and Mass Transfer. 2003; 46(2): 251–262.

23. Chen Q., Modi V. Mass transfer in turbulent impinging slot jets. International Journal of Heat and Mass Transfer. 1999; 42(5): 873–887.

24. Gardon, R., Akfirat, C. J. The role of turbulence in determining the heat-transfer characteristics of impinging jets. International Journal of Heat and Mass Transfer. 1965; 8: 1261–1272.

25. Wang, B., X., Xie, Q., Wang, Z., D., Wang, G. D. Fluid flow characteristics of single inclined circular jet impingement for ultra-fast cooling. Journal of Central South University. 2013; 20(11): 2960–2966.

26. Katti, V., Sudheer, S., Prabhu, S. V. Pressure distribution on a semi-circular concave surface impinged by a single row of circular jets. Experimental Thermal and Fluid Science. 2013; 46: 162–174.

27. Katti, V., Prabhu, S. V. Experimental study and theoretical analysis of local heat transfer distribution between smooth flat surface and impinging air jet from a circular straight pipe nozzle. International Journal of Heat and Mass Transfer. 2008; 51(17–18): 4480–4495.

28. Lin, Z., H., Chou, Y., J., Hung, Y. H. Heat transfer behaviors of a confined slot jet impingement. International Journal of Heat and Mass Transfer. 1997; 40(5): 1095–1107.

29. Ichimiya K., Yamada Y. Three-Dimensional Heat Transfer of a Confined Circular Impinging Jet With Buoyancy Effects. Journal of Heat Transfer. 2003; 125(2): 250.

30. Schlichting, H. Boundary-layer theory. SchEuropean Journal of Mechanics - B/Fluids. 1979;

31. Tani, I., Komatsu Y. Impingement of a round jet on a flat surface. Proc. of the Eleventh International Congress of Applied Mechanics (H. Gortler, Ed.), Springer-Verlag, New York. 1966; : 425–448.

32. Giralt, F., Chia, C., Trass O. Characterization of the Impingement Region in an Axisymmetric Turbulent Jet. 1977; 16(1): 21–28.

33. Ashforth-Frost, S.,Jambunathan K. Effect of nozzle geometry and semi-confinement on the potential core of a turbulent axisymmetric free jet. International Communications in Heat and Mass Transfer. 1996; 23(2): 155–162.

34. Li, Y., Ming X. Oscillations of a planar impinging jet induced by a potential-core confined airfoil. European Journal of Mechanics, B/Fluids. Elsevier Masson SAS; 2016; 57: 40–49.

35. Elison, B., Webb, B. W. Local heat transfer to impinging liquid jets in the initially laminar, transitional, and turbulent regimes. International Journal of Heat and Mass Transfer. 1994; 37(8): 1207–1216.

36. Ashforth-Frost, S., Jambunathan, K., Whitney, C. F. Velocity and turbulence characteristics of a semiconfined orthogonally impinging slot jet. Experimental Thermal and Fluid Science. 1997; 14(96): 60–67.

37. Hwang, S., D., Lee, C., H. Cho, H. H. Heat transfer and flow structures in axisymmetric impinging jet controlled by vortex pairing. International Journal of Heat and Fluid Flow. 2001; 22(3): 293–300.

38. Guo, Y., Wood, D. H. Measurements in the vicinity of a stagnation point. Experimental Thermal and Fluid Science. 2002; 25(8): 605–614.

39. Narayanan, V., Seyed-Yagoobi, J., Page, R. H. An experimental study of fluid mechanics and heat transfer in an impinging slot jet flow. International Journal of Heat and Mass Transfer. 2004; 47(8–9): 1827–1845.

40. Oyakawa, K., Umeda, A., Islam, M., D., Saji, N., Matsuda S. Flow structure and heat transfer of impingement jet. Heat and Mass Transfer. 2009; 46:

53–61.

41. Garimella,S. Nozzle-geometry effects in liquid jet impingement heat transfer. International Journal of Heat and Mass Transfer. 1996; 39(14): 2915–2923.

42. Ma, C., F., Zheng, Q., Sun, H., Wu K. Local characteristics of impingement heat transfer with oblique round free-surface jets of large Prandtl number liquid. International Journal of Heat and Mass Transfer. 1997; 40(10): 2249–2259.

43. Ma, C., F., Zheng, Q., Sun, H., Wu, K., Horii K. Local convective heat transfer from a vertical flat surface to oblique submerged impinging jets of large Prandtl number liquid. Experimental Thermal and Fluid Science. 1998; 17(3): 238–247.

44. Gabour, L. a., Lienhard, J. H. Wall Roughness Effects on Stagnation-Point Heat Transfer Beneath an Impinging Liquid Jet. Journal of Heat Transfer. 1994; 116(February): 81.

45. Bouchez, J., P., Goldstein, R. J. Impingement cooling from a circular jet in a cross flow. International Journal of Heat and Mass Transfer. 1975; 18(6): 719–730.

46. Goldstein, R., J., Timmers, J. F. Visualization of heat transfer from arrays of impinging cooling. 1982; 25(12): 1857–1868.

47. Colucci, D., W., Viskanta R. Effect of nozzle geometry on local convective heat transfer to a confined impinging air jet. Experimental Thermal and Fluid Science. 1996; 13(1): 71–80.

48. Brignoni, L., A., Garimella, S. V. Effects of nozzle-inlet chamfering on pressure drop and heat transfer in confined air jet impingement. International Journal of Heat and Mass Transfer. 2000; 43(7): 1133–1139.

49. Goldstein, R., J., Behbahani, A., I., Heppelmann, K. K. Streamwise distribution of the recovery factor and the local heat transfer coefficient to

an impinging circular air jet. International Journal of Heat and Mass Transfer. 1986; 29(8): 1227–1235.

50. Lee, J., Lee, S. J. Stagnation Region Heat Transfer of a Turbulent Axisymmetric Jet Impingement. Experimental Heat Transfer. 1999; 12(2): 137–156.

51. Hoogendoorn, C. J. The effect of turbulence on heat transfer at a stagnation point. International Journal of Heat and Mass Transfer. 1977; 20(12): 1333–1338.

52. Zu, Y., Q., Yan, Y., Y., Maltson J. Numerical Study on Stagnation Point Heat Transfer by Jet Impingement in a Confined Narrow Gap. Journal of Heat Transfer. 2009; 131(9): 94504.

53. San, J., Y., Shiao, W. Z. Effects of jet plate size and plate spacing on the stagnation Nusselt number for a confined circular air jet impinging on a flat surface. International Journal of Heat and Mass Transfer. 2006; 49(19–20): 3477–3486.

54. Lee, J., Lee, S. J. The effect of nozzle configuration on stagnation region heat transfer enhancement of axisymmetric jet impingement. International Journal of Heat and Mass Transfer. 2000; 43(18): 3497–3509.

55. Kendoush, A A. Theory of stagnation region heat and mass transfer to fluid jets impinging normally on solid surfaces. Chemical Engineering and Processing: Process Intensification. 1998; 37(3): 223–228.

56. Sakakibara, J., Hishida, K., Maeda M. Vortex structure and heat transfer in the stagnation region of an impinging plane jet (simultaneous measurements of velocity and temperature fields by digital particle image velocimetry and laser-induced fluorescence). International Journal of Heat and Mass Transfer. 1997; 40(13): 3163–3176.

57. Kuraan AM., Moldovan SI., Choo K. Heat transfer and hydrodynamics of free water jet impingement at low nozzle-to-plate spacings. International

Journal of Heat and Mass Transfer. Elsevier Ltd; 2017; 108: 2211–2216.

58. Zhou T., Xu D., Chen J., Cao C., Ye T. Numerical analysis of turbulent round jet impingement heat transfer at high temperature difference. Applied Thermal Engineering. Elsevier Ltd; 2016; 100: 55–61.

59. Huang, L., El-Genk, M. S. Heat transfer of an impinging jet on a flat surface. International Journal of Heat and Mass Transfer. 1994; 37(13): 1915–1923.

60. Lytle, D., Webb, B. W. Air jet impingement heat transfer at low nozzle-plate spacings. International Journal of Heat and Mass Transfer. 1994; 37(12): 1687–1697.

61. Guo, L., Yan, Y., Y., Zu, Y. Q. Effect of Narrow Jet Spacing on Impinging Flow and Heat Transfer. Volume 5: Heat Transfer, Parts A and B. 2011; : 1411–1419.

62. Behnia, M., Parneix, S., Shabany, Y., Durbin, P. A. Numerical study of turbulent heat transfer in confined and unconfined impinging jets. International Journal of Heat and Fluid Flow. 1999; 20(1): 1–9.

63. Wae-Hayee, M., Tekasakul, P., Eiamsa-ard, S., Nuntadusit C. Flow and Heat Transfer Characteristics of in-Line Impinging Jets With Cross-Flow At Short Jet-To-Plate Distance. Experimental Heat Transfer. 2014; 28(6): 511–530.

64. Jensen M V., Walther JH. Numerical Analysis of Jet Impingement Heat Transfer at High Jet Reynolds Number and Large Temperature Difference. Heat Transfer Engineering. 2013; 34(10): 801–809.

65. San, J., Y., Tsou, Y., M., Chen, Z. C. Impingement heat transfer of staggered arrays of air jets confined in a channel. International Journal of Heat and Mass Transfer. 2007; 50(19–20): 3718–3727.

66. Choo, K., Friedrich, B., K., Glaspell, A., W., Schilling, K. A. The influence of nozzle-to-plate spacing on heat transfer and fluid flow of submerged jet impingement. International Journal of Heat and Mass Transfer. Elsevier

Ltd; 2016; 97: 66–69.

67. Dutta, R., Dewan, A., Srinivasan B. Large Eddy Simulation of Turbulent Slot Jet Impingement Heat Transfer at Small Nozzle-to-Plate Spacing. Heat Transfer Engineering. 2016; 0(ja): 0.

68. Yong, S., Zhang, J., Z., Gong-Nan X. Convective heat transfer for multiple rows of impinging air jets with small jet-to-jet spacing in a semi-confined channel. International Journal of Heat and Mass Transfer. Elsevier Ltd; 2015; 86: 832–842.

69. Shin, C., H., Kim, K., M., Lim, S., H., Cho, H. H. Influences of nozzle-plate spacing on boiling heat transfer of confined planar dielectric liquid impinging jet. International Journal of Heat and Mass Transfer. Elsevier Ltd; 2009; 52(23–24): 5293–5301.

70. San, J., Y., Lai M. Optimum jet-to-jet spacing of heat transfer for staggered arrays of impinging air jets. International Journal of Heat and Mass Transfer. 2001; 44(21): 3997–4007.

71. Donaldson, C., D., Snedeker RS. A study of free jet impingement. part 1. mean properties of free and impinging jets. 1971; 45(2): 281–319.

72. Donaldson, C., D., Snedeker RS. A study of free jet impingement. Part 2. Free jet turbulent structure and impingement heat transfer. Journal of Fluid Mechanics. 1971; 45(3): 477–512.

73. Robinson, A., J., Schnitzler E. An experimental investigation of free and submerged miniature liquid jet array impingement heat transfer. Experimental Thermal and Fluid Science. 2007; 32(1): 1–13.

74. Hee Lee, D., Youl Won, S., Taek Kim, Y., Suk Chung Y. Turbulent heat transfer from a flat surface to a swirling round impinging jet. International Journal of Heat and Mass Transfer. 2001; 45(1): 223–227.

75. Wen, M., Y., Jang, K. J. An impingement cooling on a flat surface by using circular jet with longitudinal swirling strips. International Journal of Heat and

Mass Transfer. 2003; 46(24): 4657–4667.

76. Singh D., Premachandran B., Kohli S. Effect of nozzle shape on jet impingement heat transfer from a circular cylinder. International Journal of Thermal Sciences. Elsevier Masson SAS; 2015; 96: 45–69.

77. Lee, D., H. Song, J., Jo, M. C. The Effects of Nozzle Diameter on Impinging Jet Heat Transfer and Fluid Flow. Journal of Heat Transfer. 2004; 126(4): 554.

78. Koseoglu, M., F., Baskaya S. The role of jet inlet geometry in impinging jet heat transfer, modeling and experiments. International Journal of Thermal Sciences. Elsevier Masson SAS; 2010; 49(8): 1417–1426.

79. Whelan, B., P., Robinson, A. J. Nozzle geometry effects in liquid jet array impingement. Applied Thermal Engineering. Elsevier Ltd; 2009; 29(11–12): 2211–2221.

80. Yang, G., Choi, M., Lee, J. S. An experimental study of slot jet impingement cooling on concave surface: Effects of nozzle configuration and curvature. International Journal of Heat and Mass Transfer. 1999; 42(12): 2199–2209.

81. Attalla, M., Salem M. Effect of nozzle geometry on heat transfer characteristics from a single circular air jet. Applied Thermal Engineering. Elsevier Ltd; 2013; 51(1–2): 723–733.

82. Gulati, P., Katti, V., Prabhu, S. V. Influence of the shape of the nozzle on local heat transfer distribution between smooth flat surface and impinging air jet. International Journal of Thermal Sciences. Elsevier Masson SAS; 2009; 48(3): 602–617.

83. Hui, H, Kobayashi, T., Wu, S., Shen G. Changes to the vortical and turbulent structure of jet flows due to mechanical tabs. Proceedings of the Institution of Mechanical Engineers -- Part C. 1999; 213(4): 321–329.

84. Camci, C., Herr F. Forced Convection Heat Transfer Enhancement Using a Self-Oscillating Impinging Planar Jet. Journal of Heat Transfer. 2002;

124(August 2002): 770.

85. Göppert, S., Gürtler, T., Mocikat, H., Herwig H. Heat transfer under a precessing jet: Effects of unsteady jet impingement. International Journal of Heat and Mass Transfer. 2004; 47(12–13): 2795–2806.

86. Kanokjaruvijit, K., Martinez-Botas, R. F. Jet impingement on a dimpled surface with different crossflow schemes. International Journal of Heat and Mass Transfer. 2005; 48(1): 161–170.

87. Kanokjaruvijit, K., Martinez-Botas, R. F. Heat Transfer and Pressure Investigation of Dimple Impingement. ASME Conference Proceedings. 2005; 2005: 717–728.

88. Zhang D., Qu H., Lan J., Chen J., Xie Y. Flow and heat transfer characteristics of single jet impinging on protrusioned surface. International Journal of Heat and Mass Transfer. Elsevier Ltd; 2013; 58(1–2): 18–28.

89. Kim, W., S., Lee, S. Y. Behavior of a water drop impinging on heated porous surfaces. Experimental Thermal and Fluid Science. Elsevier Inc.; 2014; 55: 62–70.

90. Beitelmal, A., H., Saad, M. A. Effects of surface roughness on the average heat transfer of an impinging air jet. International Communications in Heat and Mass Transfer. 2000; 27(1): 1–12.

91. Celik, N. Effects of the surface roughness on heat transfer of perpendicularly impinging co-axial jet. Heat and Mass Transfer/Waerme- und Stoffuebertragung. 2011; 47(10): 1209–1217.

92. Xing,Y., Weigand, B. Experimental investigation of impingement heat transfer on a flat and dimpled plate with different crossflow schemes. International Journal of Heat and Mass Transfer. Elsevier Ltd; 2010; 53(19–20): 3874–3886.

93. El-Gabry, L., A., Kaminski, D. A. Experimental Investigation of Local Heat Transfer Distribution on Smooth and Roughened Surfaces Under an Array

of Angled Impinging Jets. Journal of Turbomachinery. 2005; 127(3): 532.

94. Sharif, M., A., R., Ramirez, N. M. Surface roughness effects on the heat transfer due to turbulent round jet impingement on convex hemispherical surfaces. Applied Thermal Engineering. Elsevier Ltd; 2013; 51(1–2): 1026–1037.

95. Spring, S., Xing, Y., Weigand B. An Experimental and Numerical Study of Heat Transfer From Arrays of Impinging Jets With Surface Ribs. Journal of Heat Transfer. 2012; 134(8): 82201.

96. Andrews, G., E., Abdul Hussain, R., A., A., Mkpadi, M. C. Enhanced Impingement Heat Transfer: The Influence of Impingement X/D for Interrupted Rib Obstacles (Rectangular Pin Fins). ASME Conference Proceedings. 2004; 2004(41685): 919–931.

97. Xing Y., Spring S., Weigand B. Experimental and numerical investigation of impingement heat transfer on a flat and micro-rib roughened plate with different crossflow schemes. International Journal of Thermal Sciences. Elsevier Masson SAS; 2011; 50(7): 1293–1307.

98. Caliskan S. Flow and heat transfer characteristics of transverse perforated ribs under impingement jets. International Journal of Heat and Mass Transfer. Elsevier Ltd; 2013; 66: 244–260.

99. Nuntadusit C., Wae-hayee M., Bunyajitradulya A., Eiamsa-ard S. Thermal visualization on surface with transverse perforated ribs. International Communications in Heat and Mass Transfer. Elsevier Ltd; 2012; 39(5): 634–639.

100. Wan, C., Rao, Yu., Chen P. Numerical predictions of jet impingement heat transfer on square pin-fin roughened plates. Applied Thermal Engineering. Elsevier Ltd; 2015; 80: 301–309.

101. Choi EY., Choi YD., Lee WS., Chung JT., Kwak JS. Heat transfer augmentation using a rib-dimple compound cooling technique. Applied

Thermal Engineering. Elsevier Ltd; 2013; 51(1–2): 435–441.

102. Akansu, Y., E., Sarioglu, M., Kuvvet, K., Yavuz T. Flow field and heat transfer characteristics in an oblique slot jet impinging on a flat plate. International Communications in Heat and Mass Transfer. 2008; 35(7): 873–880.

103. Bhagwat AB., Sridharan A. Numerical Simulation of Oblique Air Jet Impingement on a Heated Flat Plate. Journal of Thermal Science and Engineering Applications. 2016; 9(1): 11017.

104. Tong, A. Y. On the impingement heat transfer of an oblique free surface plane jet. International Journal of Heat and Mass Transfer. 2003; 46(11): 2077–2085.

105. Ingole SB., Sundaram KK. Experimental average Nusselt number characteristics with inclined non-confined jet impingement of air for cooling application. Experimental Thermal and Fluid Science. Elsevier Inc.; 2016; 77: 124–131.

106. Parida, P., R., Ekkad, S., V., Ngo K. Experimental and numerical investigation of confined oblique impingement configurations for high heat flux applications. International Journal of Thermal Sciences. 2011; 50(6): 1037–1050.

107. O'Donovan, T., S., Murray, B. D. Jet impingement heat transfer - Part I: Mean and root-mean-square heat transfer and velocity distributions. International Journal of Heat and Mass Transfer. 2007; 50(17–18): 3291–3301.

108. O'Donovan, T., S., Murray, B. D. Fluctuating fluid flow and heat transfer of an obliquely impinging air jet. International Journal of Heat and Mass Transfer. Elsevier Ltd; 2008; 51(25–26): 6169–6179.

109. Tu, J., Yeoh, G., Liu C. Computational Fluid Dynamics. A practical approach. Elsevier. 2008;

110. Hadžiabdić, M., Hanjalić K. Vortical structures and heat transfer in a round impinging jet. Journal of Fluid Mechanics. 2008; 596: 221–260.

111. Cengel, Yunus A., Boles, A. M. Thermodynamics : an engineering approach. Seventh Ed. 2007.

112. Alimohammadi, S., Murray, D., B., Persoons T. Experimental Validation of a CFD Methodology for Transitional Flow Heat Transfer Characteristics of a Steady Impinging Jet. Journal of Heat Transfer. 2014; 136: 1–35.

113. Bovo, M. On the numerical modelling of impinging jets heat transfer. 2011;

114. SHADLESKY, P. S. Stagnation point heat transfer for jet impingement to a plane surface. AIAA Journal. American Institute of Aeronautics and Astronautics; 1 August 1983; 21(8): 1214–1215.

115. Viskanta R. Heat transfer to impinging isothermal gas and flame jets. Experimental Thermal and Fluid Science. 1993; 6(2): 111–134.

116. Goldstein, R., J., Franchett, M. E. Heat Transfer From a Flat Surface to an Oblique Impinging Jet. Journal of Heat Transfer. ASME; 1 February 1988; 110(1): 84–90. Available at: http://dx.doi.org/10.1115/1.3250477

117. Beitelmal, A., H., Saad, M., A., Patel, C. D. The effect of inclination on the heat transfer between a flat surface and an impinging two-dimensional air jet. International Journal of Heat and Fluid Flow. 2000; 21(2): 156–163.

118. Popiel, C., O., Trass O. Effect of ordered structure of turbulence on momentum, heat and mass transfer of impinging round jets. Heat Transfer Conf. 1982; 6: 141–146.

119. Popiel, C., O., Trass O. Visualization of a free and impinging round jet. Experimental Thermal and Fluid Science. 1991; 4(3): 253–264.

120. Livingood, J., Hrycak P. heat transfer between a flat plate and jets of air impinging on it. Intl. Developments in Heat Transfer, Int. Heat Transfer Conf., University of Colorado, CO, USA. 1962; : 454–460.

121. Schlunder, E., U., Gnielinski V. Heat and mass transfer between surfaces and impinging jets. Chem./ng. Tech.,. 1967; 39: 578–584.

122. Goldstein, R., J., Behbahani, A. I. Impingement of a circular jet with and without cross flow. International Journal of Heat and Mass Transfer. 1982; 25(9): 1377–1382.

123. Hollworth, B., R., Gero, L. R. Entrainment effects on impingement heat transfer. Part 2. Local heat transfer measurements. J. Heat Transfer Trans. ASME. 1985; 107: 910–915.

124. Xu, P., Sasmito, A. P., Qiu S., Mujumdar, A. S., Xu L., Geng L. Heat transfer and entropy generation in air jet impingement on a model rough surface. International Communications in Heat and Mass Transfer. Elsevier Ltd; 2016; 72: 48–56.

125. Ekkad, S. V., Kontrovitz D. Jet impingement heat transfer on dimpled target surfaces. International Journal of Heat and Fluid Flow. 2002; 23(1): 22–28.

126. Zhang, Y., Wei, J., Kong, X., Guo L. Confined Submerged Jet Impingement Boiling of Subcooled FC-72 over Micro-Pin-Finned Surfaces. Heat Transfer Engineering. 2016; 37(3–4): 269–278.

127. Lee, J., Jung, S., Y., Sung, H., J., Zaki, T. A. Turbulent thermal boundary layers with temperature-dependent viscosity. International Journal of Heat and Fluid Flow. 2014; 49(C): 43–52.

128. Martin, H. Heat and mass transfer between impinging gas jets and solid surfaces. In: Advances in heat transfer. Volume 13. New York. 1977; 13: 1–60.

129. ANSYS FLUENT User’s Guide. 2013;

130. Katti V., Prabhu, S. V. Heat transfer enhancement on a flat surface with axisymmetric detached ribs by normal impingement of circular air jet. International Journal of Heat and Fluid Flow. 2008; 29(5): 1279–1294.

131. Gau C., Lee, I. C. Flow and impingement cooling heat transfer along triangular rib-roughened walls. International Journal of Heat and Mass Transfer. 2000; 35(11): 3009–3020.

132. Zhou, J. W., Wang, Y. G., Middelberg G., Herwig H. Unsteady jet impingement: Heat transfer on smooth and non-smooth surfaces. International Communications in Heat and Mass Transfer. 2009; 36(2): 103–110.

133. Gupta, S., Chaube, A., Verma P. Review on heat transfer augmentation techniques: Application in gas turbine blade internal cooling. Journal of Engineering Science and Technology Review. 2012; 5(1): 57–62.

134. Won, S., Y., Mahmood, G., I., Ligrani, P. M. Spatially-resolved heat transfer and flow structure in a rectangular channel with pin fins. International Journal of Heat and Mass Transfer. 2004; 47(8–9): 1731–1743.

135. Yang, Q., Wang M. Computational Study of Roughness-Induced Boundary-Layer Noise. AIAA Journal. 2009; 47(10): 2417–2429.

136. Wang Z. Secondary flow and extra heat transfer enhancement of ribbed surface after jet impingement. 2016; : 1–8.

137. Sanyal, A., Srinivasan, K., Dutta P. Numerical study of heat transfer from pin-fin heat sink using steady and pulsated impinging jets. IEEE Transactions on Components and Packaging Technologies. 2009; 32(4): 859–867.

138. Yang, K., S., Chu, W., H.Chen, I. Y., Wang, C. C. A comparative study of the airside performance of heat sinks having pin fin configurations. International Journal of Heat and Mass Transfer. 2007; 50(23–24): 4661–4667.

139. Rao Y., Chen P., Wan C. Experimental and numerical investigation of impingement heat transfer on the surface with micro W-shaped ribs. International Journal of Heat and Mass Transfer. Elsevier Ltd; 2016; 93:

683–694.

140. Yilbas BS., Arif AFM., Abdul Aleem BJ. Laser cutting of sharp edge: Thermal stress analysis. Optics and Lasers in Engineering. Elsevier; 2010; 48(1): 10–19.

141. Sheikh-Ahmad J., Chipalkati P. Effect of Cutting Edge Geometry on Thermal Stresses and Failure of Diamond Coated Tools. Procedia Manufacturing. Elsevier B.V.; 2015; 1(Cvd): 663–674. Available at: DOI:10.1016/j.promfg.2015.09.071

142. Yaras, M. I. Measurements of Surface-Roughness Effects on the Development of a Vortex Produced by an Inclined Jet in Cross-Flow. Journal of Fluids Engineering. 2004; 126(May 2004): 346–354.

143. Schueren, S., Hoefler, F., Wolfersdorf, J., V., Naik S. Heat Transfer in an Oblique Jet Impingement Configuration With Varying Jet Geometries. Journal of Turbomachinery. 2012; 135(2): 21010.

144. Krishna, K., Ricklick, M. A. Preliminary Investigation of an Oblique Jet Impingement Cooling on a CMC Rough Surface. 52nd AIAA/SAE/ASEE Joint Propulsion Conference. 2016; (m): 1–17.

145. Haiping, C., Taiping, H., Jingyu, Z., Dalin Z. Flow visualization of a round jet impinging on cylindrical surfaces. Experimental Thermal and Fluid Science. 1999; 20(2): 66–78.

146. Obot, N., T., Trabold, T. A. Impingement Heat Transfer Within Arrays of Circular Jets: Part 1—Effects of Minimum, Intermediate, and Complete Crossflow for Small and Large Spacings. ASME. J. Heat Transfer. 1987; 109: 872–879.

147. Chen, J., Shi, Li., Hasemann, H., Rautenberg M. EXPERIMENTAL INVESTIGATION ON IMPINGEMENT HEAT TRANSFER FROM RIB ROUGHENED SURFACE WITHIN ARRAYS OF CIRCULAR JET: Effect of Geometric Parameters. 1994;

148. Chyu, M., K., Yu, Y., Ding, H., Beach, W. P. Concavity enhanced heat transfer in an internal cooling passage. 2016; : 1–7.

149. Foss, J. F. Measurement in a large-angle oblique jet impingement flow. AIAA Journal. 1979; 17(8): 801–802.

150. Kleis, J., F., FOSS; S. J. Mean Flow Characteristics for the Oblique Impingement of an Axlisymmetric Jet. AIAA Journal. 1976; 14(6): 705–706.